DISSERTATION

Tracing dust in old stellar populations

The mid-infrared spectrum of globular cluster AGB stars

Verfasser

Mag. Hannes Richter, MA

angestrebter akademischer Grad

Doktor der Naturwissenschaften (Dr. rer. nat.)

Wien, im Dezember 2010

Mag. Hannes Richter, MA
Institut für Astronomie
Türkenschanzstraße 17
A-1180 Wien, Österreich
Email: hannes.richter@univie.ac.at

Made with LaTeX on a Mac.

To my grandparents

Anni-Oma & Otto-Opa
Mila-Hamma & Franzi-Opa

"The line [must|has to] be drawn here! This far and no further!"

Jean-Luc Picard & *Quark*, respectively
in *Star Trek: First Contact* & *Star Trek: Deep Space Nine*, respectively

&

Hannes Richter
at the very moment of finishing his PhD

Acknowledgement

Contents

Abstract

Asymptotic Giant Branch (AGB) stars are considered to be the main stellar dust producers in the universe. Their dusty circumstellar shells leave fingerprints in the mid-infrared (MIR) spectra of AGB stars and in unresolved old stellar populations. Bressan et al. (2007) showed that co-added MIR-spectra of AGB stars of known luminosity, metallicity and age (like those found in the Galactic globular cluster NGC 104) can be used to model the $10\,\mu$m dust excess in early-type galaxies. This work aims to improve our understanding of the MIR-spectra of old stellar populations with respect to their metallicities by studying a large sample of AGB stars in Galactic globular clusters.

A sample of AGB stars (taken from Lebzelter et al. 2006 and Sloan et al. 2010) is used to produce co-added MIR-spectra of globular cluster combinations for three metallicity groups. Each group consists of several globular clusters with similar age and metallicity. Combining the clusters leads to a higher number of AGB stars with available *Spitzer* spectra in each group. The low metallicity group (Z = 0.0038) consists of five globular clusters with 18 AGB star spectra, the intermediate (Z = 0.0058) and high (Z = 0.01) metallicity groups both include three clusters with eight and seven available MIR-spectra, respectively.

Stars within the 90% mass radius of each globular cluster are used to generate 2MASS Color-Magnitude diagrams (CMDs) of each cluster combination. Binning the stars in the CMDs with respect to their M_K-values results in Luminosity Functions (LFs) for the cluster combinations. The LFs based on 2MASS data are compared to LFs obtained using theoretical isochrones from the Padova group (Bertelli et al. 2008, Marigo et al. 2008). Using the 2MASS LFs integrated MIR-spectra of the three globular cluster combinations are derived by weighting the existing spectra with the total number of AGB stars within each M_K-bin of the LFs along the upper giant branch. This relies on the assumption that stars that occupy the same area in the CMD are comparably evolved and have similar MIR-spectra. The excellent coverage of the AGB in NGC 104, both photometrically and spectroscopically, allows to investigate the effect of various weighting methods like different LFs or assumptions on the frequency of TP-AGB stars in their minimum phase. In this context it is also possible to reproduce the flat dust excess and the reduced silicate domination found in early-type galaxies. For the intermediate and high metallicity groups such a study is not successful due to the limited number of spectra available in these groups.

We report that all co-added MIR-spectra are dominated by a prominent dust excess due to silicate grains present in the stellar outflows. The excess increases with increasing metallicity. A future perspective of the project would be to achieve a more complete observational coverage of stars evolving up the AGB at intermediate metallicities, which would lead to a further improved understanding of the integrated MIR-spectra of old unresolved stellar populations in general. The thesis is completed by first model calculations to predict the MIR-spectrum using the wind code by H.-P. Gail.

Zusammenfassung

In den ausgedehnten Atmosphären und kühlen stellaren Winden von Sternen am sog. Asymptotischen Riesenast (engl. Asymptotic Giant Branch, AGB) bieten sich optimale Bedingungen für die Entstehung von kosmischen Festkörpern. Diese Staubpartikel hinterlassen ihre Spuren in den mittleren Infrarot (MIR) Spektren von alten stellaren Populationen. Die MIR-Spektren der AGB-Sterne des Kugelsternhaufens NGC 104 konnten beispielsweise für die Erklärung des $10\,\mu$m-Infrarot-Exzesses in alten Galaxien verwendet werden. Im Rahmen dieser Dissertation soll der Einfluss der Metallizität auf das MIR-Spektrum von alten stellaren Populationen untersucht werden.

Die Grundlage für die Erstellung von integrierten MIR-Spektren bildet eine Auswahl von AGB-Sternen aus verschiedenen Kugelsternhaufen (Lebzelter et al. 2006 und Sloan et al. 2010). Diese werden entsprechend ihrer Metallizität und ihres Alters in drei Gruppen zusammengefasst. Dadurch beinhalten die jeweiligen Sternhaufen-Kombinationen eine größere Anzahl von mit dem Weltraumteleskop *Spitzer* beobachten AGB-Stern-Spektren.

Für die Erstellung von Farben-Helligkeitsdiagrammen der drei Kugelsternhaufen-Kombinationen werden die Sterne innerhalb des 90%-Massenradius der jeweiligen Sternhaufen verwendet. Um Leuchtkraftfunktionen (LFs) zu erstellen, können die Sterne anhand ihrer K-Magnitude in kleine Helligkeitsintervalle aufgeteilt werden. Diese auf 2MASS-Daten basierenden LFs werden in weiterer Folge mit LFs verglichen, die mittels theoretischer Isochronen der Padova-Gruppe (Bertelli et al. 2008, Marigo et al. 2008) berechnet werden.

Für die drei Kugelsternhaufen-Kombinationen werden mittels der 2MASS-Daten integrierte MIR-Spektren erstellt. Dafür werden die einzelnen Spektren der beobachteten AGB-Sterne mit der Sternanzahl aus den passenden LF-Intervallen gewichtet. Dies erfolgt unter der Annahme, dass Sterne mit gleicher Position im Farben-Helligkeitsdiagramm gleiche oder ähnliche MIR-Spektren aufweisen.

Die ausgezeichnete photometrische und spektroskopische Erfassung von NGC 104 erlaubt die Erforschung von unterschiedlichen Gewichtungsarten, wie beispielsweise diverser LFs oder verschiedener Häufigkeiten von TP-AGB-Sternen im Helligkeitsminimum. In diesem Zusammenhang ist es möglich, den flachen Staub-Exzess zu reproduzieren, wie er auch in Early-Type-Galaxien gefunden werden kann. Für die beiden Kugelsternhaufen-Kombinationen mit höherer Metallizität ist eine derartige Untersuchung aufgrund der geringen Anzahl an vorhandenen MIR-Spektren nicht möglich.

Alle integrierten MIR-Spektren werden von Silikat-Staubbanden dominiert. Der Staub-Exzess nimmt mit steigender Metallizität zu. Als Perspektive für unsere Forschung gilt es, für mehr Beobachtungsmaterial von Sternen, die sich am AGB befinden, zu sorgen. Dies würde zum besseren Verständnis von integrierten MIR-Spektren alter Sternpopulationen beitragen. Ein erster Vergleich mit synthetischen Sternspektren zeigt eine weitere Zugangsmöglichkeit auf und bildet einen Ausblick auf künftige Projekte.

Chapter 1

Introduction

This thesis deals with stars in the evolutionary phase of the Asymptotic Giant Branch (AGB). A brief introduction on stellar evolution is given here, however I refer to the comprehensive reviews of Iben & Renzini (1983), Iben (1991), Herwig (2005) and the book of Habing & Olofsson (2003) for a more detailed description. The important role of dust on the mid-infrared (MIR) spectra of AGB stars and old stellar populations in general is presented in order to set the stage for the main part of this study.

1.1 Asymptotic Giant Branch Stars

Stellar evolution can be illustrated using a Hertzsprung-Russel diagram (HRD) presenting the evolutionary tracks of stars with different masses (Fig. 1.1). Stars spend most of their lifetime on the main sequence[1] in a hydrostatic and thermal equilibrium, burning hydrogen (H) to helium (He) by nuclear fusion in the stellar core. As the H-burning ceases in the center, the He-core contracts and heats up resulting in a H-burning shell around the core of the star. The formation of the H-burning shell causes the star to become larger and cooler. In the HRD the star leaves the main sequence and moves to the upper right corner of the diagram, reaching the Red Giant Branch (RGB) phase. At the tip of the RGB, the fusion of He to carbon (C) and subsequently oxygen (O) in the He-core sets in.

Depending on the mass of the star, the nuclear fusion starts quite dramatically causing a He-core-flash ($M \approx 0.8 - 2.5\,M_\odot$) or more quiescent ($M \approx 2.5 - 8\,M_\odot$)[2]. In the low mass case the star's luminosity decreases moving the star to the horizontal branch or the red clump[3]. Stars

---

[1] The zero-age main sequence can be interpreted as the connection of the starting points of the evolutionary tracks in Fig. 1.1.

[2] More massive stars evolve to red supergiants and eventually explode as a supernova (cf. the evolutionary track for $25\,M_\odot$ in Fig. 1.1). Their different evolution is not discussed here.

[3] The position on the horizontal branch or the red clump depends on the metallicity of the star and its mass-loss on the RGB.
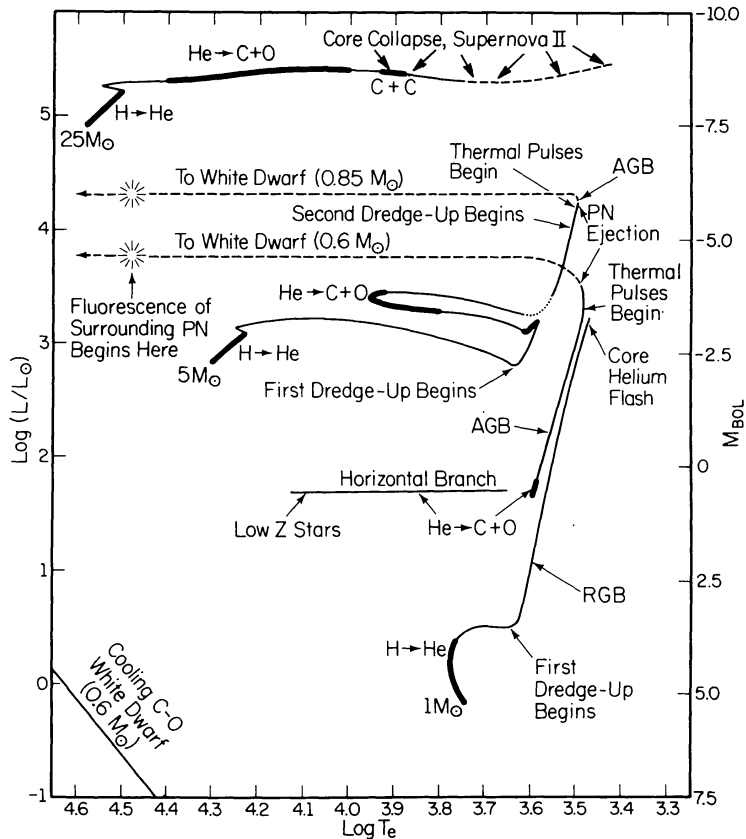
Figure 1.1: Hertzsprung-Russel diagram with typical evolutionary tracks for stars of different masses ranging from 1 to $25\,M_\odot$ (taken from Iben 1991). Stars with low to intermediate masses $(\approx 0.8-8\,M_\odot)$ reach the AGB stadium and are the main actors in this study.

with masses above the He-core-flash limit do not decrease their luminosity significantly and oscillate between warmer and cooler regions in the HRD. When He is exhausted in the core, the He-burning ceases and the developing He-burning shell around a CO-core causes the envelope of the star to expand. The star has now two burning shells (H and He) and becomes redder and cooler moving towards the upper right part of the HRD reaching the evolutionary phase of the AGB.

The AGB phase is short compared to the whole lifetime of a low or intermediate mass star and amounts only to 10^6-10^7 years (Vassiliadis & Wood 1993), nevertheless it is characterized by several important phenomena such as pulsation, mass-loss and the production of a variety of elements and dust particles. Fig. 1.2 shows a schematic view of the structure of an AGB star. In the center we find a degenerated CO core surrounded by a narrow zone where nuclear reactions take place. On top of this configuration sits an extended convective H-envelope and, finally, the large and tenuous stellar atmosphere.

During the early-AGB stage, primarily the He-burning shell is responsible for the energy supply and causes a steady expansion of the outer envelope. Thus, the stars evolve up along the AGB increasing their size and luminosity while their temperature decreases[4]. The stars are experiencing radial pulsations leading to large amplitude changes in their stellar flux. Almost

---

[4] At the tip of the AGB the luminosities reach values around $10^4\,M_\odot$, radii of a few $100\,R_\odot$ and effective temperatures of typically $2500-3500\,K$.
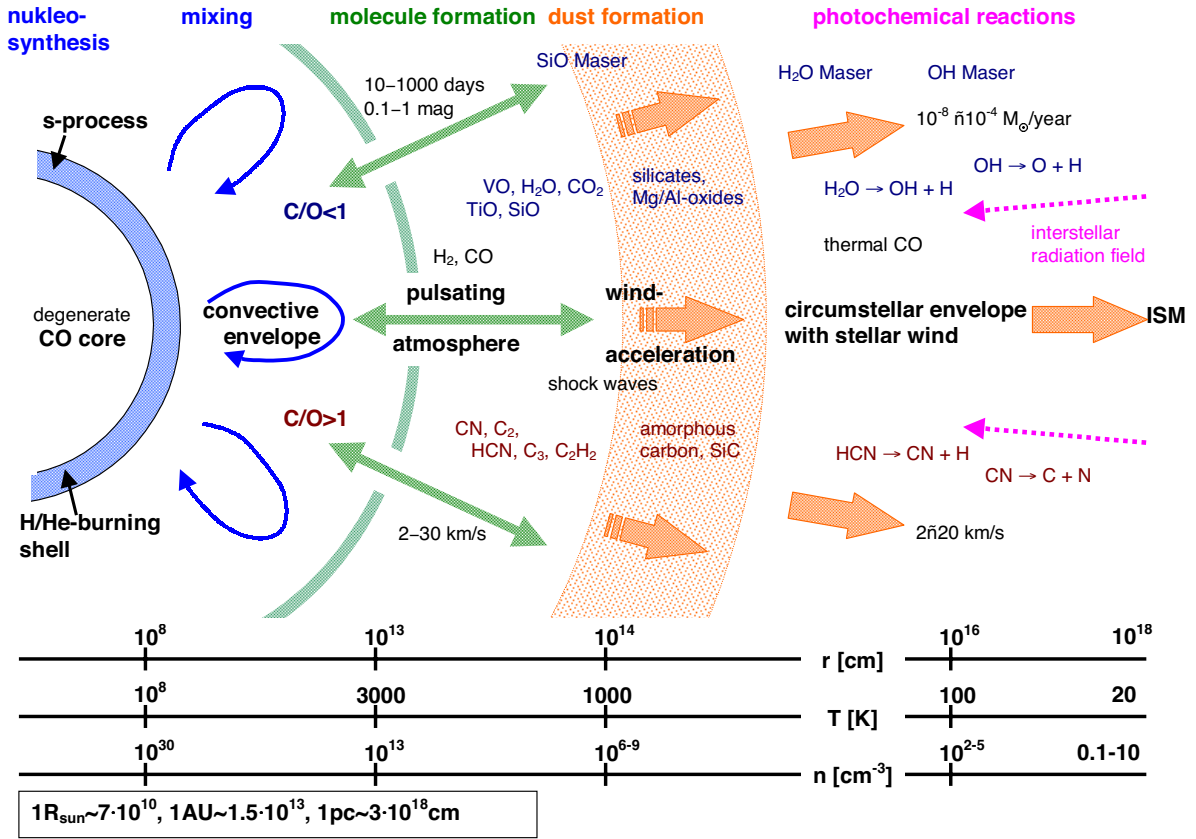
Figure 1.2: Schematic view of an AGB star (J. Hron, private communication).

all AGB stars are found to be variables and particulary distinctive flux variations are present in the so-called Mira variables with amplitudes up to 10 mag in the visual. Towards longer wavelengths the flux variations decrease to $0.5 - 1$ mag in the infrared (Le Bertre 1992)[5]. The light changes occur on long time scales of few 10 to several 100 days, thus, pulsating AGB stars are often referred to as long period variables (LPVs). While the variations are prominent in Mira stars, they are less distinctive in semiregular variables (SRVs).

At the end of the AGB phase the He-burning shell becomes thermally instable resulting in thermal pulses where explosive He-burning in the shell occurs repeatedly. During this short period the H- and He-burning shell ignite alternating and the nuclear active region around the CO-core produces heavy elements via the s-process (cf. Herwig 2005). An extended convective envelope allows the products of the nucleosynthesis to be mixed up from the stellar interior to the outer parts of the star. This dredge-up influences the chemical composition of the atmosphere and is responsible for the transition from O-rich to C-rich AGB stars. Starting with an O-rich ($C/O < 1$) composition in M-stars, the stars become S-stars ($C/O \approx 1$) and finally C-rich ($C/O > 1$) during the thermal pulse phase. Only a small fraction of all known AGB stars are C-stars due to short duration of the TP-AGB phase and the restricted mass range ($\approx 1.5 - 4\,M_\odot$) where stars can become C-stars (cf. Fig. 2 in Herwig 2005).

---

[5]Cf. Section 2.2.5 for details on the mean amplitude of Mira stars.

During the thermal pulse AGB phase strong stellar winds with typical velocities of $10-20\,\mathrm{km\cdot s^{-1}}$ develope and result in a mass-loss process that finally ends the AGB evolution. As the star expells its outer parts and loses most of its envelope it enters the post-AGB phase and eventually becomes a planetary nebula (PN). The stellar core is more or less unaffected by this envelope ejection and ends up as a white dwarf (cf. Fig. 1.1).

1.2 AGB Stars as Dust Factories

Evolved stars of low and intermediate mass are considered to be the main dust producers in the universe. In their extended atmospheres and cool stellar winds one finds perfect conditions for the condensation of dust. The evolution along the AGB is characterised by two observational facts, namely the occurrence of large amplitude pulsations and the presence of expanding dusty circumstellar envelopes. This evidence is at the base of the standard model of mass-loss in AGB stars where radial pulsation levitates matter out to a radius where dust forms and is accelerated outwards by radiation pressure, dragging the gas along.

While this standard model by Habing (1996) is well accepted, details of the process are still a matter of debate. An open issue is whether there is a steady production of dust or whether there are episodes of enhanced dust production. Both, observations (Leão et al. 2006) and dynamical model atmospheres (e.g. Sandin & Höfner 2003) indicate a quite complex nature of the dust formation and mass-loss process. Recent studies point to the presence of large dust grains of sizes around $1\,\mu\mathrm{m}$ that are efficiently driving the mass-loss around O-rich AGB stars (Höfner 2008).

The ejection of gas and dust leads to the formation of circumstellar shells that leave their fingerprints in the MIR-spectra of AGB stars. Depending on the chemistry of the stars, the C/O-ratio determines the dust species that are formed, as the less abundant element is blocked in the very stable CO molecule. Thus, in an O-rich environment silicates and iron-oxides are produced, while a C-rich environment leads to the formation of carbonaceous dust. In the circumstellar shells of AGB stars the dust particles lead to a significant change of the spectral energy distribution (SED) compared to 'naked' objects which are considered to be dust free. Dust absorbs efficiently at blue and visual wavelengths attenuating the stellar radiation and reradiates corresponding emission in the MIR leading to the manifestation of the MIR excess present in the spectra of dusty AGB stars (cf. Section 1.3) and old stellar populations like early-type galaxies (cf. Section 1.4).

The most common dust formed in M-stars is amorphous silicate (Molster & Waters 2003). However, silicate dust formation directly from the gas phase is not possible, it requires first the formation of condensation seeds. Gail & Sedlmayr (1998) proposed that in O-rich winds clusters of titanium dioxide (TiO_2, rutile modification) could act as condensation nuclei for astronomical silicates. Also alumina dust (Al_2O_3) could serve as a seed material, although it is not clear whether a condensation from the gas phase is really possible or if grain mantle reactions lead to the formation of Al_2O_3 particles (Jeong et al. 1999). While rutile has not been detected in the outflows of evolved stars so far, there is evidence of the presence of alumina dust in the spectra of AGB stars (cf. Section 1.3 and 2.3).

Beside the common amorphous silicates also crystalline silicates could be detected in the circumstellar shells of AGB stars. The two most abundant species are forsterite (Mg_2SiO_4) and enstatite ($MgSiO_3$), which are both iron-free, while there is no evidence for crystalline ferrosilica dust implying that iron-rich silicates in the form of [Mg,Fe]O are primarily amorphous (Molster & Waters 2003). Other dust species that are expected to form in O-rich AGB stars are e.g. spinel ($MgAl_2O_4$), SiO_2 and metallic Fe[6].

In the C-rich domain one of the first detected dust species was SiC (Gilra 1973). Subsequently other carbonaceous dust species like e.g. FeS and MgS were reported to form in the outflows of C-stars. The prominent $21\,\mu m$ feature present in several C-stars is often related to TiC, SiS_2 or nano-diamonds, however a clear identification of the carrier was not possible so far (Molster & Waters 2003). Also amorphous carbon is present in C-rich stars and manifests as extra source of opacity in their MIR-spectra, although it lacks of a clear spectroscopic signature. Further details on the formation and the properties of C-rich dust are not presented here because this thesis focuses on the MIR-spectra of globular cluster AGB stars which are typically O-rich due to their low masses[7].

1.3 A Dust Sequence Along the AGB

Lebzelter et al. (2006) were the first to present a detailed observational study of how the dust composition changes when the star evolves along the AGB. This work was based on *Spitzer* spectroscopy of AGB stars in the globular cluster NGC 104 (47 Tuc). Globular clusters provide well-defined, homogeneous parameters such as metallicity, ages and distances. Thus, they are perfectly suited to investigate the interrelation between dust composition, stellar variability, and evolutionary status of an AGB star. Lebzelter et al. (2006) observed twelve AGB stars distributed over a wide range in the Period-Luminosity plane. The upper left panel of Fig. 1.3 presents the positions of their targets in the $(\log P, K)$-diagram. Here the stars with lower luminosities are populating the overtone sequence (B) while high luminosity AGB stars are found to pulsate with the fundamental mode (C).

To obtain the dust residuals of the AGB stars, blackbodies resembling the stellar photospheres where subtracted from the MIR-spectra. In the resulting MIR dust excess we see the fingerprints of various dust species at 9.7, 11.5 and $13\,\mu m$. In addition a broad dust feature is located at 16-18 μm in these objects (see Fig. 1.3). However, not all dust features are visible in all AGB stars of the sample. Lebzelter et al. (2006) reported that this points to a well defined sequence of circumstellar dust species shaping the MIR dust residuals as the stars evolve along the AGB. The dust composition seems to be correlated with the position within the $(\log P, K)$-diagram. Early on the AGB we see the signatures of Mg, Al and Iron oxides (V4, V8, V13) while fainter stars do not show any dust excess and are considered to be dust free (V5, V6, V7). With further evolution amorphous silicates become the dominant species (V1, V2). The observations indicate that the $13\,\mu m$ feature appears in the least evolved stars, later loses its importance relative to the $11.5\,\mu m$ silicate peak, and finally vanishes completely in the high luminosity stars which show a prominent $9.7\,\mu m$ silicate emission only.

---

[6] See also Section 2.3 for a list of possible dust features present in the MIR-spectra of the globular cluster AGB stars this thesis is based on.

[7] A detailed discussion of carbonaceous (and also O-rich) dust can be found in the comprehensive books of Henning (2003) and Habing & Olofsson (2003).
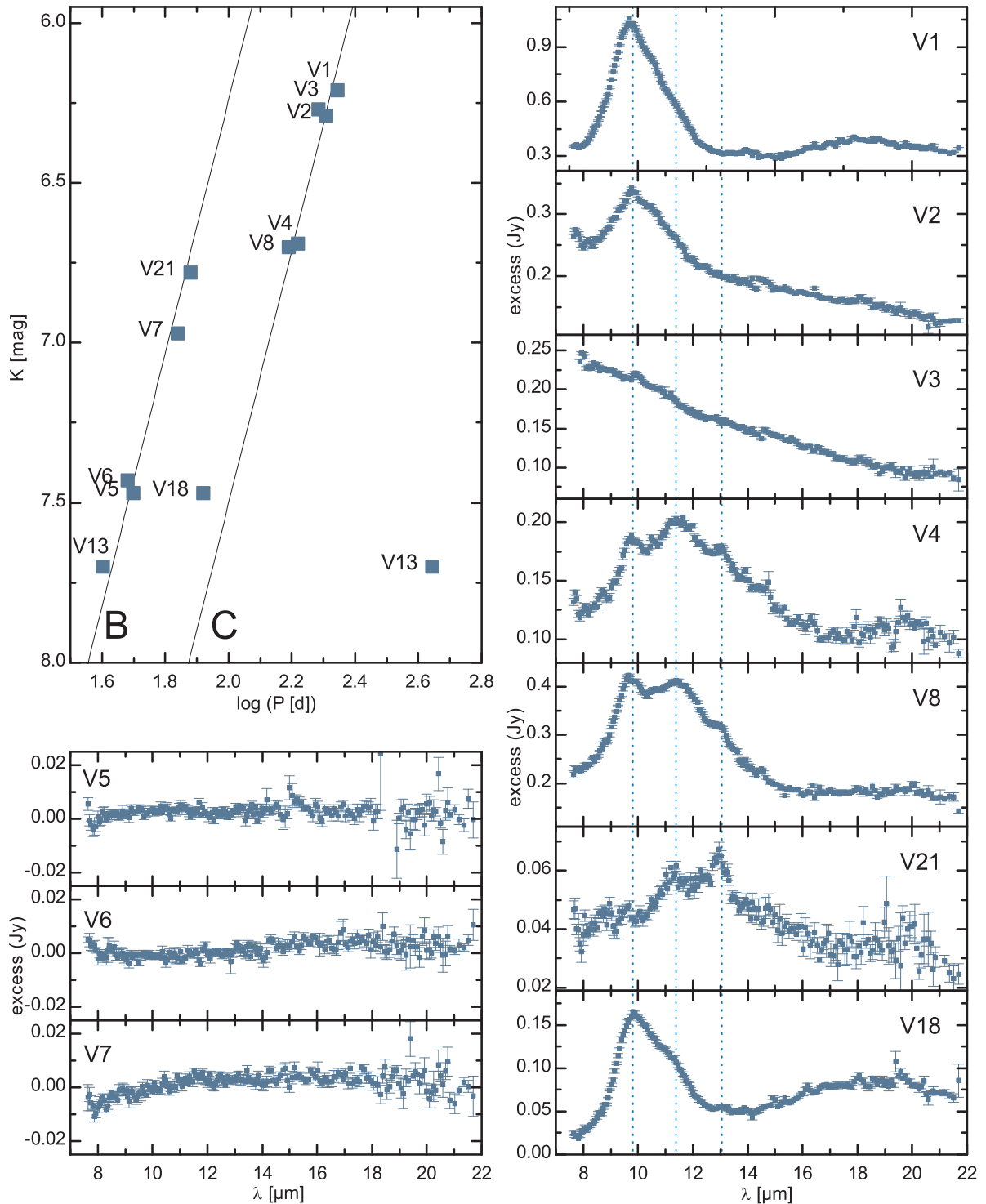
Figure 1.3: Development of the dust spectra in NGC 104 (Figure adapted after Lebzelter et al. 2006). Top left panel: Period-Luminosity diagram of the observed globular cluster AGB stars. The solid lines mark the position of the overtone-mode (B) and the fundamental-mode (C) pulsators. Right panel and bottom left panel: Dust residuals of the *Spitzer* spectra of the AGB stars in NGC 104. Possible dust feature positions at 9.7, 11.5, and 13 μm are indicated.
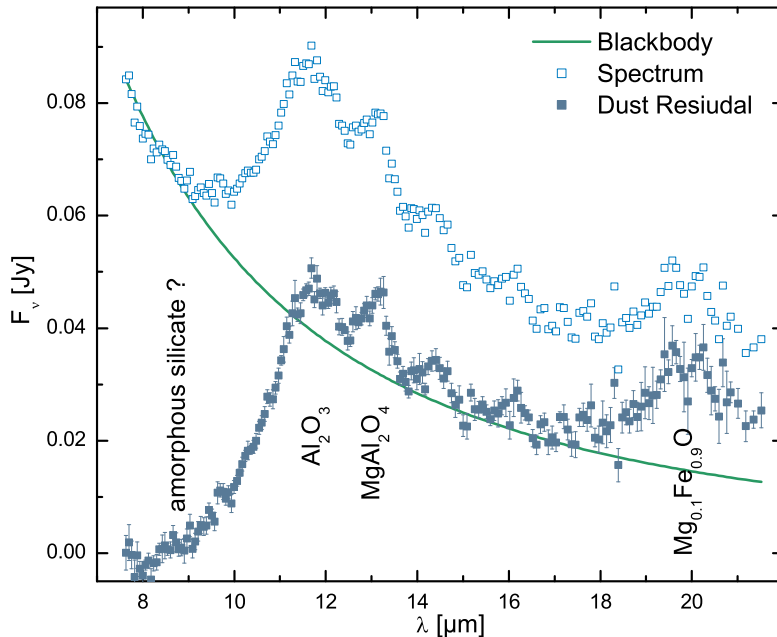
Figure 1.4: *Spitzer* spectrum and dust residual of the globular cluster AGB star NGC 104 V13 (Figure adapted after Lebzelter et al. 2006). The green line gives the blackbody used for the subtraction of the stellar photosphere. Possible dust species as carriers of the features are indicated at the peak positions. Amorphous silicate is not present in the MIR-spectrum of this particular star.

While there seems to be a clear relation between evolutionary phase along the AGB and the observed dust features, there are a few indications for a more complex behaviour and short time changes in the MIR-spectra of the NGC 104 AGB stars. The star V3 showed an unexpectedly weak silicate feature although it is positioned close to the tip of the AGB. A second star, V8, shows clear dust features fitting well into the proposed dust evolution scenario, while V8 showed no obvious dust features on a ground based MIR observation (van Loon et al. 2006).

The effective dust production is reported to start only after the star reaches the luminosity of V21 (2000 $L_\odot$). However, there are two AGB stars that show dust features although they are located below this limit. V13 and V18 show a high MIR excess in relation to their position in the ($\log P, K$)-diagram. Fig. 1.4 presents the spectrum of V13 together with the dust residual derived after subtracting a blackbody. The MIR excess is clearly dominated by peaks at 11.5, 13 and 20 μm with Al_2O_3, $MgAl_2O_4$ and $Mg_{0.1}Fe_{0.9}O$ as possible carriers. The origin of the peculiar MIR-spectrum of V13 remains unclear, since the only remarkable characterisitc of the star is its long secondary pulsation period (Lebzelter & Wood 2005).

The second peculiar AGB star, V18, shows a strong silicate feature at 9.7 μm comparable to the MIR-spectra of the most luminous stars of this study. Lebzelter et al. (2006) suggested that V18 is currently undergoing a thermal pulse event leading to an interpulse luminosity and, thus, to the strange position in the Period-Luminosity diagram[8].

A comparable study was carried out by Blommaert et al. (2006). They investigated a homogenious sample of fifty AGB stars in the Galactic Bulge using *Spitzer*. The targets where first detected in the ISOGAL survey which provided a point source catalogue in the near-infrared (NIR) and MIR (Omont et al. 2003). The observed subset of the ISOGAL sources is attributed to the 'intermediate' Galactic Bulge and, thus, are considered to belong to the Bulge stellar

---

[8] see also Sections 5.1 and 5.4 for a discussion on the impact of luminosity variations of thermal pulse AGB stars on the co-added MIR-spectrum of entire stellar populations.
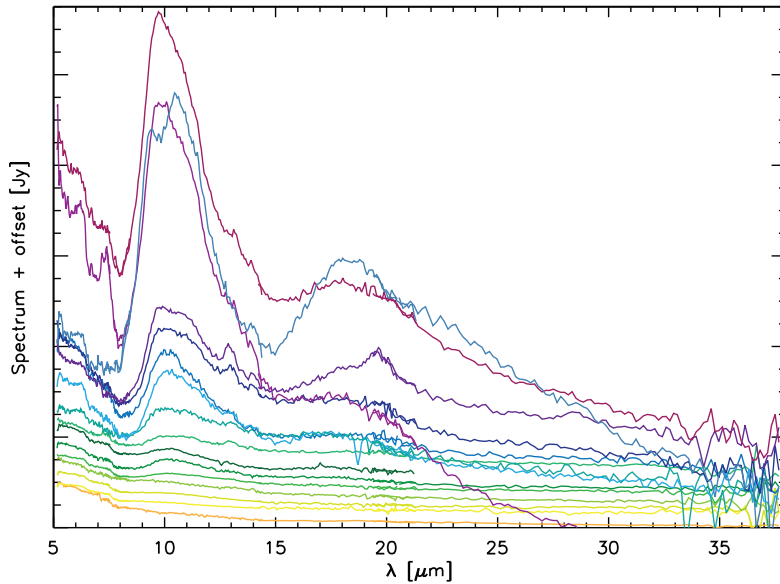
Figure 1.5: *Spitzer* spectra of Galactic Bulge AGB stars with increasing dust luminosities (Figure adapted after Blommaert et al. 2006). The spectra show a variety of dust features at 9.7, 11.5, 13 and 19.5 μm. Also a broad dust emission due to amorphous silicate is present at 16-20 μm.

population with a very narrow mass range. Groenewegen & Blommaert (2005) showed that these stars cover a mass interval ranging from 1.5 to 2 $M_\odot$. Thus, the main difference between the stars of their sample is their age on the AGB which allowed for the investigation of the evolution of Bulge AGB stars and their circumstellar shells in order to derive a dust evolution scenario similar to the study performed by Lebzelter et al. (2006). In addition Blommaert et al. (2006) were able to determine the mass-loss rates of their sample starting from the onset of dust mass-loss at $10^{-8}\,M_\odot\mathrm{yr}^{-1}$ up to mass-loss rates of $10^{-4}\,M_\odot\mathrm{yr}^{-1}$.

The resulting MIR-spectra of a subset of the sample from Blommaert et al. (2006) are presented in Fig. 1.5 and include spectral features of alumina and magnesium-iron oxides together with amorphous and various crystalline silicates. The authors reported a rough sequence of dust features as a function of increasing mass-loss rates. Similar to the results of Lebzelter et al. (2006) alumina dust is mainly found at low luminosities while amorphous silicate features dominate the high luminosity regime with high mass-loss rates. For intermediate mass-loss rates a mixture of alumina and silicate dust features is visible in the MIR-spectra. The 13 μm feature is reported to occur in a limited mass-loss and luminosity range.

Further insight in the dust formation in O-rich outflows of red giant stars was also provided by the study of Heras & Hony (2005), who used *ISO SWS*[9] data of 28 AGB field stars[10] with low mass-loss rates[11] in a parameterised study for a comparison with synthetic spectra derived with the DUSTY code (Ivezic & Elitzur 1997). They considered amorphous aluminium oxide (Al_2O_3), melilite ($Ca_2Al_2SiO_7$), spinel ($MgAl_2O_4$), $Mg_{0.1}Fe_{0.9}O$ and olivine ($Mg_{0.8}Fe_{1.2}SiO_4$) as relevant dust species for the calculation of their synthetic spectra.

---

[9] *ISO SWS: Infrared Space Observatory Short Wavelength Spectrometer*

[10] Heras & Hony (2005) investigated a sample of AGB field stars according to the 2.SE classification established by Kraemer et al. (2002) that corresponds to O-rich dust emission. The 2.SE-group is divided in three spectral classes that show (i) a broad 12 μm peak (2.SEa), (ii) 10 and 11 μm silicate features often accompanied by a 13 μm peak (2.SEb) and (iii) strong silicate emission with peaks at 10 and 18 μm (2.SEc).

[11] Low mass-loss rates ranging from $5 \cdot 10^{-8}$ to $10 \cdot 10^{-8}$ $M_\odot\mathrm{yr}^{-1}$.

With this dust mixture it was possible to reproduce the whole wavelength range of the *ISO SWS* spectra. Melilite appears in all stars in significant amounts $(25-50\%)$ and aluminium oxide is present in all but two spectra. Olivine could be detected in most objects, and its proportion increases as the proportion of aluminium oxide decreases (cf. Fig. 2 in Heras & Hony 2005). The authors reported that the presence of the latter two dust species is correlated with the gas-to-dust ratio in the stellar outflow. The higher the ratio, the higher the percentage of aluminium oxide in the cirrcumstellar shell. When there is more dust than gas present in the cirrcumstellar shell, aluminium oxide is less abundant and olivine dust is favored, pointing to a more advanced stage in the dust condensation sequence.

In addition to alumina and silicate dust, the study by Heras & Hony (2005) also included spinel which was used to explain the $13\,\mu$m feature (Posch et al. 1999). However, the laboratory analogue of $MgAl_2O_4$ shows a feature around $16.8\,\mu$m that could not be detected in their *ISO SWS* data. Thus, crystalline forms of Al_2O_3 were expected to be the origin of the $13\,\mu$m peak (Sloan et al. 2003a).

A broad variety of dust species manifesting in the MIR-spectra of evolved stars was also reported by the study of Sloan et al. (2010) where a sample of AGB stars in different globular clusters covering a wide range in metallicity were investigated[12]. The main objective of their work was to probe the effects of different metallicities on the quantity and composition of the dust present in the MIR-spectra of globular cluster AGB stars. They report that dust emission is present in a metallicity range of -0.97 $\leq$ [Fe/H] $\leq$ -0.08. Across this range, amorphous silicates, amorphous alumina and emission from crystalline dust grains are detected. Stars with lower metallicities show less dust in their spectra and circumstellar shells. Sloan et al. (2010) found signatures of alumina-rich dust at every metallicity where also silicate-rich dust is present. This result is in good agreement with the findings from Lebzelter et al. (2006) and Blommaert et al. (2006). However, a confirmation of the dust evolution scenario with a transition from alumina-rich to silicate-dominated is not possible with the data from Sloan et al. (2010) due to the low number of observed AGB stars per cluster and the resulting lack of MIR data of low luminosity globular cluster AGB stars.

The work from Sloan et al. (2010) also confirms the findings from Frogel & Elias (1988), who demonstrated that globular cluster variables which show a MIR dust excess are confined to clusters with metallicities greater [Fe/H] = -1 (cf. Fig. 1 in Frogel & Elias 1988). Furthermore, McDonald et al. (2010) reported that dust production in the metal-poor globular cluster M15 ([Fe/H] = -2.3) may not be dominated by red giants, as only three (out of 17) evolved stars showed a MIR excess (cf. Boyer et al. 2006). However, M15 is the only cluster in which intracluster gas and dust has been detected and McDonald et al. (2010) proposed episodic dust production and mass-loss as a possible explanation (cf. Origlia et al. 2002).

The diminishment of the dust excess with decreasing metallicity is also approved by the study of Origlia et al. (2002), who investigated six globular clusters using *ISOCAM* MIR photometry. The latter study resulted in the detection of 52 bright red giants close to the tips of the RGB of the respective clusters. 40% of these stars showed a strong MIR excess pointing to the presence of dusty circumstellar envelopes. Large amounts of dust were detected only in the most metal-rich clusters, however, Origlia et al. (2002) found no indication for a clear dependence of mass-loss on metallicity.

---

[12] See Chapter 2 for more details on the sample of Sloan et al. (2010) where details on the globular clusters and the hosted AGB stars are presented together with the MIR-spectra of the AGB star subsample used in this thesis.

1.4   AGB Stardust in Early-Type Galaxies

The MIR spectral region of old and intermediate age stellar populations is affected by the presence of mass-losing AGB stars that show a dust emission feature around $10\,\mu$m. Bressan et al. (1998) reported, that this dusty fingerprint should be clearly seen in relatively old populations. In a successive study Bressan et al. (2001) also showed that the MIR-spectra of early-type galaxies could be used to overcome the effects of the age-metallicity degeneracy because the dust excess in the MIR gets larger and dilutes to a broad emission that extends to wavelengths up to $15\,\mu$m as the observed stellar system gets younger and its metallicity inceases.

A systematic study with *Spitzer* resulted in low resolution MIR-spectra of 18 early-type galaxies where thirteen objects (76%) of the sample showed a domination by a broad dust emission feature at $10\,\mu$m that is extended towards longer wavelengths (Bressan et al. 2006). Models of passively evolving old simple stellar populations where used by these authors to dedicate the emission feature to the presence of silicate dust in the circumstellar envelopes of AGB giants. However, the observed $10\,\mu$m feature appears broader than predicted by the models of Bressan et al. (1998) pointing to the presence of a different dust mixture including not only silicates but also alumina-rich dust particles. Indeed, aluminium-oxide is the first astrophysically relevant species to condense in O-rich stellar outflows (Heras & Hony 2005) and is prominent in the MIR-spectra of AGB field stars (Posch et al. 1999). Studies by Lebzelter et al. (2006) and Blommaert et al. (2006) also reported that their is evidence of such dust species in the MIR-spectra of evolved stars with emission features at 11-$13\,\mu$m (cf. Section 1.3) that could lead to a broadening of the silicate dust excess. Thus, a combination of alumina and silicate dust could be used to reproduce the observation of the early-type galaxies from Bressan et al. (2006, 2007).

To further investigate the MIR dust excess present in early-type galaxies, Bressan et al. (2007) performed a comparison of the MIR-spectra of their sample with the integrated MIR-spectrum of the globular cluster NGC 104. They co-added the MIR-spectra of the red giants observed by Lebzelter et al. (2006) and subtracted a pure photosphere model normalized to the flux at $8\,\mu$m to recieve the integrated MIR excess of the cluster. Fig. 1.6 (upper panel) presents the excess derived by this co-adding method (green solid line, labelled *line a*). The excess is dominated by a strong dust emission at 10 and $20\,\mu$m due to silicate grains and shows a diminishment around 12-15 μm. The dotted line is the MIR excess of a 12 Gyr old single stellar population[13] (cf. Bressan et al. 1998) and shows the same slope as the co-added excess of NGC 104. In the same panel the black crosses indicate the excess measured for one of the early-type galaxies observed by Bressan et al. (2006). Since the sample observed by Lebzelter et al. (2006) is only a subsample of the variables hosted by NGC 104 (cf. Lebzelter & Wood 2005) there is a lack of MIR data representing the low luminosity stars with shorter periods present in the cluster. Thus, the simply co-added MIR-spectra are not representative of the entire stellar population. To overcome this problem Bressan et al. (2007) weighted the MIR-spectra of Lebzelter et al. (2006) with the number of neighboring variables in the Period-Luminosity diagram presented by Lebzelter & Wood (2005)[14]. The resulting MIR excess is indicated in the upper panel of

---

[13] The MIR excess of the single stellar population is derived by modelling dusty AGB envelopes for different evolutionary stages along the AGB with respect to various optical depths and subsequently weighting the resulting spectra with the number of equally evolved stars taken from theoretical isochrones. See Bressan et al. (1998) and Chapters 4 and 5 of this work for more details.

[14] The Period-Luminosity diagram presented in Fig. 1.3 only accounts for the stars with observed *Spitzer* spectra. See Lebzelter & Wood (2005) for the full diagram covering all known variables of NGC 104.
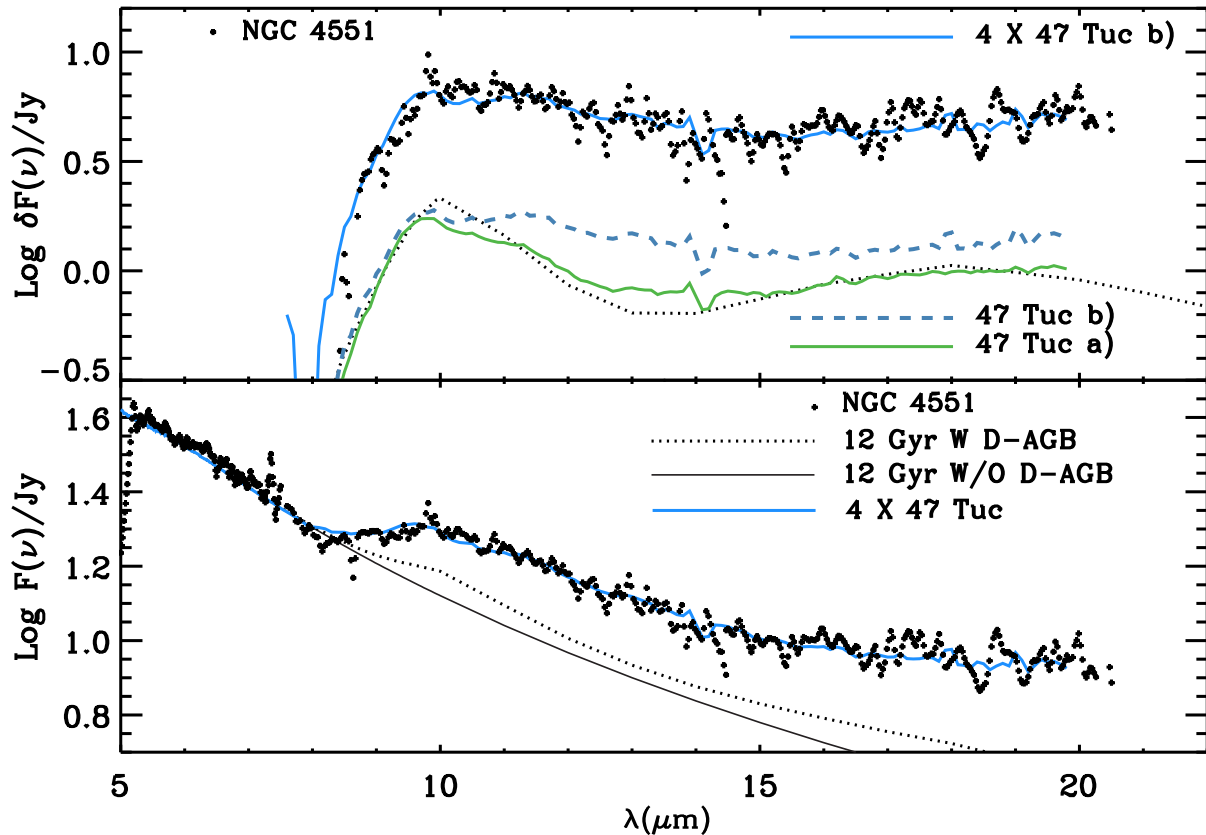
Figure 1.6: Comparison of the MIR dust excess of the early-type galaxy NGC 4551 with the integrated MIR excess of the globular cluster NGC 104 (Figure adapted after Bressan et al. 2007). The upper panel shows the excess derived by simply co-adding the MIR-spectra of the AGB stars observed in NGC 104 (green solid line) together with the excess derived by applying a weighting method based on the Period-Luminosity diagram of the cluster (blue dashed line). The blue solid line is the latter excess multiplied by a factor of four to match the flux of NGC 4551 (black crosses). The lower panel presents the integrated spectra in absolute values.

Fig. 1.6 (blue dashed line, labelled *line b*) and shows a flat dust emission ranging from 10 to 20 μm without the drop around 12-15 μm. The prominent silicate features are diminished due to the consideration of the low luminosity AGB stars present in NGC 104 that show no or weaker silicate emission on the one hand, and alumina dust on the other hand that leads to a broadening of the 10 μm feature. The blue solid line presents the flat dust excess derived with the weighting method making use of the Period-Luminosity diagram multiplied by a factor of four, to match the observations of the early-type galaxy NGC 4551. The four times larger flux was explained by Bressan et al. (2007) with the higher metallicitiy of the AGB stars hosted by the respective early-type galaxy compared to the metallicity of NGC 104.

The study of Bressan et al. (2007) points out that the MIR-spectra of individual AGB stars present in NGC 104 could be used to match the MIR excess present in the spectra of early-type galaxies. However, the authors adress that the comparison of co-added MIR-spectra of individual globular cluster AGB stars with the spectra of old stellar populations has to be done

with care due to the high stochastic effect introduced by the limited number of AGB giants with available *Spitzer* spectra and that metallicity effects on the MIR-properties of evolved stars need to be accounted for. Thus, a larger sample of AGB stars must be considered to cope with the large stochasticity and to explain possible influences of different metallicities.

Therefore, this thesis investigates the possibility of using individual AGB stars from various globular clusters to derive co-added MIR-spectra of entire stellar populations to extend the research from Bressan et al. (2007) to a broader range of metallicities and to allow for a more detailed comparison with early-type galaxies in future projects.

1.5 Outline

This study aims to shed light on the influence of different metallicities on the co-added MIR-spectra of old stellar populations. Therefore we investigate MIR-spectra of AGB stars in various Galactic globular clusters observed with *Spitzer*.

Chapter 2

introduces the globular cluster AGB star sample this study is based on. Period-Luminosity and Metallicity-Luminosity diagrams are presented. The conversion of raw *Spitzer* spectra to dereddened dust residuals is illustrated. Finally the MIR-spectra of the AGB stars this study is based on are shown.

Chapter 3

focuses on the calculation of Luminosity Functions (LFs) based on 2MASS J and K data. The data extraction is performed using the 90%-mass radius of each globular cluster. Binning procedures and the reduction of the field star contamination are explained. Three groups are defined in the Metallicity-Luminosity diagram to allow for a combination of several globular clusters with respect to their metallicity. The globular cluster LFs of the respective group members are combined to generate 2MASS LFs of three globular cluster groups of low, intermediate and high metallicites, respectively.

Chapter 4

presents a comparison of the 2MASS LFs derived in Chapter 3 with theoretical LFs (TLFs) based on different Padova isochrones. The calculation of TLFs based on YZYAR isochrones is explained together with the extraction of TLFs based on the CMD interface. The LFs of the low, intermediate and high metallicity globular cluster combinations are compared to TLFs of different ages, dust production scenarios, mass-loss rates, initial mass functions and metallicities.

Chapter 5

presents the co-added MIR-spectra and the respective dust residuals of the three globular cluster combinations. In addition the globular cluster NGC 104 is investigated independently to allow for a comparison with the results from Bressan et al. (2007). The dust residuals of the three metallicity groups are compared to highlight possible variations due to the different metallicities.

Chapter 6

discusses the results and outlines future work. A comment on stellar variability is included together with an outline to the planned comparison with synthetic MIR-spectra based on the wind code from H.-P. Gail.

Appendix A

illustrates the calculation of the period of the globular cluster AGB star IC 1276 V3.

Appendix B

gives a short explanation how to convert metallicity values given as [Fe/H] into Z and vice versa.

Appendix C

illustrates the finding charts of the globular clusters this work is based on. The postions of the hosted AGB stars are indicated for each cluster.

Appendix D

presents an example proposal for observing time on a 8 m-class telescope. More observational data on the MIR-properties of AGB stars in old stellar populations would allow for a better understanding of the various effects that influence the MIR-spectra of evolved stars. Thus, the present observing proposal focuses on the AGB stars in the globular cluster NGC 104 and outlines a plan to investigate the impact of stellar variability on the MIR-spectra.

Appendix E

presents a paper on the NIR absorption properties of oxygen-rich stardust analogs accepted to A&A. This work gives an introduction into laboratory astrophysics and astrophysical implications like the calculation of the equilibrium temperature of dust grains in a stellar radiation field.

Chapter 2

The mid-infrared Spectrum of Globular Cluster AGB Stars

2.1 The Sample of Globular Cluster AGB Stars

This study is based on two datasets from the *Spitzer Archive* (Levine et al. 2009)[1], namely the sample of LPVs in the Galactic globular cluster NGC 104[2] obtained by Lebzelter et al. (2006) (12 stars) and the study of Sloan et al. (2010) investigating the MIR-spectra of 39 variable stars in 23 Galactic globular clusters covering a wide range in metallicity[3].

After carefully studying the objects observed by Sloan et al. (2010) several stars (and their hosting globular clusters) were dismissed from that part of the sample. Four stars were dismissed because they are Cepheids of the W Vir type and not long period variables. Other stars were dismissed because they where reported to be field stars (Clement 1997), due to their extreme brightness compared to the cluster members and the globular cluster RGB tip, due to their unusual position in the Period-K diagram (see Fig. 2.1, left panel) or simply due to the lack of known periods[4]. In Figure 2.1 (right panel) the observed AGB star NGC 6171 V1 is four magnitudes brighter than the tip of the RGB and considered as a foreground object. A real cluster membership of NGC 6171 V1 would lead to an initial mass of about $5\,M_\odot$, which would be to high for the corresponding cluster age. Five stars, namely NGC 6171 V1, Palomar 6 V1, Palomar 10 V2, Terzan 5 V5 and Terzan 12 V1, were reported to be possible binary mergers (see

---

[1]Note that the Spitzer Heritage Archive (SHA) will replace the *Leopard* tool in fall 2010. For this work the *Leopard* tool was used (see Section 2.4).

[2]In this work the globular cluster 47 Tuc is named NGC 104

[3]We note that we have been in contact with Greg Sloan from the beginning of the thesis, but decided to do an independent analysis of the dataset for sake of consistency with the analysis of te other part of our sample.

[4]Not all AGB stars had reported periods in the literature before presented by Sloan et al. (2010)
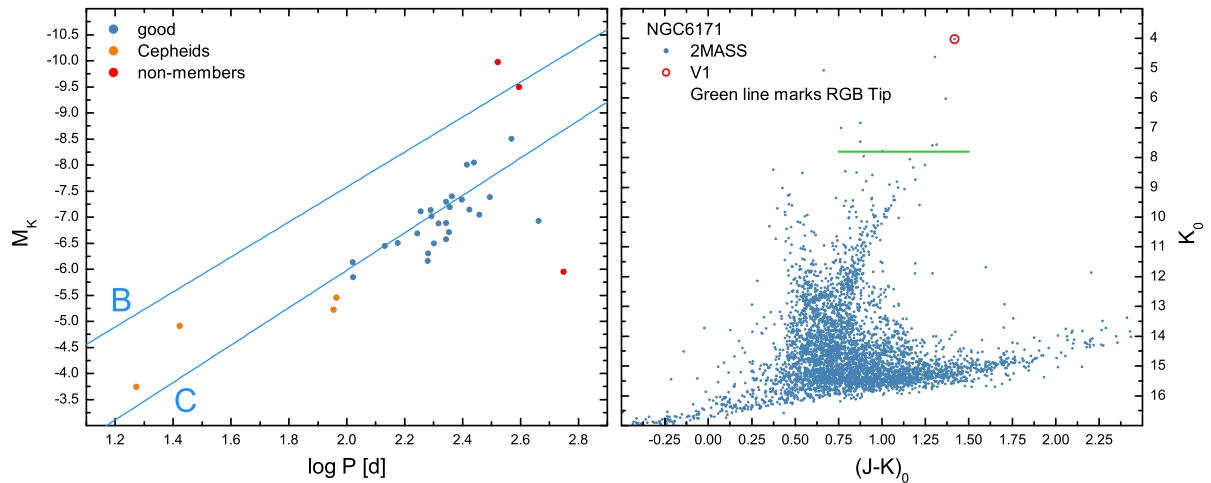
Figure 2.1: Left panel: Period-K diagram including Cepheids (orange) and field stars (red). Period-K relations for fundamental mode (C) and first overtone (B) are from Ita et al. (2004). Right panel: Color-Magnitude diagram for the globular cluster NGC 6171. V1 is marked with a red circle, the green line marks the position of the $\mathrm{Tip_{RGB}}$.

Matsunaga et al. 2005) and therefore are excluded from the main sample of this work. This target selection is in good agreement with the findings presented by Sloan et al. (2010).

2.1.1 Globular Clusters

Table 2.1 presents the globular clusters of the sample this work is based on, including information on cluster metallicity, distances and extinction parameters. After dismissing several stars from the study of Sloan et al. (2010) twelve clusters remained in the sample. NGC 104 is added to complete the sample of globular clusters with available *IRS* spectroscopy of the hosted AGB stars resulting in a total of 13 Galactic globular clusters that are investigated in this thesis. The globular clusters cover a wide metallicity range from [Fe/H] = -1.12 to [Fe/H] = -0.28. Color-Magnitude diagrams and Luminosity Functions of the clusters are presented in Section 3.3. Finding charts for each cluster are presented in Appendix C.

2.1.2 Globular Cluster AGB Stars

The final sample of AGB stars this work is based on consists of 38 individual stars hosted by the globular clusters presented in 2.1.1 and includes 26 AGB stars observed by Sloan et al. (2010) and 12 AGB stars observed by Lebzelter et al. (2006).

Table 2.2 presents the AGB stars including coordinates, K and M_K magnitudes, Periods and $\log P$-values as well as the variability class. The table is devided in two parts to easily distinguish between the stars from Lebzelter et al. (2006) and Sloan et al. (2010). The coordinates and the K magnitudes were taken from 2MASS (see Skrutskie et al. (2006) for more information on the 2MASS survey), the absolute magnitudes M_K are derived from the 2MASS K magnitudes and the distances listed in Table 2.1. The periods were taken from Clement (1997),

Table 2.1: Parameters of the Globular Cluster Sample I

GC ID	RA2000[a]	DE2000[a]	[Fe/H][b]	E(B-V)[b]	A(K)[c]	A(J)[c]	R$_\odot$ [kpc][b]
NGC 104	00 24 05.7	-72 04 52.6	-0.76	0.05	0.01668	0.04366	4.3
IC 1276	18 10 44.3	-07 12 27.0	-0.70	1.16[d]	0.38695	1.01296	4.0[d]
NGC 362	01 03 14.3	-70 50 53.6	-1.12	0.05	0.01668	0.04366	8.3
NGC 5927	15 28 00.4	-50 40 22.0	-0.37	0.47	0.15678	0.41042	7.4
NGC 6352	17 25 29.2	-48 25 21.7	-0.70	0.21	0.07005	0.18338	5.6
NGC 6356	17 23 35.0	-17 48 46.9	-0.50	0.29	0.09674	0.25324	14.6
NGC 6388	17 36 17.1	-44 44 05.8	-0.60	0.38	0.12676	0.33183	11.5
NGC 6553	18 09 15.7	-25 54 27.9	-0.25	0.78	0.26019	0.68113	4.7
NGC 6637	18 31 23.2	-32 20 52.7	-0.71	0.17	0.05671	0.14845	8.2
NGC 6712	18 53 04.3	-08 42 21.5	-1.01	0.46	0.15345	0.40169	6.7
NGC 6760	19 11 12.1	+01 01 49.7	-0.52	0.78	0.26019	0.68113	7.3
NGC 6838	19 53 46.1	+18 46 42.3	-0.73	0.25	0.08339	0.21831	3.8
Terzan 5	17 48 05.0	-24 46 48.0	-0.28	2.32	0.77390	2.02592	8.0

[a] Coordinates were taken from Simbad
[b] [Fe/H], E(B-V) and R$_\odot$ values were taken from Harris (1997)
[c] A(K) and A(J) are derived using Equations 2.2 - 2.5
[d] For IC 1276 the distance and E(B-V) are from Barbuy et al. (1998)

Lebzelter et al. (2005) and Lebzelter & Wood (submitted), the variability class is taken from Lebzelter et al. (2005) and Sloan et al. (2010). Most stars of the sample are Mira variables and fall on the fundamental mode sequence in the Period-Luminosity diagram (see Fig. 2.1.3).

A detailed description of the AGB stars in NGC 104 (47 Tuc) was published in Lebzelter et al. (2005), Lebzelter & Wood (2005) and Lebzelter et al. (2006). A brief overview on the dust evolution scenario based on *Spitzer* observations of the AGB star population in NGC 104 is given in Chapter 1 of this work. The rest of the AGB stars from Table 2.2 are also discussed in Sloan et al. (2010).

Table 2.2: Globular Cluster AGB stars

Star ID	RA2000[a]	DE2000[a]	K[a]	M_K[b]	Period [d][c]	log P	Var. Class[d]
NGC 104 V1	00 24 12.65	-72 06 39.90	6.382	-6.802	221	2.344	Mira
NGC 104 V2	00 24 18.57	-72 07 59.01	6.421	-6.763	203	2.308	Mira
NGC 104 V3	00 25 15.96	-72 03 54.81	6.309	-6.875	192	2.283	Mira
NGC 104 V4	00 24 00.53	-72 07 26.87	6.620	-6.564	165	2.219	Mira
NGC 104 V5	00 25 03.63	-72 09 31.73	7.397	-5.787	50	1.699	Regular
NGC 104 V6	00 24 25.68	-72 06 29.96	7.408	-5.776	48	1.681	SR
NGC 104 V7	00 25 20.53	-72 06 40.09	6.904	-6.280	52	1.839	SR
NGC 104 V8	00 24 08.59	-72 03 54.94	6.661	-6.523	155	2.190	Mira
NGC 104 V11[e]	00 25 09.07	-72 02 16.23	6.626	-6.558	160:	1.716	Irregular
NGC 104 V13	00 22 58.37	-72 06 56.05	7.655	-5.529	40 + long	2.643	Long period
NGC 104 V18	00 25 09.19	-72 02 39.71	7.431	-5.753	83:	1.919	Irregular
NGC 104 V21	00 23 50.38	-72 05 50.52	6.739	-6.445	76 + long	1.881	Long Period
IC 1276 V1	18 10 51.55	-07 10 54.51	6.823	-6.574	220	2.342	Mira
IC 1276 V3	18 10 50.79	-07 13 49.13	6.286	-7.111	179.7[f]	2.255	Mira
NGC 362 V2	01 03 21.85	-70 54 20.08	8.764	-5.848	105	2.021	SR
NGC 362 V16	01 03 15.10	-70 50 32.34	8.165	-6.447	135	2.130	Mira/SR
NGC 5927 V1	15 28 15.17	-50 38 09.26	8.006	-6.497	200	2.301	Mira/SR
NGC 5927 V3	15 28 00.13	-50 38 09.26	7.118	-7.385	312	2.494	Mira
NGC 6352 V5	17 25 37.52	-48 22 09.98	7.125	-6.686	175	2.243	Mira
NGC 6356 V1	17 23 33.72	-17 49 14.84	8.520	-7.399	230.6	2.363	Mira
NGC 6356 V3	17 23 33.30	-17 48 07.43	9.032	-6.887	220	2.342	Mira
NGC 6356 V4	17 23 48.00	-17 48 04.50	9.037	-6.882	207.3	2.317	Mira
NGC 6356 V5	17 23 17.06	-17 46 24.46	8.621	-7.298	219.8	2.342	Mira
NGC 6388 V3	17 36 15.04	-44 43 32.51	8.929	-6.501	150	2.176	Mira
NGC 6388 V4	17 35 58.94	-44 43 39.83	8.379	-7.051	287	2.458	Mira
NGC 6553 V4	18 09 18.84	-25 54 35.83	6.474	-7.147	265	2.423	Mira
NGC 6637 V4	18 31 21.88	-32 22 27.67	7.611	-7.015	196	2.292	Mira
NGC 6637 V5	18 31 23.44	-32 20 49.45	7.491	-7.135	195	2.292	Mira
NGC 6712 V2	18 53 08.78	-08 41 56.59	8.150	-6.134	104.6	2.020	SR
NGC 6712 V7	18 52 55.38	-08 42 32.48	8.126	-6.158	190.5	2.280	Mira
NGC 6760 V3	19 11 14.31	+01 01 46.64	7.243	-7.334	250	2.398	Mira
NGC 6760 V4	19 11 15.03	+01 02 36.84	7.866	-6.711	225	2.352	Mira
NGC 6838 V1	19 53 56.10	+18 47 16.76	6.681	-6.301	190.95	2.281	Mira/SR
Terzan 5 V2	17 47 59.46	-24 47 17.61	8.100	-7.189	227	2.356	Mira
Terzan 5 V6	17 48 09.26	-24 47 06.34	7.243	-8.046	275	2.439	Mira
Terzan 5 V7	17 47 54.33	-24 49 54.55	6.782	-8.507	370	2.568	Mira
Terzan 5 V8	17 48 07.18	-24 46 27.06	7.277	-8.012	260	2.415	Mira
Terzan 5 V9	17 48 11.86	-24 50 16.34	8.358	-6.931	460	2.663	Mira

[a] Coordinates and K magnitudes were taken from 2MASS

[b] M_K is derived from K using Eq. 2.1

[c] Periods were taken from Clement (1997), Lebzelter et al. (2005) and Lebzelter & Wood (submitted)

[d] Variability class from Lebzelter et al. (2005) and Sloan et al. (2010)

[e] The spectrum of NGC 104 V11 was not presented in Lebzelter et al. (2006) due to problems with the *Spitzer* pipeline.

[f] For IC 1276 V3 the period is derived after Kinman & Rosino (1962), see Appendix A.

2.1.3 Periods and Metallicities

The Period-K relation and the Metallicity-K relation for the sample of globular cluster variables are presented in Figs. 2.2 and 2.3, respectively. The dereddened absolute K magnitudes are derived using A(K) and globular cluster distances R[pc] from Table 2.1 and Equation 2.1. A(K) values were derived according to the interstellar extinction relations (Eq. 2.2 - 2.5) presented by Mathis (1990)[5] in his Table 1.

$$M_K = m_K + 5 - 5 \log R[pc] - A(K) \tag{2.1}$$

$$A(V) = 3.1 \cdot E(B - V) \tag{2.2}$$

$$\frac{A(V)}{A(J)} = 3.55 \tag{2.3}$$

$$\frac{A(K)}{A(J)} = 0.382 \tag{2.4}$$

$$A(K) = 0.333577 \cdot E(B - V) \tag{2.5}$$

In Fig. 2.2 three different Period-Luminosity relations are illustrated. The AGB stars of the sample are located on the fundamental mode pulsation sequence except for Terzan 5 V9[6] and NGC 104 V13[7]. One PL-Relation is taken from Ita et al. (2004), one from Lebzelter et al. (2005)[8] and one from Whitelock et al. (2008). While the relation from Lebzelter et al. (2005) is best to fit the stars from the globular cluster NGC 104, the relations from Ita et al. (2004) and Whitelock et al. (2008) are well suited to fit the stars of the entire sample. Table 2.3 presents the Period-Luminosity relations in detail.

Table 2.3: Period-Luminosity Relations

Reference	PL-Relation	Distance Modulus
Ita et al. (2004)	19.698 - 3.599 [log P] - 18.5	18.5 (LMC)
Lebzelter & Wood (2005)	15.420 - 3.959 [log P] - 13.5	13.5 (NGC 104)
Whitelock et al. (2008)	M_K = -3.51 [log P - 2.38] - 7.15	18.39 (LMC)

---

[5] Note that Sloan et al. (2010) used estimates for the interstellar extinction by Rieke & Lebofsky (1985)

[6] Terzan 5 V9 will be not included in the calculation of the co-added spectrum of the "high" metallicity group (see Section 3.4.1 for more information.

[7] Also NGC 104 V5, NGC 104 V6, NGC 104 V7, NGC 104 V13, NGC 104 V21 (and in principle also NGC 104 V18) do not fall on the fundamental mode sequence. These stars are not shown in Fig. 2.2. See Lebzelter et al. (2005) and Lebzelter et al. (2006) for a detailed discussion

[8] The Period-Luminosity relation from Lebzelter et al. (2005) presented in Table 2.3 is reconstructed after their Fig. 14.
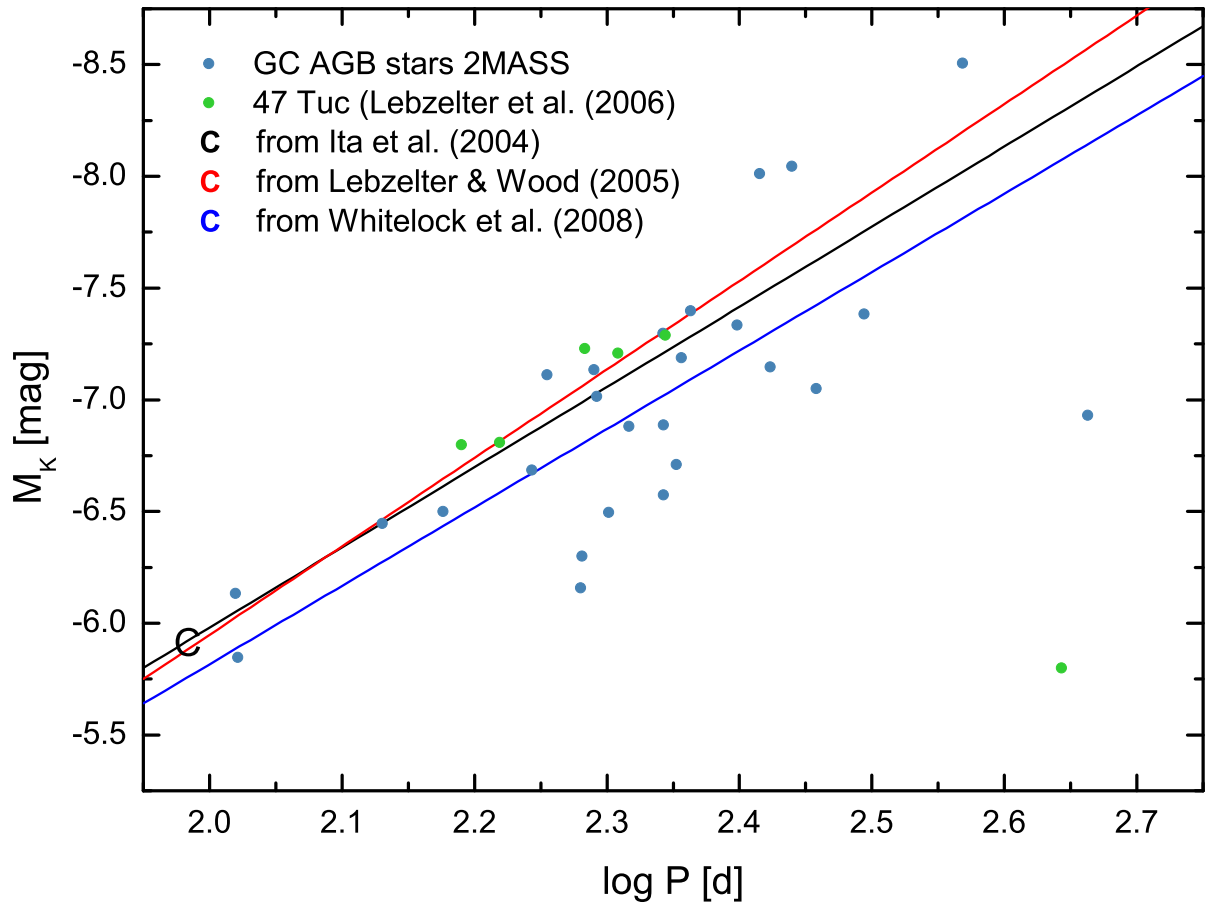
Figure 2.2: Period-Luminosity diagram of the globular cluster AGB stars with available *Spitzer IRS* spectra. Blue dots are refering to stars observed by Sloan et al. (2010), green dots are refering to stars observed by Lebzelter et al. (2006). Three different Period-K relations from Ita et al. (2004), Lebzelter et al. (2005) and Whitelock et al. (2008) are included.

The Metallicity-Luminosity diagram (Fig 2.3) presents the metallicity distribution of the globular clusters. The observed AGB stars in each cluster build vertical "lines" at the corresponding [Fe/H] value. With increasing metallicity the luminosity of the AGB stars increases, leading to a brighter tip of the AGB. To illustrate this effect the position of the RGB tip is included in the diagram. For this Equation 2.6[9], where [M/H] is the total metal amount, is combined with Equation 2.7[10] to derive the dependence of the luminosity of the RGB tip on the metallicity given in [Fe/H] values from Harris (1997) and not in [M/H] used by Bellazzini et al. (2004). In the latter equation $\log f_\alpha$ equates the average enhancement of the α-elements and [α/H] = 0.2±0.05 for clusters with [Fe/H] ≥ -1.0 (see Marín-Franch et al. 2009). The combination of Eq. 2.6 and Eq. 2.7 leads to Eq. 2.8 that results in the blue line in Fig 2.3 representing the shift of the RGB tip.

---

[9]from Bellazzini et al. (2004)
[10]from Salaris et al. (1993)
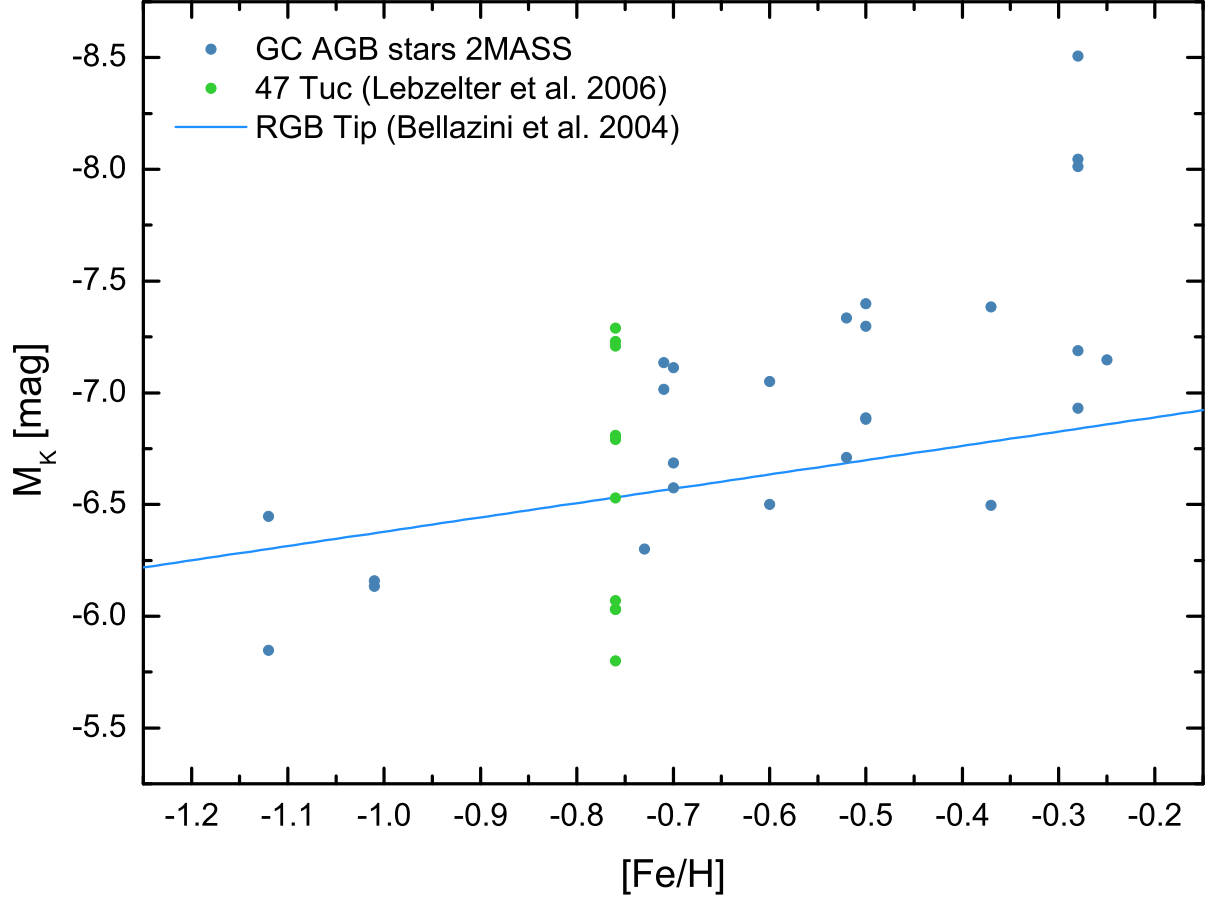
Figure 2.3: Metallicity-Luminostiy diagram of the AGB stars with observed *Spitzer IRS* spectra. Blue dots are refering to stars observed by Sloan et al. (2010), green dots are refering to stars observed by Lebzelter et al. (2006). The mean M_K increases with increasing metallicity. The blue line marks the postion of the tip of the RGB (derived after Bellazzini et al. (2004))

$$M_{\text{RGBTip}} = -0.64 \left[\frac{M}{H} \right] - 6.93 \tag{2.6}$$

$$\left[\frac{M}{H} \right] = \left[\frac{Fe}{H} \right] + \log \left[0.638 f_\alpha + 0.362 \right] \tag{2.7}$$

$$M_{\text{RGBTip}} = -0.64 \left[\left[\frac{M}{H} \right] + \log \left[0.638 f_\alpha + 0.362 \right] \right] - 6.93 \tag{2.8}$$

Regarding the stars and their MIR-spectra over the entire metallicity range in Fig. 2.3, Sloan et al. (2010) reported an increase of the dust emission with increasing metallicity. While the AGB stars with low metallicity ([Fe/H] < -0.8) show no significant dust emission and are reported to be "naked" stars, AGB stars with higher metallicities ([Fe/H] > -0.8) show emission

from alumina and silicate dust. This proposition is based on the very low number of available MIR-spectra from globular cluster AGB stars. Since the observed stars in the sample from Sloan et al. (2010) are only the brightest AGB stars in the according clusters it is hard to define a dust emission trend with respect to the metallicity. More details about the AGB star spectra are presented in Section 2.3.

2.2 From *Leopard* to Processed Spectra

The AGB stars used in this work were observed with the *IRS Spectrograph* on board the *Spitzer Space Telescope*. A detailed description of the observations can be found in Lebzelter et al. (2006) for the NGC 104 stars, and in Sloan et al. (2010) for the rest of the sample presented in Table 2.2.
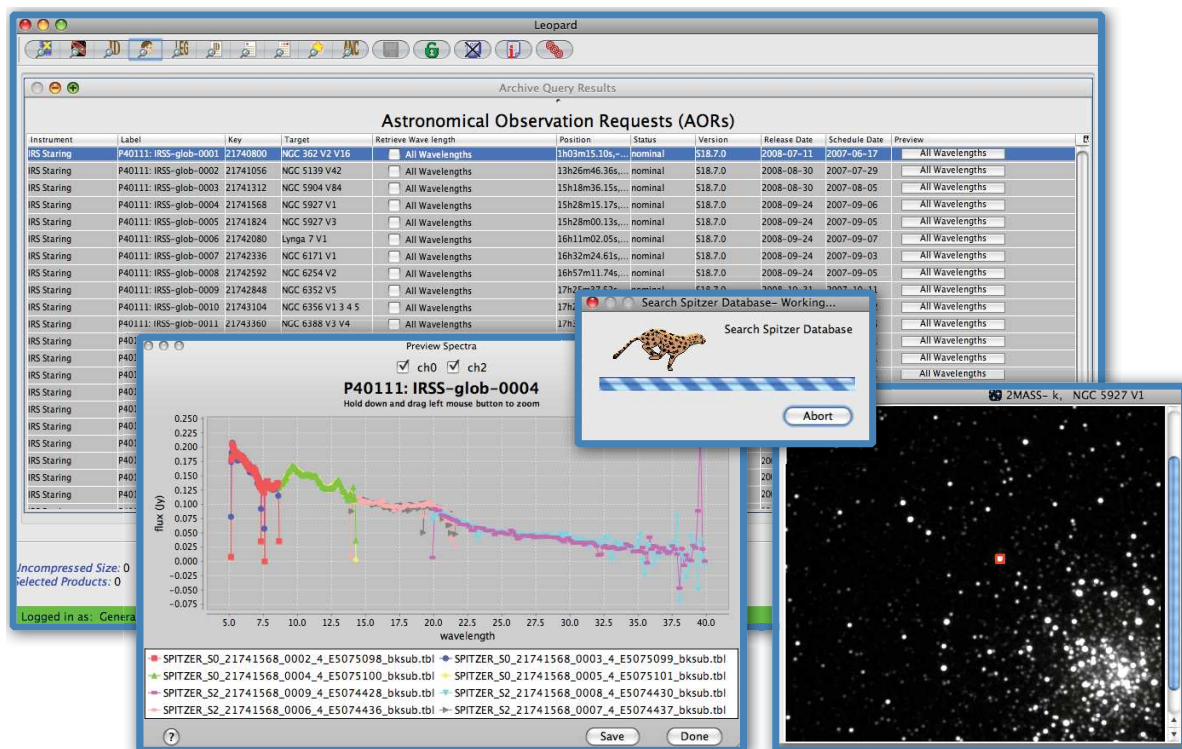

Figure 2.4: Compilation of the *Leopard* interface. The AOR list of the 40111 program, the quick-view spectrum (NGC 5927 V1) and the image of the globular cluster NGC 5927 with the position of V1 is shown. The name *Leopard* obviously had an inspiring effect on the SCC software engineers.

2.2.1 The *Spitzer Archive*

The MIR-spectra of the observed AGB stars were extracted from the *Spitzer Archive* using the *Leopard*[11] tool. *Leopard* allows for a detailed seach for observed objects. In this case the search based on the the observer names to find the proper observation campaigns[12] to access the Astronomical Observation Requests (AOR) including all the data. The data can be downloaded as raw data, basic calibrated data (BCD), and post-BCD data. Also calibration data can be accessed. Fig. 2.4 shows a compilation of the *Leopard* interface presenting the AOR list of the sample from Sloan et al. (2010), one quick-view spectrum (NGC 5927 V1) and one globular cluster image with the target position.

2.2.2 Extraction

Leopard was used to find the AGB stars in the archive and to extract the observational data from the *Spitzer Archive*. In this case the post-BCD data were downloaded for each AOR. Some AORs consisted only of one target star, others included several targets. For each observed star various data files were included in the AOR-data. For this work the spectra of the AGB stars where extracted from the *bksub.tbl* files. The spectra cover a wavelength range from 5.2 to 38.0 μm[13] and were composed of four smaller wavelength areas (saved in four different *bksub.tbl* files). Nodded observations lead to the production of two spectra per target and four additional *bksub.tbl* files for each star. These eight different *bksub.tbl* files were used to produce the MIR-spectrum for each observed AGB star. Table 2.4 presents the four wavelength areas that are combined to produce a full MIR-spectrum[14]. Fig. 2.5 (left panel) shows the four parts of the spectrum of the AGB star NGC 5927 V1 (only one nod-position is shown). The four wavelength areas do overlap with each other allowing to assemble the full MIR-spectrum ranging from 5.2 to 38.0 μm. In some cases the individual parts of the spectra were shifted with respect to the measured flux. To remove the shifts, each spectrum was compared with a blackbody mounted at the K-flux[15] of the observed star[16]. The blackbody temperatures were derived using MARCS models (see Section 2.2.5 for more details on the blackbody temperature). The slopes of the blackbody curves illustrated the expected slopes of the MIR-spectra and were used to scale the shifted parts of the spectra up or down to overlap with each other at the proper flux levels[17]. Subsequently the two separate observations from the two different nodding positions were used to derive the mean spectrum of each target star in order to reduce the noise of the single spectra and to get rid of contaminating outliers. Fig. 2.5 (right panel) shows the final spectrum of NGC 5927 V1.

---

[11] *Leopard* is available at `http://ssc.spitzer.caltech.edu/warmmission/propkit/spot/` [December 30, 2010]. The detailed introduction how to use *Leopard* is found in the User Guide also available at the webpage.

[12] For the stars from Sloan et al. (2010) the campaign P40111 "The mass-loss and dust composition of evolved stars in globular clusters" was used to extract the sample.

[13] Note that for the stars from NGC 104 a wavelength coverage of only 7.4 to 21.3 μm is available.

[14] More details on the *IRS Spectrograph* is found in the *IRS* Instrument Handbook available at: `http://ssc.spitzer.caltech.edu/` [December 30, 2010]

[15] To derive the K-flux, the 2MASS K magnitude was used. See Eq. 2.13

[16] Note that in Section 2.3 the blackbody is mounted at the K-flux from IRSF observations (see. Table 2.6) and not on the K-flux from 2MASS observations.

[17] Note that for the spectrum of NGC 5927 V1 in Fig. 2.5 no shift occured and no up oder down scaling was necessary.
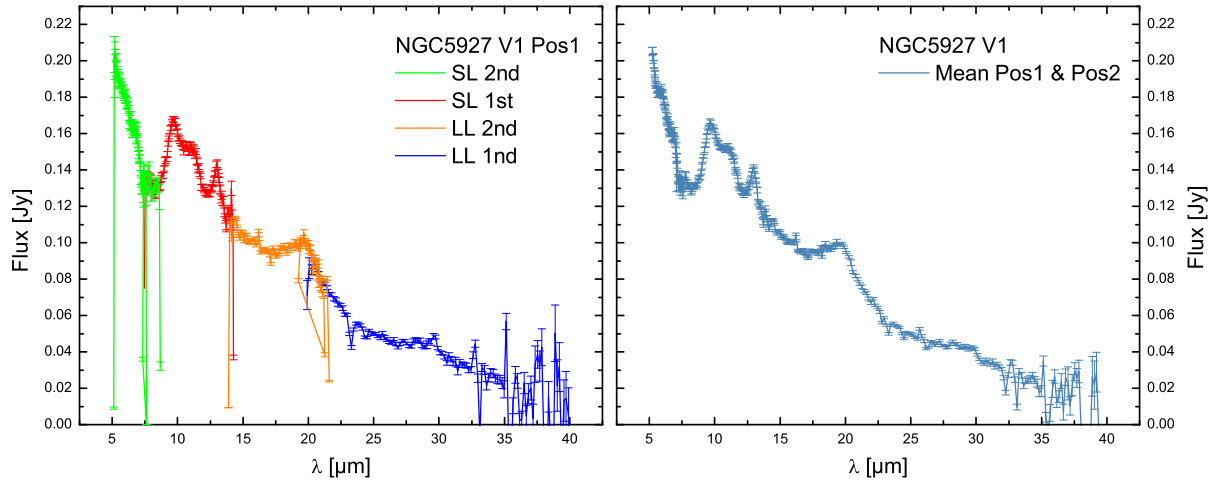
Figure 2.5:   Left panel: *Spitzer* spectrum of the globular cluster AGB star NGC 5927 V1 in Jansky. The spectrum consists of four parts, each covering a different wavelength range. Only one nod position is shown. Right panel: Mean spectrum of NGC 5927 V1 in Jansky derived from the two nodding positions.

Table 2.4: Spitzer *IRS* Operating Wavelengths

IRS Module	Wavelength [μm]	Color in Fig. 2.5
Short-Low 2nd order (SL2)	5.2 – 8.7	green
Short-Low 1st order (SL1)	7.4 – 14.5	red
Long-Low 2nd order (LL2)	14.0 – 21.3	orange
Long-Low 1nd order (LL1)	19.5 – 38.0	blue

2.2.3   Dereddening the Spectra

The dereddening of the K magnitudes of the globular cluster AGB stars is presented in Section 2.1.3 and relies on A(K) from Mathis (1990) and the globular cluster distances taken from Harris (1997). To deredden the entire MIR-spectrum of the observed stars one needs to take all the extrinction values into account that fall into the wavelangth range from 5 to 35 μm. Mathis (1990) presented in his Table 1 a detailed list of interstellar extinction values from 0.002 to 250 μm. With the A(λ)/A(J) values covering the MIR-range it is possible to derive the extinction values for each wavelength using Equation 2.9. The A(J) values are derived using E(B-V) values from Harris (1997) and a R$_V$ of 3.1.

$$A(\lambda) = \frac{A(\lambda)}{A(J)} \cdot A(J) \tag{2.9}$$

$$(m_{dereddened} - m_{observed}) = A(\lambda) = -2.5 \log \frac{F_{dereddened}}{F_{observed}} \Rightarrow F_{dereddened} = F_{observed} \cdot 10^{\frac{A(\lambda)}{2.5}} \tag{2.10}$$
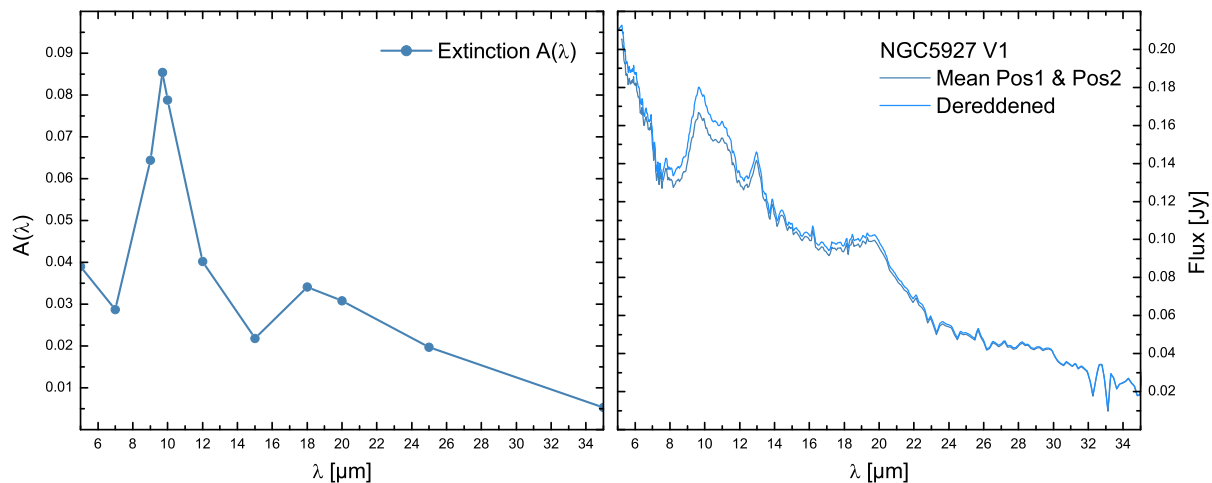
Figure 2.6: Interstellar extinction as a function of λ (left panel). Observed and dereddened spectrum of the AGB star NGC 5927 V1 (right panel).

The derived A(λ) relates to the flux ratio given by the observed and the dereddened flux, but is still specified as a magnitude. Fig. 2.6 (left panel) shows the extinction A(λ) as a function of λ. To get the flux ratio in Jansky Equation 2.10 is used.

To retrieve the dereddened flux of the MIR spectra the flux values of the observed spectrum are multiplied with the flux ratio from Eq. 2.10 that describes the extinction in the MIR-range. Both, the observed spectra and the flux ratio values need to have values at the same wavelength grid points to allow for a proper multiplication and dereddening. Using the interpol-routine in IDL the observed spectra and the flux ratio values are interpolated to occupy the same λ-grid. The new λ-grid ranges from 5 to 40 μm with R = 500. Once all spectra and the respective flux ratio tables have values at the same wavelength values the dereddening is possible with a simple value-to-value multiplication. Fig. 2.6 (right panel) shows the observed spectrum of NGC 5927 V1 and the spectrum after the dereddening. The flux around 10 and 20 μm is increased due to the strong interstellar extinction at this wavelength region due to silicates present in the line of sight, while at longer wavelengths the extinction is not significant (cf. Fig. 2.6 (left panel))[18].

2.2.4 Absolute Flux

After dereddening the observed spectra of the globular cluster AGB stars it is straightforward to derive the absolute flux for each spectrum using Equation 2.11 with the distance modulus or Equation 2.12 using the distance of the globular clusters in parsec[19].

$$F_{absolute} = F_{apparent} \cdot 10^{0.4(m-M)} \tag{2.11}$$

$$F_{absolute} = F_{apparent} \left[\frac{R_{\odot}}{10\,[pc]} \right]^2 \tag{2.12}$$

---

[18] Note that Mathis (1990) reports an uncertainty of a factor of two for $\lambda > 15\,\mu$m

[19] For this work Eq. 2.12 was used. $R_{\odot}$ is taken from Harris (1997)

25

In order to derive the absolute flux in Jansky for the K magnitude, the NIR data from 2MASS and IRSF (see Table 2.2 and Table 2.6, respectively) and the zero-magnitude attributes from Cohen et al. (2003) are used. The zero-magnitude attributes are presented in Table 2.5 and included in Equation 2.13 to derive the K flux. The absolute K fluxes of the globular cluster AGB star sample according to the mean IRSF K and M_K magnitudes are presented in Table 2.6[20].

$$F_K\,[Jy] = \frac{6.67 \cdot 10^{-24}}{\exp[\frac{K}{2.5}]} \cdot 10^{26} = \frac{667}{\exp[\frac{K}{2.5}]} \tag{2.13}$$

Table 2.5:   Zero-Magnitude Attributes

Filter	$\lambda\,[\mu\mathrm{m}]$	Flux $[\mathrm{W\,m^{-2}\,Hz^{-1}}]$	Flux $[\mathrm{W\,cm^{-2}\,Hz^{-1}}]$	Flux [Jy]
J	1.235	$1.59 \cdot 10^{-23}$	$3.14 \cdot 10^{-13}$	1594
H	1.662	$1.02 \cdot 10^{-23}$	$1.11 \cdot 10^{-13}$	1024
K	2.159	$6.67 \cdot 10^{-24}$	$4.29 \cdot 10^{-14}$	667

---

[20]Note that in Section 2.3 the absolute K flux from IRSF data is plotted. The 2MASS absolute K flux is not included.

Table 2.6: IRSF Data and absolute Flux

Star ID	K^a	Flux [Jy]^b	$M_K{}^c$	Flux$_{abs}$ [Jy]^b	$+0.3\,\mathrm{mag}^d$	$-0.3\,\mathrm{mag}^d$
IC 1276 V1	6.760	1.319	-6.637	301318.325	397214.9124	228573.3243
IC 1276 V3	6.600	1.528	-6.797	349160.852	460283.646	264865.5924
NGC 362 V2	8.920	0.180	-5.692	126169.261	166323.4783	95709.17191
NGC 362 V16	8.220	0.344	-6.392	240410.570	316922.8543	182370.0674
NGC 5927 V1	7.870	0.474	-6.633	300124.707	395641.4177	227667.8726
NGC 5927 V3	7.330	0.780	-7.173	493516.582	650581.5598	374370.612
NGC 6352 V5	7.060	1.000	-6.751	334597.241	441085.068	253817.9639
NGC 6356 V1	8.820	0.198	-7.099	460814.862	607472.2973	349563.8207
NGC 6356 V3	8.950	0.175	-6.969	408814.675	538922.7007	310117.6451
NGC 6356 V4	9.050	0.160	-6.869	372843.415	491503.3446	282830.6538
NGC 6356 V5	8.621	0.238	-7.298	553511.282	729669.9776	419881.2462
NGC 6388 V3	8.970	0.172	-6.460	255991.308	337462.2662	194189.2653
NGC 6388 V4	8.470	0.273	-6.960	405718.881	534841.6484	307769.2446
NGC 6553 V4	6.670	1.433	-6.951	402158.775	530148.5157	305068.6286
NGC 6637 V4	7.611	0.602	-7.015	426616.392	562389.9338	323621.6283
NGC 6637 V5	7.491	0.673	-7.135	476472.169	628112.648	361441.1028
NGC 6712 V2	8.150	0.367	-6.134	189520.171	249836.2424	143765.7517
NGC 6712 V7	7.570	0.625	-6.714	323337.026	426241.2132	245276.217
NGC 6760 V3	7.680	0.565	-6.897	382690.388	504484.1827	290300.3465
NGC 6760 V4	7.960	0.437	-6.617	295697.439	389805.1334	224309.4416
NGC 6838 V1	6.590	1.542	-6.392	240463.424	316992.5293	182410.1612
Terzan 5 V2	7.650	0.581	-7.639	758343.219	999691.059	575262.1603
Terzan 5 V6	7.500	0.667	-7.789	870694.514	1147798.91	660489.3327
Terzan 5 V7	7.030	1.028	-8.259	1342350.126	1769562.099	1018276.703
Terzan 5 V8	7.440	0.705	-7.849	920165.207	1213013.985	698016.6915
Terzan 5 V9	8.420	0.286	-6.869	373134.846	491887.5245	283051.7263

[a] IRSF data from Matsunaga (private communication)
[b] Dereddened K Flux is derived with Eq. 2.13
[c] Derived from K IRSF
[d] Maximum and minimum flux values are derived after Whitelock et al. (2000) with a mean Mira amplidude of 0.6 mag.

2.2.5 Dust Residuals

In order to derive the dust residuals of the AGB stars of the globular cluster sample this work is based on, the dereddened AGB star spectra in absolute flux units are now combined with the absolut K flux from IRSF data presented in Table 2.6. The K flux is used to attach a blackbody to each spectrum which is subsequently subtracted to retrieve a continuum reduced spectrum - the dust residuals. Unfortunately the NIR photometric measuements of both, the 2MASS survey and the IRSF observations, have not been performed simultaneously with the MIR spectroscopy performed with the *Spitzer* satellite. Due to the AGB star variability this difference in the observing date can directly affect the subtraction of the backbody that is attached to the NIR fluxes, since the MIR flux of the dust residuals is depending on the flux level of the NIR flux with respect to the variability phase the stars were observed in. In various cases the blackbody mounted at the K flux of the respective star lies at a lower flux level compared to the MIR flux of the *Spitzer* spectrum. This effect was already reported by Lebzelter et al. (2006)[21] and is also seen in this work (Section 2.3).

Fig. 2.7 (left panel) shows the MIR-spectrum of the AGB star NGC 5927 V1 together with the blackbody mounted on the K flux. A second backbody is mounted at 8 μm. To illustrate the effects of the variability on the K flux, the mean K amplitude of a typical Mira star is shown in Fig. 2.7 (left panel) and the figures in Section 2.3. The mean amplitude is derived using δK values from Whitelock et al. (2000). Whitelock et al. (2000) presented in their Table 3 the amplitudes of a large sample of Mira stars. The mean amplitude of this sample amounts to 0.6 mag in the K band and is used as a representative value for the variability of Mira stars in K. This mean amplitude is centered at the mean K flux from IRSF data leading to a ± 0.3 mag
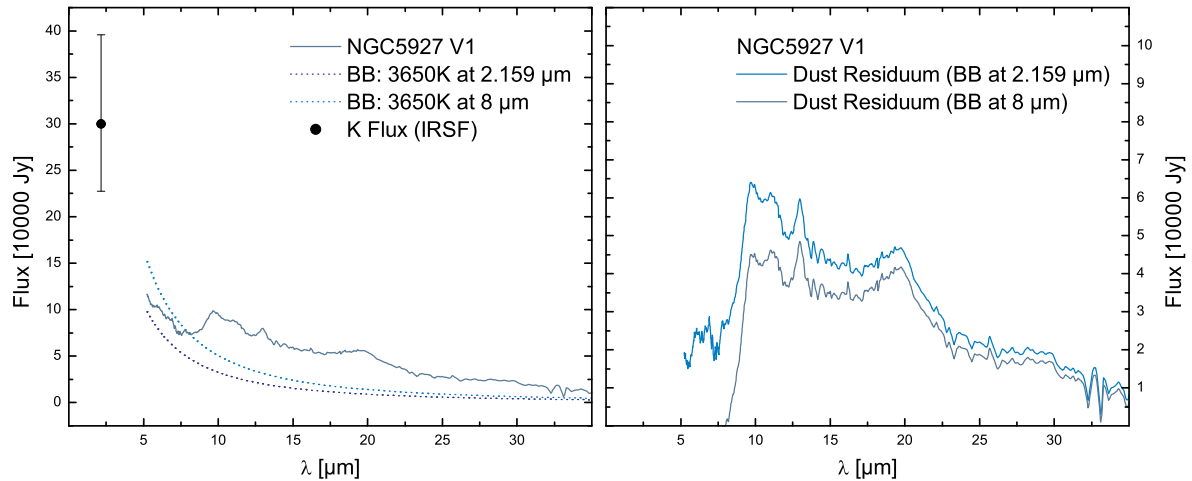

Figure 2.7: Left panel: *Spitzer* spectrum of the globular cluster AGB star NGC 5927 V1. Absolute Flux in Jansky. IRSF K flux is shown with possible amplitude variations. Two blackbody curves with $T_{BB} = 3650$ K are overlayed, mounted at K and 8 μm, respectively. Right panel: Dust residuals after blackbody subtraction.

---

[21] Note that in the case of NGC 104 the K photometry and the *IRS* spectroscopy were performed almost simultaneously.

variability and is used to derive the minimum and the maximum M_K magnitude, which is subsequently converted to flux units in Jansky. This minimum and maximum flux values are illustrated as "error" bars in Fig. 2.7 (left panel) and again in the figures in Section 2.3. Table 2.6 presents the mean K flux according to the IRSF mean K magnitude from Matsunaga (private communication) as well as the minimum and maximum flux values derived with the mean Mira star amplitude.

The variability of AGB stars can be used to explain low flux levels of the blackbodies attached to the K flux for several stars presented in Section 2.3. Therefore it is convenient to attach a second blackbody at $8 \, \mu$m. This wavelength marks the point in the MIR-spectra where the dust features start to dominate and are easily separated from the stellar continuum. In Fig. 2.7 (right panel) the dust residuals derived with the two blackbodies (one attached at K, one attached at $8 \, \mu$m) of NGC 5927 V1 are shown.

The temperatures of the subtracted blackbodies are derived using a Color-Temperature-Relation on the basis of MARCS models from Aringer et al. (2009). The relation is based on the photometric Bessel system (see Bessell & Brett 1988 and Bessell et al. 1998) and makes use of the $(J - K)$ color. To use the $(J - K)_0$ color derived from J and K presented in the Tables 2.2 and 2.7 the color is converted to the Bessel system applying Equation 2.14 taken from Carpenter (2001). Table 2.7 presents the converted color and the blackbody temperatures. Fig. 2.8 shows the Color-Temperature-Relation used to derive the blackbody temperatures (left panel) and the distribution of the temperatures of the globular cluster AGB stars of the sample from Sloan et al. (2010) (right panel). The temperature distribution shows peaks at 3550 K and 3950 K. The hottest star is NGC 362 V2 and is reported to be a "naked" star with no significant dust emission. Three stars (all from the globular cluster Terzan 5) are too red in $(J - K)_0$ to derive a good temperature estimate. For these stars a low temperature of 3000 K is adopted.

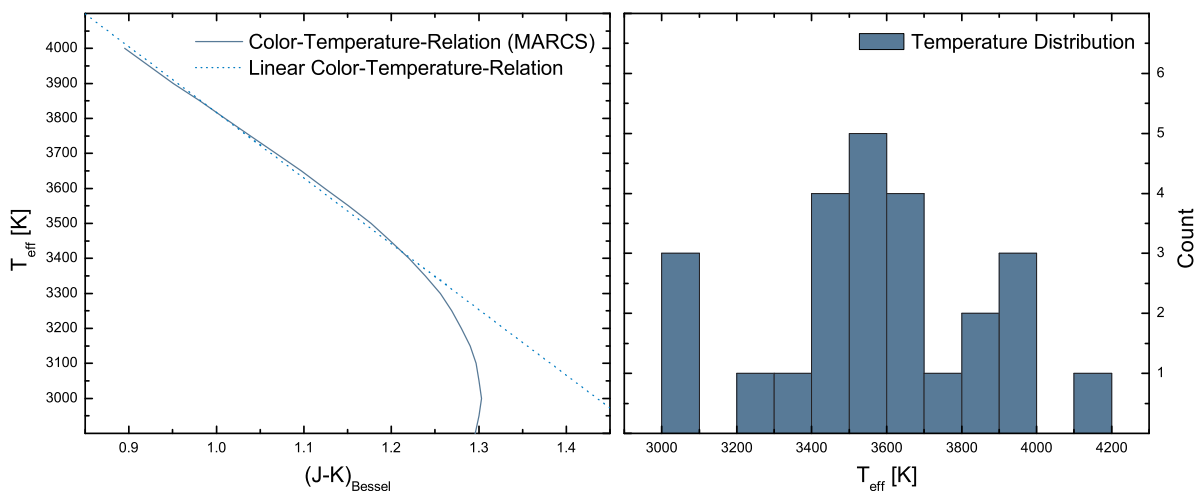$$(J - K)_0 = (0.972 \pm 0.006) \cdot (J - K)_{Bessel} + (-0.011 \pm 0.005) \tag{2.14}$$

Figure 2.8: Left panel: Color-Temperature-Relation from MARCS models. The linear relation is described with $-1877 \, x + 5694$. Right panel: Temperature distribution of the globular cluster AGB stars this work is based on.

Table 2.7: AGB Star Temperature

Star ID	J^a	$(J-K)_0$ IRSF[b]	$(J-K)_0$ Bessel[c]	T [K][d]
IC 1276 V1	8.430	1.044	1.085	3650
IC 1276 V3	8.260	1.034	1.075	3650
NGC 362 V2	9.730	0.783	0.817	4100
NGC 362 V16	9.130	0.883	0.920	3950
NGC 5927 V1	9.160	1.036	1.078	3650
NGC 5927 V3	8.730	1.146	1.191	3450
NGC 6352 V5	8.330	1.157	1.201	3400
NGC 6356 V1	10.170	1.193	1.239	3350
NGC 6356 V3	10.200	1.093	1.136	3550
NGC 6356 V4	10.330	1.123	1.167	3500
NGC 6356 V5	9.933	1.155	1.200	3450
NGC 6388 V3	10.310	1.135	1.179	3500
NGC 6388 V4	9.640	0.965	1.004	3800
NGC 6553 V4	8.180	1.089	1.132	3550
NGC 6637 V4	8.844	1.141	1.185	3450
NGC 6637 V5	8.658	1.075	1.118	3550
NGC 6712 V2	9.100	0.702	0.733	4200
NGC 6712 V7	8.720	0.902	0.939	3900
NGC 6760 V3	9.120	1.019	1.060	3650
NGC 6760 V4	9.390	1.009	1.049	3700
NGC 6838 V1	7.630	0.905	0.942	3850
Terzan 5 V2	9.780	0.878	0.915	3900
Terzan 5 V6	10.020	1.268	1.316	3250
Terzan 5 V7	9.740	1.458	1.511	3000
Terzan 5 V8	9.790	1.098	1.141	3000
Terzan 5 V9	11.420	1.748	1.810	3000

[a] IRSF data from Matsunaga (private communication)

[b] $(J-K)_0$ IRSF is derived using J from this Table and K from Table 2.6. Dereddening is performed with Equations 2.2 - 2.5.

[c] $(J-K)_0$ Bessel ist derived using Eq. 2.14

[d] Temperatur is derived after the Color-Temperatur-Relation presented in Fig. 2.8

2.2.6   Bolometric Correction and Luminosity

In order to derive the luminosity of the globular cluster AGB stars the bolometric K magnitude is used. Applying the least-squares polynomial presented in Equation 2.15 the bolometric correction (taken from Whitelock et al. 2000) is performed as a function of the $(J-K)_0$ color. The bolometric correction is given in Table 2.8 together with the bolometric magnitude M_{bol}, which is derived with Equation 2.16 using the M_K-values from Table 2.6. Equation 2.17 is used to derive the luminosity of the AGB stars in units of $L_\odot$, where $M_{bol\odot}$ is 4.72 mag. Bolometric magnitudes and luminosity against $\log P$ values are presented in Fig. 2.9 and in Table 2.8.

$$BC_K = 10.86 - 38.10(J-K)_0 + 64.16(J-K)_0^2 -$$
$$-50.72(J-K)_0^3 + 19.48(J-K)_0^4 - 2.94(J-K)_0^5 \tag{2.15}$$

$$BC_K = M_{\mathrm{bol}} - M_K \tag{2.16}$$

$$\frac{L}{L_\odot} = 10^{-0.4(M_{\mathrm{bol}} - M_{\mathrm{bol}\odot})} \tag{2.17}$$

In Fig. 2.9 red symbols mark the stars of the most metal-rich cluster of the sample, Terzan 5. Most of the stars are very luminous compared to the rest of the globular cluster AGB stars. The exception is Terzan 5 V9, which is heavily reddened at K, thus the bolometric correction may be incorrect (see Fig. 3.6). Sloan et al. (2010) reported that V9 could be a member of a younger population present in Terzan 5. Indeed Ferraro et al. (2009) detected a young stellar population with an age of 6 Gyrs alongside the known old population with an age of 12 Gyrs. Terzan 5 seems to be a special case[22] because all stars with available *Spitzer* spectrum (except V2) are very red. V6, V7 and V8 are also very luminous but still reported to be members of the cluster. It is possible that all the bright AGB stars observed by Sloan et al. (2010) are members of the young population in Terzan 5. In Chapter 4 it is shown that an isochrone with the age of the old population is not suited to explain the luminous AGB stars in Terzan 5. On the other hand an isochrone with an age of the young population described in Ferraro et al. (2009) provides an AGB tip with high luminosities around L = 8500 L$_\odot$, i.e. consistent with the luminosities found for the AGB stars.
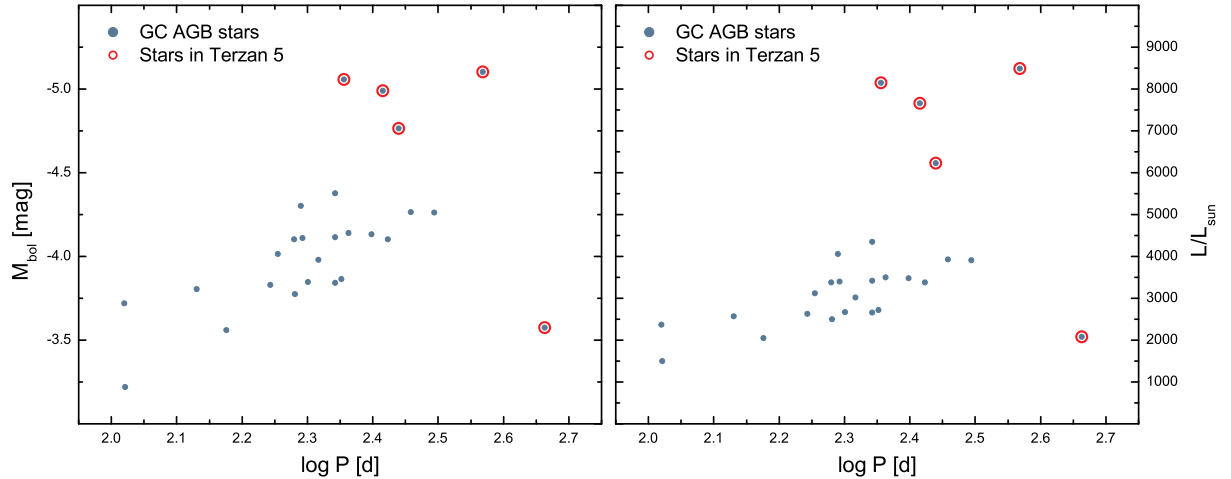

Figure 2.9: Left panel: Period-M$_{\mathrm{bol}}$ diagram. Blue symbols refer to the globular cluster AGB star sample presented in Table 2.2 (without NGC 104), red circles mark stars in Terzan 5. Right panel: Period-$\frac{L}{L_\odot}$-Diagram. Same color coding as in the left panel.

---

[22] Ferraro et al. (2009) reports the cluster to be the first stellar aggregate discovered in the galactic bulge that has globular-cluster-like properties but also the signatures of a much more complex star formation history.

Table 2.8: Bolometric Correction and Luminosity

Star ID	$(J-K)_0$ IRSF	BC[a]	M_{bol}[b]	$L\,[L_\odot]$[c]
IC 1276 V1	1.044	2.795	-3.842	2659.785
IC 1276 V3	1.034	2.783	-4.014	3117.227
NGC 362 V2	0.783	2.472	-3.220	1499.416
NGC 362 V16	0.883	2.588	-3.804	2569.076
NGC 5927 V1	1.036	2.786	-3.847	2672.233
NGC 5927 V3	1.146	2.911	-4.262	3914.321
NGC 6352 V5	1.157	2.922	-3.829	2628.026
NGC 6356 V1	1.193	2.958	-4.140	3500.513
NGC 6356 V3	1.093	2.854	-4.115	3419.240
NGC 6356 V4	1.123	2.887	-3.981	3024.048
NGC 6356 V5	1.155	2.921	-4.377	4352.240
NGC 6388 V3	1.135	2.899	-3.561	2052.974
NGC 6388 V4	0.965	2.695	-4.266	3928.901
NGC 6553 V4	1.089	2.849	-4.102	3379.319
NGC 6637 V4	1.141	2.906	-4.109	3400.343
NGC 6637 V5	1.075	2.833	-4.302	4063.251
NGC 6712 V2	0.702	2.415	-3.719	2374.015
NGC 6712 V7	0.902	2.612	-4.102	3379.191
NGC 6760 V3	1.019	2.764	-4.133	3475.704
NGC 6760 V4	1.009	2.752	-3.865	2717.059
NGC 6838 V1	0.905	2.616	-3.776	2503.107
Terzan 5 V2	0.878	2.581	-5.058	8151.817
Terzan 5 V6	1.268	3.024	-4.765	6225.437
Terzan 5 V7	1.458	3.157	-5.102	8491.637
Terzan 5 V8	1.098	2.859	-4.991	7660.042
Terzan 5 V9	1.748	3.294	-3.576	2080.931

[a] Derived after Whitelock et al. (2000) using Eq. 2.15
[b] Derived with Eq. 2.16
[c] Luminosity is derived with Eq. 2.17

2.3 The MIR-Spectra

The following pages show the Figures 2.11 to 2.36 presenting the MIR-spectra[23] and the dust residuals of the globular cluster AGB stars from Table 2.2[24].

The upper panels of Figures 2.11 to 2.36 show the MIR-spectra including the NIR K flux from IRSF data (see Table 2.6) and the mean K flux amplitudes derived after Whitelock et al. (2000). Also shown in the upper panels are the blackbodies attached to the K flux and the $8\,\mu m$ MIR flux, respectively. The blackbody temperatures are presented in Table 2.7. The lower panels of Figures 2.11 to 2.36 show the dust residuals after subtraction of the two different blackbodies. Possible dust feature positions in the MIR range are indicated in both panels.

The spectra of the globular cluster AGB stars can be separated into stars without significant dust emission and stars with prominent dust features from silicates and alumina[25]. The silicates manifest themselfs with peak positions at 9.7, 12.3, 18 and $20.5\,\mu m$, while the alumina dust results in a peak at $11.3\,\mu m$. Possible carriers of these dust features can be determined in laboratory measurements. The corresponding dust species for the oxygen-rich regime are listed in Table 2.9. Also some carbon dioxide emission lines can be detected at 13.48, 13.87,14.98, 16.18 and $16.80\,\mu m$.

Three stars show the presence of both crystalline silicate and alumina dust, and are presented in Fig. 2.10. The $10\,\mu m$ emission from amorphous silicate dust is splitted into two components at 9.7[26] and $11.3\,\mu m$. A strong $13\,\mu m$ feature is present in all three spectra. Which specific dust species produces the $13\,\mu m$ feature remains unclear. A possible carrier could be spinel ($MgAl_2O_4$) or even chromium doped spinel (cf. Posch et al. 1999 and Richter et al. 2005). Also the $20\,\mu m$ feature points to an enhanced crystallinity in the three sources. Possible carriers of the $20\,\mu m$ emission are cystalline silicates (Sloan et al. 2003b) or oxides like [Mg,Fe]O (Posch et al. 2002).

For a detailed study of the distribution of the various dust features with respect to the metallicity range of the observed globular clusters see Sloan et al. (2010).

For the Galactic globular cluster NGC 104 a detailed discussion of the MIR-specta of the AGB star population is found in Lebzelter et al. (2006). The authors reported a change of the dust composition when the star evolves along the AGB. Early on the AGB the dust species manifest in Mg, Al and Fe oxides, while with further evolution amorphous silicates become the dominant species. Beside this dust evolution scenario Lebzelter et al. (2006) reported two special cases, namely V13 and V18 that to not fit the scenario due to their large IR excess in relation to their position in the Period-K diagram. While V18 can be explained as a star in the minimum of a thermal pulse, the characteristics of V13 are still a matter of debate (cf. Section 1.3).

---

[23]Errorbars are generally smaller than the width of the plotted spectrum
[24]Without the AGB stars from the globular cluster NGC 104, which are studied in detail in Lebzelter et al. (2006)
[25]See also Table 2.9 for detailed feature positions
[26]Terzan 5 V6 shows a 9.7 feature shifted to $9.3\,\mu m$

Table 2.9:   Dust Feature Positions

Dust Species	Feature Positions [μm] (FP)[a]		
	FP 1	FP 2	FP 3
Quartz SiO_2	8.6	12.3	20.5
Astronomical Silicates	9.7	18	–
Alumina Al_2O_3	11.3	–	–
Spinel $MgAl_2O_4$	13	17	32
Hibonite $CaAl_12O_19$	12.3	15.9	35
Magnesio-Wustite (Mg,Fe)O	16.5 – 20	–	–

[a] Dust species presented here are only a subsample of the dust species of the O-rich regime.
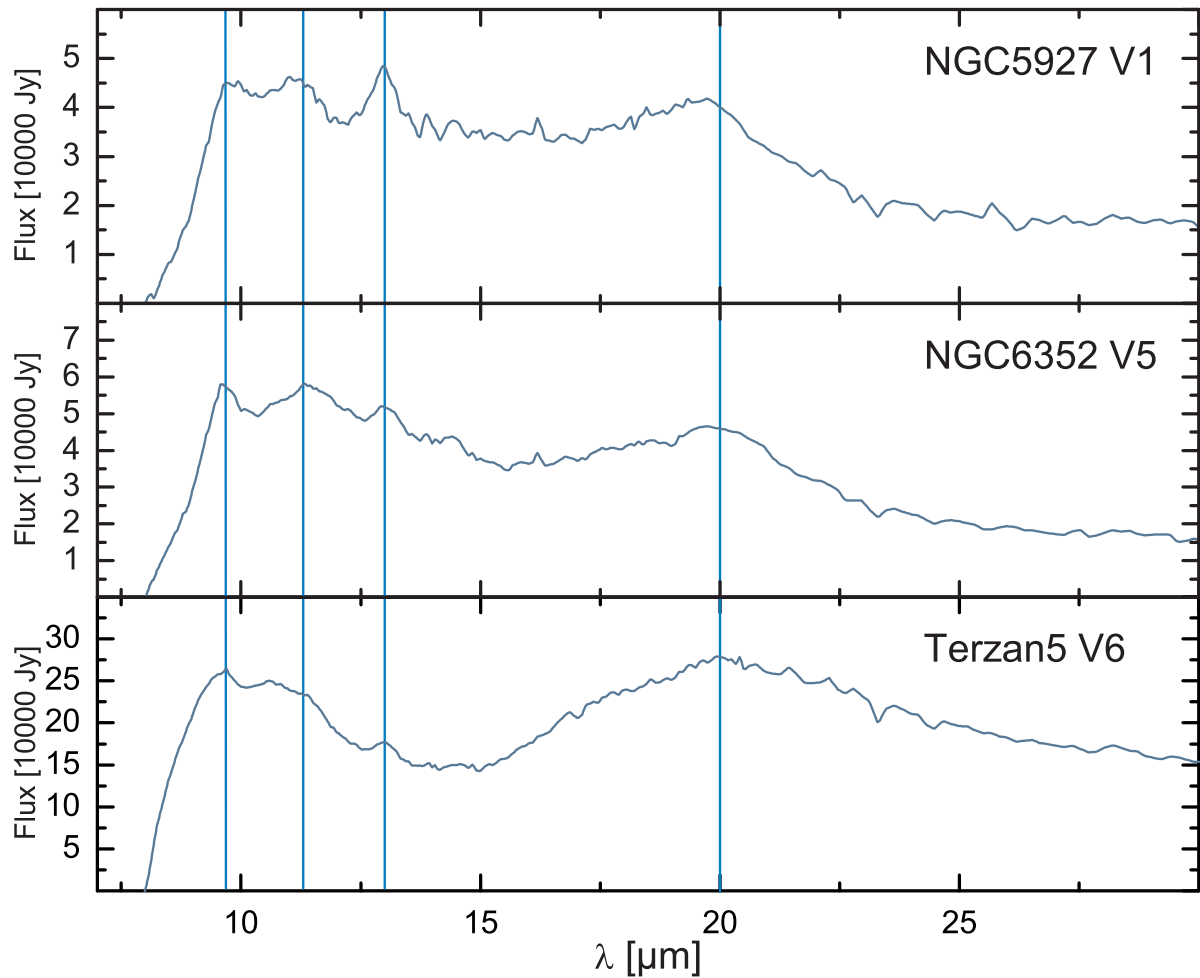
Figure 2.10:   Continuum subtracted MIR-spectra of the stars NGC 5927 V1, NGC 6352 V5 and Terzan 5 V6.   Dust features at 9.7, 11.3, 13.0 and 20.0 μm are indicated pointing to the presence of crystalline dust in the vicinity of the stars.
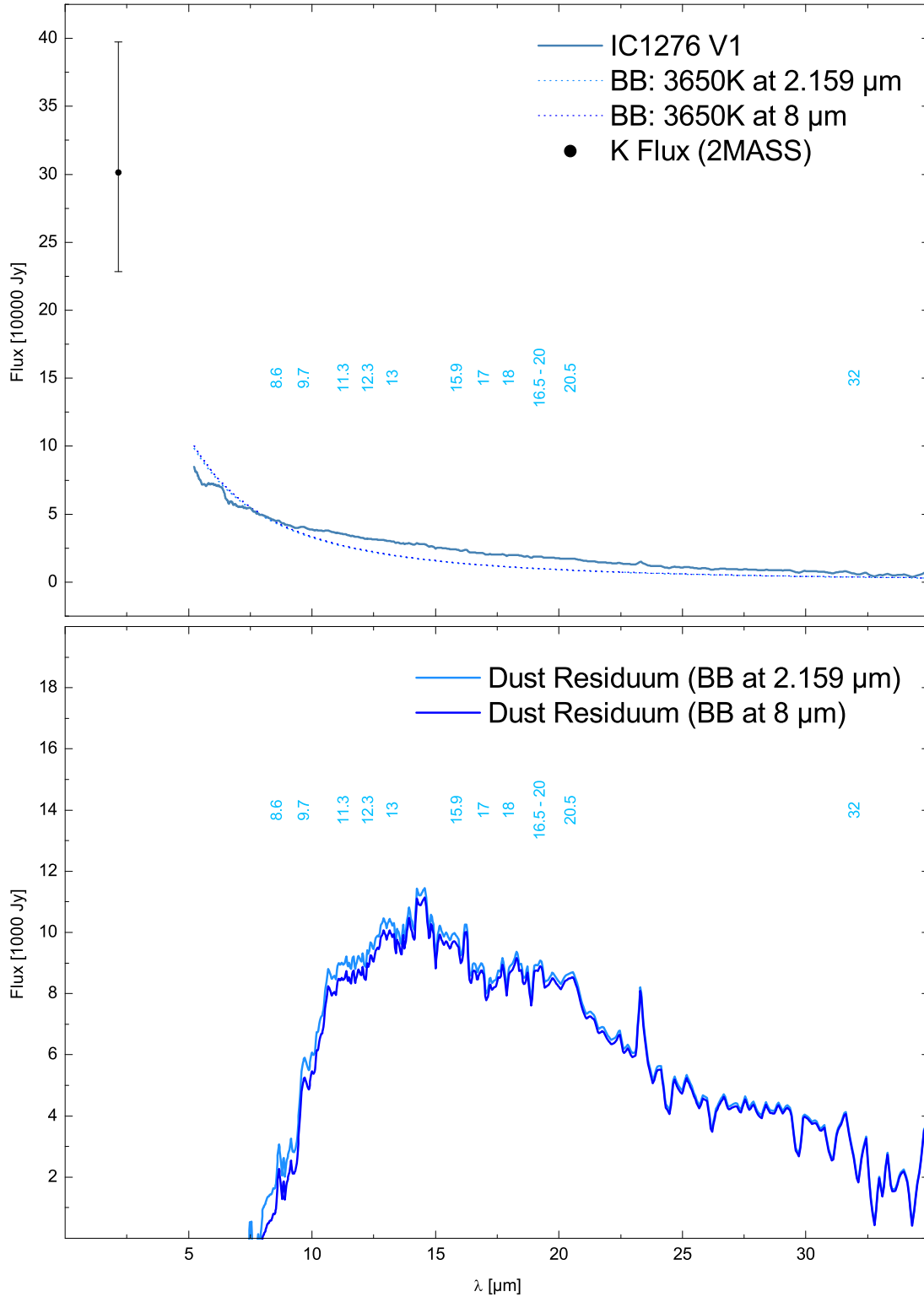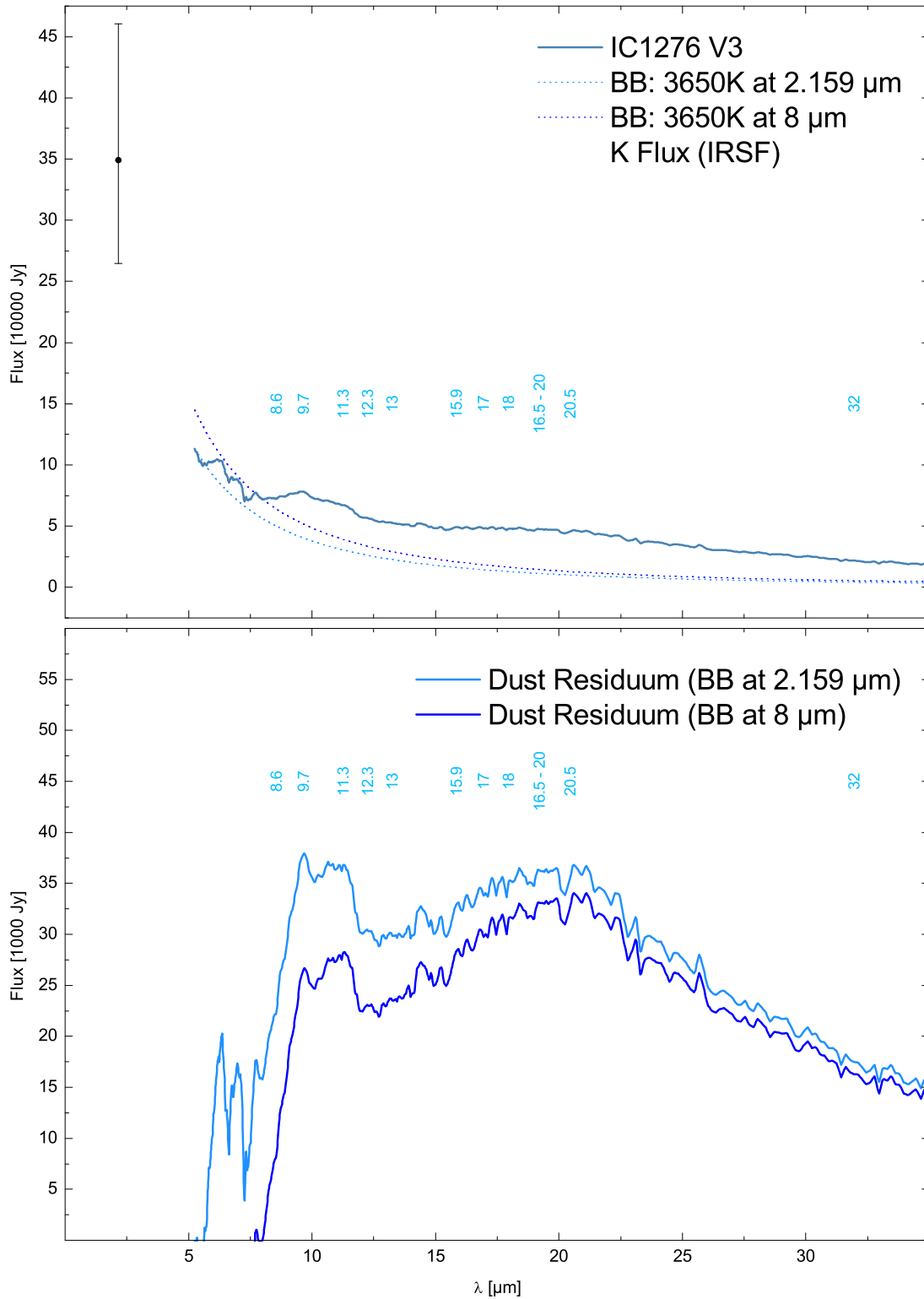
Figure 2.11: Upper panel: *Spitzer* spectrum of the globular cluster AGB star IC 1276 V1 in Jansky at a distance of 10 pc. Possible dust feature positions are indicated (see Table 2.9). Two blackbody curves with $T_{BB} = 3650$ K are overlayed, mounted at K and $8\,\mu$m, respectively. K Flux is derived from IRSF data. Lower panel: Dust residuals after blackbody subtraction.

Figure 2.12:   Upper panel: *Spitzer* spectrum of the globular cluster AGB star IC 1276 V3 in Jansky at a distance of 10 pc. Possible dust feature positions are indicated (see Table 2.9). Two blackbody curves with $T_{BB} = 3650$ K are overlayed, mounted at K and 8 μm, respectively. K Flux is derived from IRSF data. Lower panel: Dust residuals after blackbody subtraction.
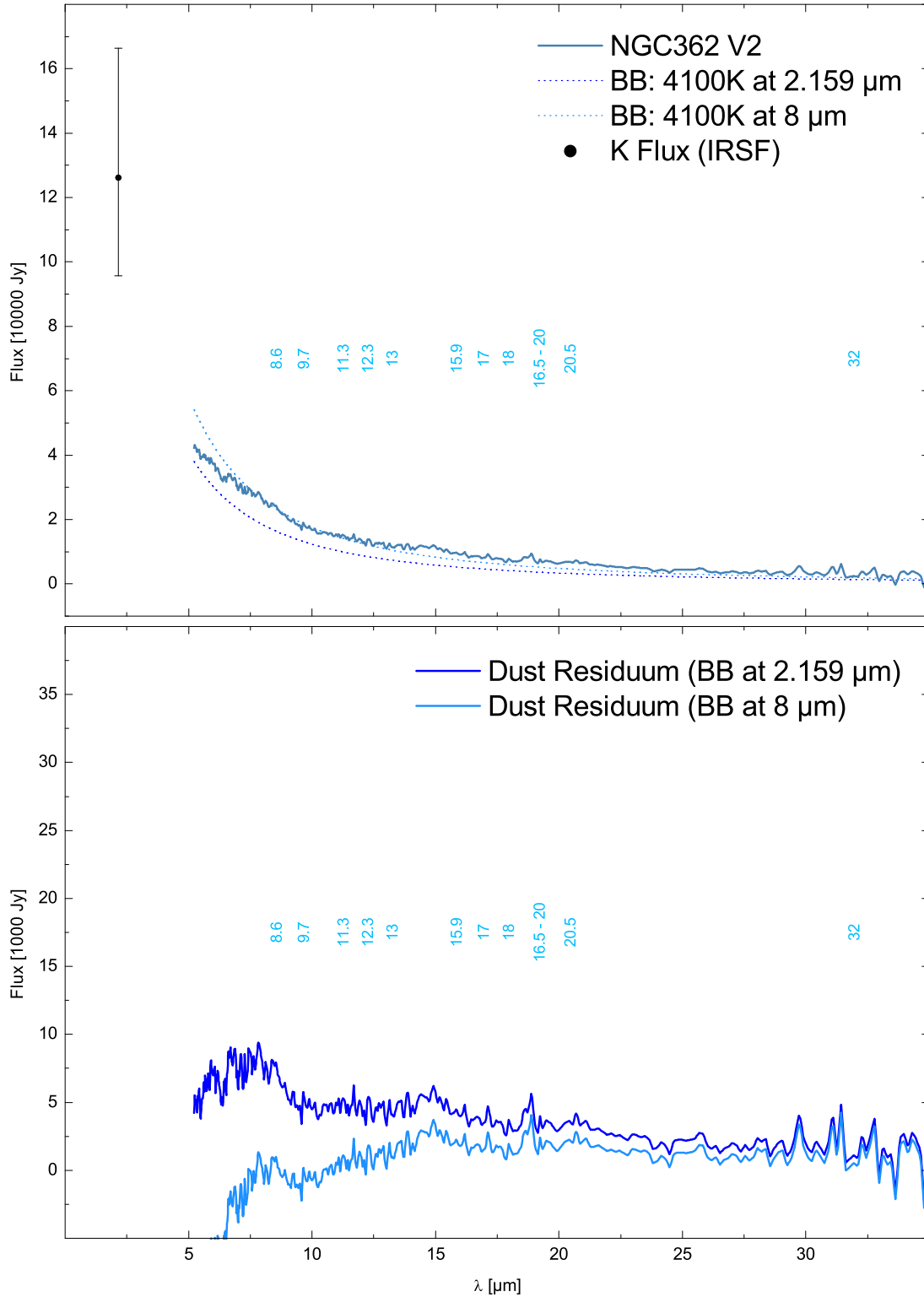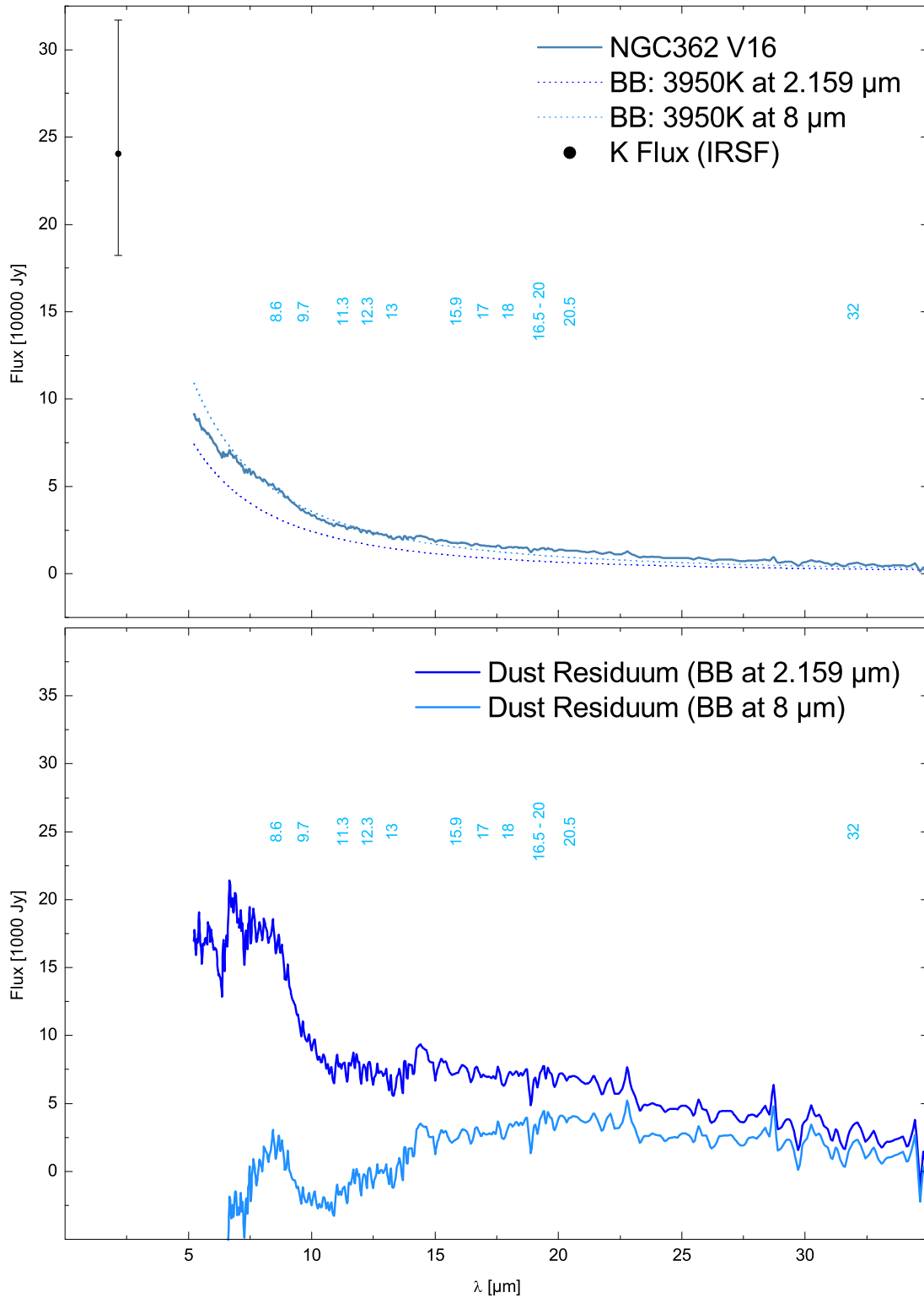
Figure 2.13: Upper panel: *Spitzer* spectrum of the globular cluster AGB star NGC 362 V2 in Jansky at a distance of 10 pc. Possible dust feature positions are indicated (see Table 2.9). Two blackbody curves with $T_{BB} = 4100\,K$ are overlayed, mounted at K and $8\,\mu m$, respectively. K Flux is derived from IRSF data. Lower panel: Dust residuals after blackbody subtraction.

Figure 2.14:   Upper panel: *Spitzer* spectrum of the globular cluster AGB star NGC 362 V16 in Jansky at a distance of 10 pc. Possible dust feature positions are indicated (see Table 2.9). Two blackbody curves with $T_{BB} = 3950$ K are overlayed, mounted at K and $8\,\mu$m, respectively. K Flux is derived from IRSF data. Lower panel: Dust residuals after blackbody subtraction.
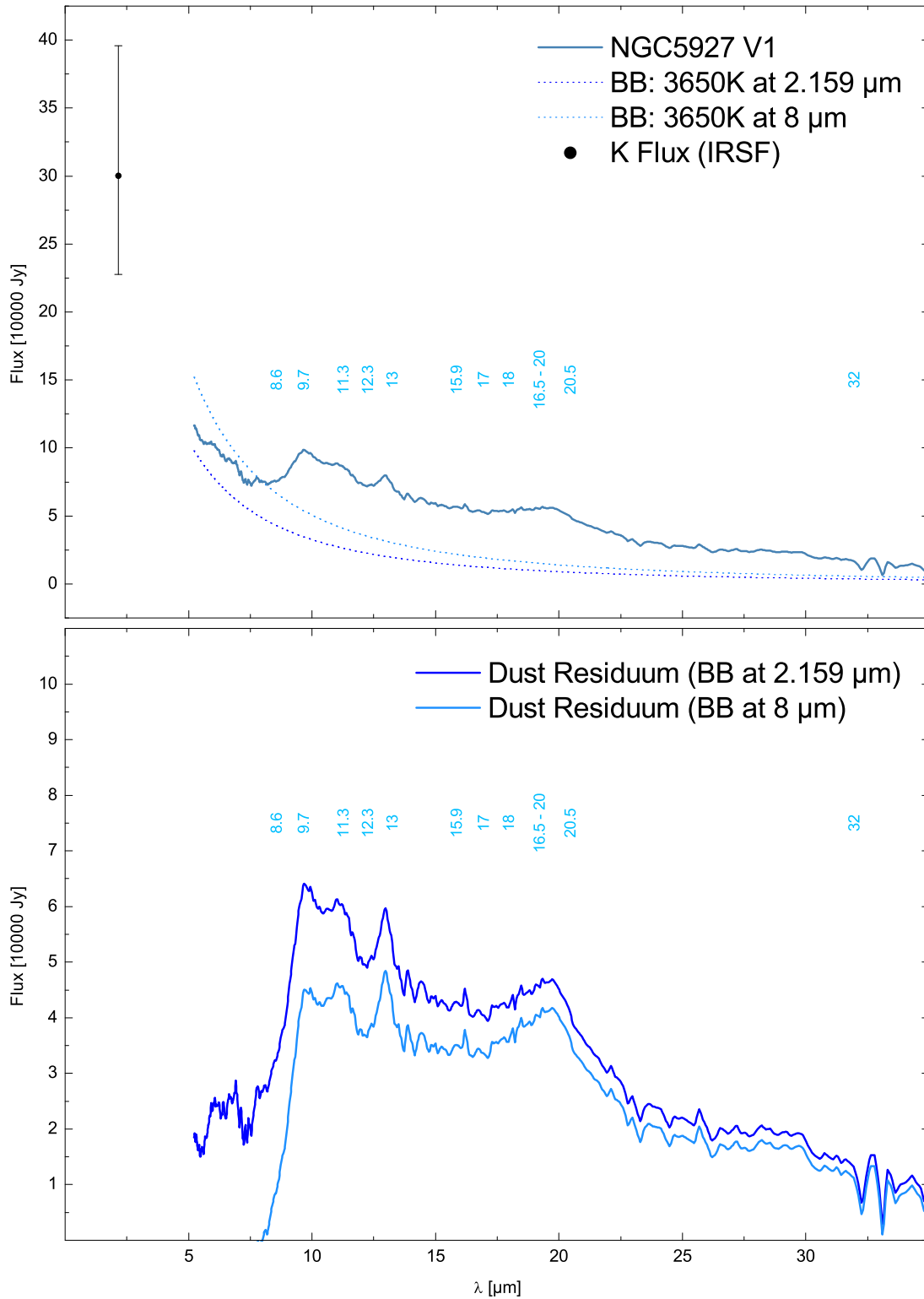
Figure 2.15: Upper panel: *Spitzer* spectrum of the globular cluster AGB star NGC 5927 V1 in Jansky at a distance of 10 pc. Possible dust feature positions are indicated (see Table 2.9). Two blackbody curves with $T_{BB} = 3650\,K$ are overlayed, mounted at K and $8\,\mu m$, respectively. K Flux is derived from IRSF data. Lower panel: Dust residuals after blackbody subtraction.
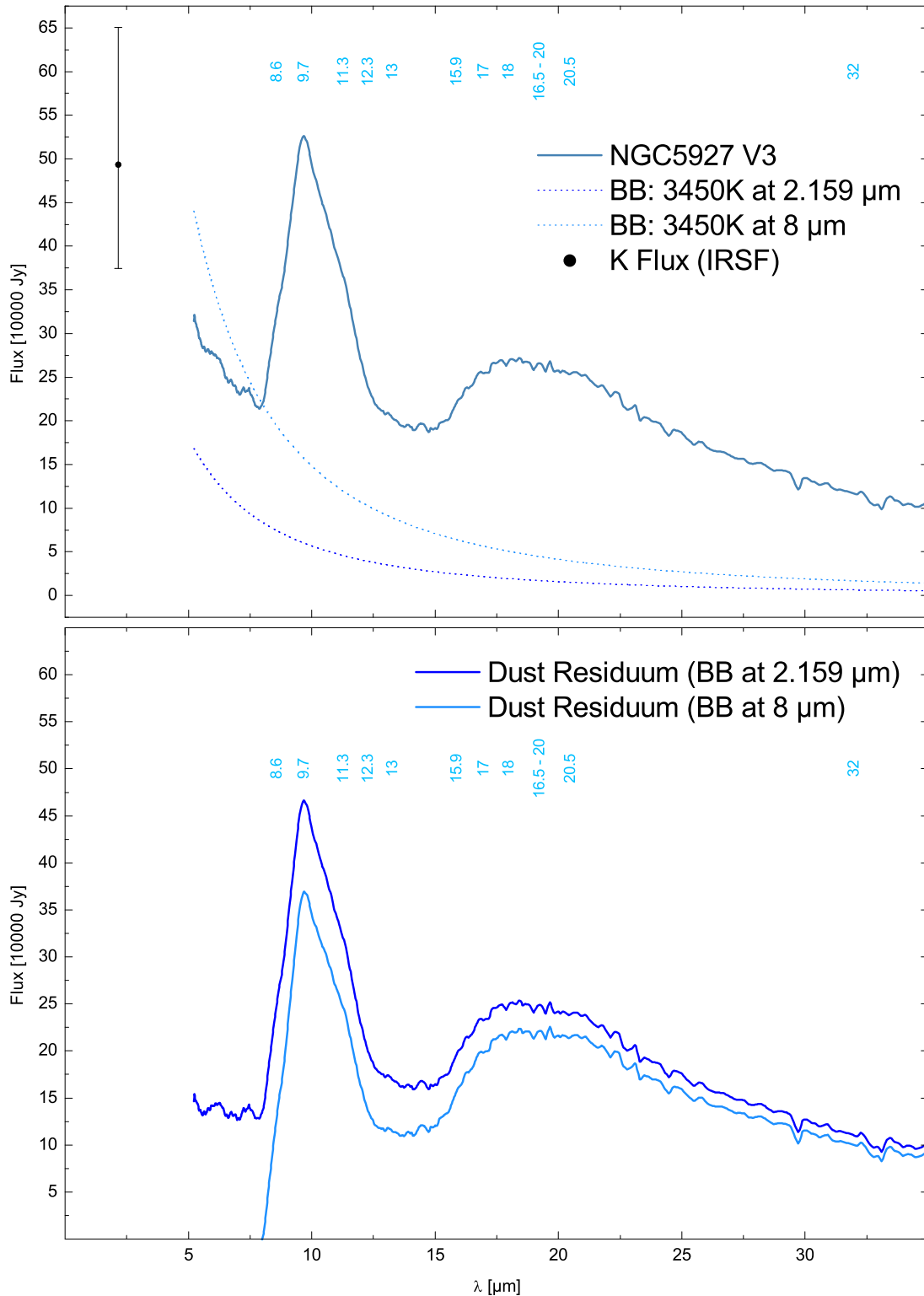
Figure 2.16: Upper panel: *Spitzer* spectrum of the globular cluster AGB star NGC 5927 V3 in Jansky at a distance of 10 pc. Possible dust feature positions are indicated (see Table 2.9). Two blackbody curves with $T_{BB} = 3450\,K$ are overlayed, mounted at K and $8\,\mu m$, respectively. K Flux is derived from IRSF data. Lower panel: Dust residuals after blackbody subtraction.

Figure 2.17: Upper panel: *Spitzer* spectrum of the globular cluster AGB star NGC 6352 V5 in Jansky at a distance of 10 pc. Possible dust feature positions are indicated (see Table 2.9). Two blackbody curves with $T_{BB} = 3400\,K$ are overlayed, mounted at K and $8\,\mu m$, respectively. K Flux is derived from IRSF data. Lower panel: Dust residuals after blackbody subtraction.
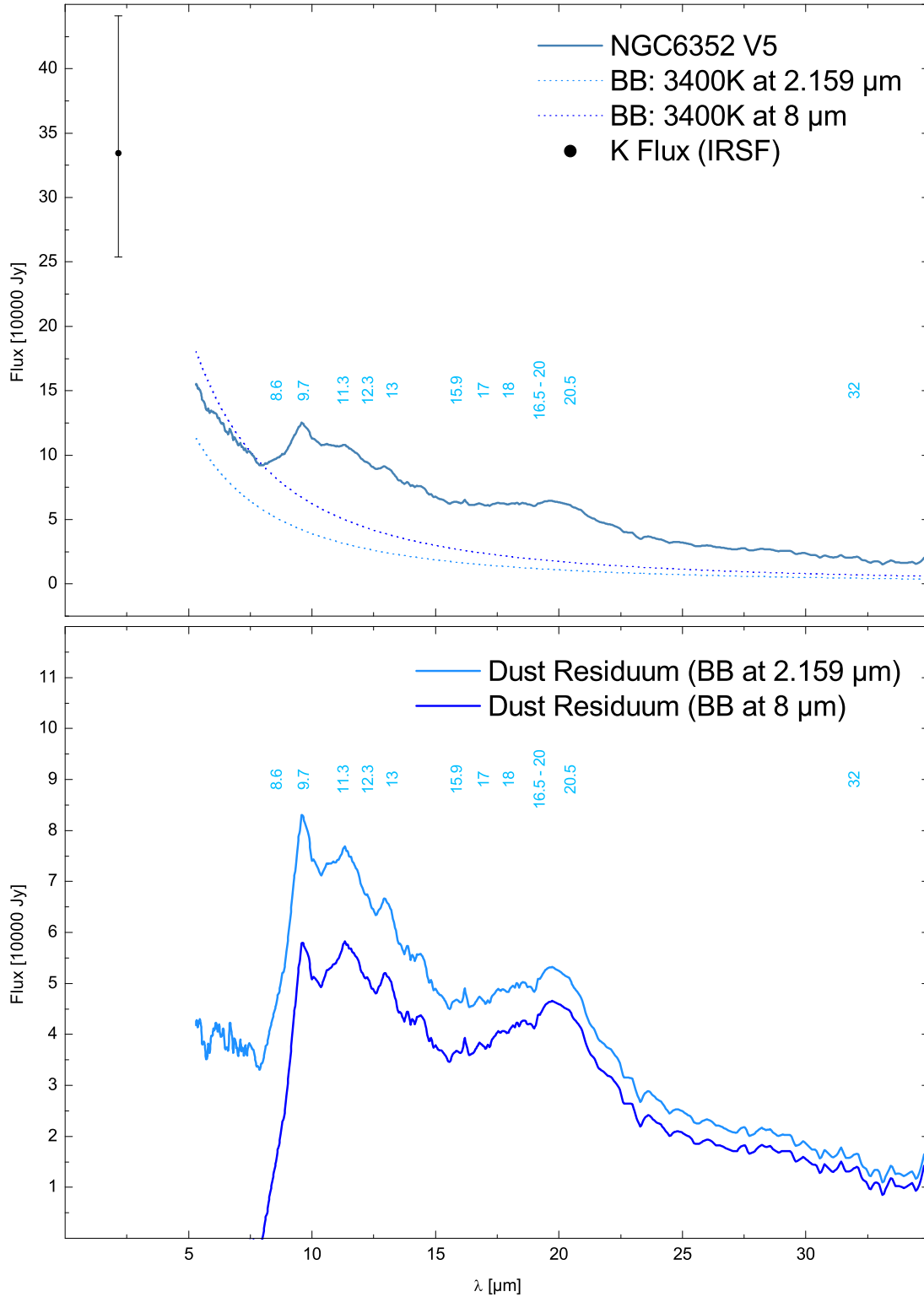
Figure 2.18:   Upper panel: *Spitzer* spectrum of the globular cluster AGB star NGC 6356 V1 in Jansky at a distance of 10 pc. Possible dust feature positions are indicated (see Table 2.9). Two blackbody curves with $T_{BB} = 3350$ K are overlayed, mounted at K and $8\,\mu$m, respectively. K Flux is derived from IRSF data. Lower panel: Dust residuals after blackbody subtraction.
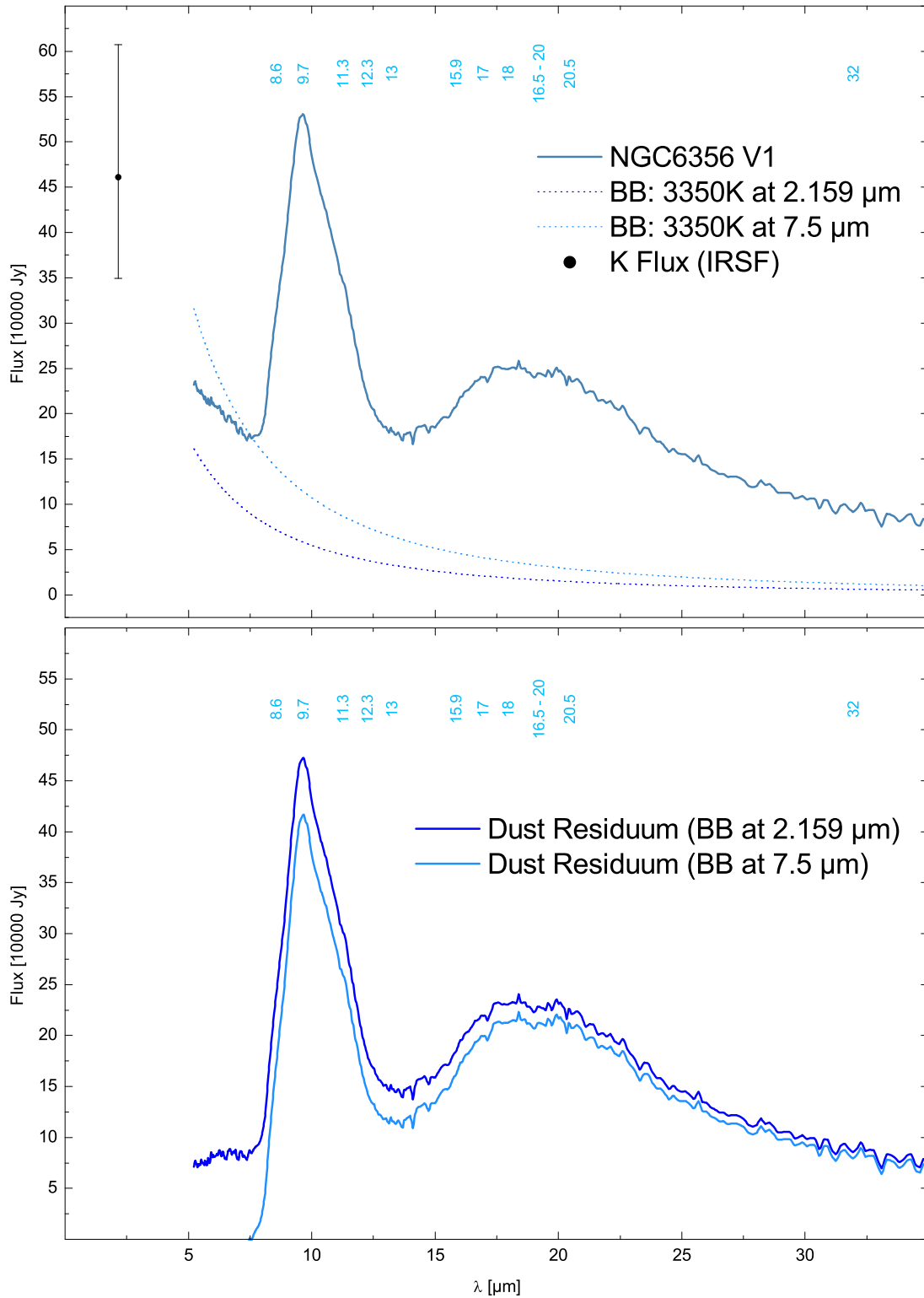
Figure 2.19: Upper panel: *Spitzer* spectrum of the globular cluster AGB star NGC 6356 V3 in Jansky at a distance of 10 pc. Possible dust feature positions are indicated (see Table 2.9). Two blackbody curves with $T_{BB} = 3550\,K$ are overlayed, mounted at K and $8\,\mu m$, respectively. K Flux is derived from IRSF data. Lower panel: Dust residuals after blackbody subtraction.
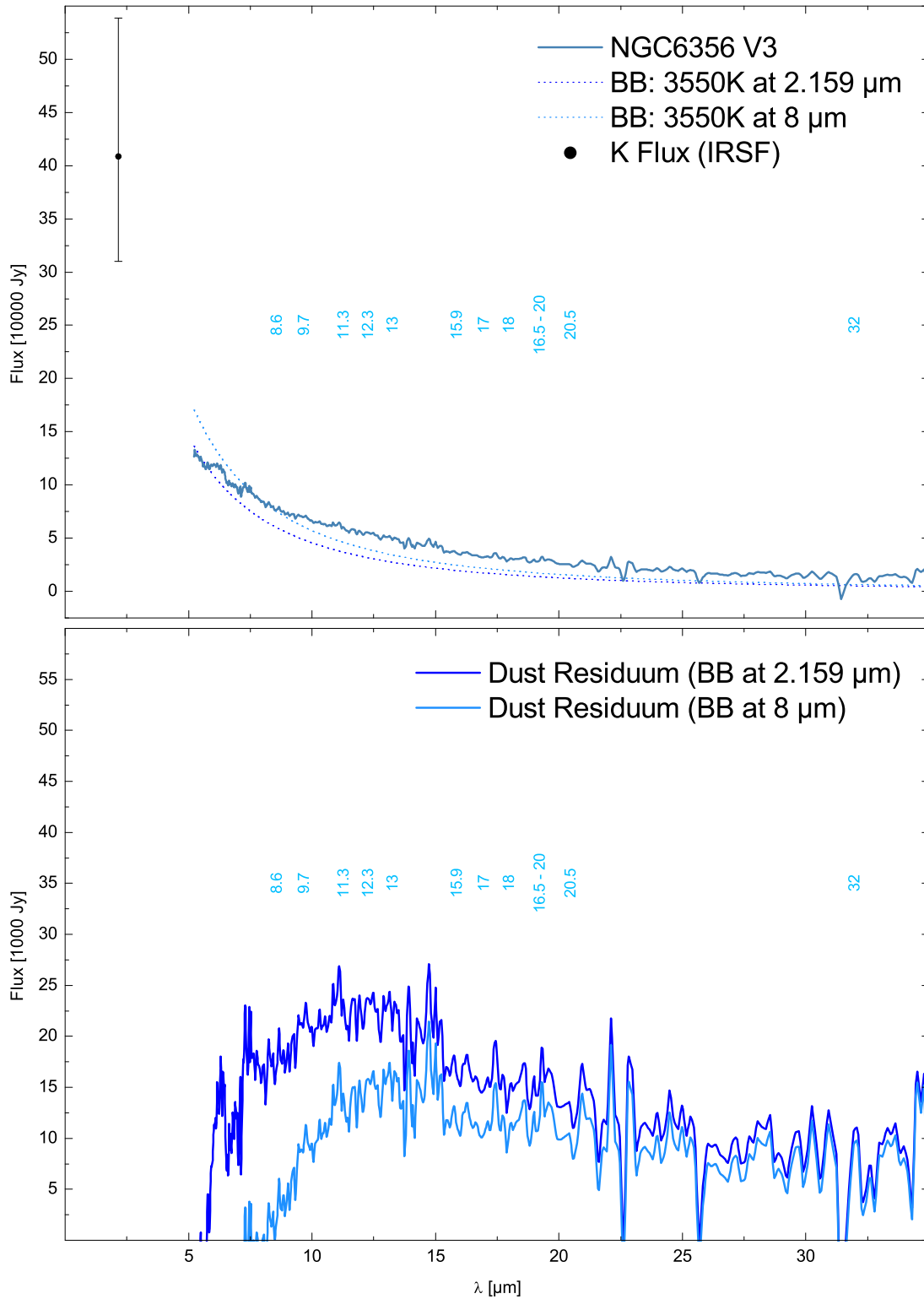
Figure 2.20:   Upper panel: *Spitzer* spectrum of the globular cluster AGB star NGC 6356 V4 in Jansky at a distance of 10 pc. Possible dust feature positions are indicated (see Table 2.9). Two blackbody curves with $T_{BB} = 3500\,K$ are overlayed, mounted at K and $8\,\mu m$, respectively. K Flux is derived from IRSF data. Lower panel: Dust residuals after blackbody subtraction.

Figure 2.21: Upper panel: *Spitzer* spectrum of the globular cluster AGB star NGC 6356 V5 in Jansky at a distance of 10 pc. Possible dust feature positions are indicated (see Table 2.9). Two blackbody curves with $T_{BB} = 3450$ K are overlayed, mounted at K and $8\,\mu$m, respectively. K Flux is derived from IRSF data. Lower panel: Dust residuals after blackbody subtraction.
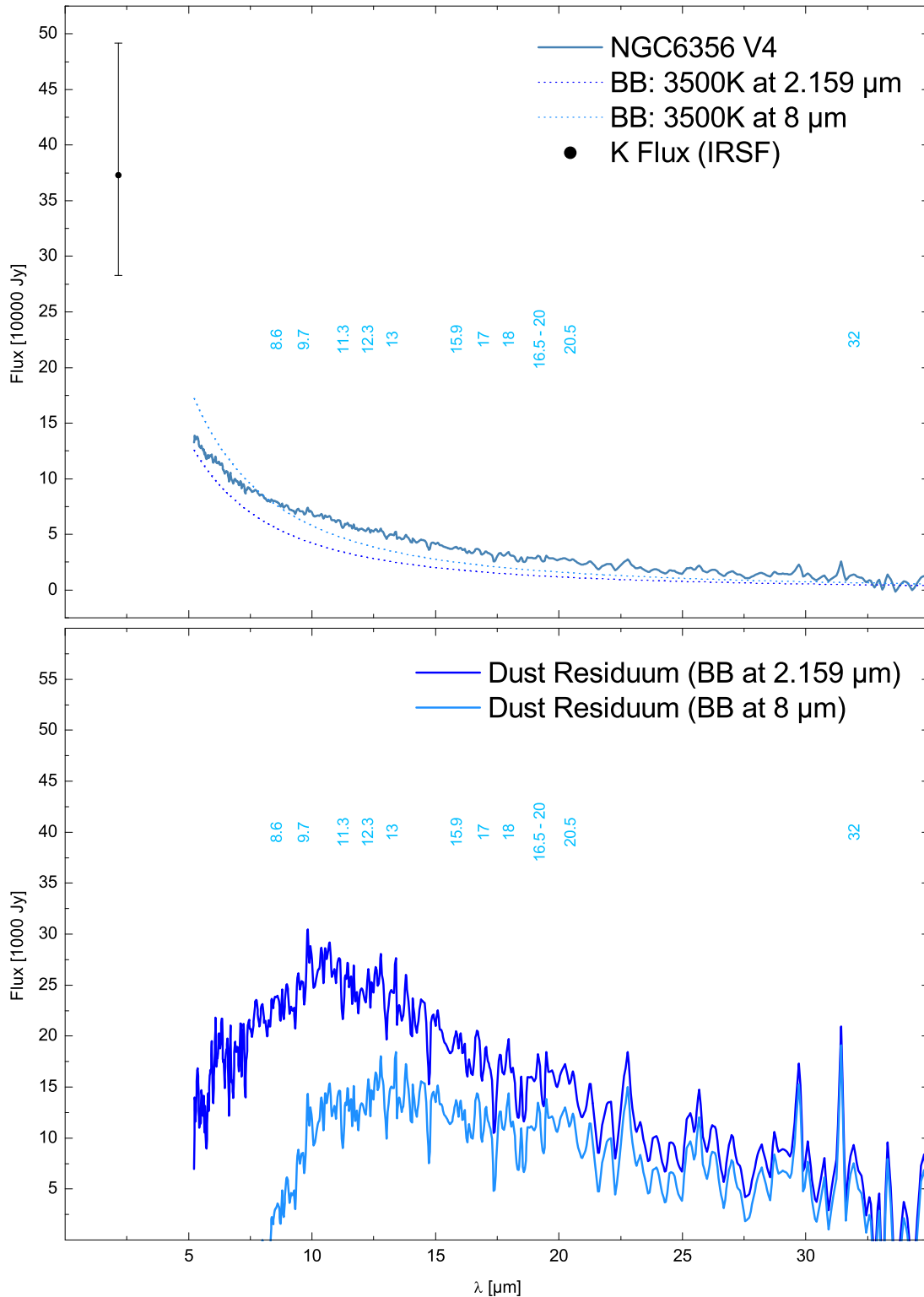
Figure 2.22: Upper panel: *Spitzer* spectrum of the globular cluster AGB star NGC 6388 V3 in Jansky at a distance of 10 pc. Possible dust feature positions are indicated (see Table 2.9). Two blackbody curves with $T_{BB} = 3500$ K are overlayed, mounted at K and 8 μm, respectively. K Flux is derived from IRSF data. Lower panel: Dust residuals after blackbody subtraction.
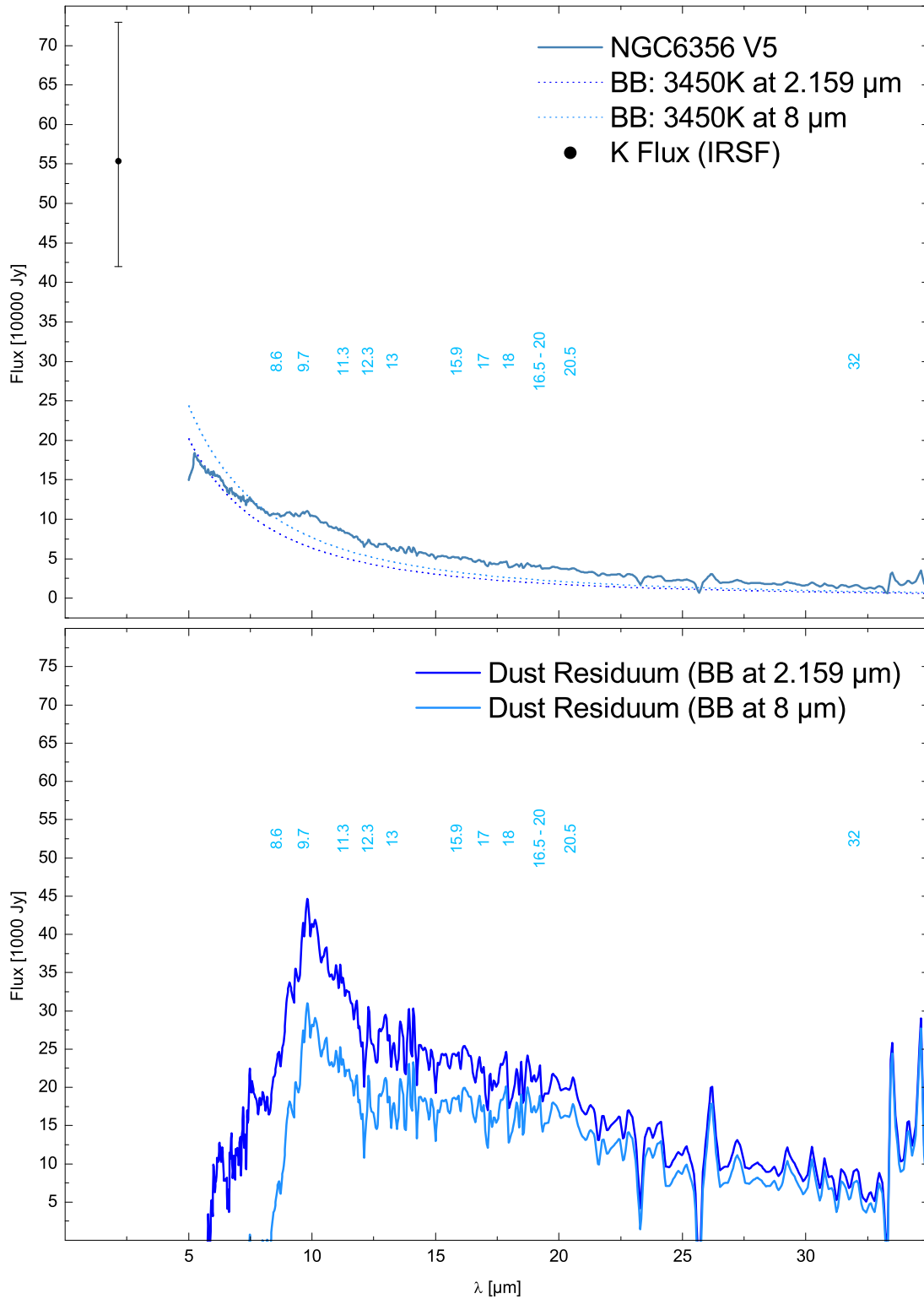
Figure 2.23: Upper panel: *Spitzer* spectrum of the globular cluster AGB star NGC 6388 V4 in Jansky at a distance of 10 pc. Possible dust feature positions are indicated (see Table 2.9). Two blackbody curves with $T_{BB} = 3800$ K are overlayed, mounted at K and $8\,\mu$m, respectively. K Flux is derived from IRSF data. Lower panel: Dust residuals after blackbody subtraction.
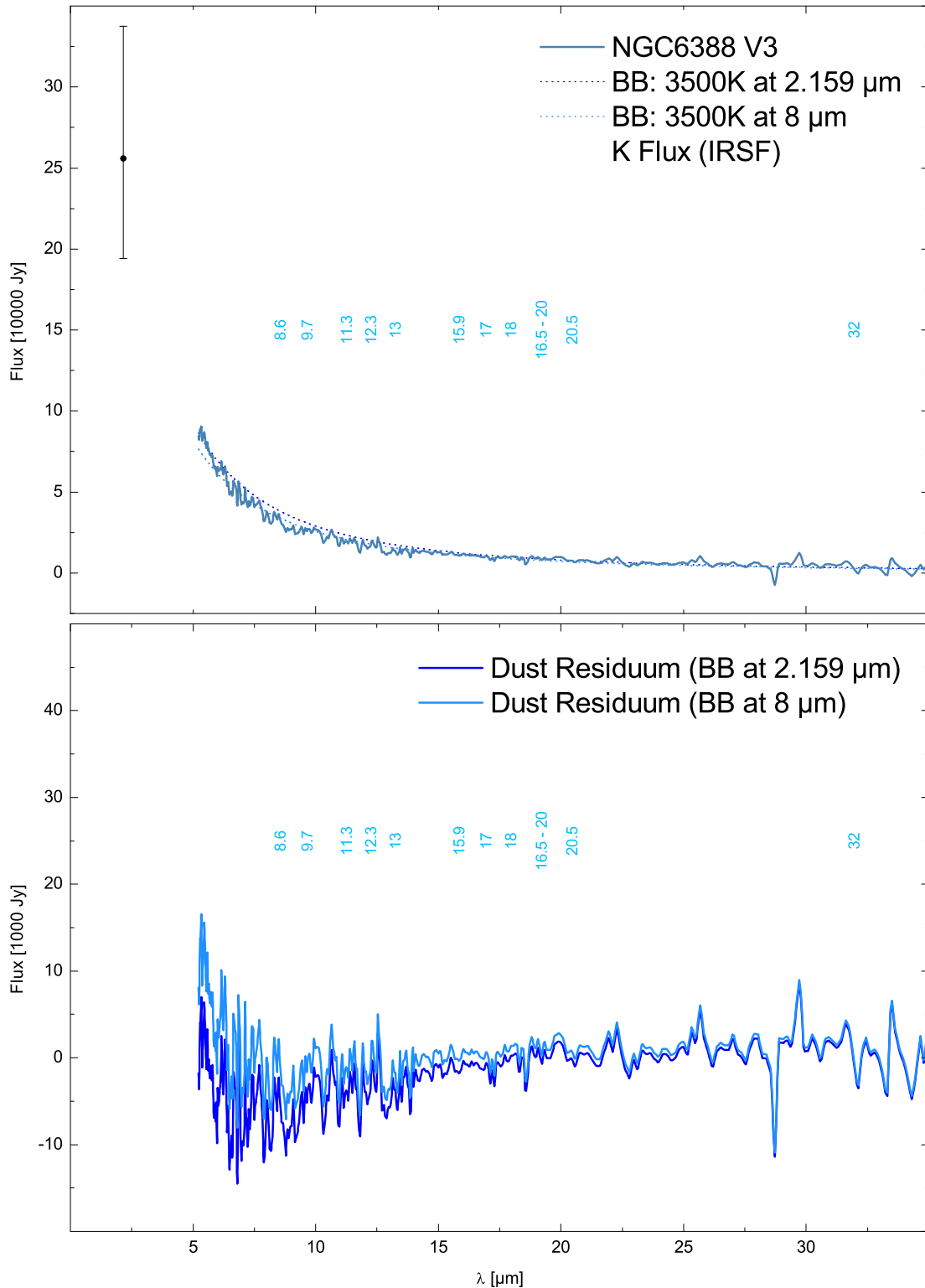
Figure 2.24: Upper panel: *Spitzer* spectrum of the globular cluster AGB star NGC 6553 V4 in Jansky at a distance of 10 pc. Possible dust feature positions are indicated (see Table 2.9). Two blackbody curves with $T_{BB} = 3550$ K are overlayed, mounted at K and $8\,\mu$m, respectively. K Flux is derived from IRSF data. Lower panel: Dust residuals after blackbody subtraction.

Figure 2.25: Upper panel: *Spitzer* spectrum of the globular cluster AGB star NGC 6637 V4 in Jansky at a distance of 10 pc. Possible dust feature positions are indicated (see Table 2.9). Two blackbody curves with $T_{BB} = 3450$ K are overlayed, mounted at K and $8\,\mu$m, respectively. K Flux is derived from IRSF data. Lower panel: Dust residuals after blackbody subtraction.
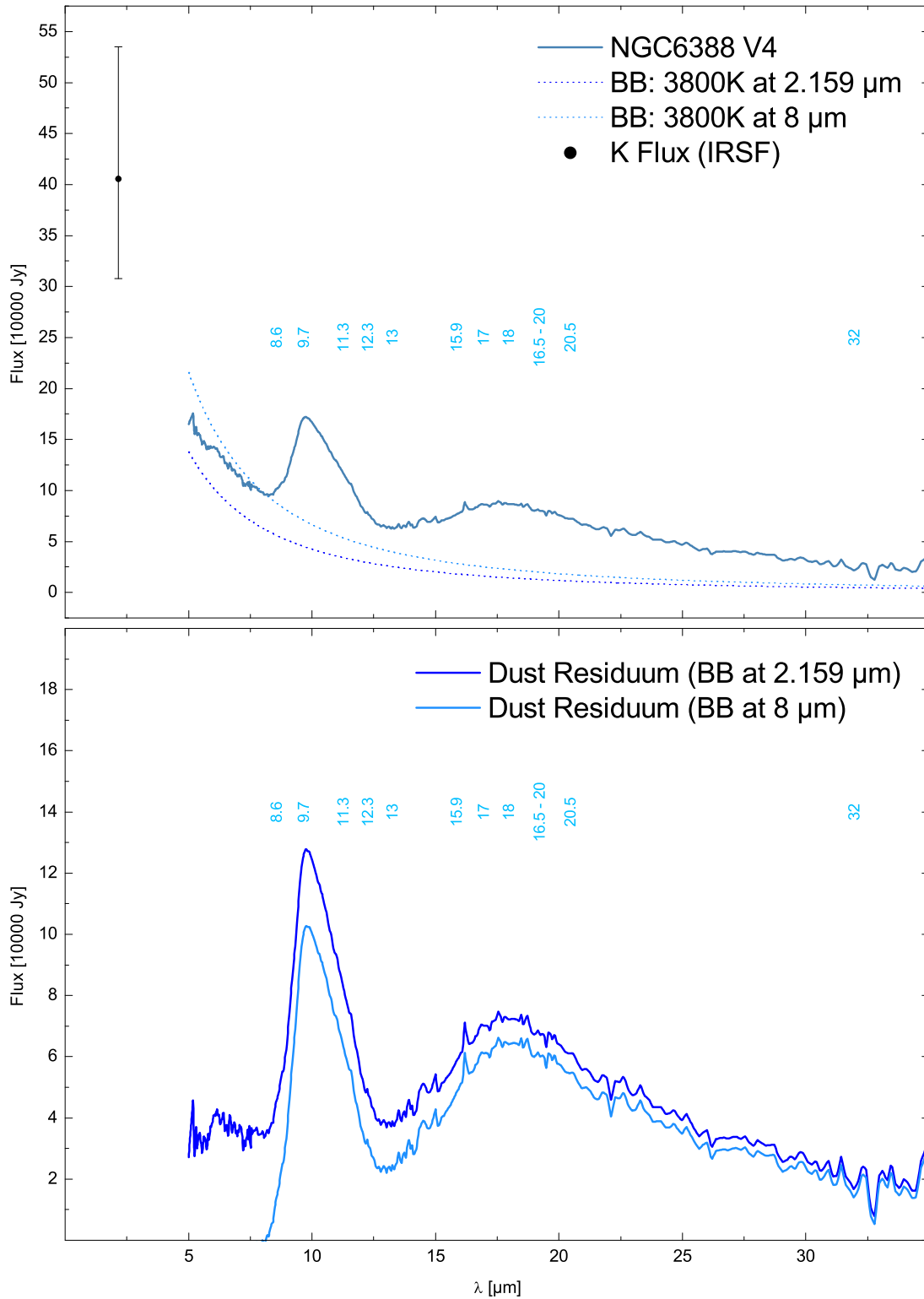
Figure 2.26:   Upper panel: *Spitzer* spectrum of the globular cluster AGB star NGC 6637 V5 in Jansky at a distance of 10 pc. Possible dust feature positions are indicated (see Table 2.9). Two blackbody curves with $T_{BB} = 3550$ K are overlayed, mounted at K and $8\,\mu$m, respectively. K Flux is derived from IRSF data. Lower panel: Dust residuals after blackbody subtraction.
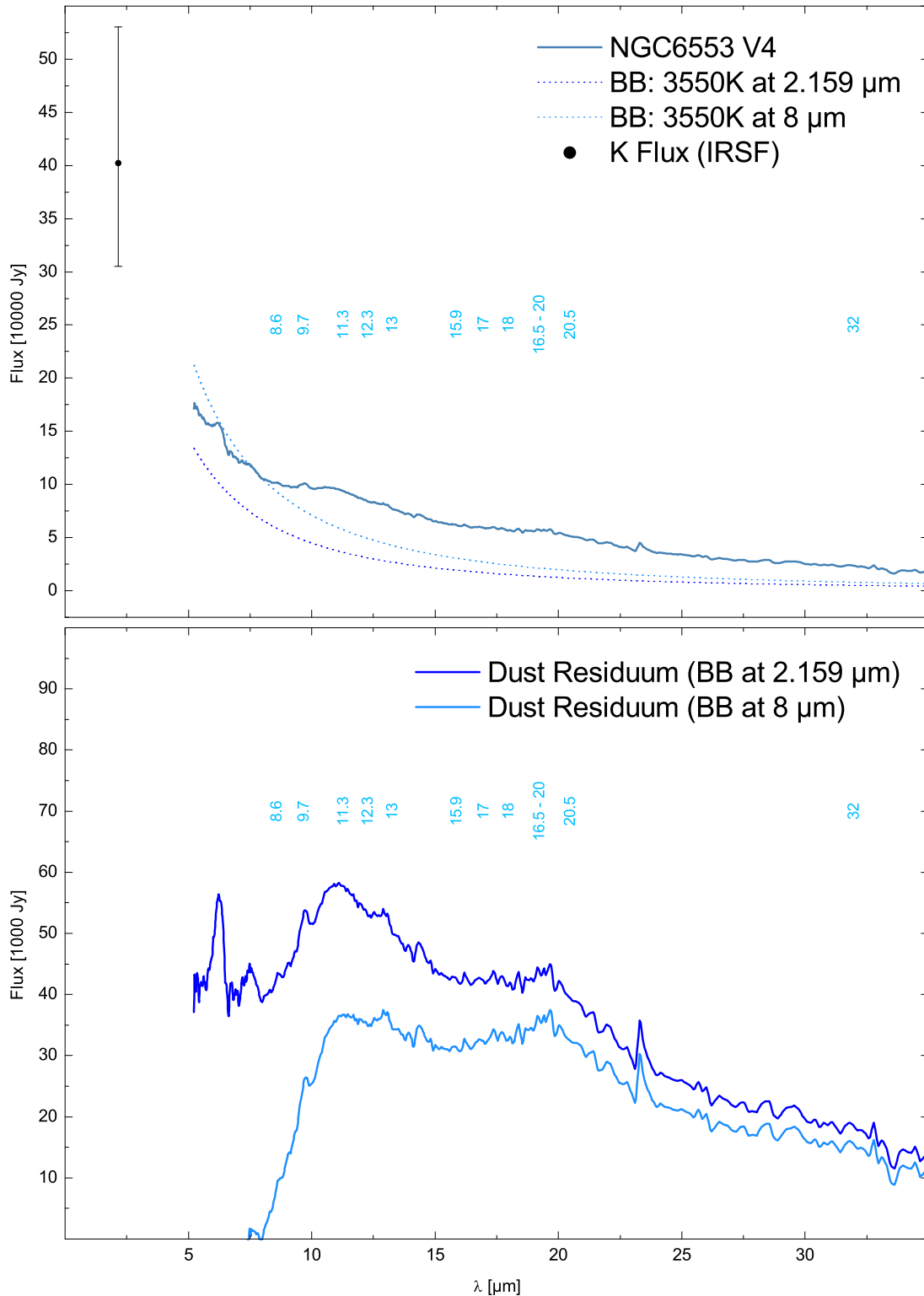
Figure 2.27: Upper panel: *Spitzer* spectrum of the globular cluster AGB star NGC 6712 V2 in Jansky at a distance of 10 pc. Possible dust feature positions are indicated (see Table 2.9). Two blackbody curves with $T_{BB} = 4200\,K$ are overlayed, mounted at K and $8\,\mu m$, respectively. K Flux is derived from IRSF data. Lower panel: Dust residuals after blackbody subtraction.
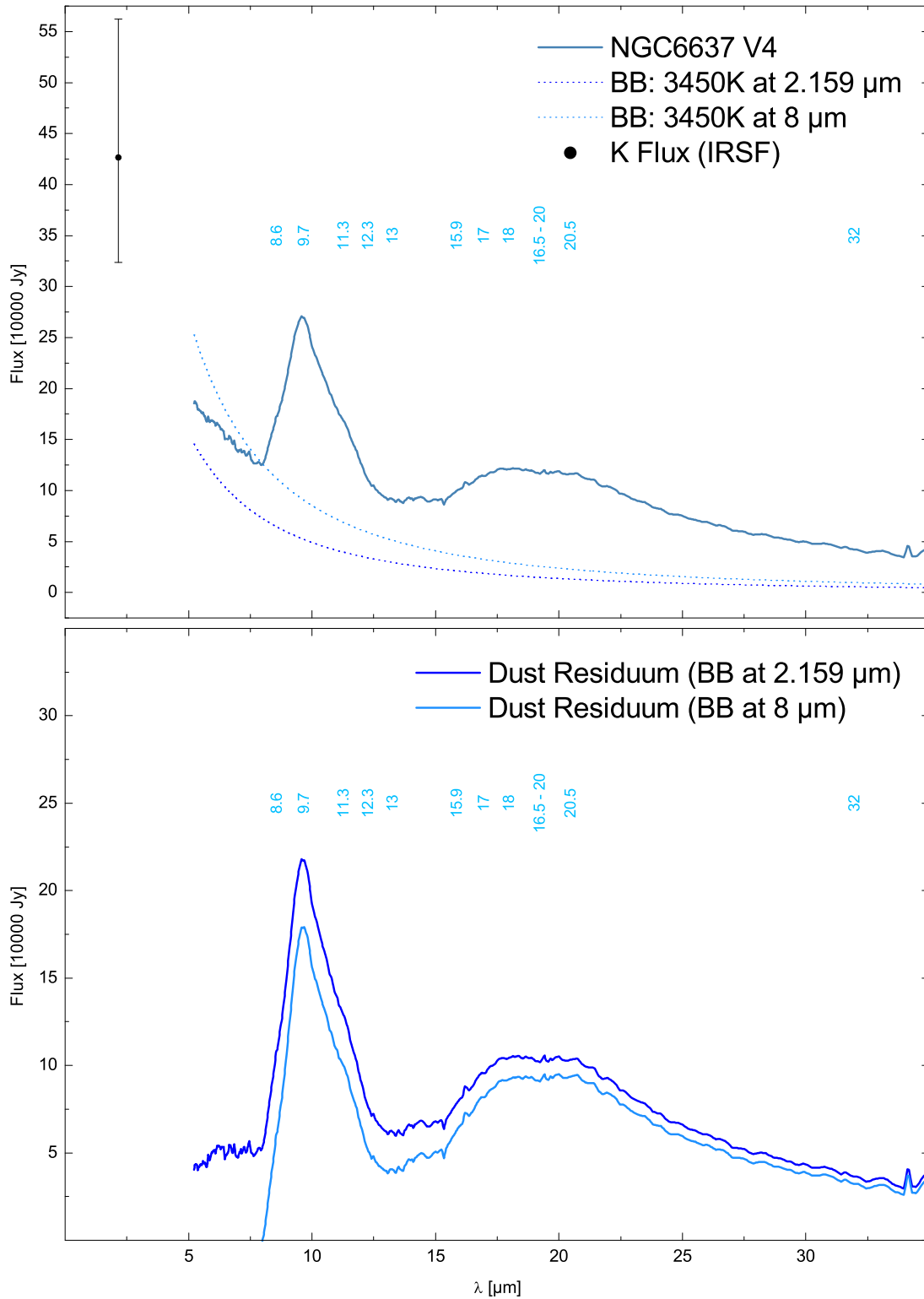
Figure 2.28:   Upper panel: *Spitzer* spectrum of the globular cluster AGB star NGC 6712 V7 in Jansky at a distance of 10 pc. Possible dust feature positions are indicated (see Table 2.9). Two blackbody curves with $T_{BB} = 3900\,K$ are overlayed, mounted at K and $8\,\mu m$, respectively. K Flux is derived from IRSF data. Lower panel: Dust residuals after blackbody subtraction.

Figure 2.29: Upper panel: *Spitzer* spectrum of the globular cluster AGB star NGC 6760 V3 in Jansky at a distance of 10 pc. Possible dust feature positions are indicated (see Table 2.9). Two blackbody curves with $T_{BB} = 3650$ K are overlayed, mounted at K and $8\,\mu$m, respectively. K Flux is derived from IRSF data. Lower panel: Dust residuals after blackbody subtraction.
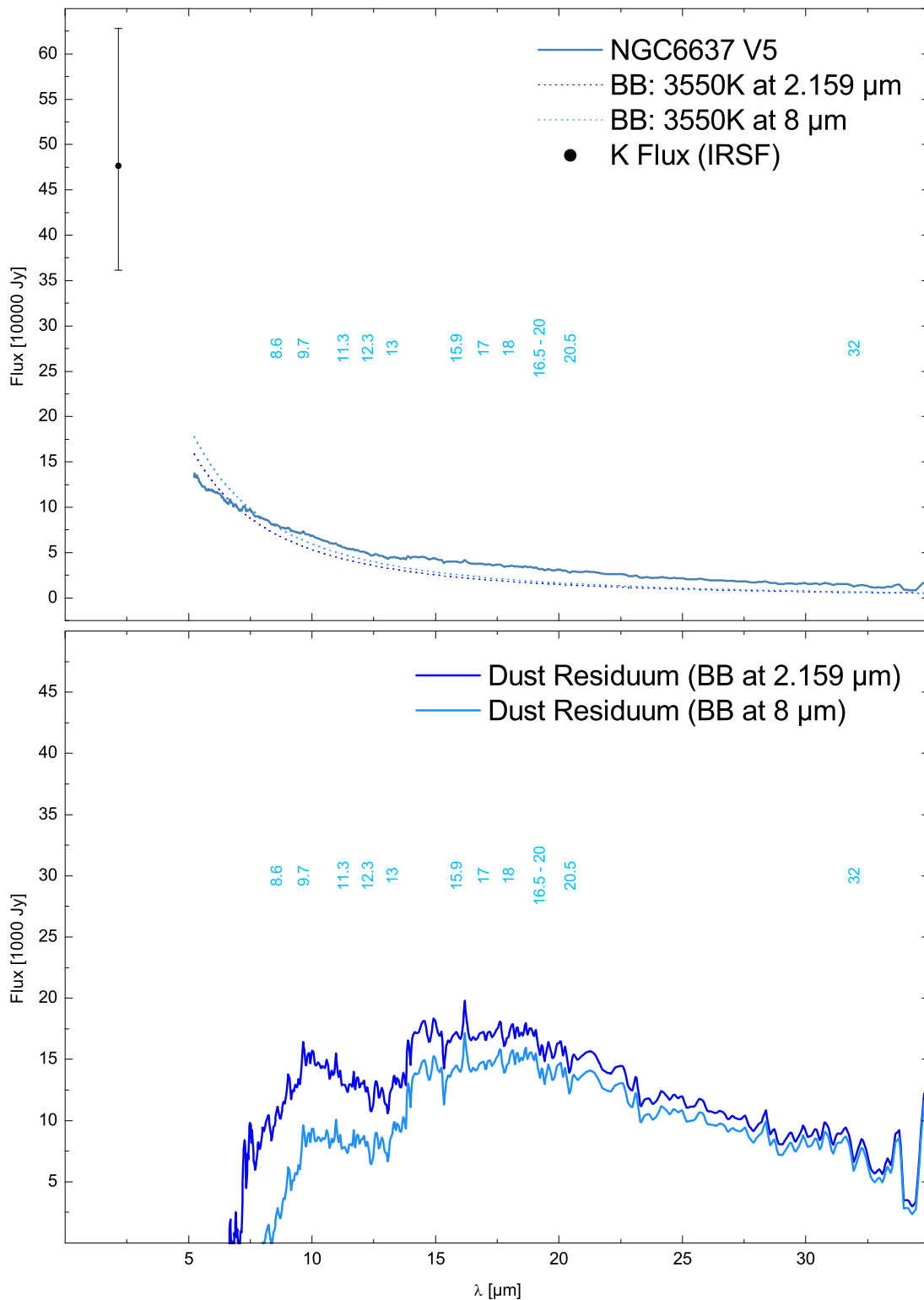
Figure 2.30: Upper panel: *Spitzer* spectrum of the globular cluster AGB star NGC 6760 V4 in Jansky at a distance of 10 pc. Possible dust feature positions are indicated (see Table 2.9). Two blackbody curves with $T_{BB} = 3700$ K are overlayed, mounted at K and $8\,\mu$m, respectively. K Flux is derived from IRSF data. Lower panel: Dust residuals after blackbody subtraction.
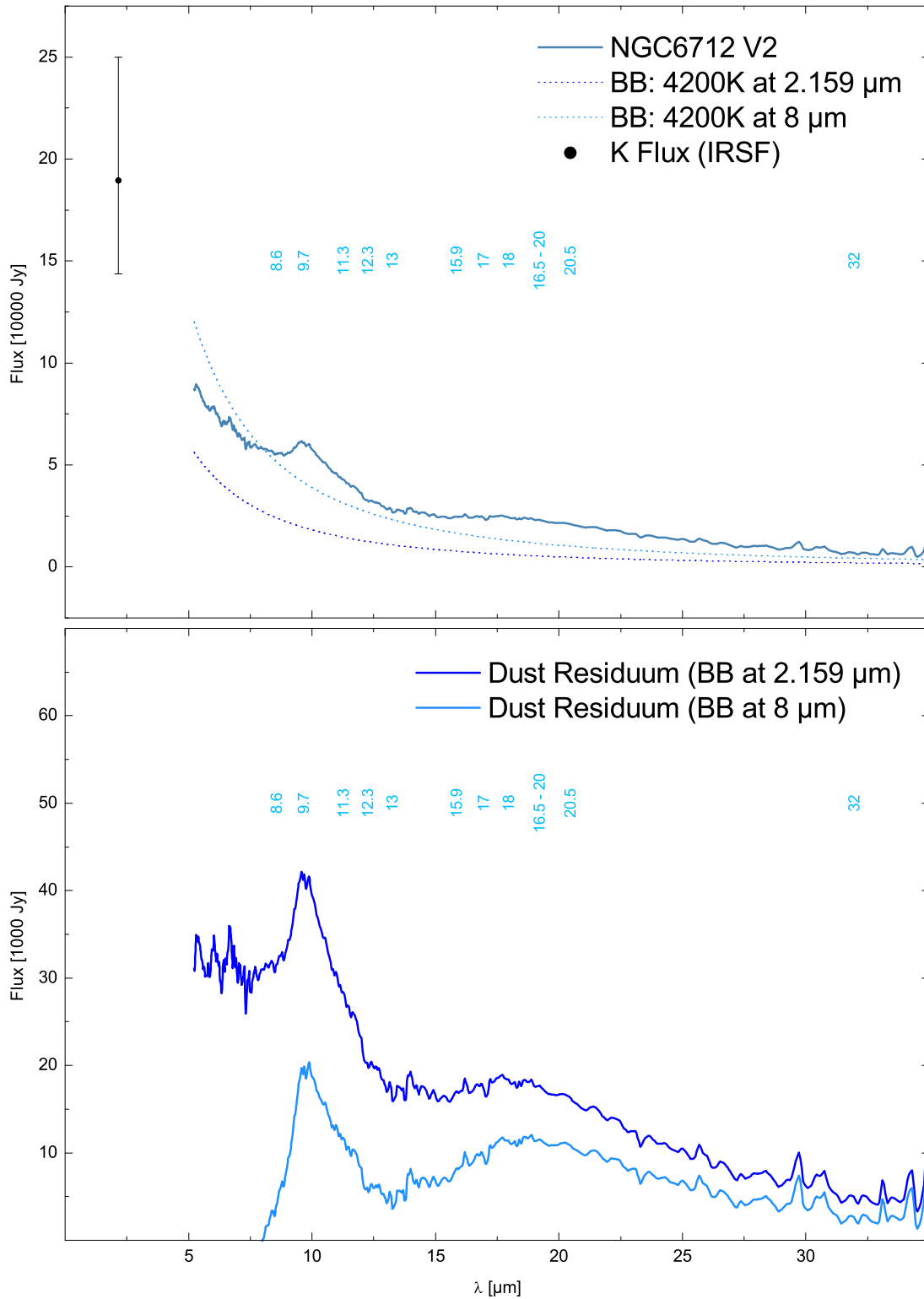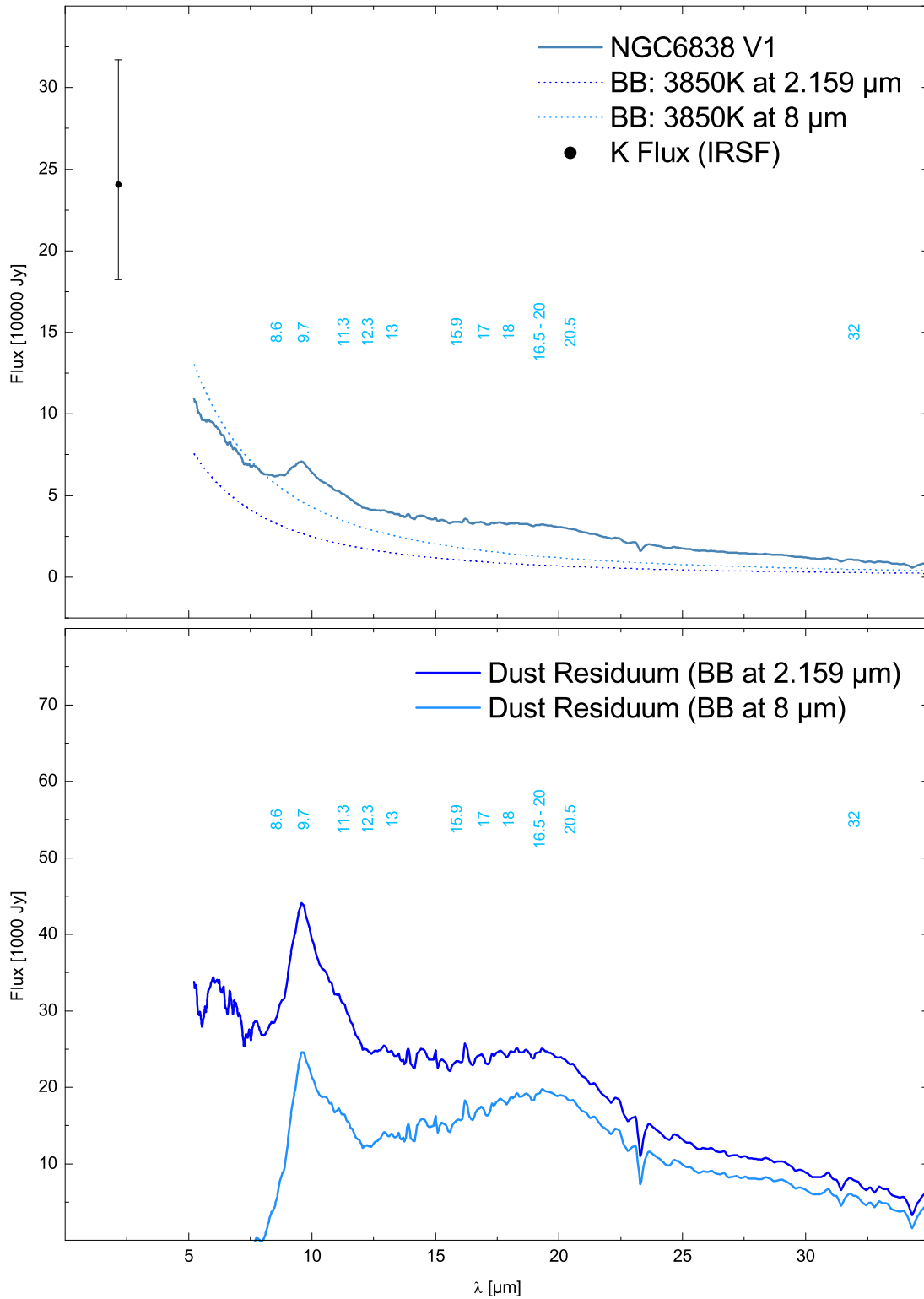
Figure 2.31: Upper panel: *Spitzer* spectrum of the globular cluster AGB star NGC 6838 V1 in Jansky at a distance of 10 pc. Possible dust feature positions are indicated (see Table 2.9). Two blackbody curves with $T_{BB} = 3850$ K are overlayed, mounted at K and $8\,\mu$m, respectively. K Flux is derived from IRSF data. Lower panel: Dust residuals after blackbody subtraction.
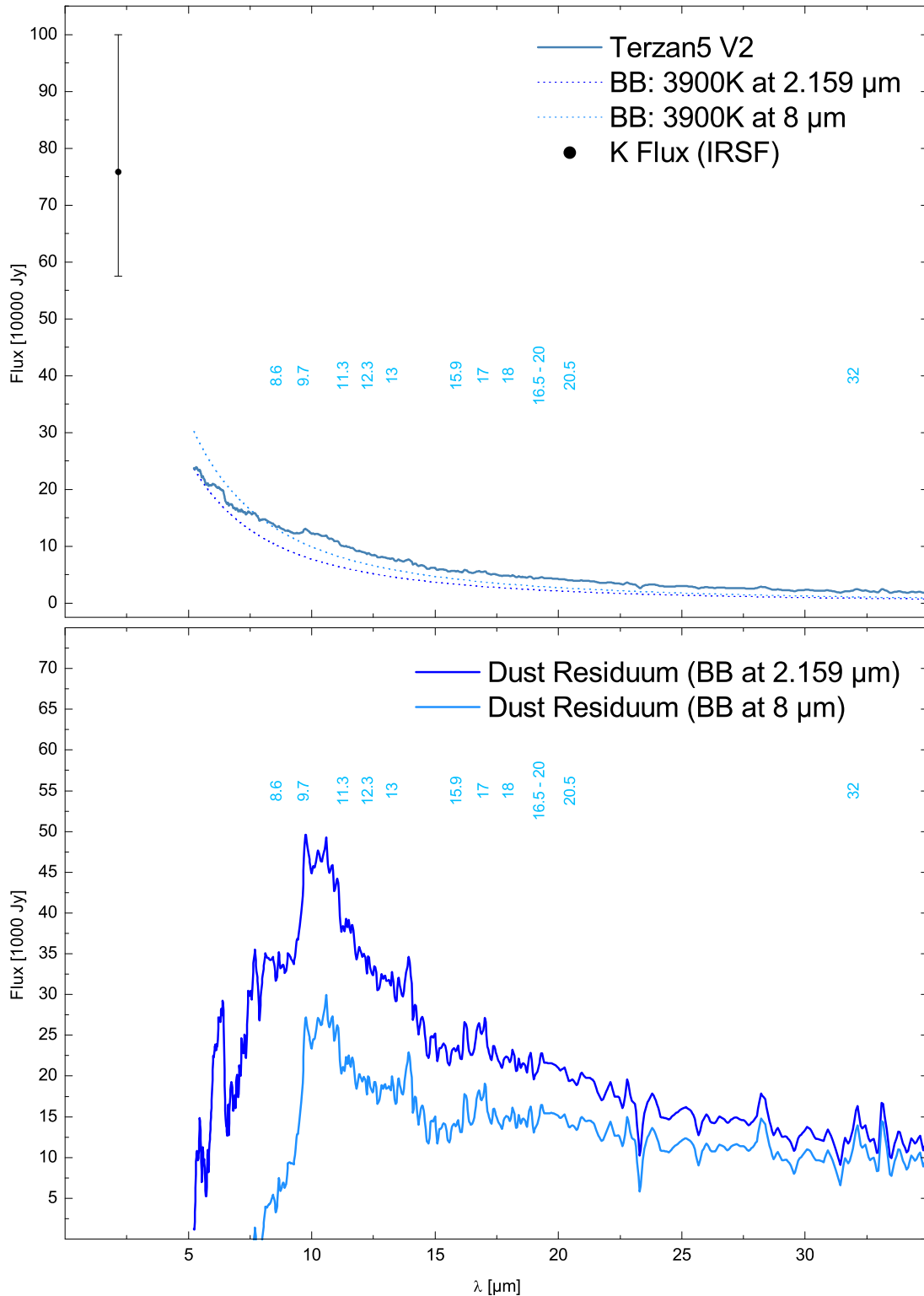
Figure 2.32: Upper panel: *Spitzer* spectrum of the globular cluster AGB star Terzan 5 V2 in Jansky at a distance of 10 pc. Possible dust feature positions are indicated (see Table 2.9). Two blackbody curves with $T_{BB} = 3900$ K are overlayed, mounted at K and $8\,\mu$m, respectively. K Flux is derived from IRSF data. Lower panel: Dust residuals after blackbody subtraction.
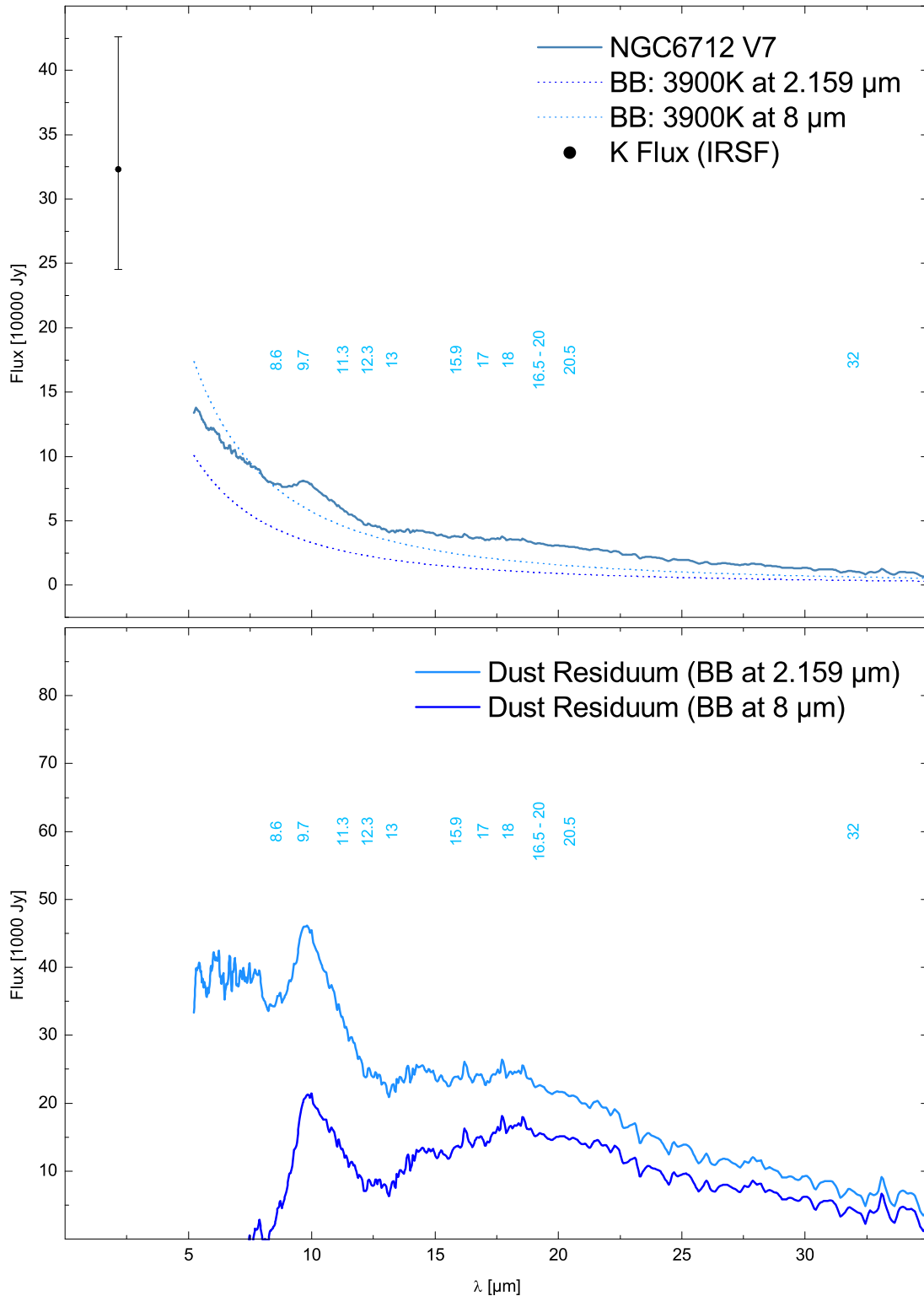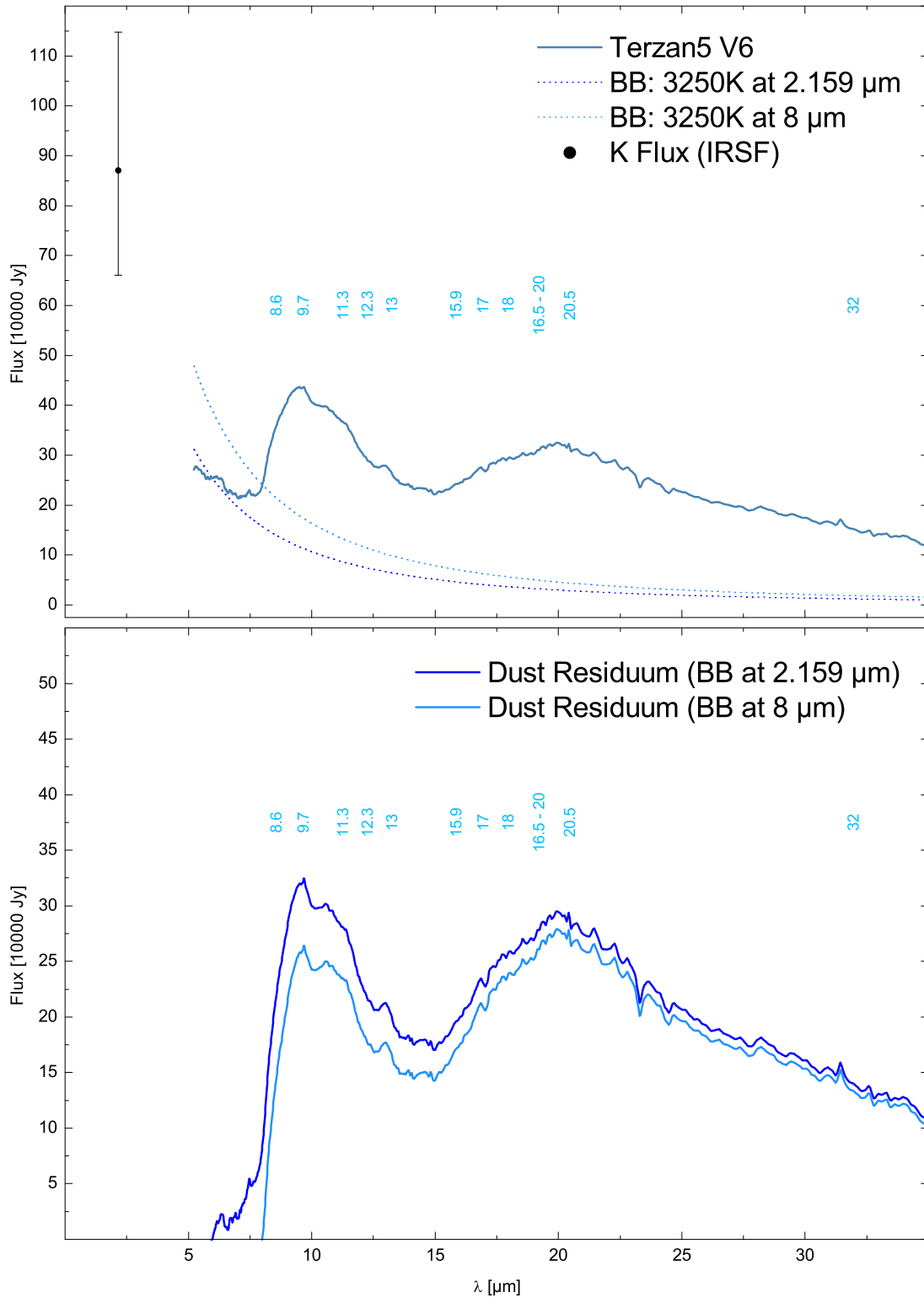
Figure 2.33: Upper panel: *Spitzer* spectrum of the globular cluster AGB star Terzan 5 V6 in Jansky at a distance of 10 pc. Possible dust feature positions are indicated (see Table 2.9). Two blackbody curves with $T_{BB} = 3250$ K are overlayed, mounted at K and 8 μm, respectively. K Flux is derived from IRSF data. Lower panel: Dust residuals after blackbody subtraction.
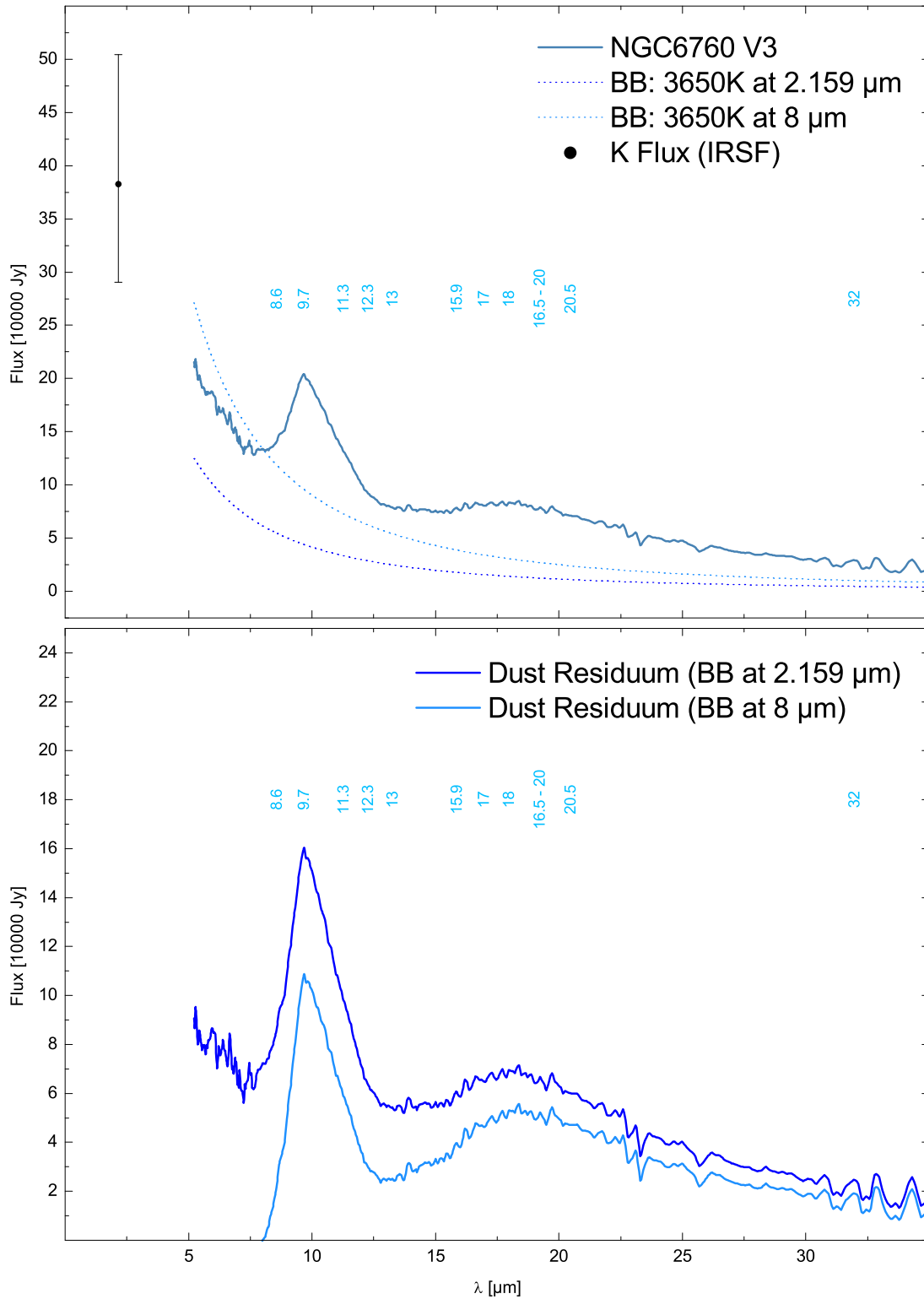
57
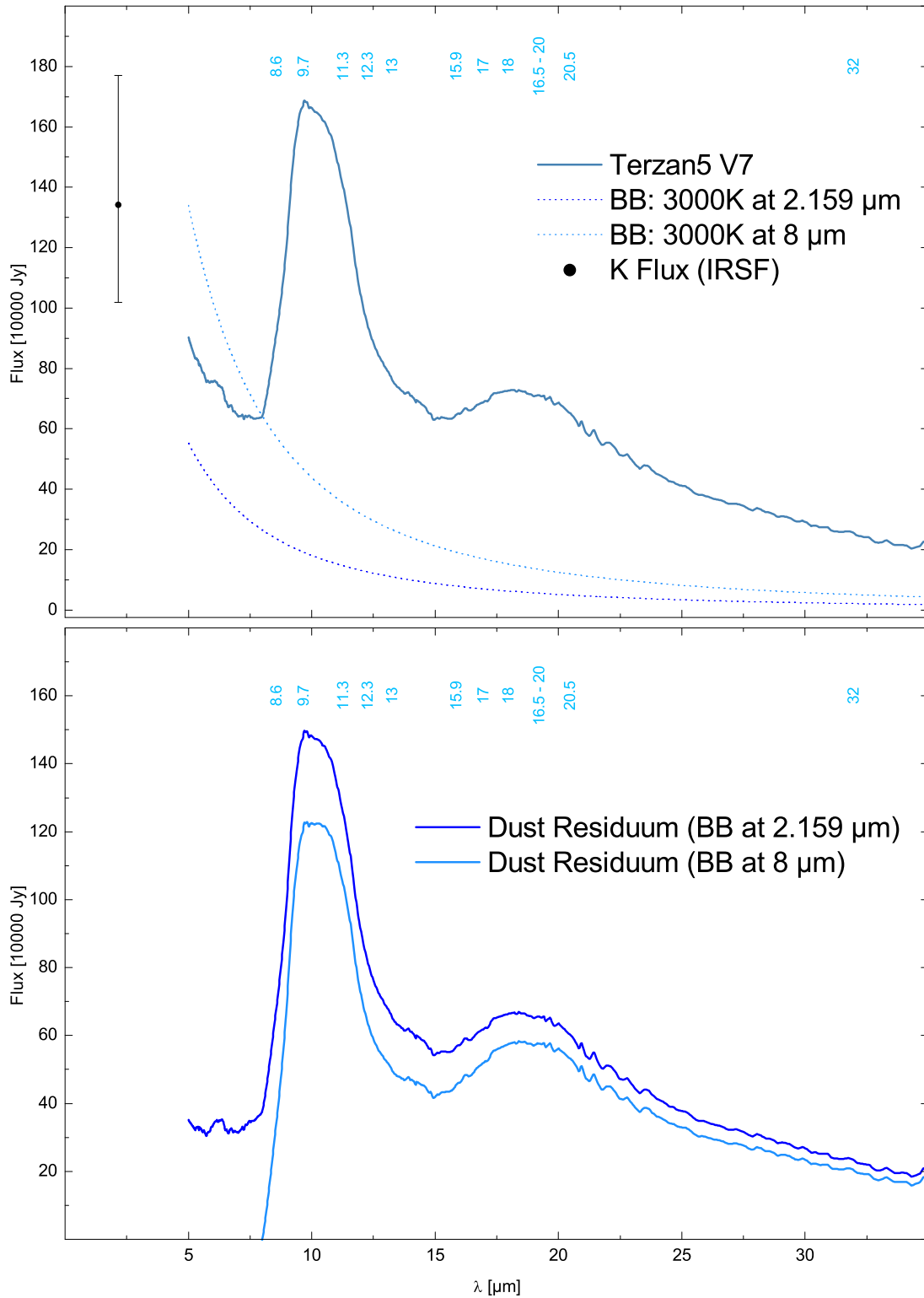
Figure 2.34: Upper panel: *Spitzer* spectrum of the globular cluster AGB star Terzan 5 V7 in Jansky at a distance of 10 pc. Possible dust feature positions are indicated (see Table 2.9). Two blackbody curves with $T_{BB} = 3000$ K are overlayed, mounted at K and $8\,\mu$m, respectively. K Flux is derived from IRSF data. Lower panel: Dust residuals after blackbody subtraction.
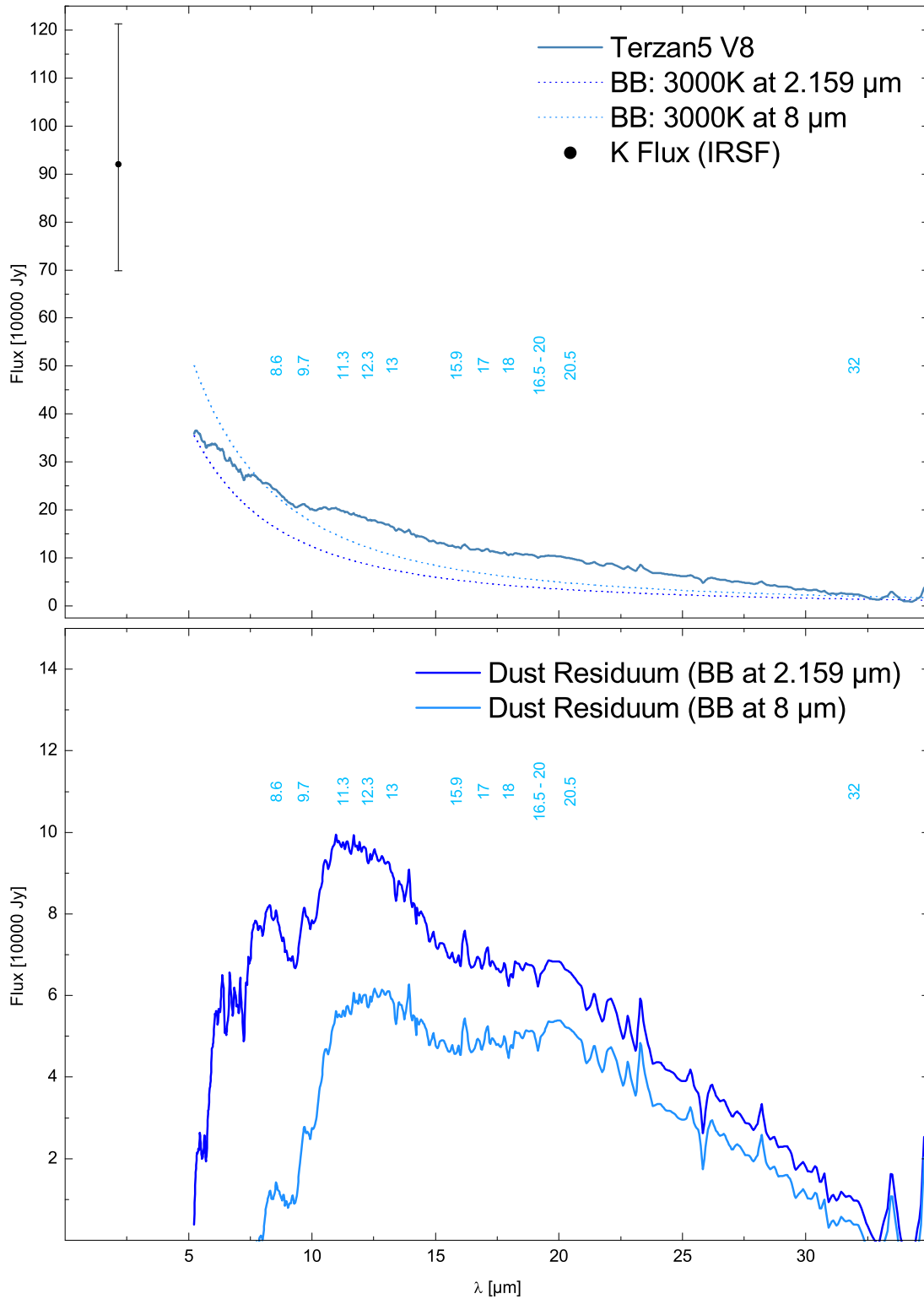
Figure 2.35: Upper panel: *Spitzer* spectrum of the globular cluster AGB star Terzan 5 V8 in Jansky at a distance of 10 pc. Possible dust feature positions are indicated (see Table 2.9). Two blackbody curves with $T_{BB} = 3000\,K$ are overlayed, mounted at K and $8\,\mu m$, respectively. K Flux is derived from IRSF data. Lower panel: Dust residuals after blackbody subtraction.
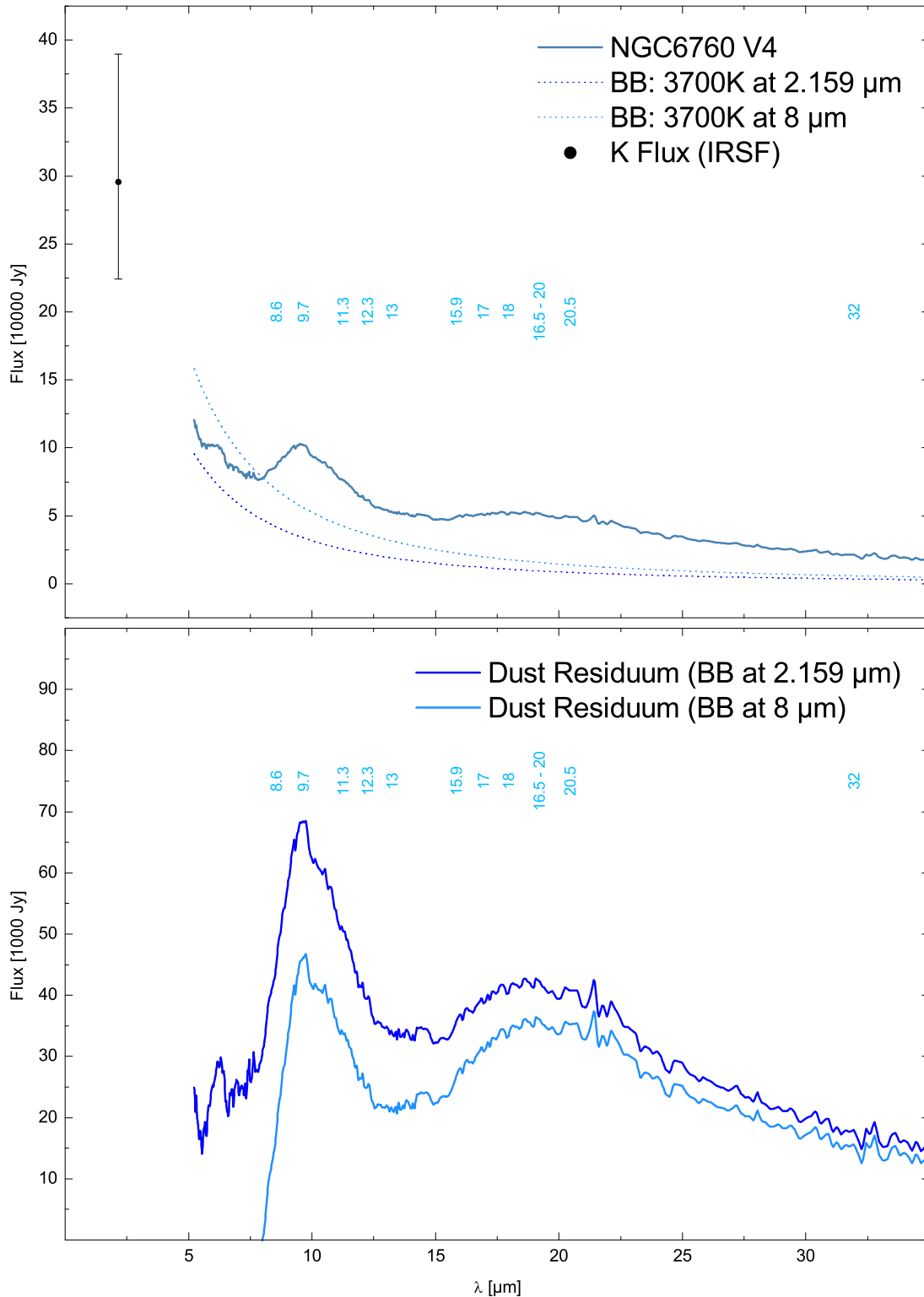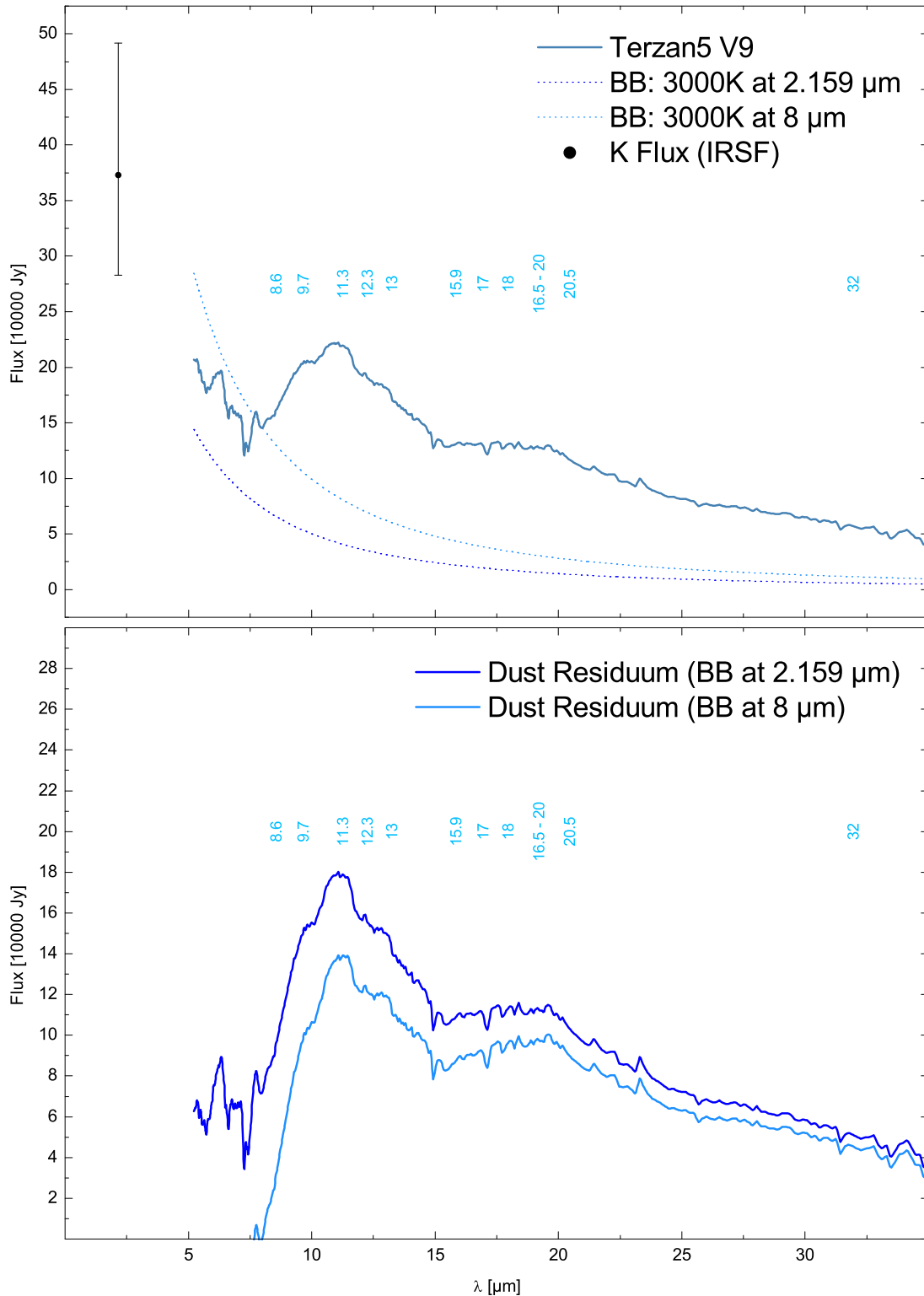
Figure 2.36: Upper panel: *Spitzer* spectrum of the globular cluster AGB star Terzan 5 V9 in Jansky at a distance of 10 pc. Possible dust feature positions are indicated (see Table 2.9). Two blackbody curves with $T_{BB} = 3000\,K$ are overlayed, mounted at K and $8\,\mu$m, respectively. K Flux is derived from IRSF data. Lower panel: Dust residuals after blackbody subtraction.

Chapter 3

2MASS Luminosity Functions of Globular Clusters

3.1   2MASS Color-Magnitude Diagrams

In order to derive Luminosity Functions (LFs) of the Galactic globular clusters of the sample presented in Table 2.1, NIR data from the 2MASS survey (Skrutskie et al. 2006) are used. The 2MASS all sky survey provides JHK photometry for individual stars in all clusters of our sample. The NIR $(J - K)_0$ color[1] is used to construct a Color-M_K diagram for each cluster. The Color-Magnitude diagrams rely on a well chosen radius around the centers of the globular clusters, because the 2MASS data are available for the entire sky and only the area around the clusters is of interest. This radius should cover almost the entire cluster but should avoid a large contamination by field stars. We decided to use a 90%-mass radius[2] in the 2MASS query to extract the NIR data from the NASA/IPAC Infrared Science Archive[3]. The extracted 2MASS data include error flags for each of the photometric bands defining the quality of the measurement[4]. For this work only J and K data of best quality were used[5]. The quality flags of the H band were neglected since this band is not used to generate the Color-Magnitude diagrams. In Section 3.2.1 a 2MASS Color-Magnitude diagram of the globular cluster NGC 5927 is presented covering the entire accessible brightness range of the cluster stars (see Fig. 3.1,

---

[1] Note that the J magnitude is dereddened in the same manner as the K magnitude, cf. Section 2.1.3.

[2] See Section 3.1.1 for the details on the 90%-mass radius

[3] The 2MASS query is performed using the 2MASS database available at http://irsa.ipac.caltech.edu/applications/Gator/ [December 30, 2010]

[4] The photometric quality flag is a three character flag with one character per band [$JHKs$], that provides a summary of the net quality of the default photometry in each band. The quality flags range from AAA to XXX.

[5] The number of stars that that were eliminated with this method is only significant for the faint regime in the Color-Magnitude diagrams. This regime will not be used to derive the LFs.

left panel). Only stars within the 90%-mass radius are shown. The two stars with observed MIR-spectra are marked. From Section 3.3 on the focus is layed on the bright part of the Color-Magnitude diagrams showing the AGB of the globular cluster stellar populations. Thus, the full brightness range of the diagrams is not shown although these data are used for the comparison with isochrones in Chapter 4.

3.1.1 90%-Mass Radius

Harris (1997) presented two characteristic radii for Galactic globular clusters, namely the half-mass radius and the core radius. The half-mass radius describes the area around the center of the cluster that contains 50% of the total cluster mass; the core radius defines the distance from the cluster center at which the apparent surface luminosity has dropped by half[6].
The core radius r_c and the central concentration c (also presented by Harris 1997) can be used to derive the tidal radius r_t for a globular cluster using $c = \log[\frac{r_t}{r_c}]$[7]. The tidal radius defines the border of gravitational influence between the globular cluster and the galaxy. It allows for the separation of stars gravitationally bound to the cluster from stars not belonging to the cluster.

In order to derive a Color-Magnitude diagram of a globular cluster a certain area around the cluster center has to be defined. Both, the half-mass and the tidal radius, are not suited for the 2MASS data extraction. The half-mass radius defines only a narrow area around the center of the cluster missing 50% of the population due to the fact that the stars are not located close to the center. Certainly the core radius is not suited as well, since it only defines the core of the cluster and is even smaller then the half-mass radius. The tidal radius on the other hand is often very extended covering a large area on the sky. Therefore also the tidal radius is not suited for the NIR data query since this would lead to a extrem contamination with field stars from the fore- and background of the globular cluster.
The need of a well suited radius defining the "size" of the globular clusters leads to the utilisation of the 90%-mass radius. Assuming a plummer sphere to describe the globular cluster, the density declines rapidly towards the outskirts of the cluster. Outside of the 90%-mass border, the cluster density alignes with the background density of the surrounding field. Thus, a larger radius than the 90%-mass radius would result in an increased number of field stars.

The 90%-mass radius is derived using the half-mass radius from Harris (1997) presented in Table 3.1. Applying a plummer model according to Aarseth et al. (1974) the mass m inside a sphere of the radius r is

$$m(r) = M\left[1 + \frac{a^2}{r^2}\right]^{-\frac{3}{2}},\tag{3.1}$$

with M being the total mass of the cluster and a a value describing the core radius. Assuming that $M = 1$ and $a = 1$ Equation 3.1 is converted to the Equation 3.2 and subsequently to Equation 3.3. The latter equation gives the radius of the globular cluster in relation to the mass fraction inside the respective radius.

---

[6]The core radius is different but comparable to the half-light radius which describes the distance to the center at which half of the total luminosity of the cluster is recieved.
[7]This relation is not valid for core-collapsed globular clusters (see Trager et al. 1993).

$$m(r) = r^3 \left[1 + r^2 \right]^{-\frac{3}{2}} \tag{3.2}$$

$$r(m) = \left[m^{-\frac{2}{3}} - 1 \right]^{-\frac{1}{2}} \tag{3.3}$$

With Equation 3.3 it is possible to derive various radii for different mass fractions (see Table 3.2). The value of the 50%-mass radius is the starting point to derive the factors to convert r_h from Harris (1997) to any other radius defining a certain mass fraction of the globular cluster. Dividing the values for the different mass fractions from Table 3.2 with the value of the 50%-mass radius one recieves the factor which can subsequently be multiplied with the r_h (given in arcmin) leading to the respective mass fraction radius in arcmin (see Equation 3.4[8]). The factor $x = 2.8412$ is corresponding to a plummer sphere with 90% of the total mass of the globular clusters and is used with the half-mass radius to derive the 90%-mass radius in arcmin. The 90%-mass radii derived that way are used for the 2MASS query to extract the NIR data which are then used for the CMDs.

$$x = \frac{r(0.9)}{r(0.5)} = \frac{3.70711}{1.30477} \Rightarrow x = 2.8412 \tag{3.4}$$

Table 3.1: Parameters of the Globular Cluster Sample II

GC ID	Fe/H[a]	Z[c]	[M/H][d]	R$_{50}$ [']^{a,b}	R$_{90}$ [']	RGB$_{Tip}$[e]
NGC104	-0.76	0.0035	-0.62	2.79	7.95	-6.5332
IC1276	-0.70	0.0039	-0.56	2.35	6.68	-6.5716
NGC362	-1.12	0.0015	-0.91	0.81	2.30	-6.3476
NGC5927	-0.37	0.0085	-0.23	1.15	3.27	-6.7828
NGC6352	-0.70	0.0039	-0.56	2.00	5.68	-6.5716
NGC6356	-0.50	0.0063	-0.36	0.74	2.10	-6.6996
NGC6388	-0.60	0.0050	-0.46	0.67	1.90	-6.6356
NGC6553	-0.25	0.0112	-0.11	1.55	4.40	-6.8596
NGC6637	-0.71	0.0038	-0.57	0.83	2.36	-6.5652
NGC6712	-1.01	0.0019	-0.87	1.37	3.89	-6.3732
NGC6760	-0.52	0.006	-0.38	2.18	6.19	-6.6868
NGC6838	-0.73	0.0037	-0.59	1.65	4.68	-6.5524
Terzan 5	-0.28	0.0105	-0.14	0.83	2.36	-6.8404

[a] [Fe/H] and R$_{50}$ values were taken from Harris (1997)
[b] R$_{50}$ is the nomenclature for the half-mass radius r_h chosen by the author.
[c] Z is derived using the relations in Appendix B
[d] [M/H] is derived using Eq. 2.7
[e] The RGB$_{Tip}$ is derived using [Fe/H] and [M/H] from this table in Equations 2.6 to 2.8.

---

[8]Note that M and a cancel out by applying this relation approving their normalisation.

Table 3.2: Mass Fraction Radii

Mass Fraction	r(m)[a]	x[b]
50 %: r(0.50)	1.30477	1
90%: r(0.90)	3.70711	2.84120
95 %: r(0.95)	5.36157	4.10921
98 %: r(0.98)	8.58770	6.58177

[a] Radius for the mass fraction $m(r)$ from Eq. 3.2
[b] Factor to derive the mass fraction radius in arcmin using the half-mass radius in arcmin.

3.2   Observed Luminosity Functions

In order to convert the 2MASS Color-Magnitude diagrams of the various globular clusters to LFs describing each cluster, the distribution of stars in the Color-Magnitude diagram has do be derived. This was done using the statistics tools of ORIGIN[9]. The frequency-analysis of the software allows to count the number of stars in a defined brightness intervall distributed to a choosen bin size and results in a histogram representing the cluster. Since all cluster AGB stars with observed *Spitzer* spectra are brighter than M_K = -5 mag, focus is layed on the bright parts of the Color-Magnitude diagrams.

3.2.1   Binning of the Cluster Stars

To derive the LFs of the globular clusters a bin size of 0.2 mag is adopted. This bin size proofed to be a good solution to retrieve a typical LF of an old stellar population. Smaller or larger bin sizes have been ruled out after a examination of the resulting LFs. Too small bins would lead to a "constant" distribution of stars over the entire brightness range, while too large bins would result in smeared out LFs with no details, such as the tip of the RGB, identifiable.

For each globular cluster it is possible to derive the respective LF using the 0.2 mag bin size and the tip of the RGB as a starting point to define the luminosity range in the Color-Magnitude diagram where the LF is extracted. The tip of the RGB of each cluster is derived using [Fe/H] and [M/H] in Equations 2.6 to 2.8 and is presented in Table 3.1. Unfortunately, using these values as starting points for the luminosity range defined for the frequency-analysis would lead to LFs that could not be combined or compared since their bins have no matching borders.

The combination of several globular clusters to a "super" cluster is aspired in this study to reduce the stochasticity of the LFs and to increase the number of stars with observed MIR-spectra per cluster combination. Therefore the lack of matching luminosity bins must be obliterated. Thus, identical starting points of the luminosity bins have been established to allow for a proper

---

[9]The ORIGIN plotting software is available at `http://www.originlab.com/`. [December 30, 2010]

Table 3.3: Tip of the Red Giant Branch

Metallicity Group	[M/H]	RGB$_{Tip}$[a]
Low[b]	-0.58	-6.56
Intermediate[b]	-0.40	-6.67
High[b]	-0.16	-6.83

[a] The RGB$_{Tip}$ is derived using [M/H] from this table in Equations 2.6 to 2.8.
[b] Globular Cluster Combinations and Metallicity Groups are introduced in Section 3.4.1.
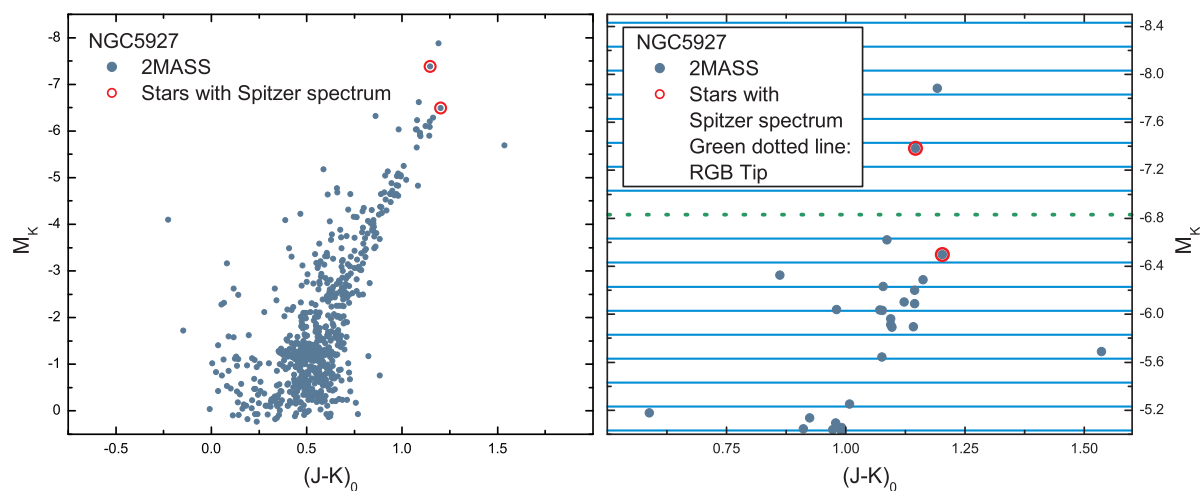
Figure 3.1: Left panel: 2MASS Color-Magnitude diagram of the globular cluster NGC 5927. Stars with an *AXA* quality flag and located within the 90% mass radius are shown. Red circles mark the stars with observed *Spitzer* spectrum. Right panel: Color-Magnitude diagram of NGC 5927 (only stars brighter than $M_K \geq$ -5 mag are shown). The green dotted line marks the tip of the RGB. The blue lines illustrate the brightness-binning starting at the tip of the RGB with a bin size of 0.2 mag.

combination of the LFs. Therefore not the individual RGB tip of each globular cluster is used, but the mean luminosity of the different tips of the RGB of the various clusters.

In Section 3.4.1 three globular cluster groups are defined according to the metallicity of the clusters. For these groups the mean RGB tips are derived from the mean [M/H] values using again Equations 2.6 to 2.8. The mean RGB tips are presented in Table 3.3. With increasing metallicity the mean tip borders of the RGB are positioned at higher luminosities. Emanating from these starting points the 0.2 mag bins are defined to cover a luminosity ranging from $M_K =$ -5 mag to the brighterst stars in the Color-Magnitude diagrams. Fig. 3.1 (right panel) shows the bright part of the CMD of the globular cluster NGC 5927 as an example.

The luminosity bins are indicated with blue horizontal lines. The green dotted line marks the starting point for the luminosity bins and is defining the mean RGB tip of the globular cluster

group with the highest metallicity at $M_K \approx$ -6.83 mag[10]. All globular clusters are treated that way to produce the LFs presented in Section 3.3. Three different starting points due to the different tips of the RGB are adopted.

3.2.2 Field Star Contamination

In order to retrieve globular cluster LFs with no field star contamination, the LFs derived from the 2MASS Color-Magnitude diagrams using the 90%-mass radius have to be further processed. For each cluster four comparison fields are choosen to estimate the number of field stars in the Color-Magnitude diagrams. These comparison fields are of the same areal size as the 90%-mass radius area around the cluster center[11], but located at distances of 15 arcmin to the center[12]. This ensures that none of the four comparison fields per cluster is overlapping with the area used to derive the 2MASS Color-Magnitude diagram of the respective cluster. For each comparison field the same 2MASS query is applied to extract the NIR photometry data as for the globular clusters itself (cf. Section 3.1). The NIR data are used to generate Color-Magnitude diagrams for the various comparison fields representing the bright part of the stars within the field with $M_K \leq$ -5 mag. In these diagrams it is possible to define a $(J-K)_0$-bin to exclude field stars that do not fall in the same color range as the AGB stars present in the globular clusters. Table 3.4 presents the color range for the comparison fields for each globular cluster.

Table 3.4: Color Range of the Comparison Fields

GC ID	Color Range
NGC104	$0.50 \leq (J-K)_0 \leq 1.50$
IC1276	$0.79 \leq (J-K)_0 \leq 1.15$
NGC362	$0.50 \leq (J-K)_0 \leq 1.50$
NGC5927	$0.86 \leq (J-K)_0 \leq 1.20$
NGC6352	$0.83 \leq (J-K)_0 \leq 1.29$
NGC6356	$0.76 \leq (J-K)_0 \leq 1.25$
NGC6388	$0.83 \leq (J-K)_0 \leq 1.24$
NGC6553	$0.85 \leq (J-K)_0 \leq 1.50$
NGC6637	$0.97 \leq (J-K)_0 \leq 1.14$
NGC6712	$0.79 \leq (J-K)_0 \leq 1.25$
NGC6760	$0.63 \leq (J-K)_0 \leq 1.22$
NGC6838	$0.95 \leq (J-K)_0 \leq 1.13$
Terzan 5	$0.75 \leq (J-K)_0 \leq 1.20$ for $M_K \leq$ -6.5 and $0.90 \leq (J-K)_0 \leq 1.5$ for $M_K >$ -6.5

---

[10] Note that the mean brightness of the RGB tips from Table 3.3 are rounded to two positions after decimal point while the M_K values of the stars from the Color-Magnitude diagrams have more positions after the decimal point. This minimises the risk of luminosity values from stars falling exactly on the border of one bin, thus resulting in a double count for the LFs.

[11] For the majority of the globular cluster sample R_{90} is used to define the size of the comparison fields. Only four clusters are treated in a different manner (see text).

[12] Only for NGC 362 a distance of 30 arcmin is chosen to locate the comparison fields not on an area on the sky with an inhomogeneous star distribution.

The number of stars per comparison frame and luminosity bin is divided through the area spanned by the 90%-mass radius around the center of the globular cluster to derive the star density in the field. This star density is used to derive the mean star density of the four comparison frames by simply computing the average of the respective comparison frames. This mean density is then multiplied with the area (given in arcmin^2) again to derive the mean field star count per bin for the mean comparison frame. This mean field star count per bin is then subtracted from the total number of stars per luminosity bin of the 2MASS LF of the respective globular cluster (see figures in Section 3.3). For the clusters NGC 6388 and NGC 6637 the 97% and 95%-mass radius, respectively, were used instead of the 90%-mass radius to derive the mean star density and the mean star number in the comparison frames[13].

For IC 1276 and Terzan 5 it was not possible to use four comparison fields with a homogeneous star distribution due to a strong gradient in the star distribution of the surrounding sky. Therefore a comparison field in the shape of a ring around the cluster was used. The mean star density and star count of these comparison rings were derived using the 95% and the 98%-mass radii for IC 1276 and the 98.7%-mass radius together with the tidal radius for Terzan 5[14]. The densities of the areas spanned with the outer radii are subtracted from the densities of the areas spanned with the inner radii resulting in the mean densities per luminosity bin of the rings surrounding the respective clusters. The mean densities per bin of these rings are then multiplied with the area given in arcmin^2 resulting in the mean star count of the comparison rings per luminosity bin. The mean star counts are subtracted from the star count per bin of the two clusters leading to the field star contamination reduced star counts plottet in the respective figures in Section 3.3.

3.3 2MASS CMDs and Luminosity Functions

The following pages present the 2MASS Color-Magnitude diagrams and the LFs of the Galactic globular clusters this work is based on. The Color-Magnitude diagrams show the stars of the clusters within their 90%-mass radius that are brighter than $M_K = $ -5 mag (see Fig. 3.2 to 3.6, left panels). The stars with observed *Spitzer* spectra from Lebzelter et al. (2006) and Sloan et al. (2010) are marked with red symbols. The 2MASS J and K photometric data together with M_K[15] and the $(J - K)_0$ color for the AGB stars of the globular clusters are presented in Table 3.5.

The LFs are presented in two different styles (see Fig. 3.2 to 3.6, right panels). The lower panels show the star densities per luminosity bin including the field star contamination of the respective clusters (dark grey) together with the star densities per luminosity bin of the respective mean comparison fields (light grey). The densities are given in star count per arcmin^2. The upper panels show the star count of the clusters after subtraction of the contamining field stars. These are the final LFs that are used in Section 3.4.1 to generate the cluster combinations with respect to their metallicity. Note that not all AGB stars that have observed MIR-spectra are

---

[13]The larger radii are used to reduce the stochasticity in the field star count of the respective clusters.

[14]The tidal radius r_t of Terzan 5 amounts to 9.89" and is derived using the concentration factor c and the core-radius r_c from Harris (1997).

[15]Derived for the 2MASS K magnitude. Note that in Section 2.3 the IRSF K magnitude is used.

located within the 90%-mass radius of their hosting globular cluster. In order not to miss these stars in the final LFs they were added to the star count of the proper luminosity bin. The respective stars are labeled in Table 3.5.

While in the low metallicity globular cluster combination no star needs to be added, three stars are added to the intermediate group and two stars to the high metallicity group. For the intermediate metallicity group it is convenient to add the three AGB stars with observed MIR-spectra to the LF if one compares the distribution of stars in the 2MASS LF to a theoretical luminosity function derived after a compatible isochrone[16]. For the theoretical LF, the number of stars present above the mean tip of the RGB amounts to 10% of the number of stars occuppying a luminosity interval ranging from $M_K = -5$ mag up to the RGB tip luminosity. For the 2MASS LF this number amounts to 9% and includes already the three additional stars above the RGB tip. This lower ratio of stars above and below the RGB tip in the 2MASS data implies that still 1% of stars above the tip are missing, when comparing the star count to the theoretical LF. By changing the position of the mean RGB tip derived after Bellazzini et al. (2004) to the RGB tip apparent in the 2MASS LF of the intermediate group, the ratios are amounting to 13.4% for the 2MASS data and 19.7% for the theoratical data, respectively. Again, the number of stars above the RGB tip in the 2MASS luminosity function is smaller than predicted by the isochrone. This fortifies the dicison of adding stars to the observed LF.

For the high metallicity group two stars from the cluster Terzan 5 are added to the star counts in the respective LF of the cluster combination. This stars are possible members of the young stellar population present in the cluster. Therefore a comparison of the ratio of stars above and below the RGB tip is not possible due to the fact that the theoretical LF describing the high metallicity group is only valid to represent the old stellar population in the cluster combination (see Section 4.2.3 for details).

---

[16]See Chapter 4 for more details on isochrones and theoretical luminosity functions.

Table 3.5: Near-Infrared Data from 2MASS

Star ID	J^a	K^a	$M_K{}^b$	$(J-K)_0$
NGC 104 V1	7.607	6.382	-6.802	1.198
NGC 104 V2	7.676	6.421	-6.763	1.228
NGC 104 V3	7.461	6.309	-6.875	1.125
NGC 104 V4	7.813	6.620	-6.564	1.166
NGC 104 V5	8.465	7.397	-5.787	1.041
NGC 104 V6	8.481	7.408	-5.776	1.046
NGC 104 V7	8.072	6.904	-6.280	1.141
NGC 104 V8	7.866	6.661	-6.523	1.178
NGC 104 V11	7.837	6.626	-6.558	1.184
NGC 104 V13	8.744	7.655	-5.529	1.062
NGC 104 V18	8.504	7.431	-5.753	1.046
NGC 104 V21	7.953	6.739	-6.445	1.187
IC 1276 V1	8.527	6.823	-6.574	1.078
IC 1276 V3	8.065	6.286	-7.111	1.153
NGC 362 V2^c	9.667	8.764	-5.848	0.876
NGC 362 V16	9.100	8.165	-6.447	0.908
NGC 5927 V1	9.462	8.006	-6.497	1.202
NGC 5927 V3	8.5183	7.118	-7.385	1.146
NGC 6352 V5	8.506	7.125	-6.686	1.268
NGC 6356 V1	9.872	8.520	-7.399	1.196
NGC 6356 V3	10.438	9.032	-6.887	1.250
NGC 6356 V4^c	10.379	9.037	-6.882	1.186
NGC 6356 V5^c	9.933	8.621	-7.298	1.156
NGC 6388 V3	10.226	8.929	-6.501	1.092
NGC 6388 V4^c	9.607	8.379	-7.051	1.023
NGC 6553 V4	8.060	6.474	-7.147	1.165
NGC 6637 V4	8.844	7.611	-7.015	1.141
NGC 6637 V5	8.658	7.491	-7.135	1.075
NGC 6712 V2	9.347	8.150	-6.134	0.949
NGC 6712 V7	9.426	8.126	-6.158	1.052
NGC 6760 V3	8.869	7.243	-7.334	1.205
NGC 6760 V4	9.509	7.866	-6.711	1.222
NGC 6838 V1	7.943	6.681	-6.301	1.127
Terzan 5 V2	10.328	8.100	-7.189	0.976
Terzan 5 V6	9.799	7.243	-8.046	1.304
Terzan 5 V7^c	9.539	6.782	-8.507	1.505
Terzan 5 V8	9.975	7.277	-8.012	1.446
Terzan 5 V9^c	11.082	8.358	-6.931	1.472

^{a} J and K magnitudes were taken from 2MASS
^{b} M_K is derived from K using Eq. 2.1
^{c} This star is not located within the 90%-mass radius.
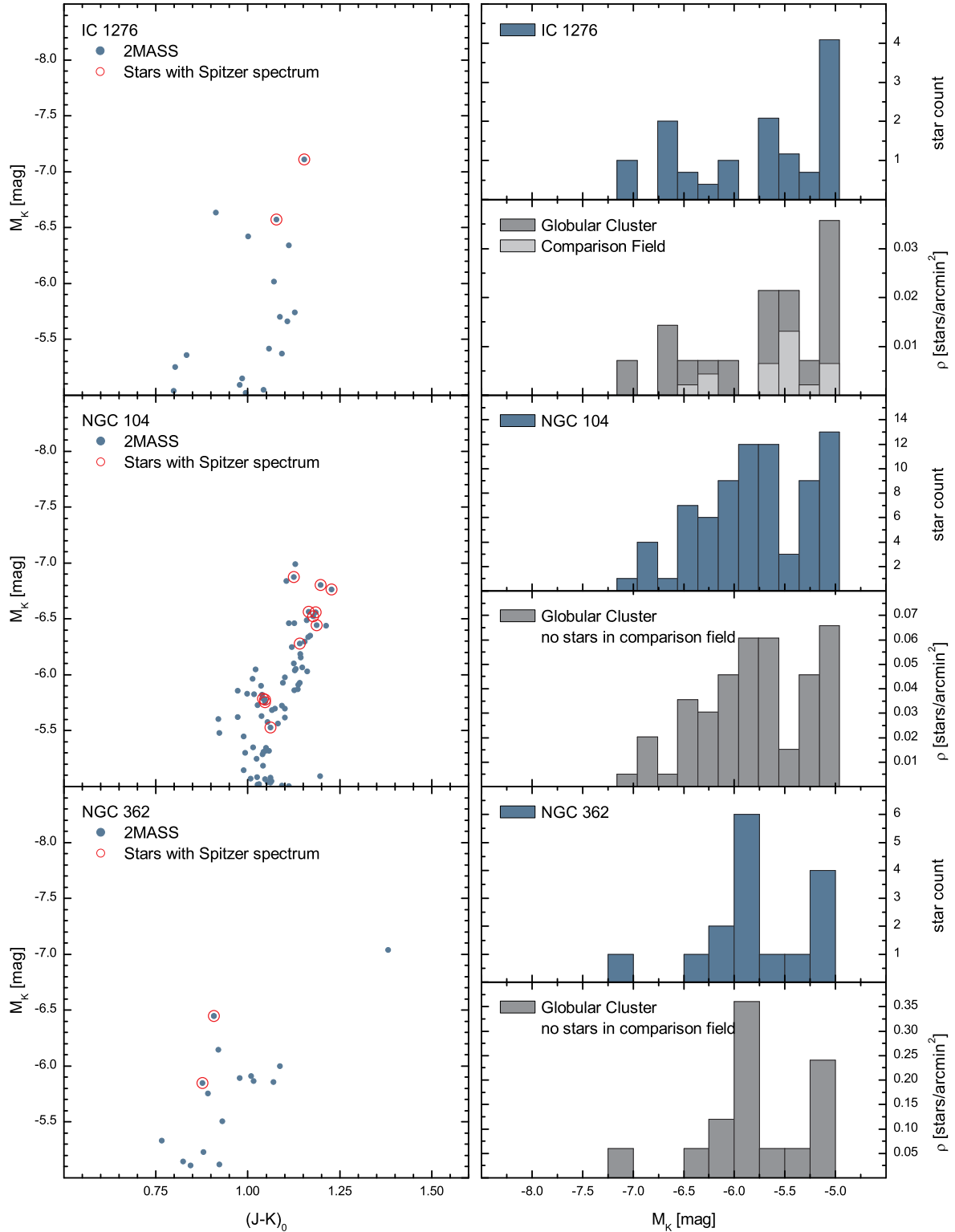
Figure 3.2: Color-Magnitude diagrams (left) and Luminosity Functions (right) for the globular clusters IC 1276, NGC 104 and NGC 362 within R_{90}. Red circles in the CMDs mark stars with observed *Spitzer* spectrum. Luminosity Functions for the cluster and the average comparison field are shown in the respective lower sub-panels and for the cluster after the field star subtracted in the upper sub-panels.

Figure 3.3: Same as Fig. 3.2 for NGC 5927, NGC 6352 and NGC 6356.

Figure 3.4: Same as Fig. 3.2 for NGC 6388, NGC 6553 and NGC 6637.
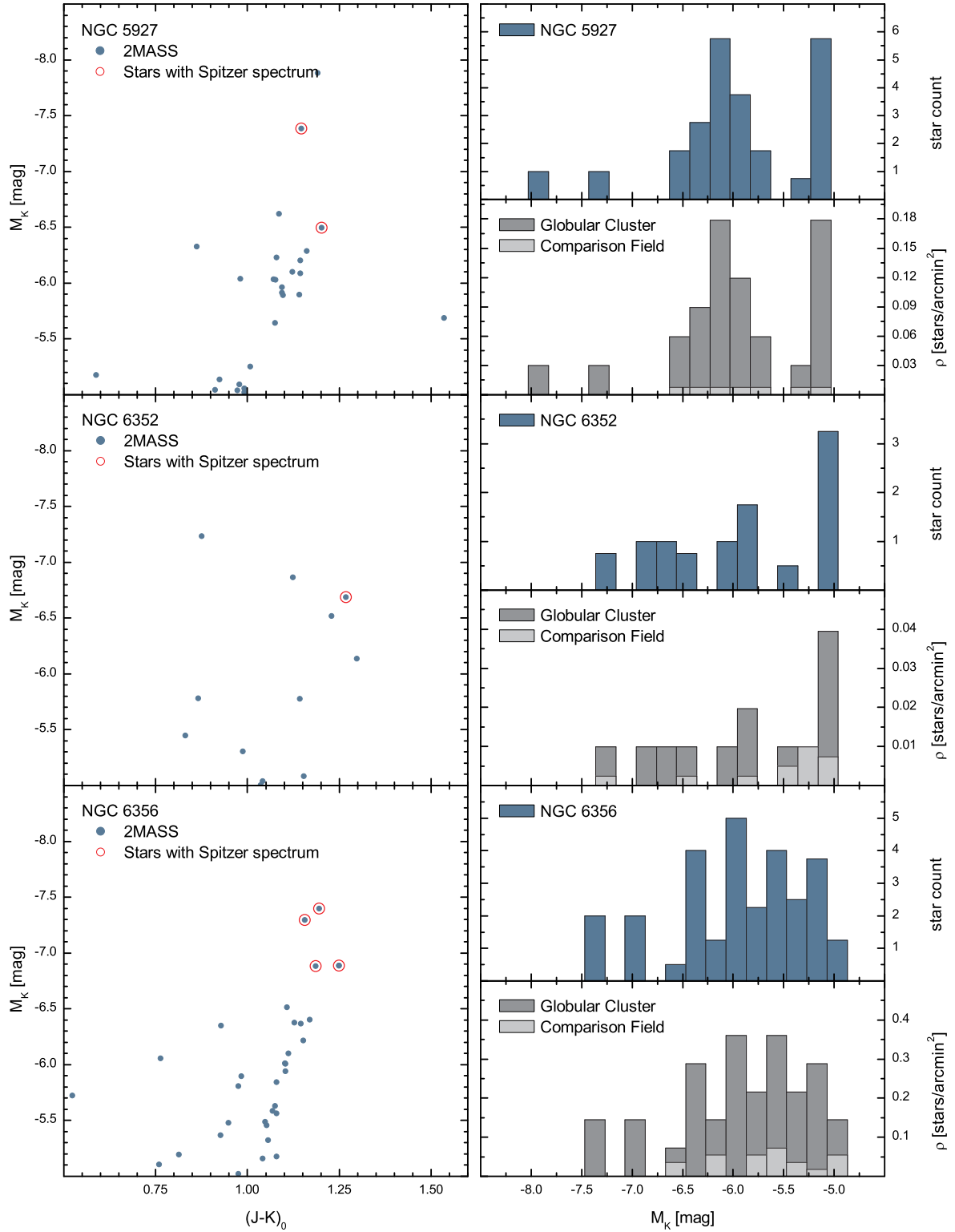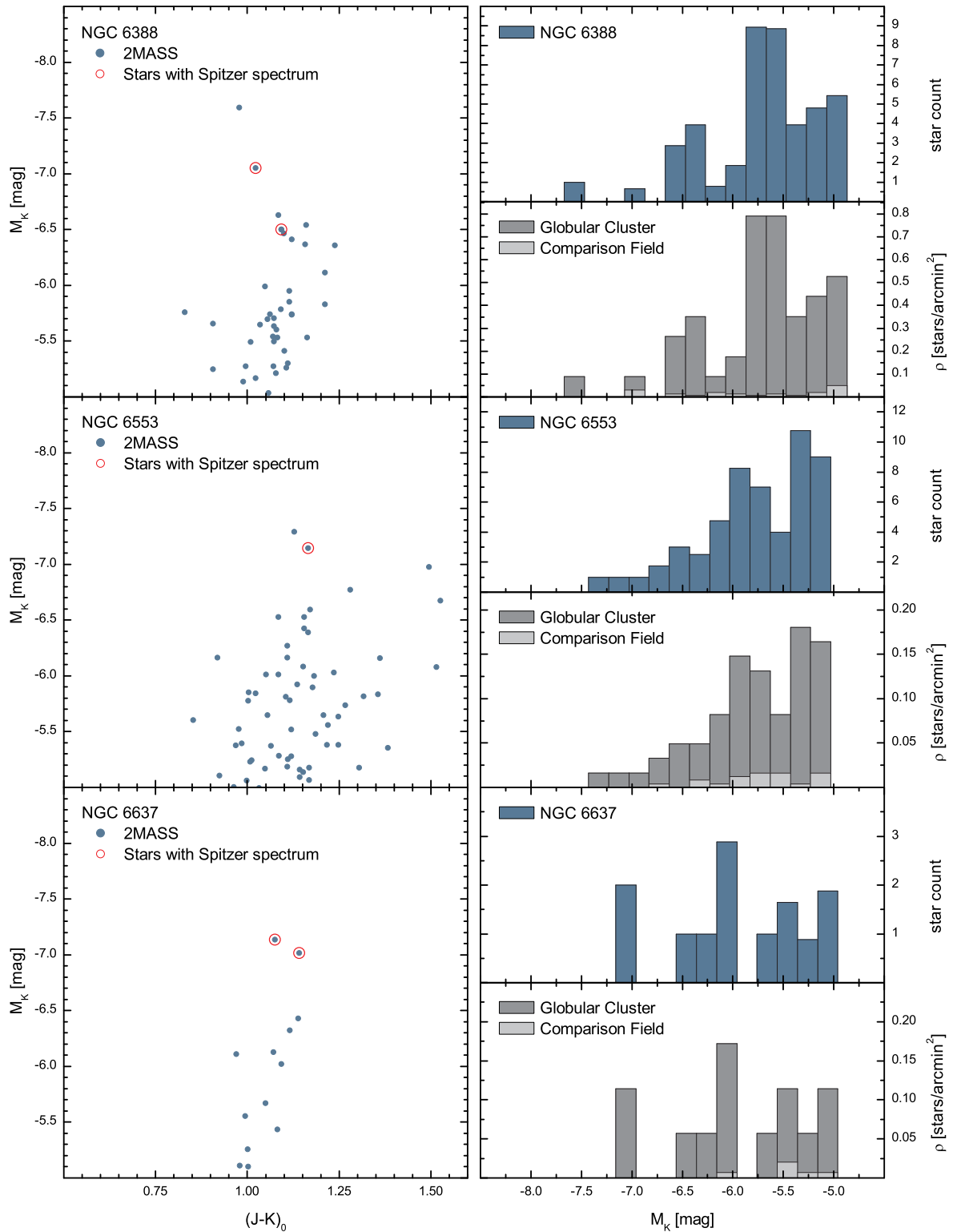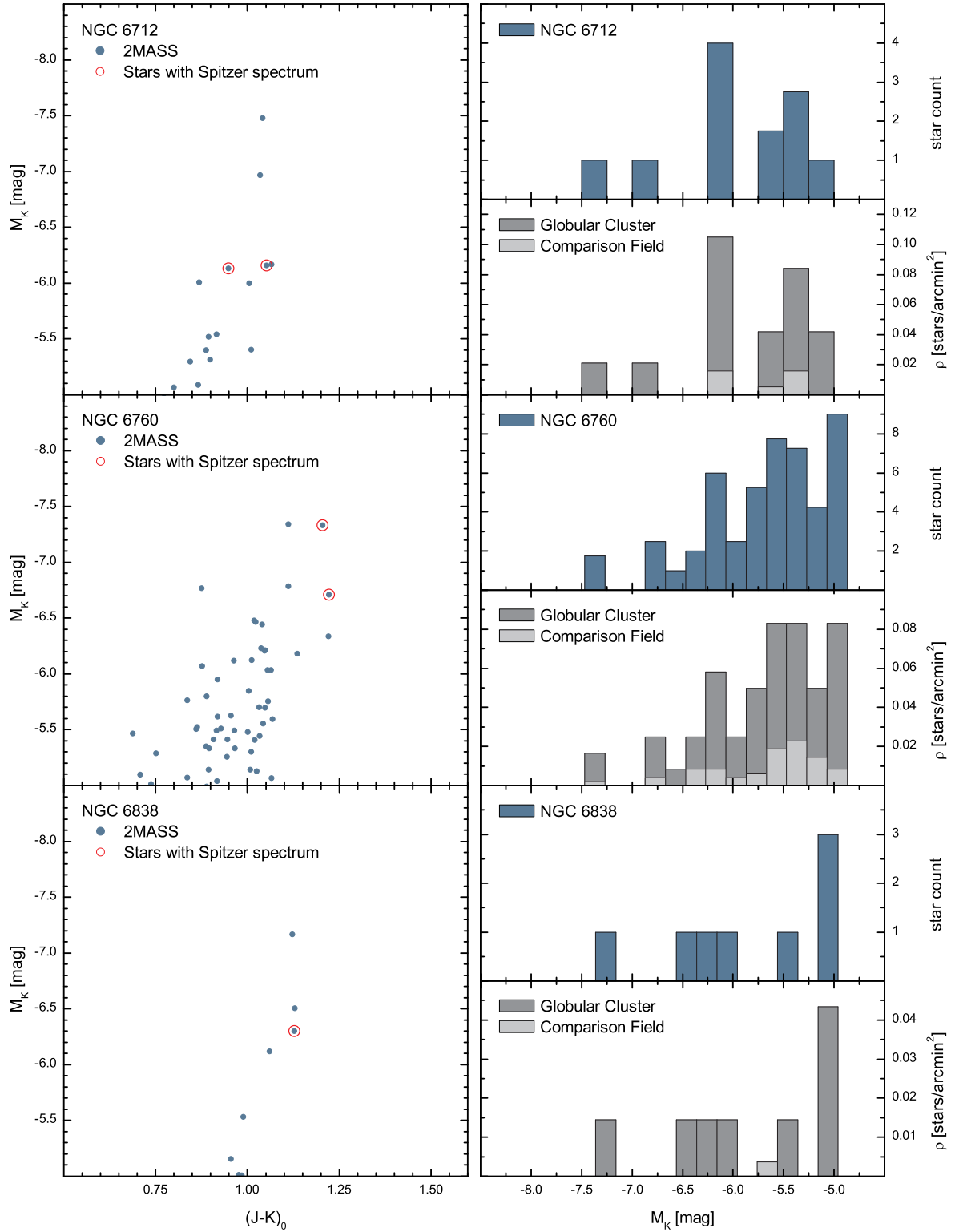
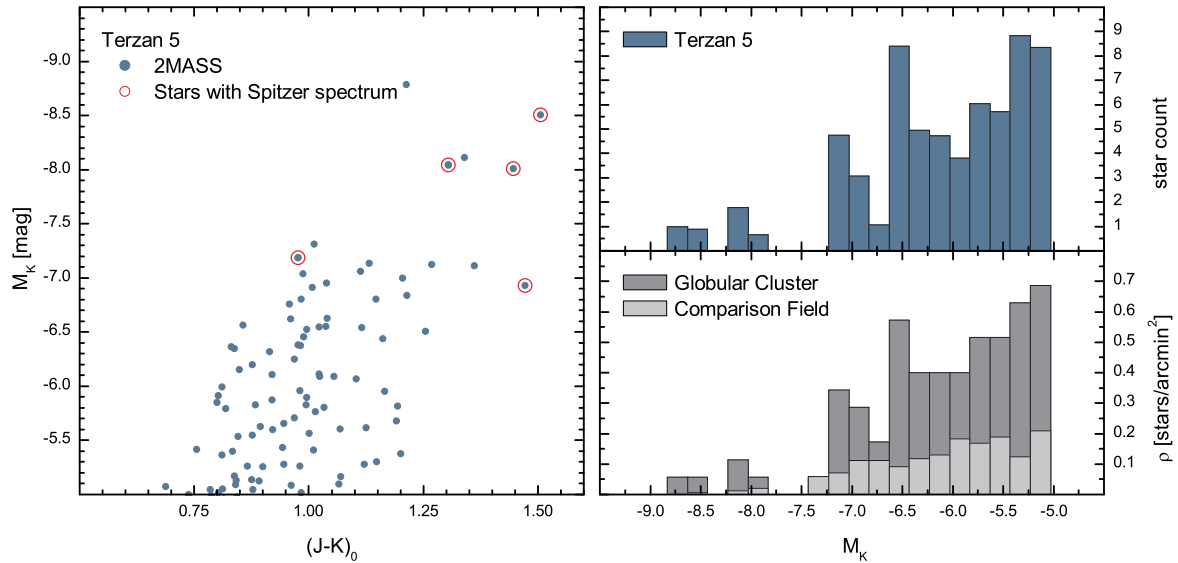**Figure 3.5:** Same as Fig. 3.2 for NGC 6712, NGC 6760 and NGC 6838.

Figure 3.6: Same as Fig. 3.2 for Terzan 5.

3.4 Combining Globular Clusters

Bressan et al. (2007) derived a co-added MIR-spectra using the available AGB star spectra from Lebzelter et al. (2006) to explain the $10\,\mu$m dust excess in various early-type galaxies. This study was based only on data of the AGB population of a single globular cluster, namely NGC 104. The aim of the present work is to derive co-added MIR-spectra representing various globular clusters covering a wide range of metallicities to improve the understanding of the MIR-spectra of old stellar populations on a more broad basis.

In order to produce co-added MIR-spectra the LFs of the globular clusters can be used to weight the available spectra with the number of stars in the respective luminosity bins. Due to the low number of observed AGB stars in each globular cluster, co-adding of the spectra for each cluster is not suffcient. The resulting mean MIR-spectra of the clusters would rely only on two individual AGB star spectra for most of the clusters in the sample. Only three clusters, namely NGC 104, NGC 6356 and Terzan 5, provide more than two AGB star spectra[17], while some clusters only provide a single AGB star spectrum[18] and would not support any co-adding.

To overcome the problem of the low number of AGB star spectra per cluster we follow the strategy of grouping the globular clusters of our sample with respect to their metallicity. This approch results in a higher number of observed MIR-spectra from AGB stars in each combined group, allowing for a better covering of the LFs and a reduction of stochastic fluctuations of the the star count in each luminosity bin.

---

[17] From the sample taken from Sloan et al. (2010) the clusters NGC 6356 and Terzan 5 provide four and five MIR-spectra of AGB stars observed with *Spitzer*, respectively. Twelve MIR-spectra are available for NGC 104 from Lebzelter et al. (2006).

[18] See Table 2.2 for a list of observed AGB stars per globular cluster.

Table 3.6: Globular Cluster Ages

GC ID	R_{gc} [kpc][a]	[M/H][b]	Age [Gyrs]	TO Initial Mass [$M_\odot$][d]
NGC104	7.3	-0.62	12.288	0.839
IC1276	3.6	-0.56	11.136[c]	0.858
NGC362	9.2	-0.91	10.752	0.845
NGC5927	4.5	-0.23	11.264	0.945
NGC6352	3.3	-0.56	11.520	0.851
NGC6356	7.0	-0.36	11.136[c]	0.899
NGC6388	4.4	-0.46	11.520	0.892
NGC6553	3.3	-0.11	11.136[c]	0.948
NGC6637	1.5	-0.57	12.288	0.839
NGC6712	3.5	-0.87	11.136[c]	0.843
NGC6760	4.8	-0.38	11.136[c]	0.899
NGC6838	6.7	-0.59	12.554	0.834
Terzan 5	0.6	-0.14	11.136[c]	0.947

[a] R_{gc} is taken from Harris (1997).
[b] [M/H] values are derived with [Fe/H] from Harris (1997) and are different from the values presented by Marín-Franch et al. (2009).
[c] Mean age of the "old" globular cluster group from Marín-Franch et al. (2009).
[d] Turn-off (TO) initial mass of an isochrone with the respective globular cluster age and metallicity.

A combination of several clusters is possible because the LFs presented in Section 3.3 rely on (i) M_K and not on apparent K magnitudes, (ii) the same criterion for the NIR data extraction from the 2MASS database, and (iii) approximately equal ages of the underlying globular clusters.

While (i) and (ii) are determined in this work, (iii) relies on globular cluster ages from Marín-Franch et al. (2009) from their Table 4, where they present relative globular cluster ages[19]. These relative ages are given in units of the average age of their low metallicity globular cluster group[20] which amounts to 12.80±0.17 Gyrs. With this reference point and the relative ages it is possible to derive the absolute ages of the globular clusters by simply multiplying the relative age value from their Table 4 with the reference age from the low metallicity group. The absolute ages are presented in Table 3.6 and rely on the D07[21] stellar evolution library (see Dotter et al. 2007) applied by Marín-Franch et al. (2009).

Not all globular clusters of the sample this work is based on are part of the work of Marín-Franch et al. (2009). For the clusters IC 1276, NGC 6356, NGC 6553, NGC 6712, NGC 6760 and Terzan 5 the mean age of the "old" globular cluster group defined by Marín-Franch et al.

[19] Marín-Franch et al. (2009) used a *Hubble Space Telescope* ACS Survey to derive the relative ages of 64 Galactic globular cluster by comparing relative position of the clusters' main-sequence turnoffs.
[20] The low metallicity globular cluster group from Marín-Franch et al. (2009) covers a [Fe/H]-range from -0.8 to -0.3 dex. This range actually covers the total metallicity range used in this work.
[21] Note that in Table 4 of Marín-Franch et al. (2009) two D07 relative ages are listed. For this work the $D07_{ZW}$ relative ages are used refering to metallicities by Zinn & West (1984).

(2009) in their Fig. 11 is adopted. This approach is based on the idea that the above mentioned clusters belong to this "old" group. This is convenient because their galactic distances R_{gc} and their metallicities [M/H] allow a assignment to the "old" group using Fig. 12 from Marín-Franch et al. (2009).

The ages of the globular clusters are varying in the literature, e. g. the uncertainty of the age of even the best studied globular cluster, namely NGC 104, is reported to be 1 Gyr (cf. McDonald et al. in prep.). The ages used in this work are all within or close to a ±1 Gyr uncertainty around the mean age of 11.136 Gyrs of the "old" group from Marín-Franch et al. (2009). Therefore the combination of the various globular clusters is still convenient even though there are age differences of the members within the cluster combinations.

The different globular cluster ages are correlated with different turn-off (TO) initial masses of the respective stellar populations. Table 3.6 presents the initial masses of the main sequence turn-off for each globular cluster. These initial masses are extracted from isochrones representing the respective globular clusters with respect to their age and metallicity. The used isochones are based on stellar tracks from Marigo et al. (2008), an initial mass function from Kroupa (1998) and a dust evolution scenario from Groenewegen (2006)[22]. The initial masses clearly illustrate that the age difference of the various globular clusters is only significant when comparing the entire sample of clusters. Due to the aspired grouping of the globular clusters with respect to their metallicity, three subsamples of TO initial mass values are of importance. Within the three subsamples the difference of the TO initial masses and hence the age differences are not significant. However, the mean values of the TO initial masses of the respective subsamples[23] illustrate that the age diffences between the three groups are significant, showing a trend to higher TO initial masses with increasing metallicity. The mean TO initial masses for the three subsamples are $0.844\,M_\odot$ for the low metallicity group, $0.897\,M_\odot$ for the intermediate metallicity group and $0.947\,M_\odot$ for the high metallicity group.

The cluster combinations also rely on neglecting age differences due to multiple stellar populations within the globular clusters. While Conroy & Spergel (2010) conclude that nearly all globular clusters studied to date show evidence for multiple stellar populations, only for two globular clusters that are part of this work multiple populations are reported, namely NGC 6388 and Terzan 5. Piotto (2008) reports that there is evidence for two stellar groups in NGC 6388 due to a split in the sub giant branch in the cluster. For Terzan 5 Ferraro et al. (2009) reports an additional young population (see Section 2.2.6).

---

[22]See Chapter 4 for a detailed discussion of the use of isochrones.

[23]These subsamples are later defined as low, intermediate and high metallicity groups. Metallicity groups are introduced in Section 3.4.1

3.4.1 Metallicity Groups

The sample of Galactic globular clusters can be devided into three different metallicity groups according to their [Fe/H] values from Harris (1997) presented in Table 3.1. The nomenclature is defined as "low", "intermediate" and "high" metallicity for the three groups[24].

The three metallicity ranges defining the globular cluster combinations are presented in Table 3.7 together with the number of globular clusters per group and the number of observed *Spitzer* spectra available in each group. The high number of available MIR-spectra in the low metallicity group is due to the membership of the globular cluster NGC 104 which provides twelve individual AGB star spectra. For each group a mean metallicity is defined as the arithmetric mean of the individual metallicities of the group members presented in Table 3.1. The respective mean metallicity is given in Table 3.7 in [Fe/H] and Z. How to convert from [Fe/H] to Z values and vice versa is explained in Appendix B.

Table 3.7: Properties of the Globular Cluster Combinations

Metallicity Group	[Fe/H] Range	$\overline{[Fe/H]}^a$	$\overline{Z}^a$	$n_{GC}{}^b$	$n_{spec}{}^c$	Members
Low	$-0.80 \leq [Fe/H] \leq -0.67$	-0.72	0.0038	5	18	IC 1276 NGC 104 NGC 6352 NGC 6637 NGC 6838
Intermediate	$-0.63 \leq [Fe/H] \leq -0.47$	-0.54	0.0058	3	8	NGC 6356 NGC 6388 NGC 6760
High	$-0.40 \leq [Fe/H] \leq -0.23$	-0.30	0.01	3	7	NGC 5927 NGC 6553 Terzan 5

[a] $\overline{[Fe/H]}$ and $\overline{Z}$ define the mean metallicity.
[b] n_{GC} is the number of globular clusters per metallicity group.
[c] n_{spec} is the number of *Spitzer* spectra used in each metallicity group.

In Fig. 3.7 the three metallicity groups are illustrated with colored boxes in the [Fe/H]-M_K-plane. The plotted AGB stars have been introduced in Table 2.2. Blue symbols refer to stars observed by Sloan et al. (2010) and green symbols to stars observed by Lebzelter et al. (2006). The green dashed line marks the tip of the RGB derived after Bellazzini et al. (2004). The most metal-poor Galactic globular clusters, namely NGC 362 and NGC 6712, are neglected and not grouped together to a fourth globular cluster combination because of the low number of observed AGB stars in the respective clusters. The stars from these two clusters are marked with the circle on the left side of Fig. 3.7.

---

[24] Note that the names of the metallicity groups are refering to the metallicity range of the globular clusters used in this work. This metallicity range is not really low in general but still named that way in this work.
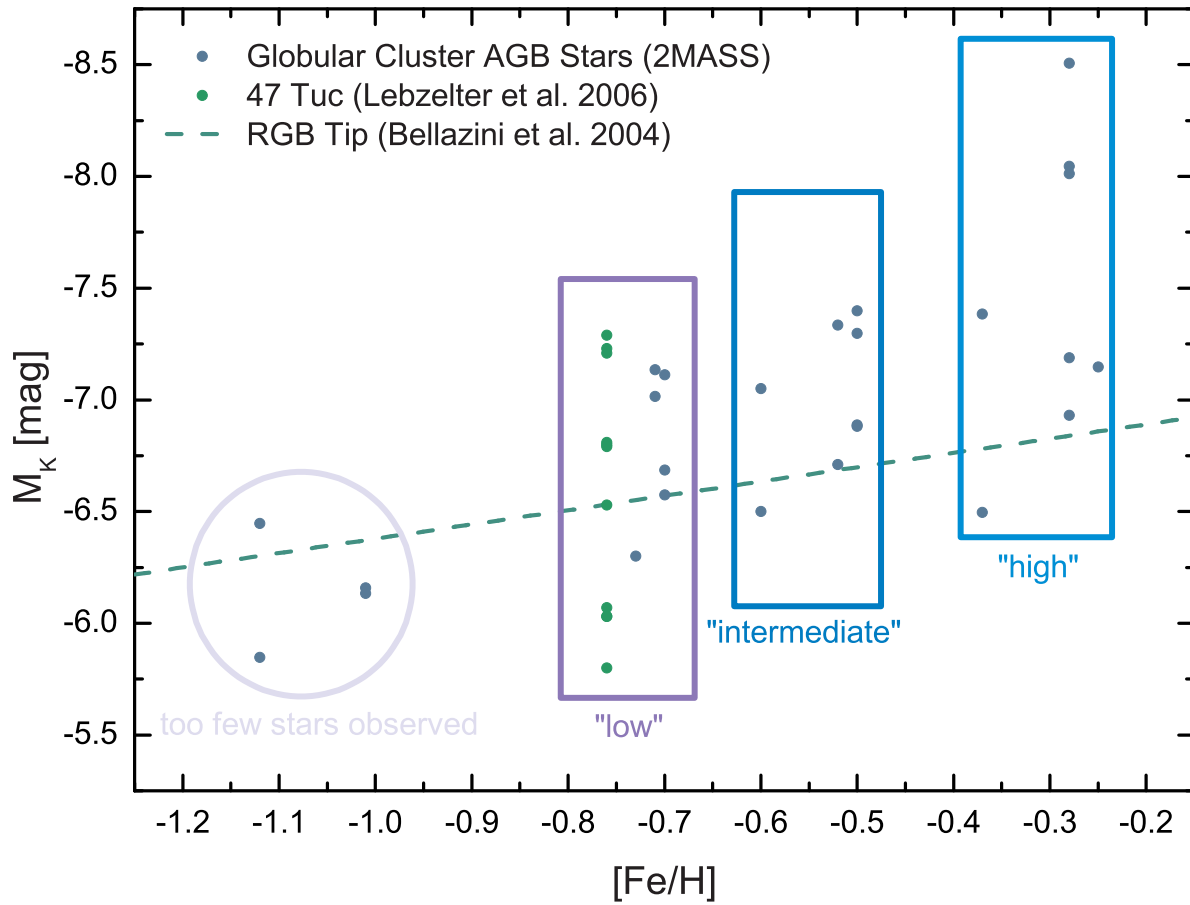
Figure 3.7: Metallicity-Luminosity diagram of the globular cluster AGB star sample. Three metallicity groups are defined. The stars in the most metall-poor clusters are neglected. The green dashed line marks the tip of the RGB.

The metallicity groups presented in this work are in good agreement with the metallicity groups defined by Sloan et al. (2010) to compare the MIR-spectra of individual stars according to the metallicity of their hosting globular clusters.

3.4.2 Low Metallicity Group

The low metallicity group consists of five Galactic globular clusters, namely IC 1276, NGC 104, NGC 6352, NGC 6637 and NGC 6838, with metallicities ranging from -0.76 < [Fe/H] < -0.70 (also see Table 3.7 for the metallicity interval chosen for this group). Fig. 3.8 presents the Color-Magnitude diagram of the globular cluster combination (full CMD, lower panel; zoom on the luminous part of the CMD, upper panel). AGB stars with observed *Spitzer* spectrum are indicated with red symbols, the tip of the RGB is marked with a green line. Eight observed AGB stars[25] are located below the mean tip of the RGB presented in Table 3.3. This makes the low metallicity group the best canditate for the calculation of a co-added MIR-spectrum of the combined globular clusters, because the information gained from these lower luminosity stars can be assigned to stars occupying the same area in the Color-Magnitude diagram allowing for
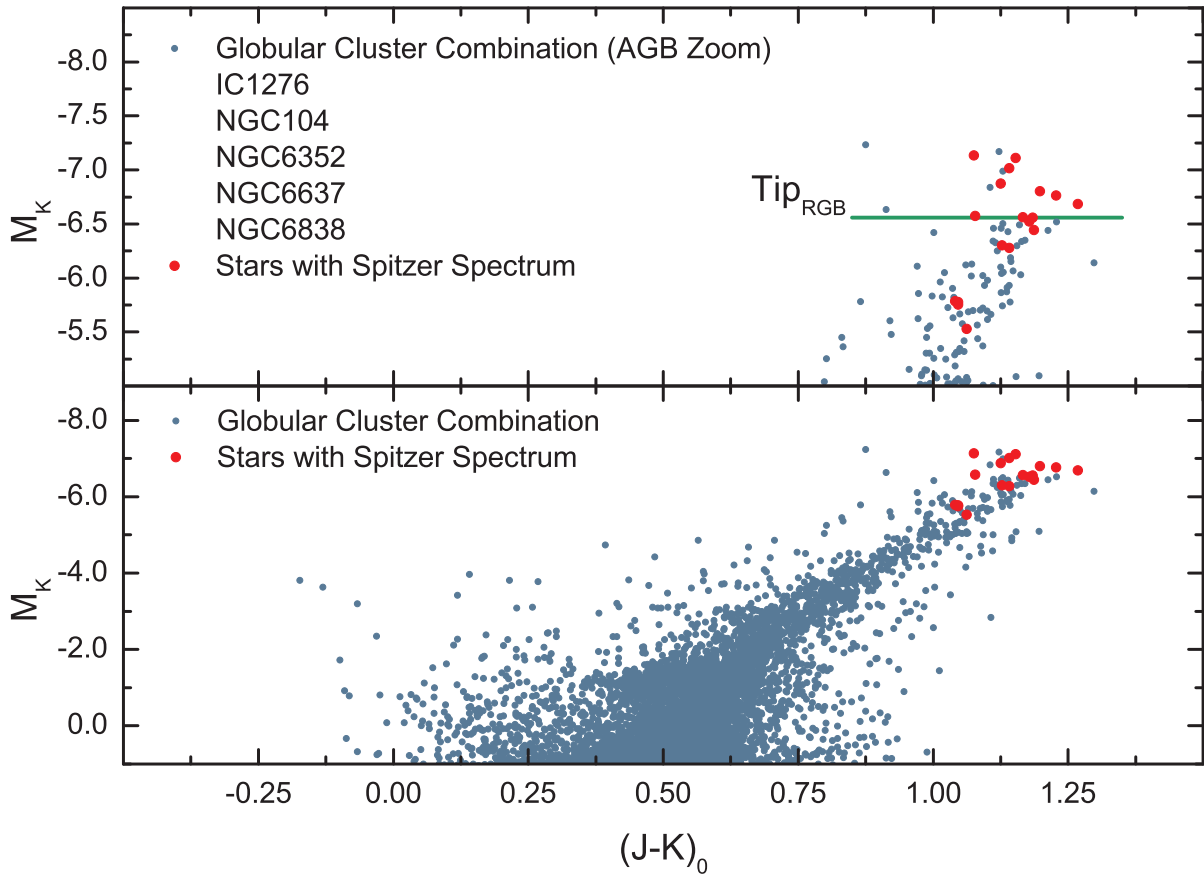

Figure 3.8: Color-Magnitude diagram of the low metallicity group. Lower panel: CMD of the entire globular cluster combination. Red symbols mark stars with observed *Spitzer* spectrum. Upper panel: Zoom on the luminous part of the CMD. Red symbols mark stars with observed *Spitzer* spectrum. The green line indicates the tip of the RGB. AGB stars that are located below this line are from the globular custers NGC 104 and NGC 6838 (only on star).

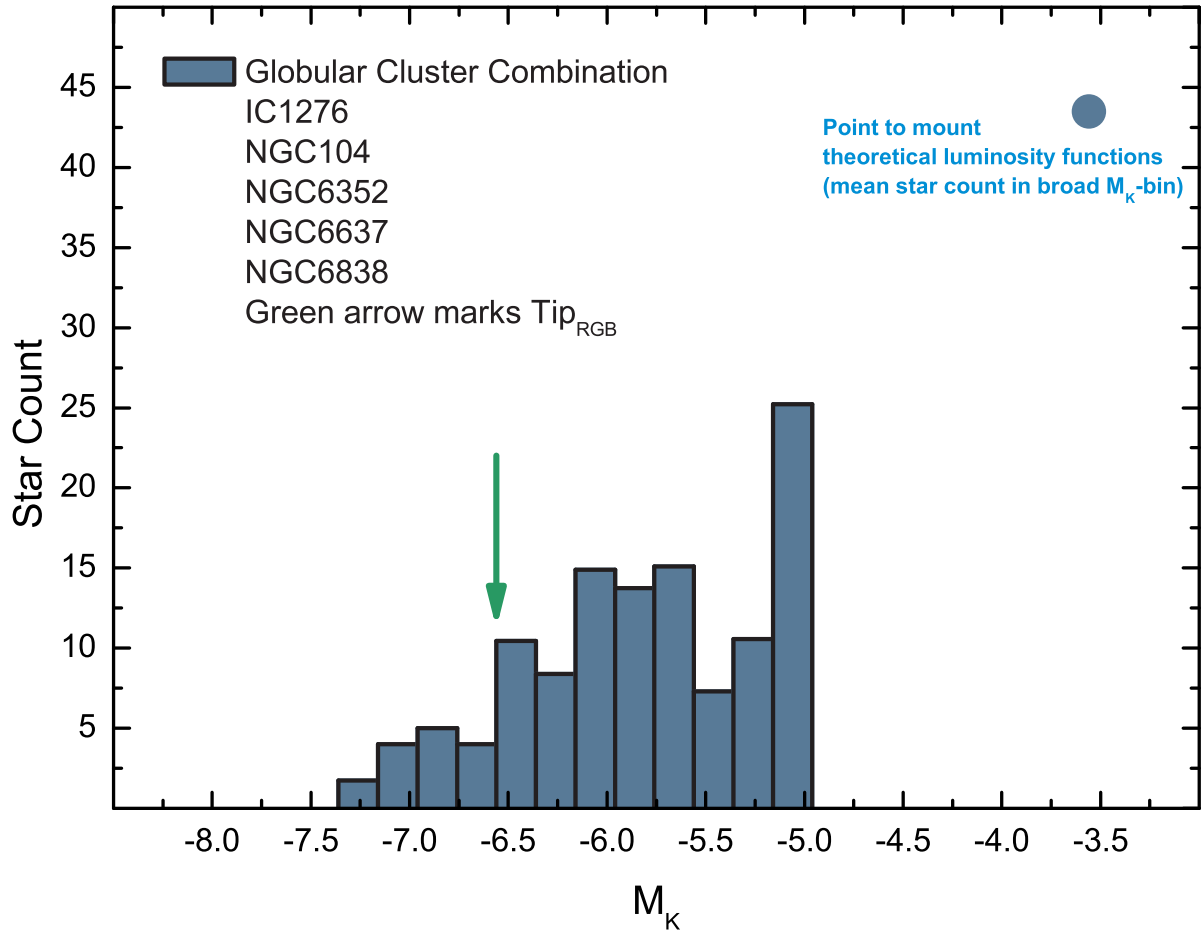[25] Seven AGB stars from NGC 104; one AGB star from NGC 6838.

Figure 3.9: Luminosity function of the low metallicity globular cluster combination. The symbol at the top right corner indicates the star count used to mount theoretical luminosity functions derived from Padova isochrones. The green arrow marks the tip of the RGB.

a more deepened understanding of the integrated globular cluster combination MIR-spectrum[26].

The LF of the low metallicity globular cluster combination is presented in Fig. 3.9 and is dominated by the globular cluster NGC 104, which accounts for 63.4% of the total star count of the group. The tip of the RGB derived after Bellazzini et al. (2004) is indicated in Fig.3.9 with a green arrow at $M_K = $ -6.56 mag and is perfectly positioned at the point of the LF where the number of stars drops. This drop in the star count reflects the fact that only AGB stars are present at higher luminosities than M_K of the RGB_{Tip}. Below the tip the number of stars is higher because stellar evolution favors the number of RGB stars compared to the number of AGB stars at a given time. Some AGB stars will still be found below the tip of the RGB in the Color-Magnitude diagram of the globular cluster combination since the AGB begins at luminosities of the horizontal branch or the red clump. Between this regions and the RGB tip we see a sum of the present RGB and AGB stars. In addition individual AGB stars, which

---

[26]The MIR-spectrum of the low metallicity group is presented in Section 5.1.

actually are expected to be more luminous than the RGB tip due to their evolutionary state, can occupy areas below the RGB tip due to the occurence of luminosity drops during thermal pulsation events (see e. g. Lebzelter et al. 2006).

In Fig. 3.9 the symbol on the right of the LF indicates the star count of a broad luminosity bin which is centered at $M_K = $ -3.56 mag. This luminosity is chosen with respect to the mean RGB tip of the low metallicity group and positioned 3 mag below the tip luminosity. For each globular cluster from the low metallicity group the mean star count of the broad bin is derived using the star count of two bins with a size of 0.2 mag each on either side of the center. The mean star count of each globular cluster is subsequently added together to derive the mean star count of the globular cluster combination. Again the star count is dominated by NGC 104 and amounts to 43.5 at $M_K = $ -3.56 mag. This star count is used in Chapter 4 to mount theoretical LFs to the observed LF of the low metallicity globular cluster combination.

3.4.3 Intermediate Metallicity Group

The intermediate metallicity group consists of three Galactic globular clusters, namely NGC 6356, NGC 6388, and NGC 6760, with metallicities ranging from -0.60 < [Fe/H] < -0.50 (also see Table 3.7 for the metallicity intervall chosen for this group). Fig. 3.10 presents the Color-Magnitude diagram of the globular cluster combination (full CMD, lower panel; zoom on the luminous part of the CMD, upper panel). AGB stars with observed *Spitzer* spectrum are indicated with red symbols, the tip of the RGB is marked with a green line. While only one star with an observed MIR-spectrum, namely NGC 6388 V3, is located below the tip, 64% (seven of eleven) of the stars located above the tip were observed with *Spitzer*.

The LF of the intermediate globular cluster combination is presented in Fig. 3.11. The tip of the RGB is indicated with a green arrow at $M_K = $ -6.67 mag and is positioned slightly off the point where the star count drops towards higher luminosities. It seems to be obvious to explain the shift of this mean RGB tip compared to the tip apparent in the 2MASS luminosity function with stellar variability. Applying the mean K-band amplitude of 0.6 mag (cf. Section 2.2.5) on the long-period variables occupying the bright region of the luminosity function, the postion of the mean RGB tip (derived after Bellazzini et al. (2004)) is well inside a 0.3 mag interval around the apparent RGB tip from the 2MASS data. However, this argumentation is not valid due to the fact that only AGB stars show large amplitude variability, and the number of AGB stars is small compared to the number of RGB stars, which show only minor variability. To obtain a perceptible effect on the shape of the LF around the RGB tip, all large amplitude stars must be at a phase minimum at the same time. Although this scenario is not feasible, it could result in a smeard out edge of the LF.

The mean RGB tip derived after Bellazzini et al. (2004) relies on the mean [M/H]-value of the three globular cluster members of the intermediate group (cf. Section 2.1.3). Deriving the RGB tip not for the mean metallicity value, but for the minimum and maximum metallicity of the cluster combination, one recieves two additional RGB tip positions flanking the mean RGB tip. However, the two new positions are too close to the mean RGB tip, and therefore are not suited to explain the difference to the 2MASS data with the chosen mean metallicity
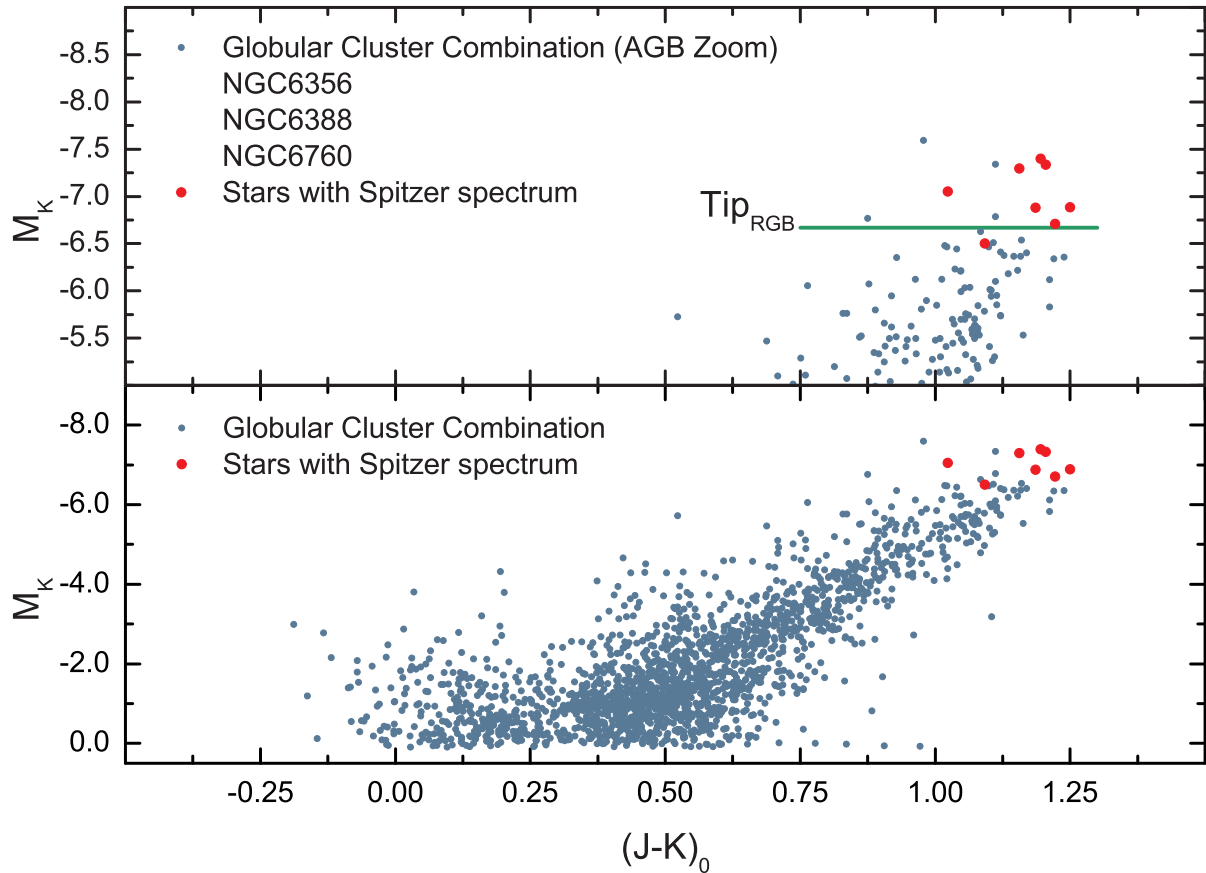
Figure 3.10: Color-Magnitude diagram of the intermediate metallicity globular cluster combination. Same as Fig 3.8.

of the intermediate group[27]. A possible explanation of the mismatch of the mean RGB tip and the apparent tip of the LF could be the adopted distance of the intermediate group. An underestimated distance would result in a too faint LF, hence, adopting a higher distance would shift the LF to higher luminosity, resulting in a better agreement with the mean RGB tip. However, it is not likely that the distances of all three globular clusters that are part of the intermediate metalllicity group are underestimated in the same way.

---

[27]The two additional RGB tip positions can be interpreted as uncertainties of the mean RGB tip: $\overline{\mathrm{RGB}}_{Tip} = 6.67 \, ^{+0.038}_{-0.026}$
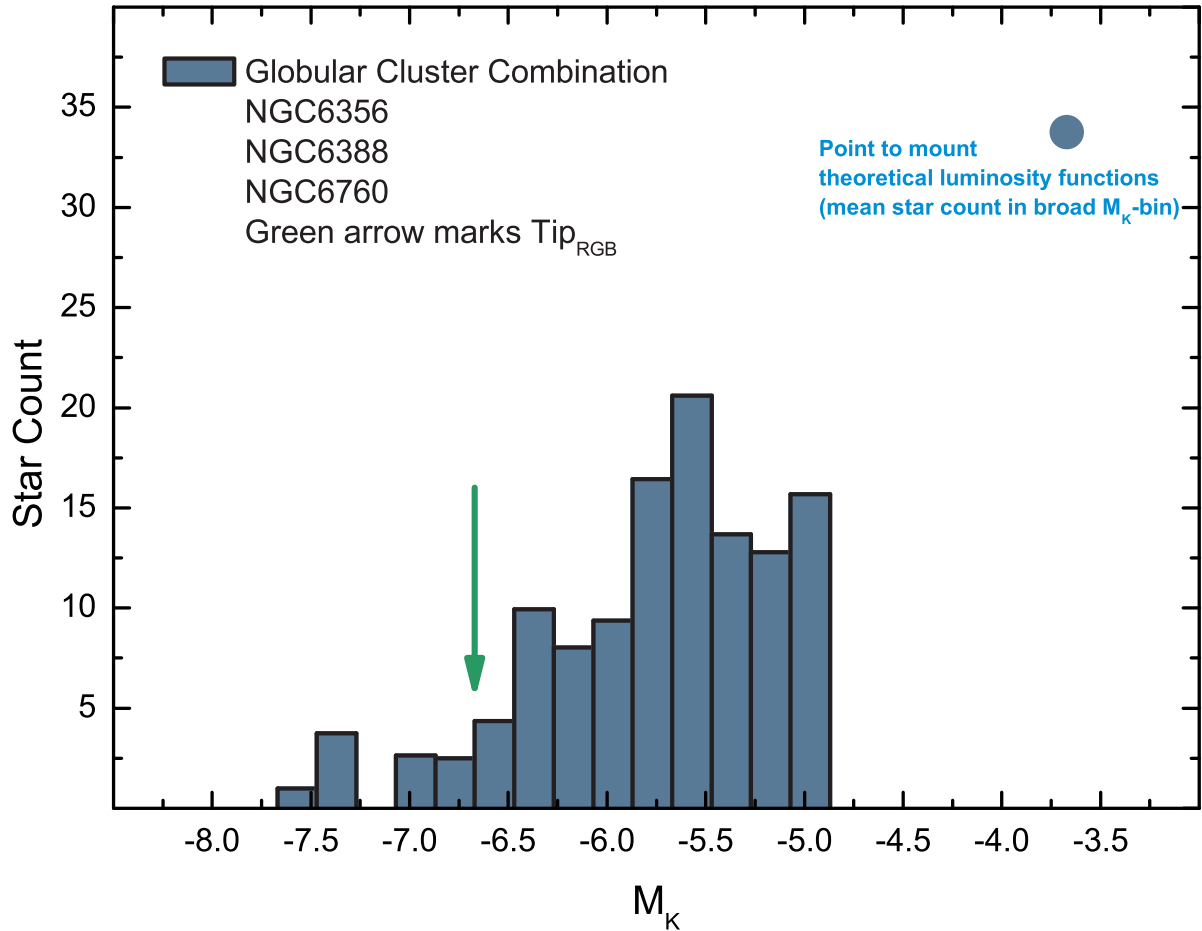
Figure 3.11: Luminosity function of the intermediate metallicity globular cluster combination. Same as Fig 3.9.

Similar to the low metallicity group a symbol on the right of the LF of the intermediate group indicates the star count of a broad luminosity bin centered 3 mag below the mean tip of the RGB (see Fig.3.11). The central luminosity M_K of the bin amounts to -3.67 mag. For each globular cluster from the intermediate metallicity group the mean star count of the broad bin is derived using the star count of two bins with a size of 0.2 mag each on either side of the center. The mean star count of each globular cluster is subsequently added together to derive the mean star count which amounts to 33.75 at $M_K = -3.67$ mag. This star count is used in Chapter 4 to mount theoretical LFs to the observed LF of the intermediate metallicity globular cluster combination relying on 2MASS data.

3.4.4 High Metallicity Group

The high metallicity group consists of three Galactic globular clusters, namely NGC 5927, NGC 6553, and Terzan 5, with metallicities ranging from -0.37 < [Fe/H] < -0.25 (also see Table 3.7 for the metallicity intervall chosen for this group). Fig. 3.12 presents the Color-Magnitude diagram of the globular cluster combination (full CMD, lower panel; zoom on the luminous part of the CMD, upper panel). AGB stars with observed *Spitzer* spectrum are indicated with red symbols, the tip of the RGB is marked with a green line and positioned at $M_K = -6.83$ mag. Like in the intermediate metallicity group, only one star with an observed MIR-spectrum, namely NGC 5927 V1, is located below the tip, while above the tip only a small fraction (32%) of stars has available MIR-specta from *Spitzer*.

The LF of the high metallicity globular cluster combination is presented in Fig. 3.13. The tip of the RGB is indicated with a green arrow and is again slightly positioned off the point where the star count drops towards higher luminosities. Like for the intermediate group, long period variability could only account for a smeared out edge of the LF, but not for a 0.3 mag shift of the apparent RGB tip. Furthermore, the shift can not be explained with the metallicity interval
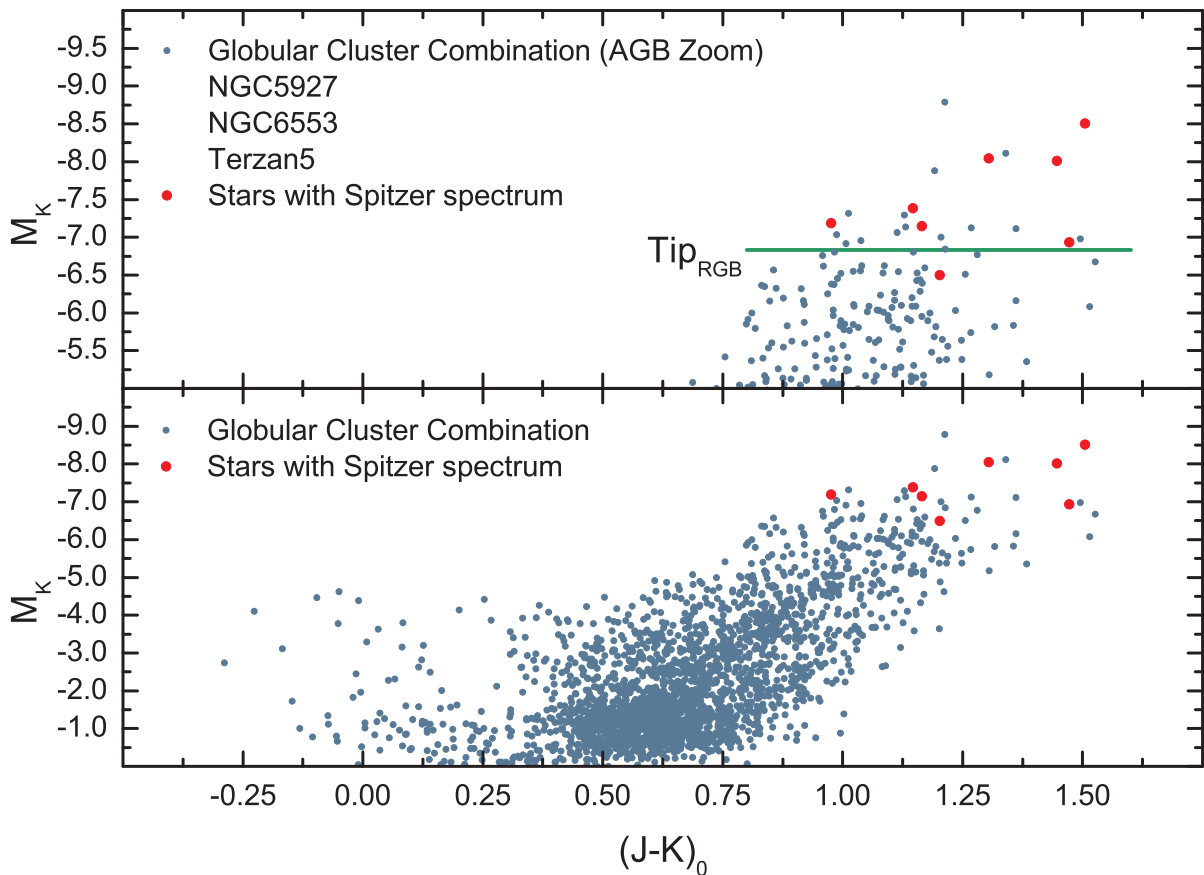

Figure 3.12: Color-Magnitude diagram of the high metallicity globular cluster combination. Same as Fig 3.8.
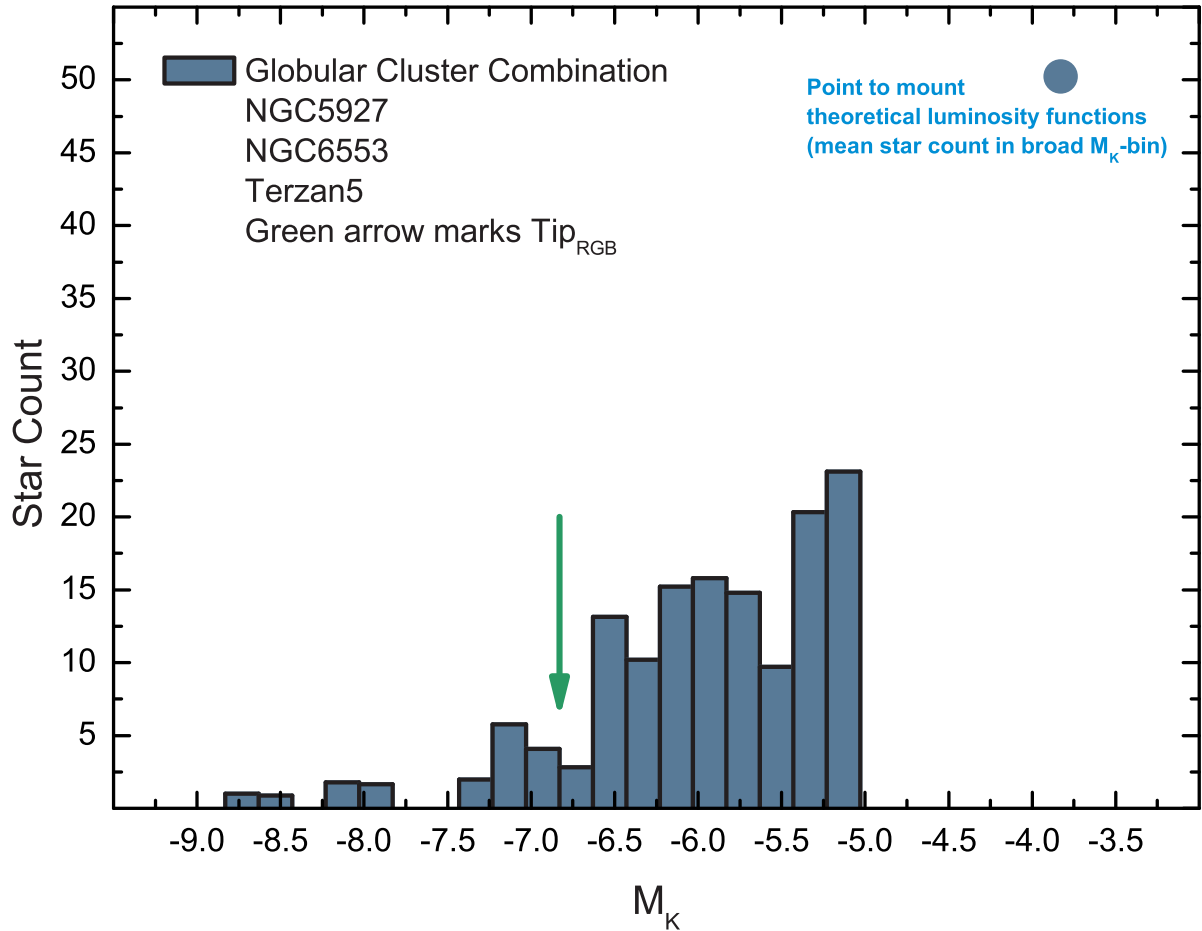
Figure 3.13: Luminosity function of the high metallicity globular cluster combination. Same as Fig 3.9.

of the high metallicity group spanned by the three group members. The resulting uncertainties of the mean RGB tip are not large enough to allow for a significant variation of the RGB tip luminosity[28].

The LF shows the presence of stars at explicitly high luminosities detached from the main part of the LF. All stars in this region are from Terzan 5 and are possible members of the young stellar population of the cluster with an age of 6 Gyrs (see Section 2.2.6 and Ferraro et al. (2009)).

Again a symbol on the right of the LF in Fig. 3.13 indicates the star count of a broad luminosity bin centered 3 mag below the mean tip of the RGB. The central luminosity of the bin amounts to -3.83 mag. For each globular cluster from the high metallicity group the mean star count of the broad bin is derived using the star count of two bins with a size of 0.2 mag each on either side of the center. The mean star count of each globular cluster is subsequently added together to derive the mean star count of the cluster combination which amounts to 50.25 at the centered $M_K = $-3.83 mag. This star count is used in Chapter 4 to mount theoretical LFs to the observed LF of the high metallicity globular cluster combination relying on 2MASS data.

---

[28]Mean RGB tip uncertainties: $\overline{\text{RGB}}_{Tip} = 6.83^{+0.045}_{-0.013}$

Chapter 4

A Comparison with
Theoretical Luminosity Functions

In modern astrophysics, theoretical Isochrones are used for a wide range of applications, going from the determination of basic parameters, such as age, distance, reddening and metallicity, of star clusters (see e.g. McDonald et al. in prep.) to the derivation of star formation histories of resolved galaxies (see e.g. Bressan et al. (1998)). In this study isochrones are used to derive theoretical luminosity functions (TLFs) of old stellar populations for various metallicities, ages and mass-loss rates. These TLFs are compared with observed 2MASS luminosity functions of the Galactic globular cluster combinations presented in Chapter 3.

4.1   From Isochrones to Luminosity Functions

Isochrones are based on a selection of basic ingredients such as metallicity, age, evolutionary tracks, the initial mass function and dust models. The metallicity and age parameters are defined to represent the stellar population that should be described by the isochrone. The evolutionary tracks are ranging from the zero-age main sequence (ZAMS) up to the post-AGB phase[1] and characterise the evolution of single stars with a given mass. The mass distribution of the entire population is described with the inital mass function that defines the number of stars born with a certain mass. During the late stages of stellar evolution, dust models are included to account for the effects of the formation and destruction of solid particles and the development of dust driven stellar winds and mass-loss. All these ingredients are used to derive isochrones containing all important information to characterise various stellar populations. Depending on the used isochrone calculation tools and interfaces, different content can be optained in the output data. The main information in the output data includes some of

---

[1]Not all evolutionary tracks are covering the stellar evolution until the post-AGB phase. Some models stop at the end of the AGB phase or even at the beginning of the termal puls AGB phase.

the chosen input ingredients, such as age and metallicity, together with parameters like intital mass, actual mass, luminosity, temperature and magnitudes for various photometric systems. For each inital mass value these parameters are listed in the isochrone output files, waiting for further processing.

In this study, the LFs derived from 2MASS data are compared with two sets of Padova isochrones from Marigo et al. (2008)[2] and Bertelli et al. (2008)[3], respectively. While the CMD interface for the isochrones from Marigo et al. (2008) does not allow for a change of the helium content, the α-enrichment or the mass-loss rate, the YZVAR interface for the isochrones from Bertelli et al. (2008) allows both, the helium content and the mass-loss rate to be changed, but again no variations of the α-enrichment. In the latter interface the mass-loss can be varied by the user by choosing different η-values for the Reimers-law (Reimers 1975). The default value for η in the YZVAR isochrones is 0.35 which is well suited to explain the Horizontal Branch morphologies observed in Galactic globular clusters (Renzini & Fusi Pecci 1988). The variation of the η-parameter can be used to influence the shape of the isochrones, for instance an $\eta = 0.6$ would suppress the late stages of stellar evolution i.e. the entire Horizontal Branch and the AGB phase, as RGB stars would lose their entire envelope before He-ignition in the core (Renzini & Fusi Pecci 1988). A low η and, thus, a low mass-loss rate results in an increasing luminosity of the tip of the AGB. This effect is used in this work to produce isochrones and subsequently TLFs to fit the bright AGB star populations in the 2MASS LFs from Chapter 3.

In this work only different ages, metallcities and mass-loss rates are used. While for the extraction of CMD isochrones various ages and metallicites are defined at the interface, the YZVAR isochrones are extracted with various ages, metallicities and η-values[4]. At the YZVAR interface the helium content is fixed to 0.25 and not varied in this study.

4.1.1 The YZVAR Isochrones and Luminosity Functions

The extracted YZVAR isochrones include information on various stellar parameters of the stars of the described stellar population, such as luminosity, temperature, $\log g$, initial mass and current mass along the isochrone. Also the absolute magnitudes of various photometric bands are included. An example isochrone is presented in Fig. 4.1 (left panel) for an age of 12 Gyrs, a metallicity of $Z = 0.0038$[5] and an η of 0.2. Typically an isochrone is displayed in a temperature-luminosity plane. Since in this work the favored display is the Color-Magnitude diagram, the isochrone in Fig. 4.1 is presented in a $(J-K)_0$-M_K plane[6] illustrating main sequence, turn-off, RGB, horizontal branch and AGB prominently.

In order to derive TLFs from the YZVAR isochrone data, the total number of stars occupying selected areas along the isochrone have to be calculated. For this a look on the underlying physics of an isochrone is needed. On the following pages the path from the extracted isochrone data to the TLFs is elucidated.

---

[2] http://stev.oapd.inaf.it/cgi-bin/cmd [December 30, 2010]
[3] http://stev.oapd.inaf.it/YZVAR/cgi-bin/form [December 30, 2010]
[4] See Sections 4.2.1 to 4.2.3 for details on the used ages, metallicities and mass-loss rates.
[5] This metallicity corresponds to the low metallicity group from Section 3.4.2.
[6] J and K magnitudes are taken from the extracted isochrone table from the YZVAR interface where they are given in absolute units.
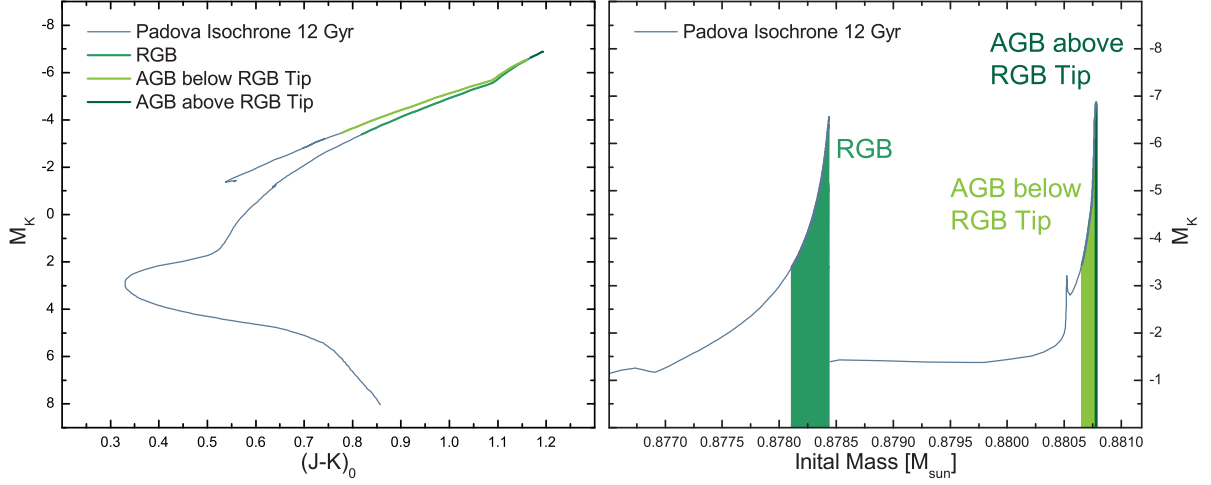
Figure 4.1: Padova isochrone extracted from the YZVAR interface with an age of 12 Gyrs, a metallicity of $Z = 0.0038$ and an η of 0.2. Left panel: Color-Magnitude diagram presenting the isochrone of the respective stellar population. Three selected evolutionary phases are indicated with different colors, namely the bright part of the RGB phase, the bright part of the AGB phase below the RGB tip luminosity and the brigthest AGB phase above the RGB tip luminosity. Right panel: Initial-mass-Magnitude diagram describing the isochrone. The increasing luminosity during the RGB and AGB phase are clearly visible. The evolutionary phases for the RGB part, and the two AGB parts are again indicated with different colors.

In the isochrone output files of the YZVAR interface the indefinite integral of the initial mass function (IMF) by number over the mass is named *Flum* and defined by

$$Flum = \int \Phi(M) dM. \tag{4.1}$$

This integral is calculated assuming the Salpeter law for the initial mass function given by

$$\Phi(M) = A \cdot M^{-\alpha}, \tag{4.2}$$

with M being the initial mass associated to the current mass along the isochrone, $\alpha = 2.35$ and the normalisation constant $A = 1$, leading to Equation 4.3.

$$Flum = \frac{M^{1-\alpha}}{1-\alpha} \Rightarrow Flum = \frac{M^{-1.35}}{-1.35} \tag{4.3}$$

The difference between two values of *Flum* is proportional to the number of stars born in the corresponding mass interval. The ratio between two differences of *Flum* gives the relative number of stars in the corresponding evolutionary phases (see Bertelli et al. 1994 and Bertelli et al. 2008).

To derive the total number of stars N that occupy a certain evolutionary phase of the isochrone, the integral given by Equation 4.1 is solved as

$$N = \int\limits_{m_{low}}^{m_{high}} m_{ini} dm, \qquad (4.4)$$

where m_{ini} is the initial mass and m_{low} and m_{high} are the initial masses enclosing the respective evolutionary phase along the isochrone.

The isochrone output file contains values for m_{ini} that can not be used directly for the calculation of the total number of stars, because they are given only to a insufficent accuracy[7]. Therefore the *Flum*-values from the isochrone output file are used in Equation 4.3 to derive initial mass values that can be used for the calculation of N. This is convenient because *Flum* is given with a high accuracy obviating any "doubled" values for the entire isochrone, and hence result in a high accuracy initial mass grid.
The resulting m_{ini}-grid of the isochrone is now interpolated to retrieve a refined m_{ini}-grid. This interpolation is necessary in order to provide enough data points along the isochrone that allow for the calculation of the total star number N not only for a wide mass interval given by a insufficent number of data points, but also for many very narrow mass intervals. These narrow intervals together add up to certain evolutionary phases of the isochrone. It is important to use a high number of m_{ini}-values in order to allow for narrow brightness-bins during the calculation of TLFs (see below). A low number of m_{ini}-values would only result in very broad brightness bins and, thus, in an insufficiently accurate TLF.

After the interpolation a fine grid of high-accuracy initial masses is available which makes it possible to derive the number of stars of the entire stellar population described by the isochrone or for selected phases along the evolutionary path using Equation 4.4. The integration results in the total number of stars occupying a certain part of the isochrone. By defining the m_{low} and m_{high} integration limits it is possible to derive the number of stars for exactly the three evolutionary phases that are illustrated in Fig. 4.1.
In the refined m_{ini}-grid the three different phases are defined by selecting three initial mass intervals that define the limits for three seperate integrations. The first interval describes the RGB phase of the stellar population while the second and the third intervals represent the AGB phase which is seperated into two parts. The first AGB part (equivalent to the second interval in Fig 4.1) describes the AGB ranging from the early AGB up to the tip-luminosity of the RGB. The second part (equivalent to the third interval) describes the AGB above the tip-luminosity of the RGB. In the initial mass grid the three intervals are well separated and on account of the refinement of the grid offers a high number of data points for the computation of TLFs. The separated intervals are illustrated in the right panel of Fig. 4.1, where three colors indicate the three different phases along the isochrone.

All three phases together describe the most luminous stages of stellar evolution and are the parts of the isochrone that are converted to a TLF. The TLF must occupy the same luminosity range as the 2MASS LFs presented in Chapter 3 to allow a proper comparison. Therefore the

---

[7]The m_{ini} values have only few decimal places. This leads to "doubled" values in the extracted isochone table for certain evolutionary phases along the isochrone.

final selection of the different isochrone intervals is not done with initial mass values, but with M_K-values that are defined with respect to the luminosity range of the 2MASS LFs.

The interval for the RGB phase is starting at the lowest luminosity bin of the respective 2MASS LF and reaches up to the luminosity bin of the RGB tip[8]. The interval for the first AGB part also starts at the lowest luminosity bin of the 2MASS LF and again reaches up to the luminosity of the isochrones RGB tip. The interval for the second part of the AGB starts at the RGB tip-luminosity of the isochrone and reaches to the highest luminosity of the isochrone, the tip of the AGB. The selection of these intervals according to their M_K-luminosity range results in initial mass values that enclose the respective phases of the isochrone. These initial mass values are used as integration limits in Equation 4.4.

The integration results in the total number of stars N occupying the three intervals. By recording every single integration step it is possible to derive N for each small m_{ini}-interval given in the fine m_{ini}-grid of the isochrone. The sum of all the N values from the small m_{ini}-intervals results in N of the large m_{ini}-interval given by the integration borders defined according to the 2MASS LFs for the three main intervals. The N-values of the the main intervals can be interpreted as rudimental luminosity functions consisting of only three luminosity bins. Starting again with the N-values from every single integration step it is also possible to derive the sum for smaller initial mass intervals that together add up to the main intervals. This makes it possible to derive TLFs for any M_K or M_{ini} interval. Hence it is possible to produce TLFs with the same bin size as the 2MASS LFs. By defining a set of 0.2 mag M_K intervals and hence respective m_{ini}-intervals the number of stars in these small steps is calculated for each of the main intervals.
The TLFs of the first and the second main intervals, namely the RGB and the AGB part below the tip of the RGB are subsequently added together bin per bin to retrieve the overall TLF of the isochrone part below the RGB tip[9]. Finally the TLF of the AGB part above the RGB tip is placed on top of the combined TLFs from the other two phases. This results in a final overall TLF for the selected luminosity range of the isochrone covering all three main intervals defined above.

4.1.2 The CMD Isochrones and Luminosity Functions

The above described procedures to derive TLFs from a given isochrone are only needed for the YZVAR isochrones. For the isochrones of the CMD interface from Marigo et al. (2008) it is possible not only to extract isochrones, but to directly access TLFs.

The CMD interface allows for the extraction of isochrones for various ages, metallicities, dust evolution scenarios and initial mass functions. The isochrones can be calculated for different photometric systems including the 2MASS NIR-bands used in this work. The form allows the user to choose whether the output file should contain a classical isochrone table or already a TLF or even integrated colors for the selected photometric system. When selecting the TLF output, one recieves a data file containing the TLF giving the absolute number of stars occupying each magnitude bin per unit mass of the stellar population initially born. The range of absolute

---

[8] Here the RGB Tip of the isochone is used, not the tip from the 2MASS LF.
[9] It is not possible to distinguish between the two separate parts in an overall LF.

magnitudes of the TLF can be defined by the user by setting the faintest and brightest magnitude. The optional width of the magnitude bins allows for an individual sampling of the TLF.

The TLFs from the CMD interface based on the isochrones from Marigo et al. (2008) used in this study are extracted with the following input parameters[10]:

Evolutionary tracks $\implies$ Marigo et al. (2008)

Photometric system $\implies$ 2MASS $[JHKs]$

Circumstellar dust $\implies$ Bressan et al. (1998): Silicate dust
Groenewegen (2006): 60% Silicate dust, 40% Aluminum dust

Initial mass function $\implies$ Kroupa (1998): corrected for binaries

4.1.3   Normalisation

The resulting TLFs for both the CMD and the YZVAR interfaces rely on total star numbers per luminosity bin given per unit mass of the stellar population initially born. Therefore the TLFs need to be scaled with a proper value for the normalisation constant A introduced in Equation 4.2 to allow a comparison with the 2MASS LFs of the Galactic globular cluster combinations from Chapter 3. In this study the scaling and hence the definition of A is performed with the number of stars present in the 2MASS luminosity functions. In the Sections 3.4.2 to 3.4.4 the total number of stars in a broad (0.8 mag) luminosity bin 3 mag below the tip of the RGB is derived for the three globular cluster combinations. These three star counts do not suffer a high contamination with field stars and, thus, are well suited for a comparison to the number of stars occupying the same luminosity range of the TLFs. To derive the normalisation constants A the star count from the selected broad bin of the observed LF is devided with the star number of the equvalent bin of the respective TLFs. These A-values are subsequently multiplied to the star numbers of every single luminosity bin of the TLFs, resulting in TLFs that are mounted on the star count of the 2MASS LFs.

To validate the results of the normalisation, other methods to scale the TLFs to the 2MASS data have been investigated. E.g. a normalisation to the total number of stars on the RGB[11] of the 2MASS LF result in identical values for the normalisation constant A and hence in the same comparison TLFs.

---

[10]See Sections 4.2.1 to 4.2.3 for details on the used ages and metallicities
[11]The total star count of the 2MASS LF from an interval ranging from $M_K = $-5 up to the RGB tip of the cluster combination.

4.2 Luminosity Functions

Using the CMD and the YZVAR interfaces various isochones and TLFs were derived for the three Galactic globular cluster combinations from Chapter 3. The following pages present the comparison of the 2MASS LFs of the low, intermediate and high metallicity group with selected TLFs.

4.2.1 Low Metallicity Group

In order to derive theoretical luminosity functions describing the low metallicity group of globular clusters, both, the CMD and the YZVAR interfaces were used. For the comparison with the CMD TLFs based on evolutionary tracks from Marigo et al. (2008) the input metallicity is defined as the average metallicity of the cluster combination and amounts to $Z = 0.0038$. The age of the underlying isochrone is set to 12 Gyrs, which is the mean age of the cluster combination[12]. The inital mass function is taken from Kroupa (1998)[13]. The 2MASS [$JHKs$] bands are defined as output photometric system. The luminosity range is defined to start at $M_K = 3.16$ mag and includes the broad luminosity bin used to scale the TLF to the 2MASS data[14]. A bin size of 0.2 mag reproduces exactly the luminosity bins defined in the 2MASS LF. Also one of two different dust production scenarios can be selected in the CMD interface resulting in two different TLFs for the chosen input parameters. The scenario from Groenewegen (2006) includes silicate (60%) and alumina (40%) dust and results in the orange TLF presented in Fig. 4.2 (left panel). The dust scenario from Bressan et al. (1998) includes only silicates and is plotted as light blue TLF in the same panel. Both TLFs are mounted at the mean star count of the broad luminosity bin centered at $M_K = $ -3.56 mag which is indicated as blue dot in the upper right corner of Fig. 4.2 (left panel) and amounts to 43.5. The two dust scenarios do not lead to a significant difference in the shape and slope of the two TLFs.

Both TLFs do not fit the 2MASS LF (broad blue bars) very well. The brightest stars in the TLFs come not even close to the brigthest luminosity bins of the 2MASS LF. This is due to the fact, that for the selected input parameters the CMD isochrones do not allow for the presence of stars at this bright evolutionary stages, since the evolutionary track of the respective isochrones already bends off to the post-AGB phase. Since the metallicity is a fixed parameter for the low metallicity group, the other input parameters need to be changed to generate a matching TLF. Changing the dust scenarios or the initial mass function do not result in a different apperance of the CMD LFs, leaving only the age parameter to be varied.

By setting the age of the isochrone to be significantly younger than the mean age of the low metallicity group it is possible to derive a TLF that is in good agreement with the 2MASS data. The input parameters for the CMD interface are the same as for the TLFs presented in the left panel of Fig. 4.2, but for the age which now amounts to 10 Gyrs. In the right panel of Fig. 4.2 the two resulting TLFs are presented[15]. The TLF based on the dust scenario from

---

[12] The mean age of the cluster combination is derived from the ages given in Table 3.6 and amounts to 11.96 Gyrs. For the extraction of the CMD LFs this age is rounded to 12 Gyrs.

[13] The version which accounts for a correction for binary stars in the initial mass function is chosen. See also Kroupa (2001) for information on the variation of the initial mass function.

[14] See Section 3.4.2 for details.

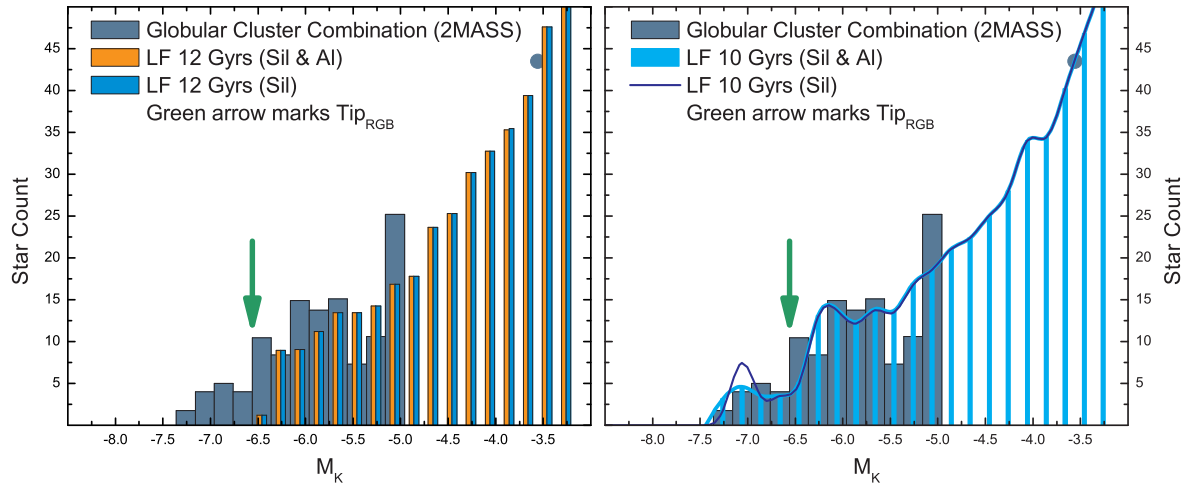[15] Again the TLFs are mounted at the broad luminosity bin at $M_K = $ -3.56 mag.

Figure 4.2: Comparison of the 2MASS LF of the low metallicity group with TLFs based on isochrones from the CMD interface. Left panel: Comparison TLFs with an age of 12 Gyrs and a metallicity of Z = 0.0038. Two different dust scenarios are indicated (orange and light blue). The bright part of the 2MASS LF is not reproduced. Right panel: Comparison TLFs derived after an isochrone with the age of 10 Gyrs and again the metallicity of the low metallicity group (Z = 0.0038). Two different dust production scenarios lead to a different shape above the tip of the RGB.

Groenewegen (2006) now is illustrated with cyan color; the dust scenario from Bressan et al. (1998) is plotted as blue line. The two different dust scenarios result in almost identical TLFs well covering the 2MASS LF. Only the most luminous part shows different star counts with respect to the different dust scenarios.

While the 12 Gyrs TLFs are not able to reproduce the 2MASS data, the TLFs with ages of 10 Gyrs almost perfectly fit the 2MASS LF representing the low metallicity group. Since the age of this globular cluster combination is older than 10 Gyrs with a mean age of 11.96 Gyrs the CMD TLFs are not the best choise for a comparison. This leads to the use of the isochrones and TLFs from the YZVAR interface based on evolutionary tracks from Bertelli et al. (2008) and a Salpeter initial mass function.

The basic input parameters for the YZVAR interface are again the age of the globular cluster combination (12 Gyrs), the mean metallicity of the group (Z = 0.0038) and now in addition the fixed helium content of Y = 0.25. To extract isochrones for different mass-loss rates, three different valus for the η parameter from the Reimers law (Reimers 1975) are used which amount to $\eta = 0.2$, 0.1 and 0.0[16]. The three different isochrones are used to derive three K-band TLFs describing the three different mass-loss rates. The details of the conversion of the isochrones to the TLFs are presented in Section 4.1.1.

---

[16]Note that the standard value of η is 0.35. This value results in a TLF with no bright stars comparable to the CMD luminosity functions for the 12 Gyrs isochrones. The three selected η-values are describing lower mass-loss rates then the standard scenario. An η of 0.0 totally suppresses any mass-loss on the AGB. This scenario is not realistic but illustrates the behaviour of the isochrones and TLFs when the mass-loss is turned off.
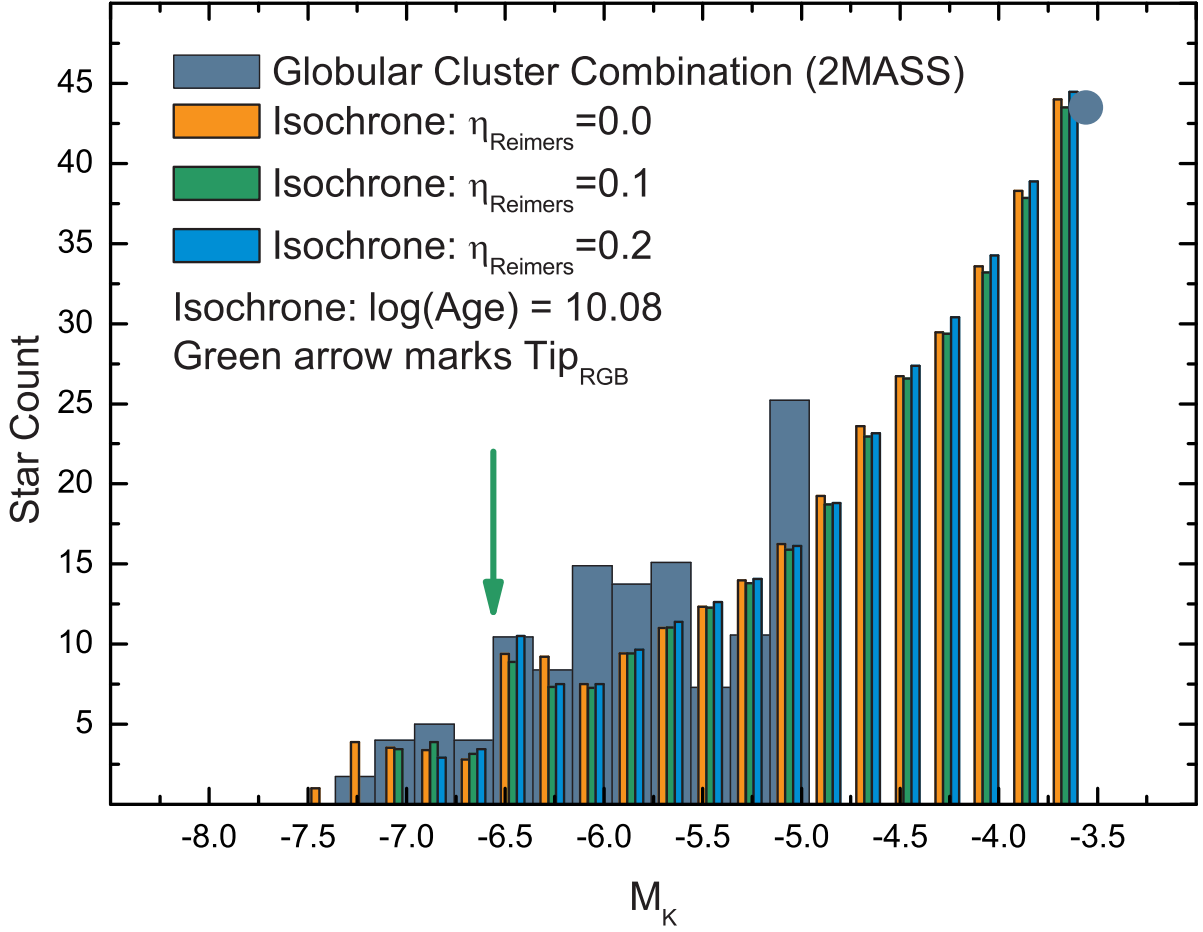
Figure 4.3: Comparison of the 2MASS LF of the low metallicity group with three TLFs derived using YZVAR isochrones with different mass-loss rates. The age is defined as 12 Gyrs, the metallicity as $Z = 0.0038$. The three different colors indicate the three different TLFs. All three versions cover the 2MASS data well up to the tip of the RGB which is indicated with a green arrow. Above the RGB tip the three different mass-loss rates lead to a different coverage of the luminous part of the 2MASS LF.

Fig. 4.3 presents the comparison of the 2MASS LF of the low metallicity group with the three YZVAR TLFs which are again normalized to the 2MASS star count of the broad luminosity bin at $M_K = -3.56$ mag. The different colors indicate the three different η-parameters, with light blue for $\eta = 0.2$, green for $\eta = 0.1$, and orange for $\eta = 0.0$. All three TLFs cover the 2MASS data well until the tip of the RGB which is indicated with a green arrow. In the 2MASS data an over-abundance is apparent from $M_K = -5.50$ to -6.25 mag, while an under-abundance is visible at lower luminosities, except for the least luminous bin of the 2MASS LF.

The 2MASS LF can be interpreted as a "snapshop" of the respective old stellar population not relying on mean M_K luminosities. Thus, the mismatch with the YZVAR TLFs could be diminished, when taking the mean amplitude of long period variables into account, which could lead to a smearing of the star counts of the respective luminosity bins, reducing the uncertainties im-

plied by the stochastic K-band photometric data from 2MASS. By assiging the observed AGB stars of the globular cluster NGC 104 to the respective brightness bins according to their K luminosities (cf. Table 2.2), we report, that the area of the 2MASS LF with the over-abundance is occupied by three stars, namely V5, V6 and V18, while the area with the under-abundance hosts one star, namely V13. While V5 and V6 show now dust emission and, thus, confirm the dust evolutionary trend reported by Lebzelter et al. (2006), V13 and V18 are special cases. The properties that enable the dust formation of V13 remain unclear, since the only remarkable characteristic of the star is its long secondary period. V18 shows the prominent silicate dust emission at 10 and 16-20 μm and is currently undergoing a thermal puls event resulting in a interpuls luminosity and a unusual position in the Period-Luminosity diagram (see Lebzelter et al. 2006) and in the 2MASS LF. All four stars are long period variables and therefore can be expected to have K-band amplitudes similar to the mean K amplitude of Mira stars of 0.6 mag derived after Whitelock et al. (2000)[17]. By neglecting the "snapshop" approach, the change of the K-band luminosity due to this mean ampitude would allow the respective AGB stars to cover a large part of the 2MASS LF. Assuming that not only the four stars with observed *Spitzer* MIR-spectrum, but also the other AGB stars occupying the same area in the LF have similar K-band amplitudes, a smearing of the star counts becomes feasible, although their number is small compared to the number of present RGB stars. In addition the YZVAR TLFs do not include stars in the thermal pulse phase, which could lead to a undersampling of the star counts below the tip of the RGB.

The different mass-loss rates used for the YZVAR TLFs result in a different behaviour at luminosities above the tip of the RGB. The TLF with an η of 0.2 (indicated with light blue bars in Fig 4.3) shows objects in two luminosity bins brighter than the RGB tip. More luminous AGB stars are suppressed due to the used mass-loss prescription, which does not allow for brighter stars at the chosen age of the stellar population. By reducing η to a value of 0.1, the TLF (indicated with green bars) extends one luminosity bin further. Turning off the mass-loss in total by using an η of 0.0 for the calculation of the isochrone and the resulting luminosity function (indicated with orange bars), leads to a full coverage of the bright part of the 2MASS luminosity function of the low metallicity globular cluster combination. The entire AGB of the stellar population is reproduced well, but also showing a slightly higher star count than in the most luminous 2MASS bin. The luminosity function representing no mass-loss at all is the best comparison achieved for the low metallicity group, although this scenario is not realistic, because mass-loss on the AGB is evidently a common concept and is supported by the presence of AGB stars with dust excess along the AGB (cf. Lebzelter et al. 2006)[18]. In addition to the stars from NGC 104[19], the presence of the dusty star NGC 6838 V1 below the mean RGB tip of the low metallicity group proofs that mass-loss occures along the AGB and not only at the tip of the AGB during a superwind.

The reason for the fact, that only YZVAR TLFs with very low mass-loss reach the AGB tip luminosity of the 2MASS data from the low metallicity group can be explained with the used isochrone models. For low mass stars ($0.6 \leq M_{ini} \leq 1.75\,M_\odot$) the calculation of the stellar tracks of the isochrones is stopped at the beginning of the first thermal pulse event. Thus, stars that

---

[17]See Section 2.2.5 for more informations on the mean amplitude of LPVs.
[18]The mass-loss in NGC 104 sets in at $M_K \sim$ -5.5 mag.
[19]Below the mean RGB tip of the low metallicity group, V8, V13, V18 and V21 show MIR dust excess.

become more luminous during the thermal pulse phase are not included in the isochrone and in the derived TLFs. The variation of the η-parameter is carried out using the maximum luminosity of the isochrone at the beginning of the thermal pulse phase. Thus, a higher mass-loss rate could still result in the presence of AGB stars brighter than shown in the YZVAR TLFs presented in this study. Furthermore, the implementation of stellar tracks that include the thermal pulse regime in the YZVAR isochrone models from Bertelli et al. (2008) could help to find well suited TLFs for the comparison with the 2MASS LF of the low metallicity globular cluster combination.

4.2.2 Intermediate Metallicity Group

The TLFs used for a comparison with the 2MASS LFs make use of both available isochrone sets, namely the CMD (Marigo et al. 2008) and the YZVAR (Bertelli et al. 2008) isochrones. The metallicity and the age of the intermediate globular cluster combination are used as input parameters and amount to $Z = 0.0058$ and $12\,\mathrm{Gyrs}$[20], respectively. For the CMD isochrone extraction a initial mass function from Kroupa (1998) is used, while a Salpeter IMF is used for the YZVAR isochrones.

Like in the case of the low metallicity group, two different dust scenarios are used for the CMD TLFs for the intermediate group, namely the silicate-alumina combination from Groenewegen (2006) and the pure silicate scenario from Bressan et al. (1998). The luminosity range for the CMD extraction interface is defined to start at $M_K = -3.07\,\mathrm{mag}$ and, thus, includes the broad luminosity bin used to scale the TLFs to the 2MASS data. Again a bin size of $0.2\,\mathrm{mag}$ is used to match the luminosity bins of the 2MASS LF. The mean star count of the broad bin (33.75 at $M_K = -3.67\,\mathrm{mag}$) is used for the normalisation of the CMD TLFs.

Fig. 4.4 presents the comparison of the 2MASS data of the intermediate metallicity group with the two CMD TLFs based on the two dust scenarios (left panel). The orange bars illustrate the TLF with silictate-alumina dust; the light blue bars the TLF with only silicate dust. Both TLFs do not reach the peak luminosity of the 2MASS LF but cover the 2MASS data well except for the tip of the AGB. From $M_K = -5.5$ to $6.0\,\mathrm{mag}$ the star count is higher in the 2MASS data than in the CMD TLFs. The mismatch at the tip of the AGB (2MASS) with both TLFs could be due to slightly overestimated distances of the globular clusters or an overestimated mass-loss along the AGB considered for the CMD isochrones. However, shorter globular cluster distances would not only lead to a shift of the 2MASS LF to smaller luminosities, but also result in a too bright and improperly positioned mean RGB tip. Taking into account the K-band luminosity amplitude of long period variables of $0.6\,\mathrm{mag}$ (cf. Section 2.2.5), the 12 Gyrs TLFs are still resulting in an encouraging comparison.

---

[20] Marín-Franch et al. (2009) presented a relative age for the globular cluster NGC 6388. For two clusters, namely NGC 6356 and NGC 6760, the mean age of their "old" globular cluster group is adopted. The mean age of the three clusters amounts 11.3 Gyrs. Theoretical luminosity functions with that age do not reach the AGB tip luminosity of the 2MASS data. A 12 Gyrs isochrone results in a luminosity function that comes closer to the respective tip luminosity. For this reason an age of 12 Gyrs is used for the comparison luminosity functions instead of the mean age of the cluster combination, which actually points out that all three clusters are old and a combination is possible. The high uncertainty of the globular cluster ages allows for a more liberal approach for the age settings (cf. Section 3.4).
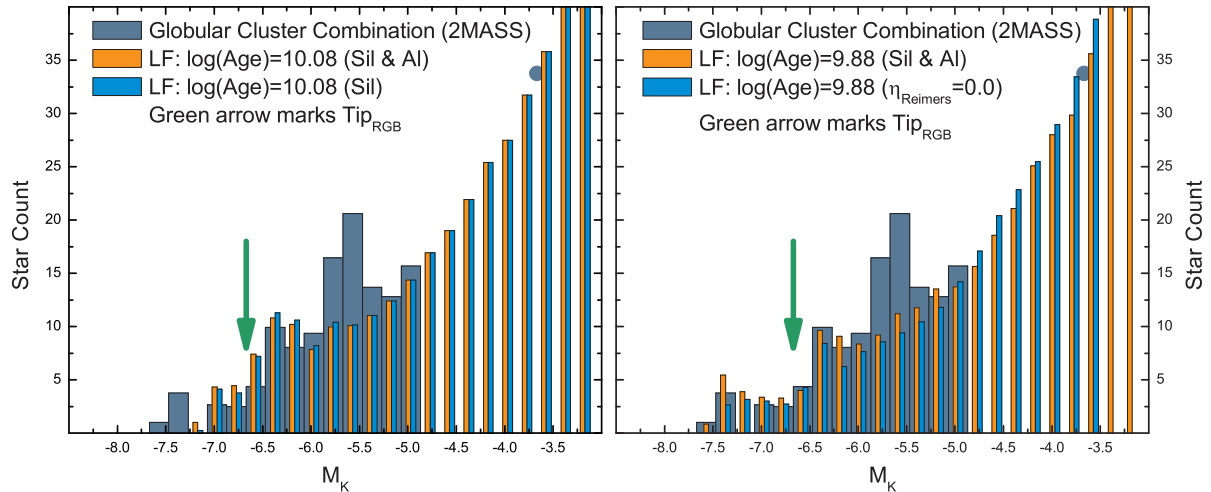
Figure 4.4: Comparison of the 2MASS LF of the intermediate metallicity globular cluster combination with TLFs based on CMD isochrones from Marigo et al. (2008) and YZVAR isochrones from Bertelli et al. (2008) with metallicities of $Z = 0.0058$. The green arrows mark the RGB tip in both panels. Left panel: Only CMD TLFs with an age of 12 Gyrs are overplotted. Orange and light blue bars illustrate the different dust scenarios from Groenewegen (2006) and Bressan et al. (1998). The most lominous part of the 2MASS data is not reproduced. Right panel: Two TLFs based on isochrones with ages of 7.6 Gyrs are compared with the 2MASS data. Both, the CMD TLF (orange) and the YZVAR TLF (light blue) reach the observed AGB tip luminosity.

A better match of the 2MASS LF is achieved using significantly younger ages for the stellar populations. Fig. 4.4 (right panel) presents two TLFs, one from a CMD isochrone with an age of 7.6 Gyrs (orange) and one from a YZVAR isochrone with no mass-loss ($\eta = 0.0$) and again an age of 7.6 Gyrs[21] (light blue). The metallicity is defined as the metallicity of the intermediate globular cluster combination and amounts again to $Z = 0.0058$. Other input parameters are left unchanged compared to the parameter sets used for the TLFs presented in the left panel of Fig. 4.4.

Again the two TLFs are normalised to the star count at $M_K = -3.67$ mag and now almost perfectly cover the entire 2MASS data. Only the high star count around $M_K = -5.5$ to 6.0 mag is again not reproduced. Both TLFs reach the same peak luminosity even though they have very different perscriptions of the mass-loss on the AGB. While the CMD TLF is based on the standard scenario from Marigo et al. (2008), the YZVAR TLF suppresses any mass-loss at all.

It is important to note, that NGC 6388 is reported to host two stellar populations. However the most luminous part of the 2MASS LF is occupied by stars from the other two globular clusters. Therefore an explanation of the mismatch with the 12 Gyrs TLFs due to a younger stellar population present in one of the clusters and manifesting in the 2MASS data is not convenient.

---

[21] Note that a YZVAR TLF with an age of 12 Gyrs is not able to reach the peak luminosity of the AGB tip, even when using an $\eta = 0$ to totally switch off the mass-loss along the AGB.

4.2.3 High Metallicity Group

The 2MASS LF of the high metallicity group is compared with two TLFs based on CMD isochrones only[22]. Both isochrones have the same input parameters for age, metallicity and initial mass function. For the latter the binary corrected IMF from Kroupa (1998) is used. The age is set to 11.2 Gyrs, which is the mean age of the three members of the high metallicity globular cluster combination. The input metallicity is the mean metallicity of the group amounting to $Z = 0.01$. The 2MASS $[JHKs]$ photometric system is chosen for the TLF output of the CMD interface. The luminosity range starts at $M_K = $ -3.03 mag and includes the broad luminosity bin from the 2MASS LF used for mounting the TLFs. The star count of the respective bin amounts to 50.25 at the centered $M_K = $ -3.83 mag and is used for the normalisation of the TLFs to the 2MASS data. A 0.2 mag bin size for the CMD extraction procedure ensures matching luminosity bins of both, the observed and the two TLFs.

Two different dust scenarios are adopted according to the scenarios used for the low and the intermediate metallicity groups. Fig. 4.5 presents the 2MASS LF of the high metallicity globular cluster combination and the two comparison TLFs from the CMD. The Groenewegen (2006) dust scenario with both silicate and alumina dust is illustrated with orange color; the pure silicate dust scenario from Bressan et al. (1998) is illustrated with the light blue color. Both luminosity functions cover the 2MASS LF well up to a brightness of $M_K = $ -7.5 mag and only show a slightly different star count with respect to the dust prescription at the two top luminosity bins. The mean RGB tip of the high metallicity group (derived after Bellazzini et al. (2004), indicated with a green arrow) exactly matches the RGB tip of the two CMD TLFs. No over abundance of the central part of the 2MASS star count compared with the CMD star count is apparent in the high metallicity group.

The most luminous parts of the 2MASS LF are not covered with the two theoretical versions which reach their maximum AGB tip luminosity at -7.5 mag. All stars brighter than this theoretical AGB tip and, thus, occupying the bright luminosity bins of the observed data are from the globular cluster Terzan 5. This cluster is reported to host two distinguished stellar populations. One with an age of the "old" cluster group from Marín-Franch et al. (2009) (11.2 Gyrs) and one with an age of approximately 6 Gyrs (cf. Section 2.2.6 and Ferraro et al. 2009).

Indeed, TLFs with significantly younger ages than assumed for the "old" clusters result in AGB tip luminosities comparable to the detected 2MASS luminosities of $M_K \sim $ -8 mag. Even when using isochrones and TLFs from the CMD interface with ages less then 5 Gyrs[23] it is still not possible to derive sufficiently bright AGB tip luminosities to cover the brightest stars with $M_K \sim $ -8.5 mag.

Also the use of YZVAR isochrones with different mass-loss rates does not result in TLFs that reach the most luminous bins of the 2MASS luminosity functions.

---

[22]TLFs based on YZVAR isochrones are not able to reach the bright part of the 2MASS LF. Therefore they are not used for a comparison with the high metallicity globular cluster combination. Note that the lack of bright AGB stars in the YZVAR TLFs is due to the neglection of the thermal pulse phase in the isochrone model.

[23]Note that this is already 1 Gyr younger than the age of the young population of Terzan 5 presented by Ferraro et al. (2009).
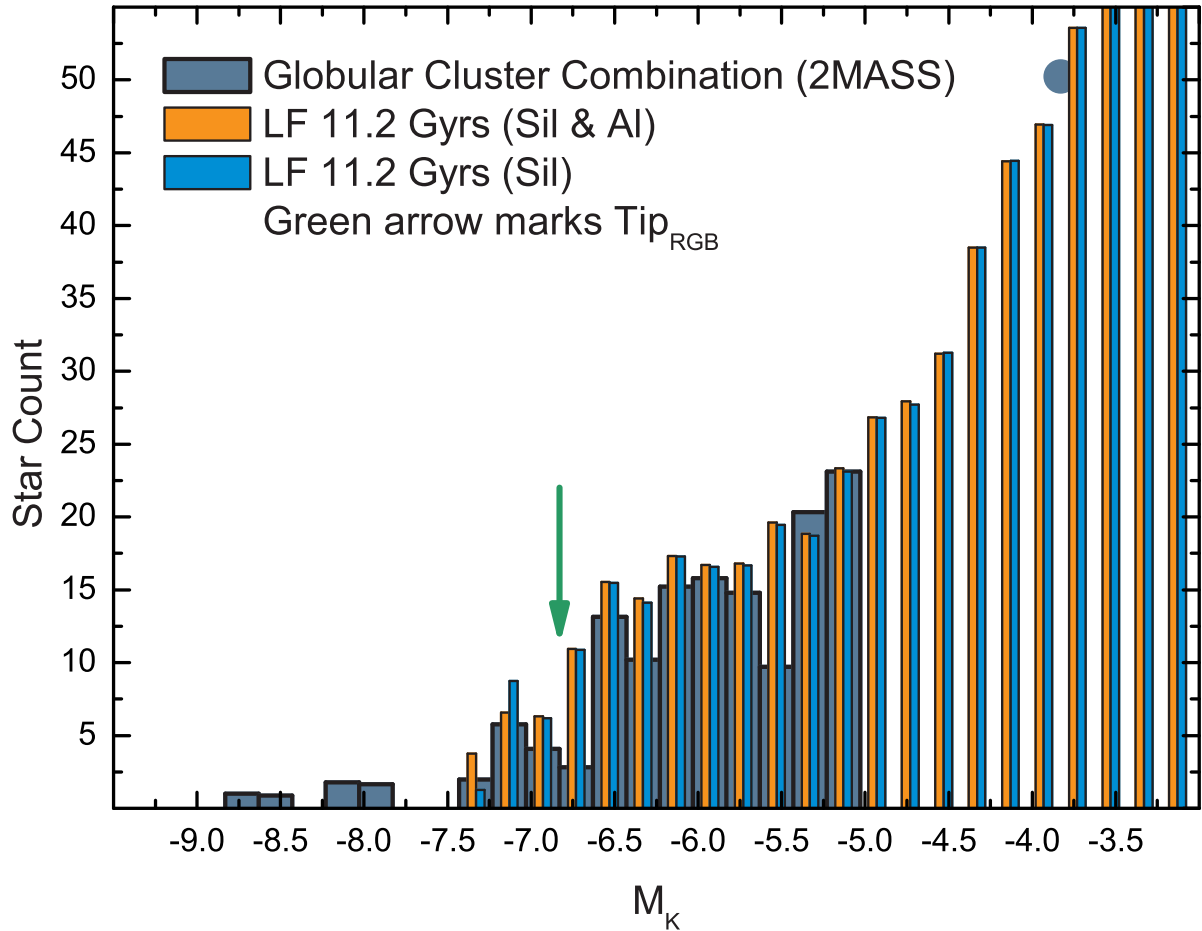
Figure 4.5: Comparison of the 2MASS LF of the high metallicity globular cluster combination with two TLFs based on CMD isochrones from Marigo et al. (2008) with metallicities of $Z = 0.01$ and ages of 11.2 Gyrs. The different dust scenarios are indicated with orange color (Groenewegen (2006)) and light blue color (Bressan et al. (1998)). The RGB tip is marked with a green arrow. The luminous part not covered with the TLFs is assembled by stars from Terzan 5 and possible can be attributed to a young stellar population.

4.2.4 TLF Summery

Three globular cluster combinations were compared to different TLFs based on CMD and YZVAR isochrones from Marigo et al. (2008) and Bertelli et al. (2008), respectively.

The 2MASS LF of the low metallicity group ($Z = 0.0038$) could not be reproduced using CMD TLFs with different dust scenarios and an age of the cluster combination amounting to 12 Gyrs. The best comparison was achieved with YZVAR TLFs with very low and even no mass lass along the AGB and an age of 12 Gyrs.

The intermediate metallicity group ($Z = 0.0058$) was best reproduced using either a CMD or a YZVAR TLF with a significant younger age (7.6 Gyrs) than the mean age of the cluster combination. TLFs with the proper age of the group (12 Gyrs) were not able to reach the most luminous parts of the 2MASS LF.

For the high metallicity group ($Z = 0.01$) the 2MASS data were compared to CMD TLFs with the mean age of the cluster combination (11.2 Gyrs) which covered the main part of the observed LF well but could not reach the brightest luminosity bins. YZVAR isochrones were not used in case of the high metallicty group, because they did not cover the respective 2MASS LF well.

In Chapter 5 the three 2MASS LFs are used for the calculation of co-added MIR-spectra of the three globular cluster combinations. For the low metallicity group also the YZVAR TLF with no mass-loss is used to generate a MIR-spectrum. For the intermediate and the high metallicity groups only the respective 2MASS LFs are used to derive the MIR-spectra, since none of the TLFs studied here resulted in an adequate comparison.

Chapter 5

The co-added MIR-Spectrum of Globular Cluster Combinations

This chapter introduces the co-added MIR-spectra of the low, intermediate and high metallicity globular cluster combinations. The spectra were derived using a weighting function based on the 2MASS LFs for all three metallicity groups. In addition an integrated spectrum of the low metallicity group based on a TLF from Bertelli et al. (2008) is presented. Within the low metallicity group the MIR-spectrum of the globular cluster NGC 104 is also investigated separately to allow for a comparison with the results from Bressan et al. (2007). A comparison of the co-added MIR-spectra and dust residuals from all three metallicity groups is shown in 5.4 to improve the understanding of metallicity effects on the MIR-spectra.

5.1 The MIR-Spectrum of the Low Metallicity Group

To interpret the MIR dust excess present in old unresolved stellar populations (e.g. globular clusters, early-type galaxies) it is important to understand the integrated MIR-spectrum of such stellar systems. As the main stellar dust producers, AGB stars have a major impact on the MIR-spectrum. Thus, a study of the co-added AGB star spectra of various globular clusters will help to improve our knowledge on the MIR characteristics of old stellar populations.

In order to produce a co-added MIR-spectrum of the low metallicity globular cluster combination based on the available MIR-spectra of the group, the individual spectra are not simply added together nor are they combined using the arithmetic mean of all spectra. Instead LFs based on 2MASS data and theoretical isochrones are used to weight the spectra. Therefore each AGB star spectrum is given in absolute and dereddened flux in Jansky to allow for a proper combination (cf. Chapter 2) and assigned to the respective luminosity bin of the LFs using the stars' M_K-values. This allows for a weighting with the star counts of the luminosity bins given by the LFs. The procedure relies on the assumption that stars that occupy the same area in

Table 5.1: Weighting: Low Metallicity Group - 2MASS LF & Isochrone TLF

Bin	Bin Center $[M_K]^a$	Star Count 2MASS LF^a	Isochrone TLF^b	N_{spec}^c	ID_{spec}^d
1	-7.26	1.75	3.88	–	–
2	-7.06	4.00	3.54	3	IC 1276 V3 NGC 6637 V4 NGC 6637 V5
3	-6.86	5.00	3.40	3	NGC 104 V1 NGC 104 V2 NGC 104 V3
4	-6.66	4.00	2.79	3	IC 1276 V1 NGC 104 V4 NGC 6352 V5
5	-6.46	10.44	9.39	3	NGC 104 V8 NGC 104 V11 NGC 104 V21
6	-6.26	8.39	9.21	2	NGC 104 V7 NGC 6838 V1
7	-6.06	14.88	7.51	–	–
8	-5.86	13.75	9.41	2	NGC 104 V5 NGC 104 V6
9	-5.66	15.08	10.99	1	NGC 104 V18
10	-5.46	7.31	12.35	1	NGC 104 V13

^{a} The *bin center* and the 2MASS *star count* are taken from the 2MASS LF presented in Fig. 3.9.
^{b} The Isochrone *star count* makes use of the same bins as the 2MASS *star count* and is taken from the TLF with $\eta = 0$ presented in Fig. 4.3. Note that there is an additional luminosity bin in the TLF centered at $M_K = $ -7.46 with a star count of 0.99.
^{c} N_{spec} defines the number of available MIR-spectra observed with *Spitzer*.
^{d} ID_{spec} presents the AGB stars with an observed MIR-spectrum for the respective luminosity bin.

the Color-Magnitude diagram (cf. Fig. 3.8) and, thus, fall in the same luminosity bin of the LFs describing the low metallicity group, are of similar mass and age and have similar MIR-spectra.

Table 5.1 presents the star counts of the luminosity bins of both the 2MASS LF of the low metallicity group and the TLF based on an isochrone from Bertelli et al. (2008) used for the weighting of the individal MIR-spectra of the globular cluster AGB stars of the group. Also the number of available MIR-spectra for each bin, together with the ID of the respective AGB star that was observed by *Spitzer* is shown.

Apparently the 2MASS LF is well covered with *Spitzer* spectra of individual AGB stars as can be seen in Table 5.1. Only two luminosity bins are empty, which means that no star with an observed MIR-spectrum falls into the respective bin when assigning the M_K-values of the stars. The other luminosity bins are occupied by up to three individual spectra. For the calculation

of the co-added MIR-spectrum of the entire stellar population a mean spectrum for each bin is needed. Therefore the mean spectra for bins with multiple spectra are derived using the arithmetic mean of the available individual MIR-spectra.

To retrieve a mean spectrum for each of the two bins with no observed *Spitzer* spectra, the mean spectra of the adjacent bins of lower luminosity were transfered to the respective empty bin. The stars in the most luminous bin (*Bin 1* in Table 5.1) are adopted to show the same spectral characteristics as the stars in *Bin 2*[1]. Thus, the mean spectrum of the second bin will be used for the brightest bin. However, the mean spectrum of *Bin 2* has a flux level adequate to the M_K of the bin. Applying this mean spectrum to *Bin 1* of the 2MASS LF would result in an underestimated MIR-flux of the stars occupying the brightest bin. To overcome this problem, the flux level of the MIR-spectrum of *Bin 2* is converted to the flux level appropriate to *Bin 1* using Equation 5.1. The difference in luminosity between two adjacent bins in our 2MASS LF amounts to $M_K = 0.2$ mag. Thus, the flux of the MIR-spectrum of the bin of lower luminosity is divided by $10^{-0.08}$ to recieve the flux values of the MIR-spectrum of the brighter luminosity bin. The same procedure applies to *Bin 7* which also hosts no stars with observed MIR-spectra. Thus, the mean spectrum of *Bin 8* (derived using the arithmetic mean of the two available spectra) is transfered to the adjacent empty bin by using Equation 5.1 to convert the flux values.

$$\left.\begin{array}{l} \mathrm{Bin}_x \\ \mathrm{Bin}_{x+1} \end{array}\right\} \quad M_{\mathrm{Bin}_{x+1}} - M_{\mathrm{Bin}_x} = -2.5\log\frac{F_{\mathrm{Bin}_{x+1}}}{F_{\mathrm{Bin}_x}} = 0.2 \Rightarrow F_{\mathrm{Bin}_{x+1}} = F_{\mathrm{Bin}_x} \cdot 10^{-\frac{0.2}{2.5}} \qquad (5.1)$$

Once all bins of the 2MASS LF are equipped with a mean MIR-spectrum, the spectra are weighted with the number of stars present in the respective luminosity bins. The star counts used for the weighting are given in Table 5.1. For example, *Bin 4* includes four stars in the 2MASS LF where three stars, namely IC 1276 V1, NGC 104 V4 and NGC 6352 V5 have observed *Spitzer* spectra. The mean spectrum for this bin is derived from these three spectra using the arithmetic mean. The resulting mean spectrum is multiplied by four to account for all the stars present in the luminosity bin. This is performed for each luminosity bin and results in a weighted mean MIR-spectrum for each bin of the 2MASS LF. By adding all these spectra together the co-added MIR-spectrum for the low metallicity globular cluster combination is derived.

Fig. 5.1 presents the co-added MIR-spectrum of the low metallicty group based on the 2MASS LF together with the co-added MIR-spectrum derived by using different star counts to weight the spectra based on the isochrone TLF with $\eta = 0.0$ (cf. Section 4.2.1). The weighting is done in the same way as for the 2MASS LF star counts. However, an additional luminosity bin is present in the TLF with a bin center at $M_K = -7.46$ and a star count of 0.99. Thus, the mean spectrum from *Bin 2* is not only transfered to *Bin 1* of the TLF, but also to the additional and most luminous bin not presented in Table 5.1. The flux conversion is done again using Equation 5.1. In addition a co-added MIR-spectrum weighted with the 2MASS LF is presented that is adopting a different mean spectrum for *Bin 9* which is occupied by the star NGC 104 V18.

---

[1] Again, this relies on the assumption that stars that occupy the same area in the LF show similar MIR-spectra due to alike ages and masses.
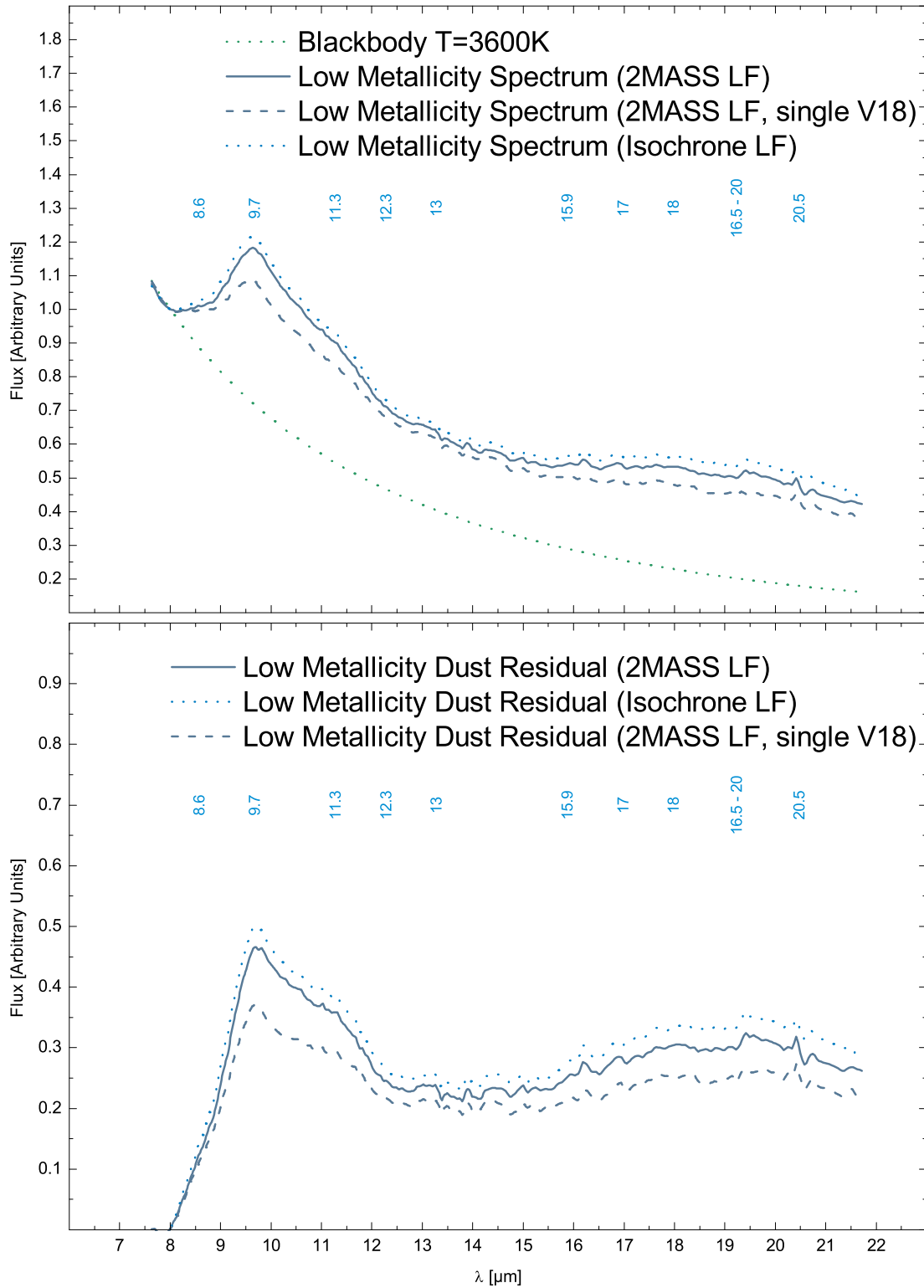
Figure 5.1: Co-added MIR-spectra (upper panel) and dust residuals (lower panel) of the low metallicity globular cluster combination based on the 2MASS LF and an isochrone TLF. Possible dust feature positions are indicated.

NGC 104 V18 shows a prominent 9.7 μm silicate feature and a broad bump around 18 μm. The star is thought to currently undergo a thermal pulse event which results in an interpulse luminosity which is lower than the star's average luminosity (Lebzelter et al. 2006). This low luminosity leads to an unusual position in the Color-Magnitude diagram and in the LF describing the globular cluster combination. The time between two concecutive thermal pulses is long ($\approx 8 \cdot 10^5$yrs) compared to the duration of the pulse itself (20-30% of the pulse cycle), therefore the probability of observing an AGB star during a thermal pulse is low (Vassiliadis & Wood 1993). Thus, the luminosity bin that is occupied by NGC 104 V18 includes a large number of stars that probably are not all undergoing a thermal pulse event and hence are not likely to show the same prominent silicate dust excess. The alternative weighting is performed by adopting only a single star of *Bin 9* to show a MIR-spectrum like NGC 104 V18. The other stars occupying the bin are expected to show spectra comparable to the dust free stars of the adjacent *Bin 8* (NGC 104 V5 & V6). Hence, the mean MIR-spectrum of *Bin 9* is not showing the same strong silicate emission as in the case of the other weighting processes described above.

The upper panel of Fig. 5.1 shows the three co-added MIR-spectra derived using star counts of the 2MASS LF (one with a full impact of NGC 104 V18, one with the alternative approach) and the TLF normalized to the flux at 8 μm together with a blackbody with a temperature of 3600 K. This temperature is used as the mean star temperature of the AGB population of the globular cluster combination and is in good agreement with the temperature adopted by Sloan et al. (2010). The blackbody is used to subtract the stellar photosphere from the co-added MIR-spectra and is also normalized to the 8 μm flux. The lower panel of Fig. 5.1 presents the dust residuals after the blackbody subtraction.

The spectra and the dust residuals are shown only from 7.4 to 21.3 μm. This is the wavelength range of the MIR-spectra available for the globular cluster NGC 104, which was only observed in two of the four *IRS* modules on board the *Spitzer* satellite (cf. Lebzelter et al. 2006). The stars from the other four clusters that are part of the low metallicity group where observed in all four modules (Sloan et al. 2010), but the additional *IRS* modules (SL2 and LL1, cf. Section 2.4) are neglected to maintain consistency in the co-added MIR-spectrum.

The co-added MIR-spectra and dust residuals of the low metallicity globular cluster combination are dominated by the the strong silicate dust emission at 9.7 and 16-20 μm[2]. Also a bump at 11.3 μm due to alumina dust is apparent. The different flux levels of the three spectra and dust residuals arise on behalf of the three different weighting processes based on the 2MASS LF (Fig. 3.9), the TLF (Fig. 4.3) and the alternative weighting with a single NGC 104 V18 spectrum in *Bin 9*.

The TLF includes more stars around the tip of the AGB and an additional bin at $M_K = $-7.46. This results in an increased overall flux of the co-added MIR-spectrum based on the TLF star counts (blue dotted lines in Fig. 5.1) because the most luminous AGB stars that were observed with *Spitzer* (IC 1276 V3, NGC 6637 V4, NGC 104 V1 & V2) gain more influence. On the other hand, the TLF contains fewer stars around $M_K = $-5.50 to -6.25 mag than the 2MASS LF. This leads to a weaker impact of the lower luminosity AGB stars which show less silicate and more alumina dust, or are even dust-free. The more influence is given to the dust-free MIR-spectra

---

[2]Possible dust feature positions are indicated in both panels. The corresponding dust species are presented in Table 2.9.

in the weighting process, the more the overall flux of the co-added spectrum is reduced. This effect becomes even more important in the weighting scenario using only a single NGC 104 V18 spectrum in *Bin 9* (dashed lines in Fig. 5.1). The silicate dust emission at 9.7 and 16-20 μm is reduced together with the overall MIR dust emission pointing to the fact that weighting the spectrum of NGC 104 V18 with a large star number (cf. solid line in Fig. 5.1) leads to a major impact on the resulting co-added MIR-spectrum of the entire stellar population resulting in a 37% higher 9.7 μm-flux compared to the co-added MIR-spectrum based on the alternative approach with only a single V18-like star present[3].

In all three versions of the co-added MIR-spectrum and the respective dust residuals the 13 μm feature present in V4, V8 and V13 from the globular cluster NGC 104 can not be detected because it is overwhelmed by the strong silicate features.

5.1.1 NGC 104

To investigate the co-added MIR-spectra of the globular cluster NGC 104 in detail and to allow for a comparison with the results from Bressan et al. (2007), the cluster is treated also separately here. The twelve available AGB star spectra are weighted in two alternative ways to produce two different co-added spectra representing the cluster.

The first approach is the same as for the hole low metallicity group. The 2MASS LF of NGC 104 (presented in Fig. 3.2) is used to weight the individual MIR-spectra. Table 5.2 presents the star counts, the number of available spectra and the ID of the observed stars per luminosity bin. The globular cluster LF includes two bins where no MIR-spectra have been observed (*Bin 1* and *Bin 6*). Again the mean spectrum of the adjacent luminosity bins are transfered to the empty bins[4] using the flux conversion given in Equation 5.1[5].

The second approach accounts for the interrelation of stellar variability and mass-loss and uses a different dataset to weight the MIR-spectra. Lebzelter & Wood (2005) presented a sample of 42 long period variables (LPVs) hosted by the globular cluster NGC 104. Using these stars, a Color-Magnitude diagram is generated (see Fig. 5.2, left panel) that consists only of LPVs[6]. From this diagram it is possible to derive a LF describing the LPV population in the cluster (see Fig. 5.2, right panel) by applying the same bin sizes and centers as in Section 3.2.1. The AGB stars with observed *Spitzer* spectrum are assigned to the respective luminosity bins with respect to the M_K-values presented in Table 1 of Lebzelter & Wood (2005). This leads to a slightly different distribution of the available MIR-spectra over the LPV LF (see Table 5.2 for the star counts and the distribution of the spectra). Now, three luminosity bins do not include an observed MIR-spectrum[7]. Thus, the mean spectrum of the adjacent bin with lower luminosity is transfered and converted as described above to provide spectra for *Bin 7* while for *Bin 6* the mean spectrum from *Bin 5* is used.

---

[3] We note that totally omitting the peculiar star NGC 104 V18 would result in a minor drop ($\sim$5%) of the flux level of the co-added MIR-spectrum and dust residual of the low metallicity group when compared to the flux level obtained by assuming the presence of a single V18-like star in *Bin 9*.

[4] *Bin 1* is accoutred with the mean spectrum from *Bin 2*, *Bin 6* with the mean spectrum of *Bin 7*.

[5] The alternative weighting of the 2MASS LF using only a single V18-like star in *Bin 8* is discussed later in this section.

[6] The AGB star LW13 is not used in the Color-Magnitude diagram due to its ambiguous luminosity. In the 2MASS data this star can not be distinguished from a close companion.

[7] *Bin 3* does not include any star at all and therefore is negelected.

Table 5.2: Weighting: NGC 104 - 2MASS LF & Variables LF

Bin	Bin Center $[M_K]^a$	2MASS LF				Variables LF			
		Star Count^a		$N_{spec}{}^c$	$ID_{spec}{}^d$	Star Count^b		$N_{spec}{}^c$	$ID_{spec}{}^d$
1	-7.06	1	$\approx 1.8\%$	–	–	1	$\approx 2.4\%$	1	V1
2	-6.86	4	$\approx 7.3\%$	3	V1 V2 V3	3	$\approx 7.3\%$	2	V2 V3
3	-6.66	1	$\approx 1.8\%$	1	V4	–	–	–	–
4	-6.46	7	$\approx 12.7\%$	3	V8 V11 V21	8	$\approx 19.5\%$	4	V4 V8 V11 V21
5	-6.26	6	$\approx 10.9\%$	1	V7	5	$\approx 12.2\%$	1	V7
6	-6.06	9	$\approx 16.4\%$	–	–	10	$\approx 24.4\%$	–	–
7	-5.86	12	$\approx 21.8\%$	2	V5 V6	8	$\approx 19.5\%$	–	–
8	-5.66	12	$\approx 21.8\%$	1	V18	5	$\approx 12.2\%$	3	V5 V6 V18
9	-5.46	3	$\approx 5.5\%$	1	V13	1	$\approx 2.4\%$	1	V13

^{a} The *bin center* and the 2MASS *star count* are taken from the 2MASS LF presented in Fig. 3.2.
^{b} The variables *star count* makes use of the same bins as the 2MASS star count and is taken from variables LF presented in Fig. 5.2 (right panel).
^{c} N_{spec} defines the number of available MIR-spectra observed with *Spitzer*.
^{d} ID_{spec} presents the AGB stars of NGC 104 with a MIR-spectrum for the respective luminosity bin.

Both methods result in a co-added MIR-spectrum representing the globular cluster NGC 104. Fig. 5.3 presents the two spectra together with the co-added spectra of the low metallicity group (weighted with the 2MASS data) and the mean spectrum of NGC 104 (not weighted). Again the spectra are normalized to the flux at $8\,\mu$m. A blackbody of $T = 3600\,$K is mounted at the same flux for the subtraction of the stellar photosphere. The lower panel of Fig. 5.3 shows the resulting dust residuals.

The co-added spectra of NGC 104 are all dominated by the strong silicate dust emission at 9.7 and 16-20 μm. The shapes of the four spectra and dust residuals plotted in Fig. 5.3 do not differ a lot. The low metallicity group spectrum (dark blue) shows the highest dust excess at 9.7 μm and has a higher flux level around the prominent 16-20 μm bump. The spectrum of NGC 104 weighted with the 2MASS LF (light blue) has the same slope but a lower overall flux level. Also the spectrum of NGC 104 that was not weighted at all (orange) shows a comparable flux level and slope. Only the flux around 12 to 15 μm is slightly higher in the unweighted version. The spectrum weighted with the LPV LF (red) shows a significantly lower flux level as the other two co-added NGC 104 MIR-spectra but is also dominated by the prominent silicate dust
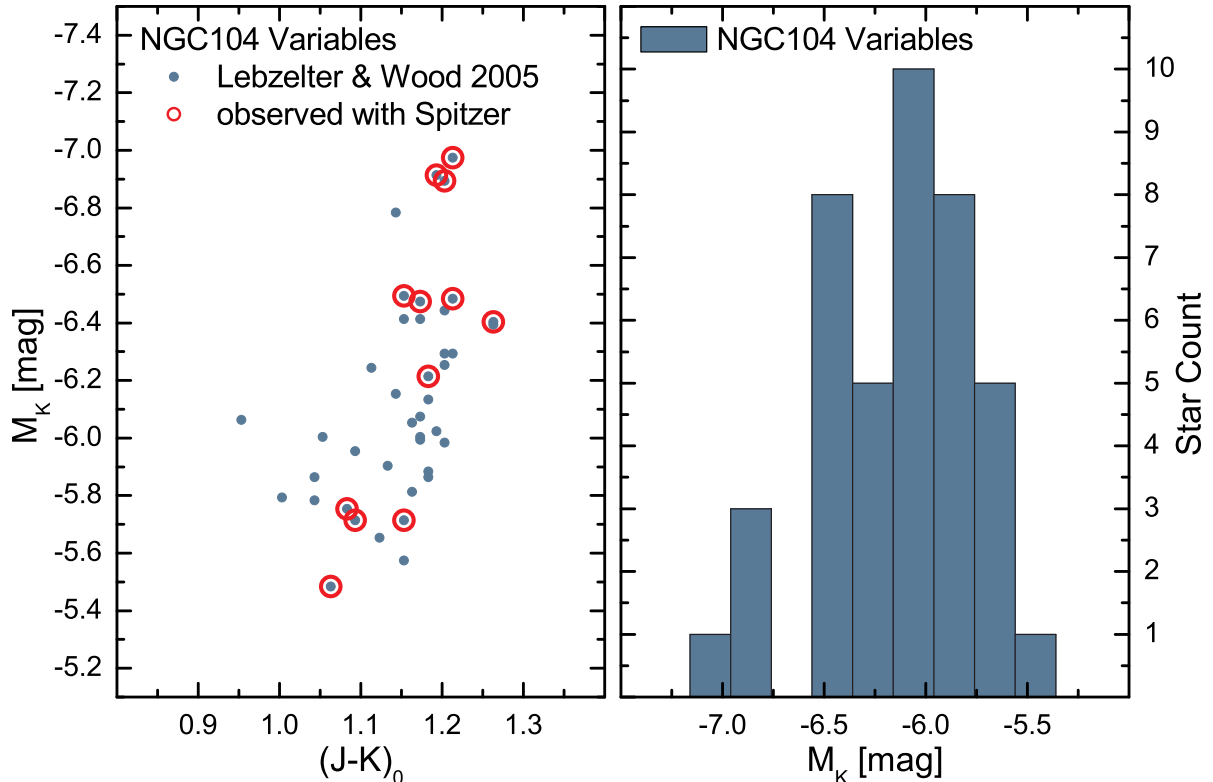
Figure 5.2: Left panel: Color-Magnitude diagram of the LPV population in the globular cluster NGC 104 (cf. Lebzelter & Wood 2005). Stars with observed MIR-spectrum are marked with red symbols. Right panel: Luminosity function based on the Color-Magnitude diagram.

emission although the overall slope is slightly more flattened. All spectra and hence all dust residuals show a bump at $11.3\,\mu$m due to alumina dust.

The co-added and unweighted spectrum of NGC 104 resembles the co-added and unweighted spectra presented by Bressan et al. (2007) (cf. *line a* in Fig. 1.6 in Chapter 1). The two approaches for weighting the MIR-spectrum with the 2MASS LF and the LPV LF are not able to produce a co-added spectra that is not dominated by the peaks at 9.7 and 16-20 μm. Each resulting MIR-spectrum shows the decreasing flux level around 12 to 15 μm. The flat dust excess presented by Bressan et al. (2007) according to *line b* in Fig. 1.6 is not reproduced by any of the presented approaches. This flat dust excess is derived by weighting the MIR-spectra with the number of LPVs from Lebzelter & Wood (2005) with respect to their position in the Period-Luminosity diagram. This points out, that the method of weighting the MIR-spectra has a crucial effect on the shape of the resulting co-added MIR-spectra describing an entire stellar population.

To investigate this effect further, another weighting-approach is performed in this study. By cutting off the used LFs at the luminosity of the faintest star that was observed by Sloan et al. (2010) a new subsample is generated for the weighting processes to estimate the importance of the MIR-spectra of faint AGB stars on the co-added MIR-spectrum.
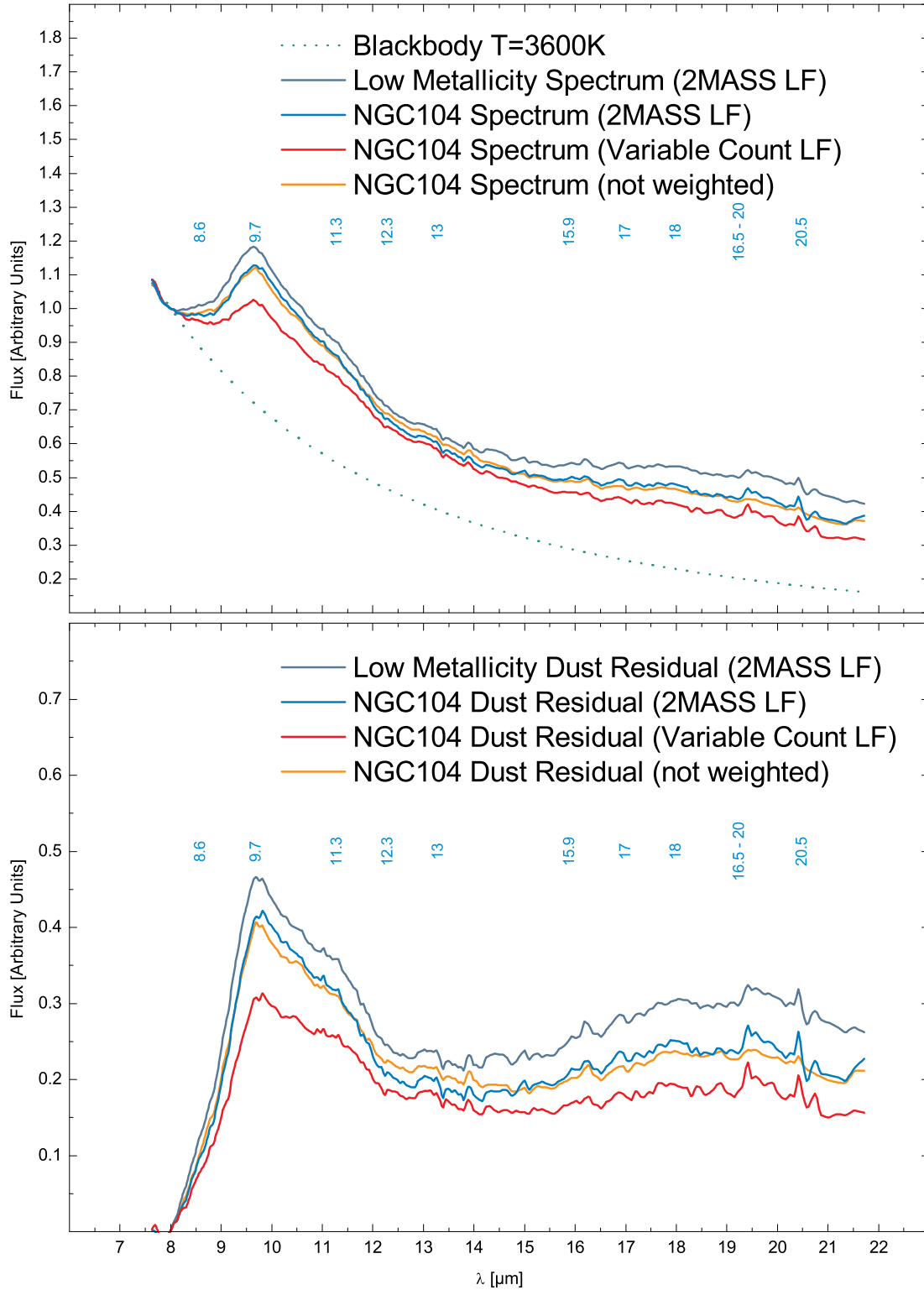
Figure 5.3: Comparison of the co-added MIR-spectra (upper panel) and dust residuals (lower panel) of the globular cluster NGC 104 based on different weigthing methods with the co-added spectrum of the low metallicity group weighted with the respective 2MASS LF. Possible dust feature positions are indicated.
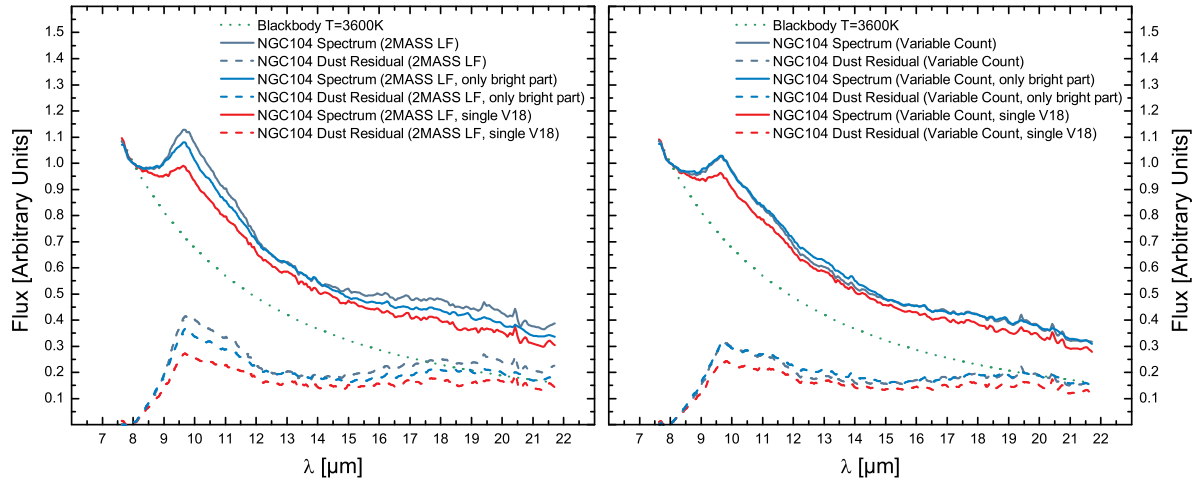
Figure 5.4: Co-added MIR-spectra and dust residuals of NGC 104. Left panel: Comparison of the results obtained using a 2MASS LF including all stars (dark blue), only the bright part of the LF (light blue) and the alternative weighting method with a single V18-like star. The latter method results in a flat MIR dust excess (see text for details). Right panel: Same comparison but with an underlying LF based on the LPVs present in the cluster. Here, the entire and the bright part of the LPV LF lead to similar MIR-spectra and dust residuals. The alternative weighting method again results in a flat dust excess.

The M_K-limit is defined to be at -6.26 mag, thus, all stars from NGC 104 below this border brightness are dismissed. The stars sorted out this way are V5, V6, V13 and V18. With this method only the five most luminous bins in the LFs describing the globular cluster are accounted for during the calculation of the co-added MIR-spectrum, which is performed in the same way as described for the low metallicity globular cluster combination. In addition, co-added MIR-spectra of NGC 104 are derived using the alternative weighting procedure adopting only a single V18-like AGB star in the entire sample for both the 2MASS LF and the LPV LF approaches.

Fig. 5.4 (left panel) presents the co-added MIR-spectrum of NGC 104 weighted with the entire 2MASS LF from Fig. 3.2 (dark blue) together with the co-added spectrum based on the new method only including the top five luminosity bins (light blue). The results from the single V18-weighting are illustrated with red color. A blackbody with a temperature of 3600 K is used to subtract the photosphere and to derive the co-added dust residual (dashed lines). Again both the spectrum and the dust residual derived using the entire 2MASS LF and the top five bins are dominated by the silicate dust emission. The excess at 9.7 and 16-20 μm is weaker in the case of the weighting based on only the bright bins of the LF. This emphasizes the effect of the consideration of V18 when calculating a co-added spectrum which leads to stronger silicate features when the MIR-spectrum of V18 is adopted for all stars in the respective luminosity bin. Skipping the low luminosity bins and, thus, dismissing *Bin 8* with V18 leads to the reduced silicate domination of the dust excess.

The silicate dust features become even weaker when the entire 2MASS LF is used for the weighting but the spectrum of the peculiar star V18 is considered only for one single star in the

respective luminosity bin. This approach is the same as the one applied for the low metallicity group and results in a rather flat integrated dust excess of NGC 104. This excess is comparable to the flat dust emission derived by Bressan et al. (2007) (cf. *line b* in Fig. 1.6).

Applying the method of cutting off the lower part of the LF to the LPV LF presented in Fig. 5.2 results in a similar co-added MIR-spectrum as in the case of considering the entire LPV LF for the weighting. Again the top five luminosity bins are used to weight the individual AGB star spectra with the LPV star count. Fig. 5.4 (right panel) shows the co-added spectrum based on the entire LPV LF (dark blue) together with the spectrum derived by only using the bright part of the LF and, thus, only the observed MIR-spectra of the respective bright AGB stars (light blue). Again a 3600 K blackbody is used for the calculation of the co-added dust residuals. Both methods lead to an identical dust emission at 9.7 and 16-20 μm. Only at 12-15 μm the flux is slightly higher in the case of the cutted LPV LF. Again the alternative weighting method that considers only a single star in *Bin 8* to show a spectrum like V18 is included in the right panel of Fig. 5.4. To derive this co-added MIR-spectrum (red solid line) and the corresponding dust residual (red dashed line) the mean MIR-spectrum of *Bin 8* is computed with respect to the LPV star count from Table 5.2 by adopting four stars to show dust free spectra (V5 & V6) and one star to show a silicate-dominated spectrum (V18). This mean spectrum is also transfered to the 'empty' *Bin 7*. The results are similar to the co-added MIR-spectrum and the respective dust residual derived with the 2MASS LF and the same weighting approach. Again a flat dust excess is retrieved that is comparable to the results of Bressan et al. (2007) (cf. *line b* in Fig. 1.6).

The flux difference between the two dust excesses derived with the 2MASS LF and the LPV LF amounts to ∼10% at 9.7 and ∼5% at 19.5 μm, respectively, when weighting the MIR-spectrum of V18 with only one star. No flux difference can be detected around 12-15 μm.

We conclude that the weighting using a 2MASS LF can be used to derive a co-added MIR-spectrum of an old stellar population and, thus, it is not obliged to know the entire LPV population of the respective stellar system like it is the case for NGC 104.

However, it is important not to simply weight the available MIR-spectra, but to carefully look at each star and its characteristics. The case of V18 might be relatively common, although it is of a low probability to observe a star in its interpulse low luminosity (Vassiliadis & Wood 1993). There is a second case to NGC 104's V18 reported in the literature, where Lebzelter & Wood (2007) detected two carbon-rich stars in the globular cluster NGC 1846 that also are observed at a very low luminosity which was explained with the occurance of thermal pulse events. The presence of interpulse AGB stars in globular clusters could be a common phenomenon that was not discussed before because of the lack of observations of low luminosity AGB stars in such stellar systems.

The difference between well weighted co-added MIR-spectra based on either a 2MASS LF or on a LPV LF is small, leading to an encouraging possibility for interpreting the MIR dust properties of globular clusters and other old stellar populations in general.

5.2 The MIR-Spectrum of the Intermediate Metallicity Group

The co-added MIR-spectrum of the intermediate metallicity globular cluster combination is derived using the 2MASS LF presented in Section 3.4.3 (cf. Fig. 3.11). The TLFs based on isochrones from Marigo et al. (2008) and Bertelli et al. (2008) are not used due to the fact that no satisfying match with the 2MASS data has been achieved considering the proper main input parameters such as age and metallicity (cf. Section 4.2.2).

The eight AGB stars with observed *Spitzer* spectra are assigned to the 2MASS LF according to their M_K luminosity. Table 5.3 presents the details of the 2MASS LF including the star count, the number of observed MIR-spectra and the respective AGB star ID for each bin of the LF[8]. Due to the fact that the intermediate metallicity group contains only the stars observed by Sloan et al. (2010) the luminosity range used for the calculation of the co-added MIR-spectrum of the group is significantly smaller than in the low metallicity case. Only one of the observed stars, namely NGC 6388 V3, is positioned below the tip of the RGB. Thus, the derived co-added spectrum reflects only the brightest part of the stellar population described by the intermediate metallicity globular cluster combination.

The most luminous bin of the 2MASS LF is not occupied with an observed AGB star and relies on the transfer of an adjacent mean MIR-spectrum. Therefore *Bin 1* is accoutred with the mean spectrum from *Bin 2* with consideration of the required flux shift derived with Equation 5.1. Just like for the low metallicity case, each mean MIR-spectrum is weighted with the star counts of the respective luminosity bins of the 2MASS LF. Subsequently the weighted spectra are co-added to derive the overall MIR-spectrum describing the intermediate metallicity group.

Table 5.3: Weighting: Intermediate Metallicity Group - 2MASS LF

Bin	Bin Center $[M_K]^a$	2MASS Star Count^a	$N_{spec}{}^b$	$ID_{spec}{}^b$
1	-7.57	1.00	–	–
2	-7.37	3.75	3	NGC 6356 V1 NGC 6356 V5 NGC 6760 V3
3	-7.17	–	–	–
4	-6.97	2.65	3	NGC 6356 V3 NGC 6356 V4 NGC 6388 V4
5	-6.77	2.50	1	NGC 6760 V4
6	-6.57	4.36	1	NGC 6388 V3

^{a} The bin center and the 2MASS star count are taken from the 2MASS LF presented in Fig. 3.11.
^{b} N_{spec} defines the number of available MIR-spectra observed with *Spitzer*.
^{c} ID_{spec} presents the AGB stars with a MIR-spectrum for the respective luminosity bin.

---

[8]The bin centers of the 2MASS LF representing the intermediate metallicity group are different to the bin centers of the low metallicity group because the respective centers are adapted to the mean tip of the RGB of the respective groups (cf. Section 2.1.3 and Bellazzini et al. 2004).
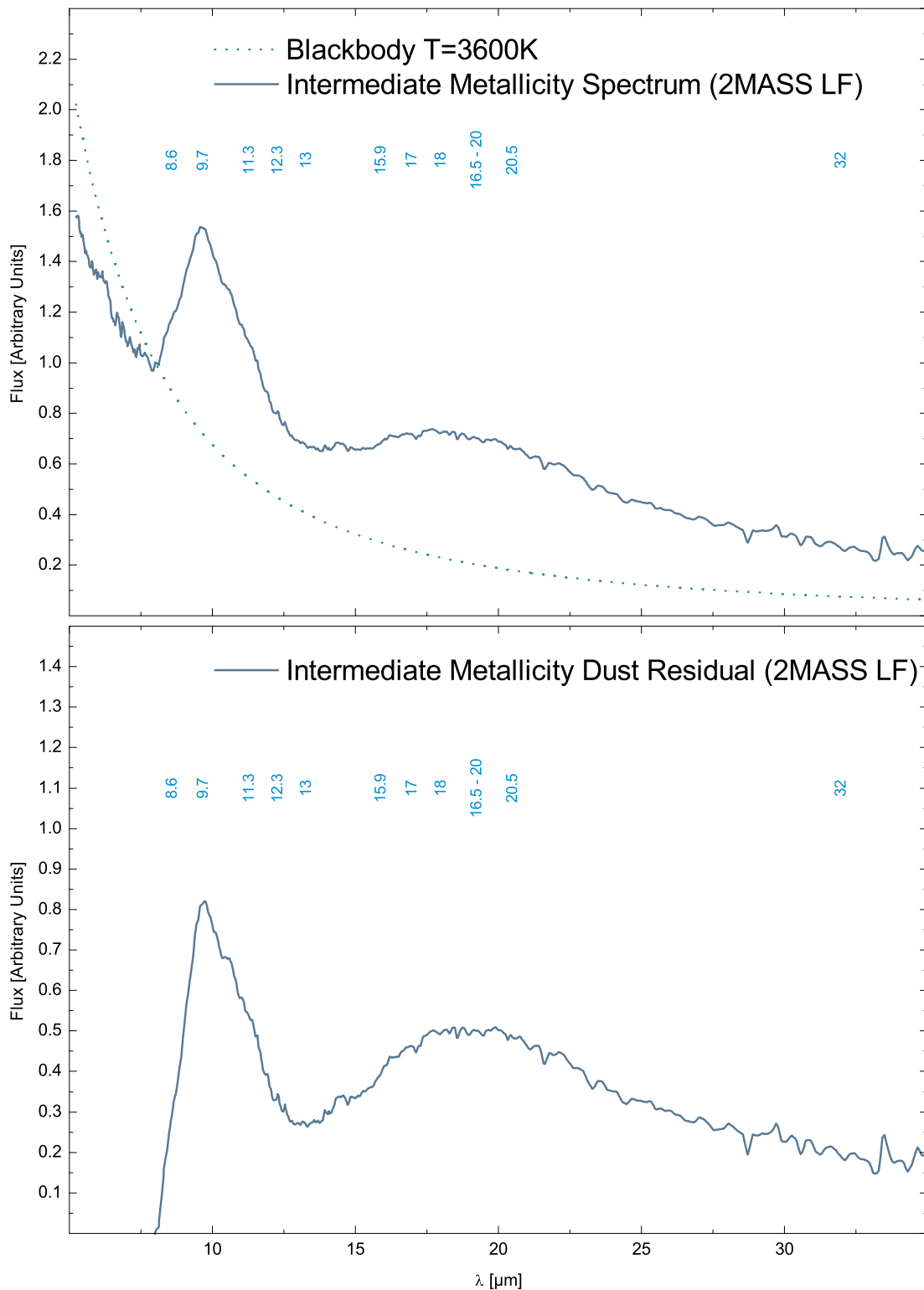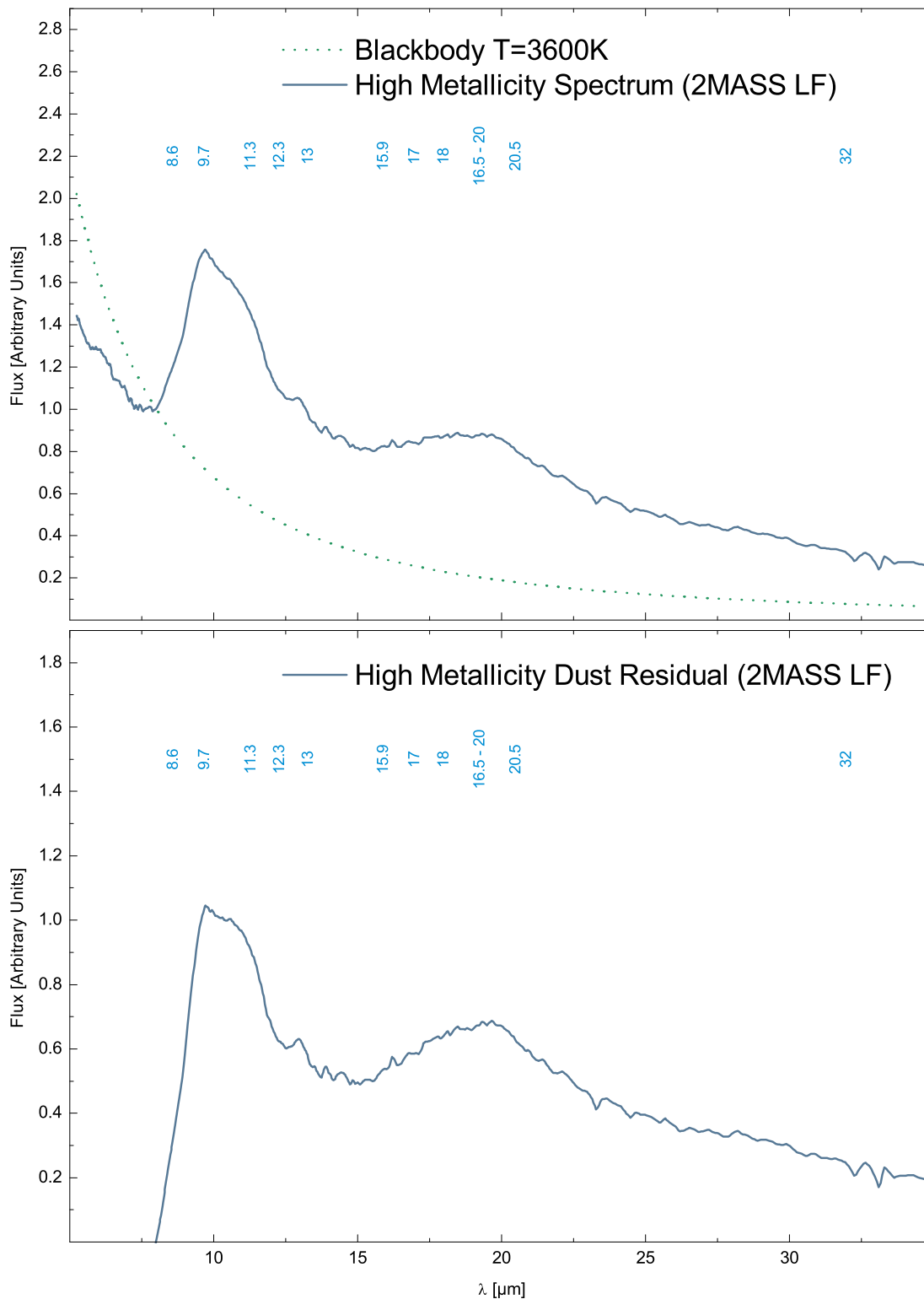
Figure 5.5: Co-added MIR-spectrum (upper panel) and dust residual (lower panel) of the intermediate metallicity globular cluster combination based on the 2MASS LF. Possible dust feature positions are indicated.

Fig. 5.5 presents the co-added MIR-spectrum normalized to the 8 μm flux (upper panel) and the dust residual derived by subtracting a blackbody with a temperature of 3600 K (lower panel). The dust emission resembles a Mira-like MIR excess and is dominated by the strong silicate features at 9.7 and 16-18 μm. The right flank of the 9.7 feature declines smoothly due to the presence of alumina dust. Clearly the co-added spectrum is dominated by the most luminous stars, namely NGC 6356 V1, NGC 6356 V5 and NGC 6760 V3, which all show prominant silicate features. NGC 6356 V1 and NGC 6760 V3 resemble the spectrum of a classic Mira star like *o Cet*, while NGC 6356 V5 shows a more sharp 9.7 μm fearure and no significant excess around 16-20 μm. The strong alumina feature at 11.3 μm present in the MIR-spectrum of NGC 6760 V4 manifests in the slope of the right flank of the 9.7 silicate feature. The faintest star NGC 6388 V3 shows no dust excess. Thus, the distribution of the observed AGB stars along the AGB is in good agreement with the dust evolution scenario presented by Lebzelter et al. (2006). However, due to the low number of stars occupying the same luminosity bin as this dust free AGB star, the weighting does not result in a co-added spectrum of the entire population that shows alleviated silicate features like in the case of the low metallicity globular cluster combination.

5.3 The MIR-Spectrum of the High Metallicity Group

The co-added MIR-spectrum of the high metallicity globular cluster combination is derived using the 2MASS LF presented in Section 3.4.4 (cf. Fig. 3.13). The TLFs based on isochrones from Marigo et al. (2008) are not used in this context due to the fact that only a part of the 2MASS LF could be properly reproduced. The bright part of the 2MASS LF contains a significant part of the AGB stars with available *Spitzer* spectra that can be used for the calculation of the co-added MIR-spectrum. The TLFs derived in Section 4.2.3 would not allow for a consideration of these spectra and, thus, are not suited for further use.

Like for the intermediate metallicity group, eight AGB stars with observed *Spitzer* spectra are assigned to the 2MASS LF according to their M_K luminosity. Table 5.4 presents the details of the high metallicity 2MASS LF including the star count, the number of observed MIR-spectra and the respective AGB star ID for each bin of the LF[9]. Again the fact that only stars from the sample of Sloan et al. (2010) are available for the high metallicity globular cluster combination leads to a limited luminosity range that can be used for the calculation of the co-added MIR-spectrum. Only the star NGC 5927 V1 is located below the mean tip of the RGB of the respective globular cluster combination. Thus, the derived co-added spectrum reflects only the brightest part of the stellar population described by the high metallicity group.

Two bins in the 2MASS LF are not occupied with AGB stars with observed *Spitzer* spectra. Therefore these bins again rely on the transfer of an adjacent mean MIR-spectrum. In the case of the most luminous *Bin 1* the mean spectrum of *Bin 2*, which actually consists only of one spectrum from the star Terzan 5 V7, is used after converting the flux level to the proper value corresponding to the center luminosity of the *Bin 1*. *Bin 10* is occupied by the star Terzan 5 V9. This star is reported to be a possible member of the young stellar population present in the

---

[9]The bin centers of the 2MASS LF differ from the centers of the two other metallicity groups due to the adaptation on the mean tip of the RGB (cf. Section 2.1.3).

Table 5.4: Weighting: High Metallicity Group - 2MASS LF

Bin	Bin Center $[M_K]^a$	2MASS Star Count^a	N_{spec}^{b}	ID_{spec}^{b}
1	-8.73	1.00	–	–
2	-8.53	0.89	1	Terzan 5 V7
3	-8.33	–	–	–
4	-8.13	1.77	1	Terzan 5 V6
5	-7.93	0.66	1	Terzan 5 V8
6	-7.73	–	–	–
7	-7.53	–	–	–
8	-7.33	1.98	1	NGC 5927 V3
9	-7.13	5.75	2	NGC 6553 V4 Terzan 5 V2
10	-6.93	4.06	1	Terzan 5 V9^d
11	-6.73	2.81	–	–
12	-6.53	13.16	1	NGC 5927 V1

^{a} The bin center and the 2MASS star count are taken from the 2MASS LF presented in Fig. 3.13.
^{b} N_{spec} defines the number of available MIR-spectra observed with *Spitzer*.
^{c} ID_{spec} presents the AGB stars with a MIR-spectrum for the respective luminosity bin.
^{d} The spectrum of Terzan 5 V9 is not included in the calculation of the co-added MIR-spectra of the high metallicity group.

globular cluster Terzan 5 (see Sloan et al. 2010 or Section 2.2.6) due to its unusual position in the Period-Luminosity diagram and its extreme reddening (cf. Fig. 2.9). Thus, Terzan 5 V9 is not included for the calculation of the co-added MIR-spectrum of the high metallicity group. Three more stars from Terzan 5 (V6, V7 and V8) are very luminous and could be members of the young population. However, these stars are reported to be members of the old population by Sloan et al. (2010) due to their position in the Period-M_{bol} diagram and therefore used to derive the co-added spectrum.

By dismissing Terzan 5 V9, *Bin 10* becomes an 'empty' bin and is filled with the mean spectrum of the adjacent *Bin 9* which includes two observed MIR-spectra. Furthermore, the spectrum characterising the stars in *Bin 12* is transferred to *Bin 11* which also does not include any AGB star with observed *Spitzer* spectrum. In both cases the proper flux levels of the transferred spectra are calculated using Equation 5.1.

After arranging each luminosity bin with a mean MIR-spectrum, the star counts of the bins in the 2MASS LF are used to weight the respective spectra in the same manner as described for the low and intermediate metallicity groups. Subsequently the weighted spectra are co-added to derive the overall MIR-spectrum describing the high metallicity globular cluster combination.

Figure 5.6: Co-added MIR-spectrum (upper panel) and dust residual (lower panel) of the high metallicity globular cluster combination based on the 2MASS LF. Possible dust feature positions are indicated.

Fig. 5.6 presents the co-added MIR-spectrum normalized to the $8\,\mu$m flux (upper panel) and the dust residual derived by subtracting a blackbody with a temperature of $3600\,$K (lower panel). The MIR excess is dominated by the strong silicate features at 10 and 16-18 μm. The $10\,\mu$m feature shows a broad peak ranging from 9.7 to $10.5\,\mu$m resembling a "double-peak". Alumina dust leads to the increased flux around $11.3\,\mu$m, although a distinct peak is not apparent. In addition a prominent $13\,\mu$m feature is manifesting in the MIR excess. Three stars, namely NGC 5927 V1, NGC 6553 V4 and Terzan 5 V6 are contributing to this feature.

5.4 A Comparison of the MIR-Spectra and Dust Residuals

The co-added MIR-spectra of the three globular cluster combinations are all dominated by the strong silicate dust excess at around 9.7 and 16-20 μm. However the spectra show different flux levels and feature shapes. Fig. 5.7 presents a comparison of the dust residuals of the low, intermediate and high metallicity groups. The dust residuals were derived by subtracting a $3600\,$K blackbody from the co-added and normalized[10] MIR-spectra of the respective group. The comparison relies on the co-added spectra derived using the weighting based on the 2MASS LFs of the three metallicity groups. The different weighting processes applied to the globular cluster NGC 104 in Section 5.1.1 to investigate the influence of differently evolved AGB stars[11] on the co-added MIR-spectra of old stellar populations could not be applied for the intermediate and high metallicity groups due to the lack of data and information on the number and periods of the LPVs in the member clusters.
The dust residual of the low metallicity group is included twice in Fig. 5.7. The green solid line illustrates the dust residual representing the globular cluster combination where every star that is occupying *Bin 9* of the respective 2MASS LF is treated as if they show prominent silicate features like NGC 104 V18. The red solid line shows the dust residual based on the alternative weighting where *Bin 9* includes only one V18-like star while the others are treated as if they where dust free AGB stars like NGC 104 V5 & V6. The intermediate and high metallicity groups are indicated with the light blue and the dark blue solid lines, respectively.

It is apparent that the high metallicity group shows the strongest overall dust excess in the MIR, followed by the intermediate metallicity group and the low metallicity group. The different flux levels of the low metallicity group dust residuals point to the fact, that the consideration of the MIR-spectra of faint and dust free AGB stars available for this group lead to a damped overall dust excess when calculating the co-added MIR-spectrum (cf. Section 5.1). The dust residual with the single V18-like star in *Bin 9* also shows the most flattened overall excess due to the then weaker silicate dust emission.

From the dust residuals of the three globular cluster combinations we conclude that the overall dust excess increases with increasing metallicity. This is in good agreement with the findings of Sloan et al. (2010), who reported such a behaviour after investigating the individual MIR-spectra of their globular cluster AGB star sample. However, it is important to note, that the flux level of the dust residuals from the intermediate and high metallicity groups could suffer a diminishment if the calculation of their co-added MIR-spectra and the respective dust resid-

---

[10] Each co-added spectrum was normalized to the $8\,\mu$m flux (cf. Sections 5.1 - 5.3).
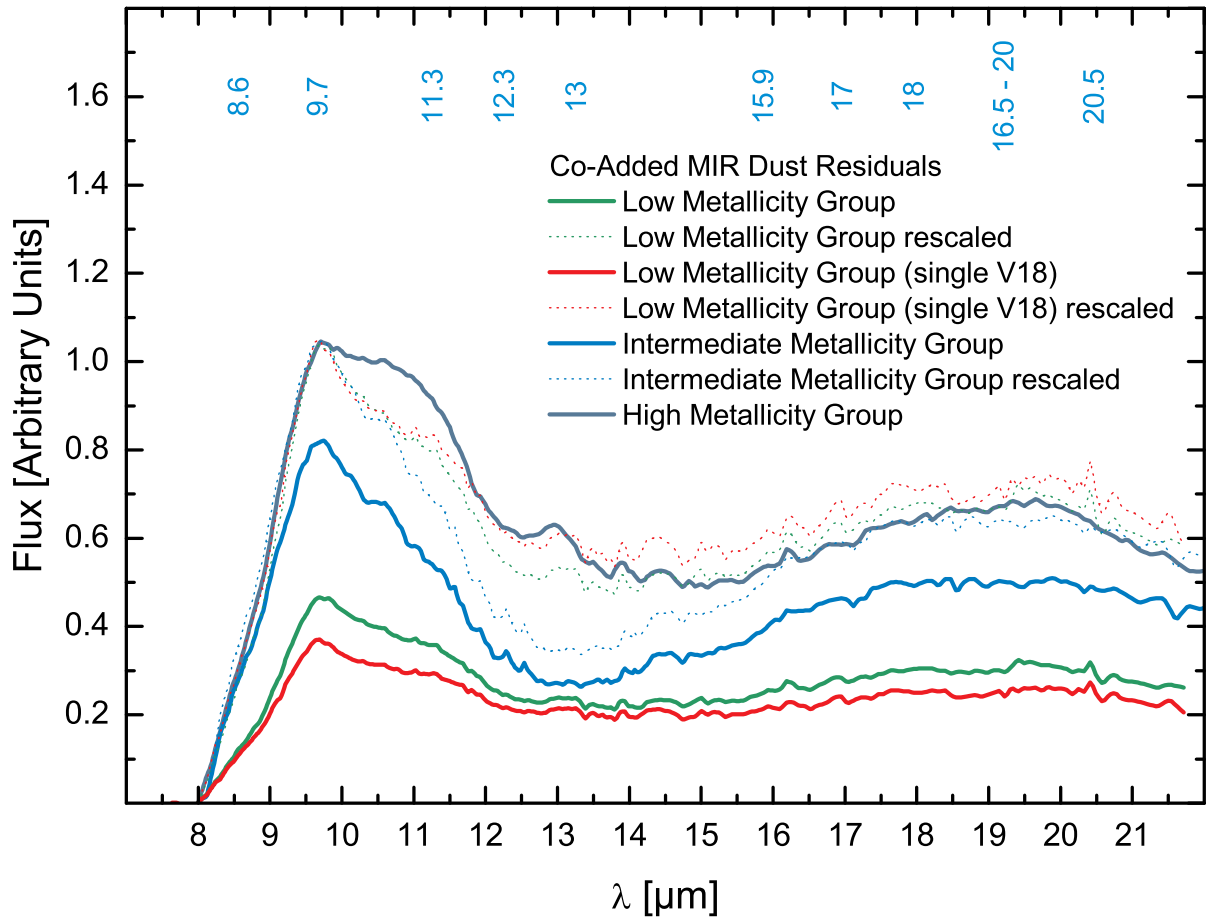[11] E.g. the dependency of different weighting methods for the peculiar star NGC 104 V18

Figure 5.7: Comparison of the co-added dust residuals of the low (green solid line), intermediate (light blue solid line) and high (dark blue solid line) metallicity globular cluster combinations based on the 2MASS LF. The red solid line indicates the dust residual of the low metallicity group derived with the alternative weighting where only a single V18-like star is considered. The dotted lines represent the rescaled dust residuals of the low and intermediate groups.

uals would include not only the brightest AGB stars. It is also feasible that the two groups would show weaker silicate features when fainter stars would contribute to their MIR-properties. Thus, observations of globular cluster AGB stars fainter than $M_K = -6.26$ mag would allow a more detailed analysis of the overall dust excess like it is possible for the low metallicity group.

To compare the shapes of the dust features of the three metallicity groups, the dust residuals from the low and the intermediate group have been scaled to match the 9.7 μm flux of the high metallicity group. In Fig. 5.7 the faint dotted lines present the dust residuals after rescaling. The dust residuals of the low and intermediate metallicity groups now differ significantly from the high metallicity group. Both groups show a sharp 9.7 μm feature with a similar decrease until 10.5 μm. In contrast, the high metallicity group shows a broad silicate feature ranging from 9.7 to 10.5 μm. This broad feature is present in three stars of the high metallicity group (namely Terzan 5 V6, V7 & V8) that are all from one globular cluster (Terzan 5) and are possible
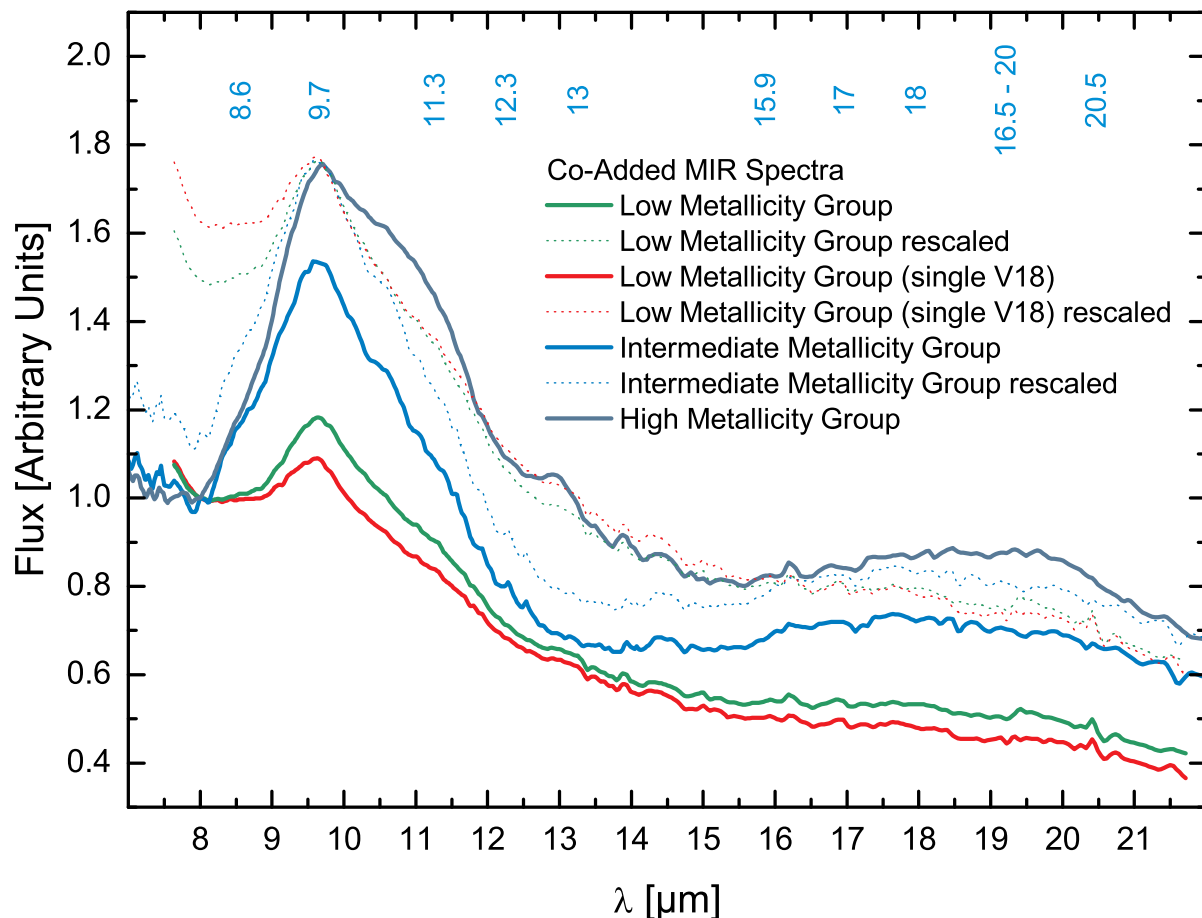
Figure 5.8: Same comparison as in Fig. 5.7 for the co-added MIR-spectra.

members of a young population hosted by the cluster (cf. Sections 2.2.6 and 4.2.3). Especially the brightest star of the group, namely Terzan 5 V7, dominates the co-added spectrum. Also the intermediate group is dominated by a few bright stars all showing a Mira-like MIR-spectrum. It is evident, that both the intermediate and the high metallicity groups have to be dealt with care due to possible selection effects caused by the low number of observed MIR-spectra.

Towards longer wavelengths, the dust excesses of the low and intermediate group show the same overall behaviour, however, the excess at $11.3\,\mu$m due to alumina dust is stronger for the low metallicity group. In addition the flux drops more intensively for the intermediate group. Both groups do not show a $13\,\mu$m feature, which is only apparent in the dust residual of the high metallicity group, although in the two former groups several stars show a $13\,\mu$m feature (see Lebzelter et al. 2006 and Sloan et al. 2010). The $13\,\mu$m feature in the high metallicity group is prominent in three out of seven stars of the group and, thus, is not overwhelmed by the silicate features present in the MIR-spectra. In the low and the intermediate group the $13\,\mu$m feature due to cristalline alumina seems to perish in the strong silicate excess and is smeared out due to the presence of stars with dust free MIR-spectra that rise the flux at wavelengths longer than $10\,\mu$m.

Table 5.5: Flux Ratios of Co-added Dust Residuals

Metallicity Group	$F_{10.5}/F_{9.7}$	$F_{11.3}/F_{9.7}$	$F_{12.9}/F_{9.7}$	$F_{19.5}/F_{9.7}$
Low (single V18)[a]	0.863	0.773	0.590	0.423
Low[b]	0.864	0.765	0.562	0.436
Intermediate	0.850	0.702	0.454	0.448
High	0.921	0.822	0.599	0.495

[a] The flux ratios correspond to the co-added MIR-spectrum weighted with only one V18-like star (red dotted line in Fig. 5.8).

[b] The flux ratios correspond to the co-added MIR-spectrum where all stars in *Bin 9* are treated as V18-like stars (green dotted line in Fig. 5.8).

A comparison of the co-added MIR spectra - no photospheric continuum subtracted - is presented in Fig. 5.8. The dust emission is again strongest in the high metallicity group, followed by the intermediate group and the low metallicity group. The weigthing method with a single V18-like star in the case of the MIR-spectrum of the low metallicity group shows the weakest and also the most flattened dust emission. After rescaling the MIR-spectra to the 9.7 μm-flux of the high metallicity group the same behaviour is apparent for the 9.7, 11.3 and 13 μm features as reported for the dust residuals presented in Fig. 5.7.

While in the dust residuals no metallicity trend could be detected, the MIR-spectra show a different result. The dust excess due to the prominent silicate emission at 16-20 μm relative to the 9.7 μm excess is the strongest in the high metallicity group, followed by the intermediate and low metallicity groups. Thus, the ratio $F_{19.5}/F_{9.7}$ decreases with decreasing metallicity indicating a dependency on metallicity. No metallicity trend could be detected for the flux ratios of the other dust features present in the co-added MIR-spectra ($F_{10.5}/F_{9.7}$, $F_{11.3}/F_{9.7}$ and $F_{12.9}/F_{9.7}$) as the flux ratios of the low metallicity group resides between the flux ratios of the two other metallicity groups (see Table 5.5). The decreased 16-20 μm flux at lower metallicities points again to the importance of the observation of low luminosity AGB stars in the MIR in order to constrain the impact of the bright stars domintated by the 9.7 μm silicate feature. It is feasible that the higher flux ratios ($F_{19.5}/F_{9.7}$) of the intermediate and the high metallicity group are only an effect that occurs due to the lacking MIR-spectra of low luminosity AGB stars that could result in a diminishment of the 16-20 μm silicate bump. Thus, the reported metallicity trend for the $F_{19.5}/F_{9.7}$ flux ratio has to be investigated further. This could be performed e.g. with imaging data from the AKARI All-Sky Survey. By reproducing the flux ratios using the AKARI filters at 9 and 18 μm the integrated photometric flux values of the respective bands could be derived to test our findings for the globular cluster combinations described in this study.

Chapter 6

Discussion and Outlook

In this thesis we presented co-added MIR-spectra for three globular cluster combinations with different metallicities. The spectra were derived using 2MASS LFs to weight the individual AGB star spectra in each group and showed a prominent MIR excess due to silicate dust. The excess increases with increasing metallicity. While for the low metallicity group it was possible to investigate different weighting methods resulting in a flattened excess and a reduction of the silicate domination (cf. Section 5.1), this could not be done for the intermediate and high metallicity groups, respectively. The dust emission of the latter two groups resembles a Mira-like MIR excess dominated by the strong silicate features at 9.7 and 16-18 μm. In the case of the high metallicity group also a distinct feature at 13 μm is present in the co-added MIR-spectrum. Due to the low number of available MIR-spectra and, thus, the lack of MIR data of low luminosity AGB stars, the results for intermediate and high metallicity groups present only a 'tip of the iceberg' approach. The faintest stars with available *Spitzer* spectra observed in the metal-rich globular cluster combinations are still bright compared to the low luminosity stars available in the metal-poor combination. Thus, the intermediate and high metallicity groups do not include AGB stars that are located way below the tip of the RGB and therefore probably do not show dust emission in their MIR-spectra. We expect that the consideration of such 'naked' stars in the calculation of the co-added MIR-spectrum of the the latter two groups could lead to a similar shape of the MIR excess as derived for the low metallicity group. Also stars like NGC 104 V18, which was observed in its interpulse luminosity, are probably missed in the intermediate and high metallicity groups. The investigation of the influence of a peculiar star like V18 on the MIR dust excess of the low metallicity group and the globular cluster NGC 104 showed that the consideration or the omission of such a star results in a dramatic change of the dust residual flux (over 30%).

Considering the high stochasticity implied by the low number of available MIR-spectra, especially for the intermediate and high metallicity groups, we conclude that one has to be cautious while generating co-added MIR-spectra that represent entire stellar populations. The need for a larger sample is evident and we stress that a more complete observational coverage of stars

that evolve up the AGB would lead to a better understanding of the integrated MIR-spectra of the hosting globular clusters and of unresolved old stellar populations in general. Thus, it is important to further extend the available sample of MIR-spectra of globular cluster AGB stars by adding existing data and by performing new observations that focus on AGB stars that are expected to show a MIR excess.

6.1 The More Stars the Better

Globular cluster AGB stars without available *Spitzer* spectra have not been taken into account in this work. However, it is important to note, that there are additional AGB stars in various globular clusters to be included in the future.

6.1.1 Searches for AGB Stars in Globular Clusters

In the comprehensive work of McDonald & van Loon (2007) 47 globular cluster AGB stars were investigated using VLT/UVES spectra. Several AGB stars were detected in their sample that showed a MIR dust excess and therefore could be used as candidates for MIR spectroscopy to extend the number of available MIR-spectra. The newly observed AGB stars could be used to improve the accuracy of our co-added MIR-spectra derived for our three different metallicity groups. E.g. in the globular cluster NGC 104 two previously unknown stars[1] were detected that show an IR excess. Adding these stars to the sample of AGB stars in the low metallicity group would rise the number of available MIR-spectra to 20. However, the two stars have not been observed in the MIR so far and, thus, can only be considered as possible candidates for ground based MIR spectroscopy. McDonald & van Loon (2007) also reported the detection of four stars with a possible IR excess in NGC 6388 and three stars in NGC 362. These stars are also nice candidates for MIR observations, especially because they would extend the number of available MIR-spectra at metallicities different to the one of the low metallicity group.

In addition to the search for possible candidates for new observations, available data can be added to our sample. A study on NGC 5139 by McDonald et al. (2009) resulted in MIR-spectra of two globular cluster AGB stars, namely V6 and V42, observed with the MIR spectrograph *T-ReCS* at Gemini South. V6 showed a 9.5 μm feature in the ground based data and V42 was also observed by Sloan et al. (2010) using *Spitzer*[2]. Adding these stars to the AGB star sample of our study would also help to establish a more extensive database of MIR-spectra available for the investigation of co-added MIR-spectra of globular clusters.

In an comparable study to the work of Lebzelter & Wood (2005) on the LPVs in the globular cluster NGC 104, Lebzelter & Wood (submitted) investigated the LPV populations in the two globular clusters NGC 362 and NGC 2808, respectively. The latter study resulted in a sample of 15 AGB stars in NGC 362 and 22 AGB stars in NGC 2808. While two AGB stars of NGC 362 were observed by Sloan et al. (2010) and are presented in Section 2.3 in this work, for none of the stars in the other cluster observed MIR-spectra are available. However, these samples

---

[1] Labelled x02 and x03 in McDonald & van Loon (2007)

[2] V42 was not included in this work because of its uncertain metallicity due to the multiple populations present in NGC 5139.

of well known AGB stars are the perfect choice for an extensive study based on ground based MIR-spectroscopy, as the majority of the sample has also known periods and, thus, would allow a similar investigation of the dust evolution along the AGB as it was possible for the globular cluster NGC 104 (cf. Lebzelter et al. 2006). In addtion the study of the intermediate age LMC cluster NGC 1846 by Lebzelter & Wood (2007) provided a sample of 22 AGB stars which could be used to investigate the effects on the MIR properties as the stars undergo the transition from O-rich to C-rich. Thus, MIR-spectroscopy of the AGB stars in NGC 1846 would allow to compare the co-added MIR-spectra of the latter cluster, that is likely dominated by the luminous C-stars, with the co-added MIR-spectra derived in this thesis. However, such a study is out of reach with the current ground based instrumentation.

6.1.2 AKARI

Possible candidates for new MIR observations can also be found using AKARI data. The AKARI infrared space mission has performed an All-Sky Survey in six infrared bands from 9 to 180 μm. Using the AKARI infrared camera point source catalogue (IRC PSC) it was possible to search for counterparts of the stars in the Color-Magnitude diagrams presented in Section 3.3 in the 9 μm band. Fig. 6.1 presents the results of this search for a subsample[3] of the globular clusters of this study. The right panels illustrate the Color-Magnitude diagrams based on 2MASS data. Stars with matching AKARI observations at 9 μm are indicated with blue squares. Stars with observed *Spitzer* spectrum are also indicated (red circles). The left panels of Fig. 6.1 illustrate the ratio of the 9 μm to the K-band flux. The dotted line represents a pure photosphere with a temperature of 3600 K. Stars that are close to this vertical line can be considered to be dust free. Stars that show a higher F_9/F_K-ratio likely show a MIR dust excess and, thus, are possible candidates for new MIR observations. E.g. the AGB star NGC 6760 V4 shows a silicate dust emission in the MIR-spectra observed by *Spitzer* and has also a high F_9/F_K-ratio. In Fig. 6.1 we see a further star in the same cluster with a comparable F_9/F_K-ratio that was not observed in the MIR so far. The high flux ratio makes this star a perfect target for new MIR observations. However, the star NGC 6760 V3 also shows a prominent silicate dust feature in its *Spitzer* MIR-spectrum, but still has a small F_9/F_K-ratio. Due to stellar variability, the position of this star in Fig. 6.1 could be different, whether it is observed in a minimum or a maximum of its light cycle (cf. Section 6.2). Nevertheless, several globular cluster AGB stars illustrated in Fig. 6.1 show noticeable F_9/F_K-ratios pointing to a consideration in future observational studies.

This simple exercise showed that AKARI data can be used to search for possible candidates for new MIR observations. However, using the IRC PSC is limited due to the low number of stars that could be extracted and correlated with a 2MASS counterpart. Searching the catalogue for stars that are located in the same area on the sky as the globular clusters of this study resulted in the data presented in Fig. 6.1. Furthermore, the catalogue query is limited to two out of the six infrared bands and allows only for the extraction of photometric flux values for 9 and 18 μm. We neglected the 18 μm flux due to the fact that the query did not result in enough data and, thus, no flux ratios including the 18 μm flux could be derived.

---

[3] IC 1276, NGC 104, NGC 6352, NGC 6712 and NGC 6760
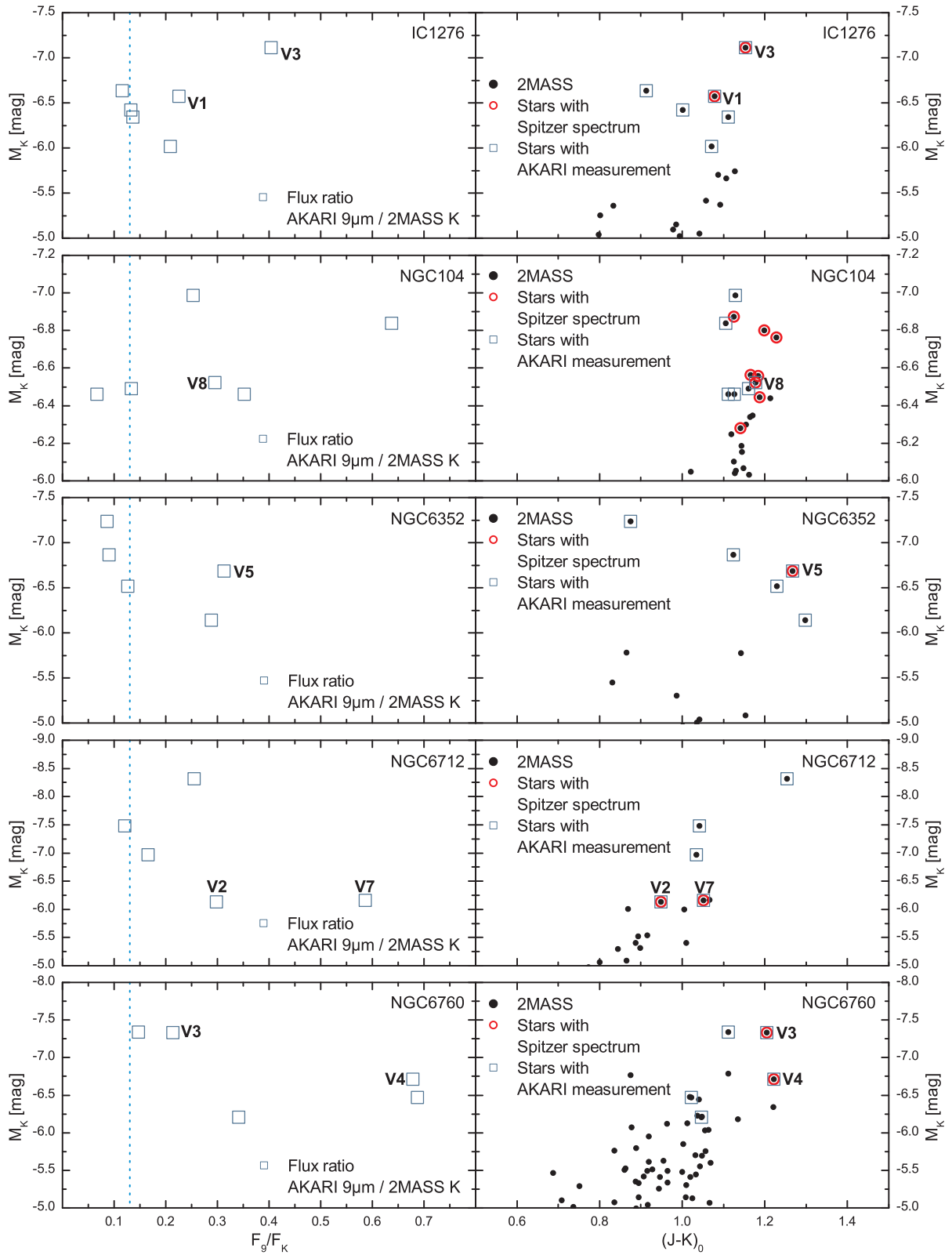
Figure 6.1: Left panels: F_9/F_K flux ratios based on AKARI measurements. The dotted line indicates a dust free photosphere. Stars with a higher F_9/F_K-ratio possibly have a MIR dust excess. Right panels: Color-Magnitude diagrams illustrating 2MASS counterparts.

Still, the AKARI All-Sky Survey allows for a more detailed search for dusty AGB stars. Ita et al. (2007) used IRC imaging to investigate two globular clusters, namely NGC 104 and NGC 362, during the AKARI in-orbit performance verifications. There analysis resulted in the identification of the entire LPV population of NGC 104 accourding to the study of Lebzelter & Wood (2005). Also for NGC 362 Ita et al. (2007) were able to identify the LPVs first detected by Clement et al. (2001) and Székely et al. (2007). In addition they detected eight very red sources in the latter cluster, where six sources do not have a 2MASS counterpart. In their study Ita et al. (2007) showed that the F_{11}/F_K and the F_{24}/F_7 flux ratios could be used to disentangle stars with dust emission from naked stars, similar to the approach illustrated in Fig. 6.1. We conclude that AKARI imaging data could be used for all the globular clusters of our sample to try to identify additional AGB stars with possible MIR dust excess. The identification of AGB stars that show dust emission comparable to NGC 104 V4 and V8, or low luminosity stars like NGC 104 V5 and V6 which are dust free, in other globular clusters could help to verify the dust evolution scenario proposed by Lebzelter et al. (2006). Our assumption that stars in the same luminosity range have similar dust properties in their MIR-spectra could be tested to to evaluate the need for more data and to provide further insight into the weighting methods applied in this work.

Another application of the AKARI IRC data could be an examination of our findings presented in Section 5.4. The comparison of the co-added MIR-spectra of the low, intermediate and high metallicity globular cluster combinations resulted in a metallicity trend manifesting in the strength of the 16-20 μm dust emission. The flux ratio $F_{19.5}/F_{9.7}$ was reported to decrease with decreasing metallicity. However, it is possible that this trend is only an effect that occures due to the low number of considered individual MIR-spectra for the intermediate and the high metallicity groups. To further investigate the reported dependency on metallicity, we plan to use AKARI measurements at 9 and 18 μm to derive the integrated photometric flux values of the respective bands for the globular clusters of our sample and subsequently of our three globular cluster combinations. Our $F_{19.5}/F_{9.7}$ flux ratios could then be compared to the F_{18}/F_9 flux ratios based on the AKARI measurements to test our findings.

6.2 Considering Stellar Variability

The MIR-spectra this study is based on represent only single epoch observations implying a constancy of the dust features on timescales short compared to the evolution on the AGB. As all observed AGB stars are variables, this assumption may be incorrect and, thus, the co-added MIR-spectra could resemble only a 'snapshot' of the three globular cluster combinations, respectively. Indeed variability in the shape of dust features of AGB stars has been reported by several authors in the past (Little-Marenin et al. 1996, Creech-Eakman et al. 1997, Monnier et al. 1998, Onaka et al. 2002). Most of these observations indicate a sharpening of the silicate dust feature when the star is in a light curve maximum. This is explained by an increase in the dust temperature and possibly also in the 'pureness' of the dust grains (Lobel et al. 2000, Monnier et al. 1998). Also in the study of Lebzelter et al. (2006) changes in the dust features of AGB stars in NGC 104 are reported (cf. Section 1.3). This variability is typically attributed to changes in the stellar luminosity and temperature as the result of stellar pulsations, which occur on time scales of a few ten to a few hundred days.

Variations on the formation and outflow of dust particles are expected to become visible on a much longer timescale due to the typical size of the circumstellar dust shells (of the order of a few AUs) and the typical outflow velocities observed ($10 \, \text{km} \cdot \text{s}^{-1}$). Long time studies of the MIR-spectrum of AGB stars are quite rare. The most extensive investigation up to now is the work of Monnier et al. (1999) where they compared IRAS low resolution spectra with ground-based observations of 29 late-type stars with substantial dust shells that where performed over several decades. In about half of their sample they found a general strengthening of the $9.7 \, \mu\text{m}$ silicate peak with respect to the underlying continuum and one case, where the peak has almost disappeared. Monnier et al. (1999) suggested two explanations for these changes, namely a change in the properties of the dust particles (composition, degree of crystallization) or a change in the dust production and mass-loss rate.

The presence of short and long time changes of the dust features point to the great impact of stellar variability on the shape of the AGB star MIR-spectrum at a given phase and, thus, should be accounted for in the approach of describing the co-added MIR-spectra of old stellar populations. The need for further observations of the AGB stars of this study is evident. Although it is a challenging task to observe AGB stars in several globular clusters again to cover their pulsation cycles it is nececcary to include possible variations of the MIR-spectrum of AGB stars in future work. In the absence of spectroscopic capabilities in space, the ground-based MIR instruments at Gemini North and South (NOAO) and the VLT (ESO) could be used to investigate the effects of variability in the MIR by observing the N-band covering the prominent silicate feature at $9.7 \, \mu\text{m}$ and the features at 11.3 and $13 \, \mu\text{m}$ due to alumina dust (cf. Appendix D). In particular, the upgrade of the MIR-spectrograph VISIR at the VLT will ease performing the needed observations within a reasonable time due to the new possibility to observe the entire N-band with only one setting[4].

6.3   Synthetic MIR-Spectra of AGB Stars

The investigation of the MIR-properties of evolved stars based on spectroscopic observations can be supported and extended by the implementation of laboratory studies (cf. Appendix F) and the use of synthetic data derived by radiative transfer models of dusty envelopes. Synthetic MIR-spectra could help to understand the influences of various stellar parameters (e.g. mass, temperature, luminosity, chemical composition, metallicity and mass-loss) on the dust mineralogy in stellar winds and on the dust features manifesting in the MIR-spectra of AGB stars and unresolved old stellar populations, but need to be validated with observed data. The compliation presented in this thesis would provide the necessary observed material.

While there are several codes available for the calculation of synthetic spectra (e.g. DUSTY, cf. Ivezic & Elitzur 1997, or the code by Groenewegen 1995) we use the comprehensive wind code developed by H.-P. Gail (Ferrarotti & Gail 2005) to complete first model computations to predict the MIR-spectrum of evolved stars. This code derives stationary wind models for mass-losing AGB stars by solving the coupled system of differential equations for a stationary outflow. For details we refer to the elaborate description given in Ferrarotti & Gail (2006).

---

[4]Before the VISIR upgrade four grating settings had to be combined for a full coverage of the N-band.

Modelling the dusty winds in the case of an O-rich chemistry is difficult as the underlying driving mechanism is still a matter of debate and there is a lack of a consistent theory of dust grain formation. Problems concerning e.g. the driving mechanism for the mass-loss of M-stars are circumvented in the code by H.-P. Gail by not calculating the onset of the wind according to the scenario of pulsation- and dust-driven winds (Höfner et al. 2003, Höfner 2008), but to specify the mass-loss rate as an input parameter. With reasonable assumptions for the initial outflow velocity, stellar effective temperature, luminosity and mass it is possible to derive wind structures resembling the average profiles of dynamic model atmospheres (Ferrarotti & Gail 2006). The code also offers the unique possibility of a sophisticated treatment of dust, yielding detailed information about the mineralogy of the stellar outflow[5]. The output includes descriptions of the dust temperature, the condensation degree, the stoichiometry, the outflow velocity, the dust density and also a simple spectrum illustrating the dust features. In addition, the low computation time enables extensive parameter studies.

As a starting point for a more detailed investigation of the dependency of the dust properties of AGB stars on the metallicity in the near future, a grid of synthetic MIR-spectra was derived for the AGB star population in the globular cluster NGC 104[6]. With this preliminary study we tried to reproduce the dust signatures in the observed MIR-spectra. The input parameters used for the calculation covered the temperature and luminosity range of the AGB star sample of the cluster (cf. Lebzelter & Wood 2005, Lebzelter et al. 2006 and Chapter 2 in this work) and are listed in the legends of Fig. 6.2.

Fig. 6.2 presents some preliminary results for the synthetic MIR-spectra derived for a comparison with the observed spectra of the AGB stars in NGC 104. The spectra are normalized to the maximum of the spectral energy distribution of the blackbody used to describe the stellar photosphere in the code[7]. We report that all derived synthetic MIR-spectra are dominated by silicate dust features at 9.7 and 16–20 μm. As the mass-loss rate increases, the overall dust excess increases. For high mass-loss rates and low luminosities we see a transition of the 9.7 μm feature from emission to self-absorption. For higher luminosities the 9.7 μm feature becomes broader as the mass-loss rate increases pointing to the presence of alumina dust. This is consistent with the development of a distinct 13 μm feature with increasing mass-loss.

This preliminary study shows, that the code from H.-P. Gail could be used to derive synthetic MIR-spectra for a comparison with observational data. However, using the input parameters of the globular cluster NGC 104 resulted in synthetic spectra that are all dominated by silicate dust. It was not possible to reproduce the MIR-spectra of AGB stars like NGC 104 V4, V8 or V13, which are all showing prominent alumina dust features and only minor silicate signatures (cf. Lebzelter et al. 2006 and Section 1.3 of this work).

---

[5]Note that we used a revised version of the wind code that allowed for the consideration of more dust species.

[6]The calculation was performed using an *Intel Fortran* compiler and no optimizations during the compilation. Compilation: *ifort codefile.f -O0 -g -o executablefile*

[7]The flux plotted in Fig. 6.2 can be converted to L_ν-values in units of [erg/s/Hz] by a multiplication with $16\pi^2 R_*^2$, where R_* is the radius of the respective star. R_* can be derived using L and T via $L = 4\pi R^2 \sigma T^4$, where σ is the Stefan-Boltzmann constant. This accounts for the normalisiation to the surface of the photosphere within the code and the fact that the program derives the first momentum of the radiation intensity H given as $F_\nu = 4\pi H$. See Ferrarotti & Gail (2006) for more details.
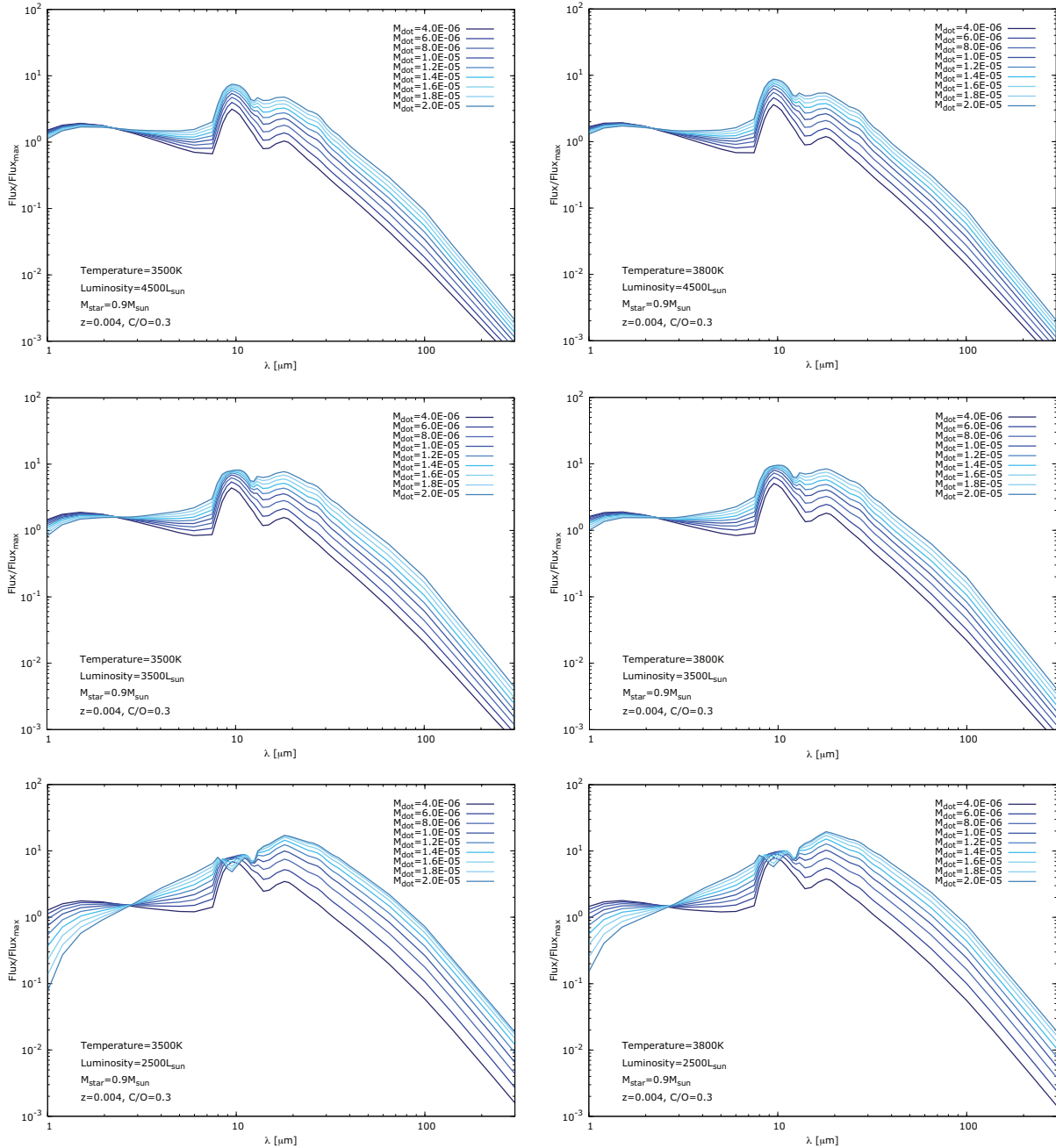
Figure 6.2: Synthetic MIR-spectra derived using the wind code by H.-P. Gail. Input parameters for temperature, luminosity, mass, metallicity, chemical composition and variable mass-loss rates are given in each panel. The parameters are set to represent the AGB star population of the globular cluster NGC 104. All spectra are dominated by silicate dust. See text for details.

To investigate this effect and to overcome the problem of silicate domination for the sets of input parameters describing the stars with no prominent silicate dust features, a collaboration with H.-P. Gail and W. Nowotny has been started. As this thesis is published, a new version of the code will have been released and will be used for future calculations of synthetic AGB star spectra. That latest version accounts not only for the coupling between the stellar radiation field and the dust grain formation, but also for the destruction of newly formed dust particles in the stellar outflow. Thus, a realistic description of the dust evolution including grain formation and growth as well as grain destruction by heating is possible. With this outlook a detailed study of the dust evolution along the AGB in the globular cluster NGC 104 marks the beginning of an extensive study of synthetic MIR-spectra for various metallicities to allow for a comparison with the integrated MIR-spectra of old stellar populations with respect to their metallicity.

Appendix A

The Period of IC 1276 V3

For the globular cluster AGB star IC 1276 V3 a pulsation period was derived using the light curve presented by Kinman & Rosino (1962). The light curve from their Fig. 2 was digitized using the software *Plot Digitizer*[1] and subsequently used as input data for *Period04*[2]. *Period04* allows for the Fourier fitting of the input data and, thus, for the determination of the period of the input light curve.

Fig. A.1 presents the digitized light curve from Kinman & Rosino (1962) (blue symbols) and the Fourier fit derived with *Period04* (blue line). The retrieved period amounts to 180 days and can be interpreted as the lower limit of the period from IC 1276 V3 because the light curve from Kinman & Rosino (1962) does not cover a full light cycle of the star. Sloan et al. (2010) presented a period of IC 1276 V3 that amounts to 300 days, derived from IRSF data covering the entire light cycle.

As the IRSF data was not released at the beginning of this study, the period derived after Kinman & Rosino (1962) is used in Fig. 2.2. The use of the longer period from Sloan et al. (2010) would result in a slightly shifted position of IC 1276 V3 in Fig. 2.2 that would still follow the presented Period-K relations.

---

[1] *Plot Digitizer* is available at `http://plotdigitizer.sourceforge.net/`. [December 30, 2010]
[2] *Period04* is available at `http://www.univie.ac.at/tops/period04/`. [December 30, 2010]
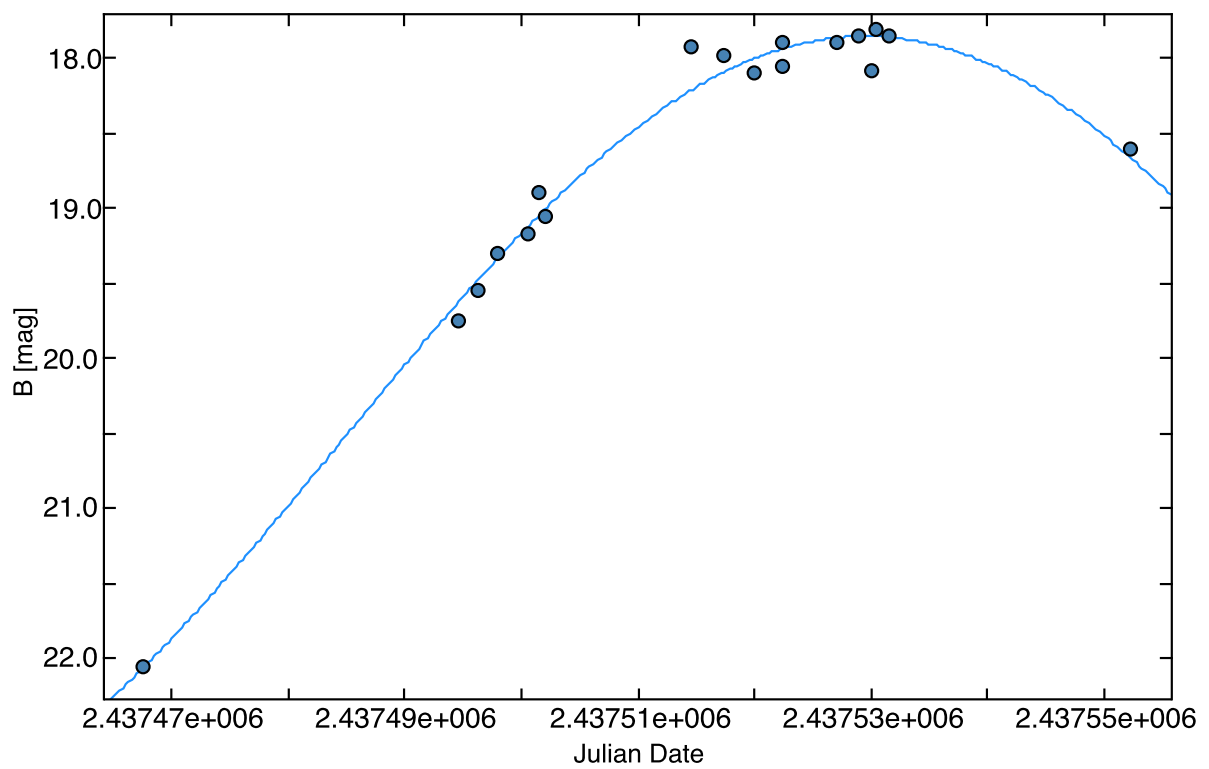
Figure A.1: Light curve of the globular cluster AGB star IC 1276 V3 taken from Kinman & Rosino (1962).

Appendix B

Metallicity

How to convert the metallicity [Fe/H] into Z and vice versa can not be found easily in the literature. Short explanations are given in Girardi & Salaris (2001) or Girardi et al. (2005). Therefore a more comprehensive explanation is given in this Appendix.

Metallicity is typically given as the ratio of iron (Fe) over hydrogen (H) and written as [Fe/H]. [Fe/H] is defined in Equation B.1 as the logarithm of the ratio of the relative number densities measured in any astronomical object and the relative number densities measured in the sun, where n(Fe) is the number density of the element iron and n(H) is the number density of the element hydrogen. Since it is a logarithmic unit e.g. a metallicity of [Fe/H] = -1 means one tenth of solar.

$$\left[Fe/H\right] = \log\left[\frac{\left[\frac{n(Fe)}{n(H)}\right]_*}{\left[\frac{n(Fe)}{n(H)}\right]_\odot}\right] \tag{B.1}$$

If an object has the same ratio of iron and hydrogen as the sun, Eq. B.1 can be written as $[Fe/H] = \log[1]$ resulting in $[\text{Fe/H}]_\odot = 0$. This is equivivalent to $Z_* = Z_\odot$ leading to $Z[Z_\odot] = 1$[1] with $Z_\odot = 0.02$.

With this background it is easy to convert [Fe/H] into Z and vice versa. The following three examples will illustrate this.

---

[1] Note that $Z[Z_\odot]$ means that Z is given in units of $Z_\odot$ and is probably not the Z found in a paper. It is Z multiplied with $Z_\odot$

Example 1:

$$\begin{aligned}
\left[Fe/H\right] = -0.5 \Rightarrow Z[Z_\odot] &= 10^{-0.5} = 0.3162 \\
\Rightarrow Z = Z[Z_\odot] \cdot Z_\odot &= 0.3162 \cdot 0.02 \\
\Rightarrow Z &= 0.006
\end{aligned}$$

Example 2:

$$\begin{aligned}
\left[Fe/H\right] = -0.7 \Rightarrow Z[Z_\odot] &= 10^{-0.7} = 0.1995 \\
\Rightarrow Z = Z[Z_\odot] \cdot Z_\odot &= 0.1995 \cdot 0.02 \\
\Rightarrow Z &= 0.004
\end{aligned}$$

Example 3:

$$\begin{aligned}
Z = 0.004 \Rightarrow Z[Z_\odot] &= \frac{0.004}{0.02} = 0.2 \\
\Rightarrow \left[Fe/H\right] &= \log Z[Z_\odot] = \log 0.2 \\
\Rightarrow \left[Fe/H\right] &= -0.6989 \approx -0.7
\end{aligned}$$

<div style="text-align: right">

Appendix C

</div>

Globular Cluster Finding Charts

This appendix presents the twelve globular clusters from the *Spitzer* program P40111 observed from Sloan et al. (2010) presented in Table 2.1[1]. Finding charts are illustrated in the Figures C.1 and C.2, respectively. North is up, East is left. The field of view (FOV) is 11.11 x 10.7 arcmin for the Galactic globular clusters NGC 362, NGC 5927, NGC 6352, NGC 6356 and NGC 6388, respectively. For IC 1276, NGC 6553 and Terzan 5 the FOV is 11.05 x 10.65 arcmin, respectively. NGC 6637 has a FOV of 11.12 x 10.71 arcmin and the clusters NGC 6712, NGC 6760 and NGC 6838 have a FOV of 12.35 x 11.9 arcmin, respectively. The globular cluster AGB stars observed with the *IRS* spectrograph are marked with colored circles in the finding charts.

The finding charts are composite pictures of the visual standard image and the 2MASS *K*-band image of the respective clusters taken from the Aladin Sky Atlas[2] which can be accessed through Simbad[3] after a simple target query. The composite is a simple RGB-color combination of the two images, but only using the red and the blue color input at the Aladin Sky Atlas RGB-composite tool. The advantage of such a composite finding chart is the fact that the important information from both images are combined in one image. The visual image shows the shape and size of the globular cluster but neglects the NIR emission of the stars leading to barely visible AGB stars in the crowded cluster. The 2MASS image shows the NIR *K*-band emission of the cluster stars leading to bright AGB stars on the one hand and a barely visually traceable globular cluster structure on the other hand. The combination makes it possible to see the extention of the globular cluster and the *K*-band emission at once. It also helps to compare the finding charts with older ones from the literature, which are only available in the visual making it difficult to find the AGB variables.

---

[1] Note that NGC 104 is not part of P40111 and is not included in the appendix.
[2] The Aladin Sky Atlas is available at `http://aladin.u-strasbg.fr/aladin.gml` [December 30, 2010]
[3] `http://simbad.u-strasbg.fr/simbad/` [December 30, 2010]
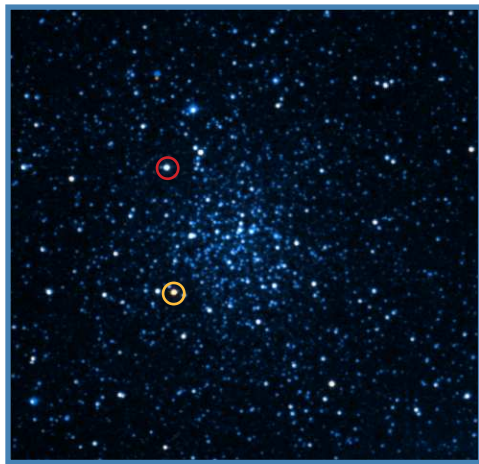
IC1276
○ V1   ○ V3
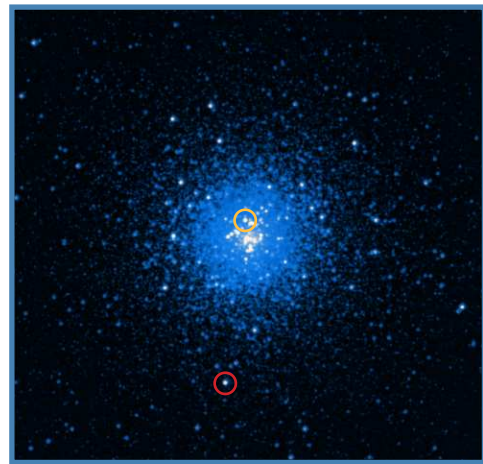
NGC362
○ V2   ○ V16
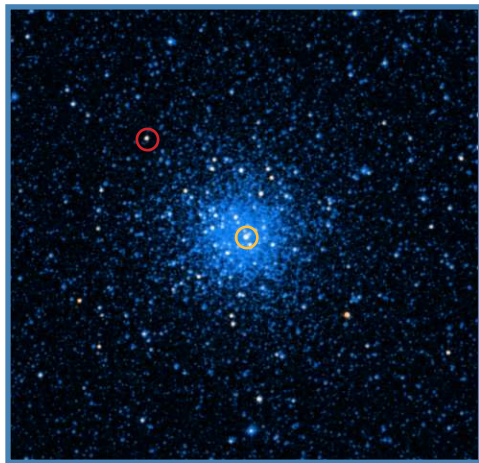
NGC5927
○ V1   ○ V3
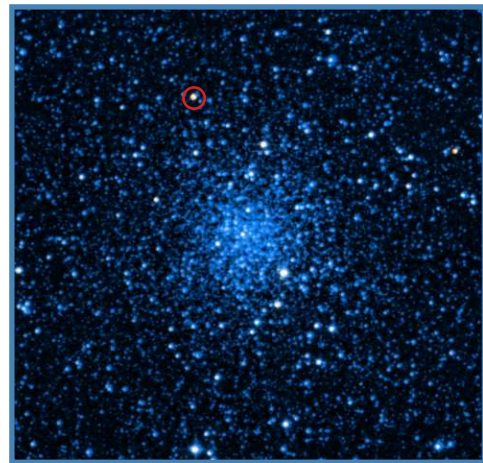
NGC6352
○ V5
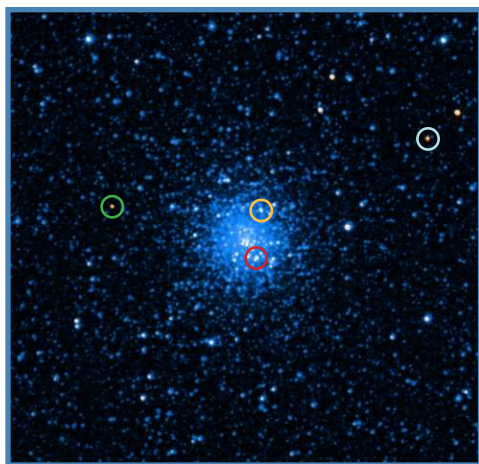
NGC6356
○ V1   ○ V3   ○ V4   ○ V5
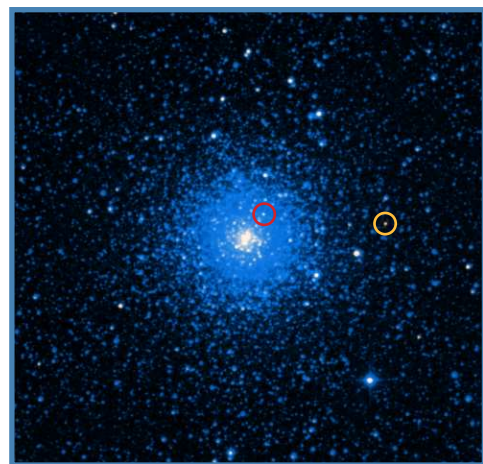
NGC6388
○ V3   ○ V4

Figure C.1: Finding Charts for the Galactic globular clusters I

138
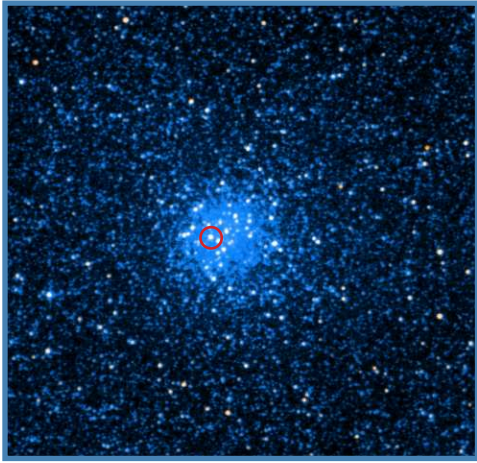
NGC6553
○ V4
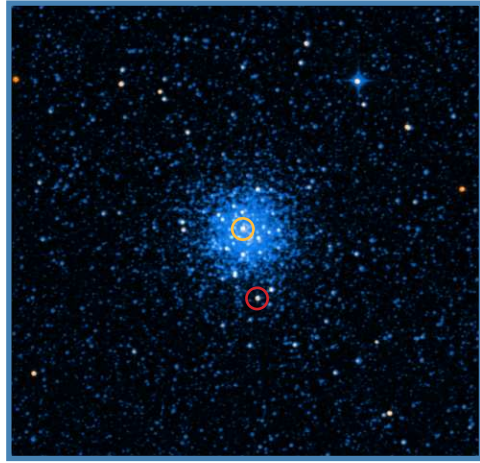
NGC6637
○ V4   ○ V5
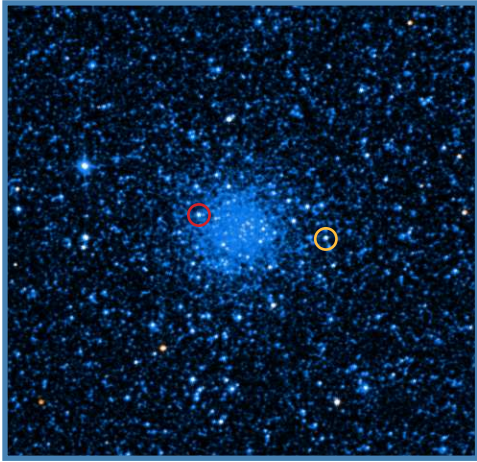
NGC6712
○ V2   ○ V7
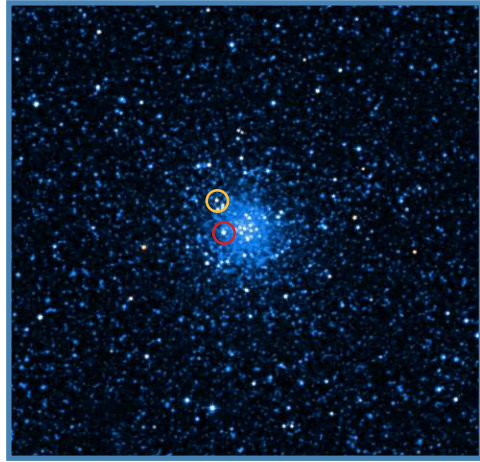
NGC6760
○ V3   ○ V4
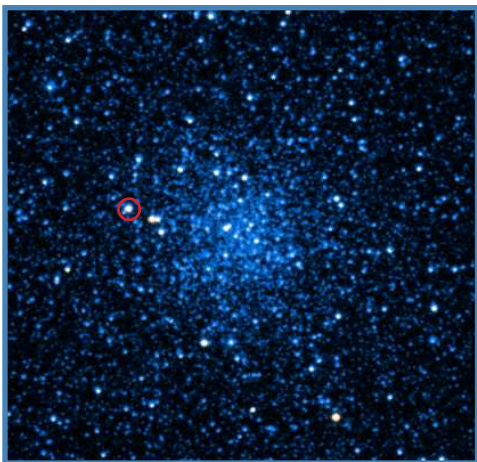
NGC6838
○ V1
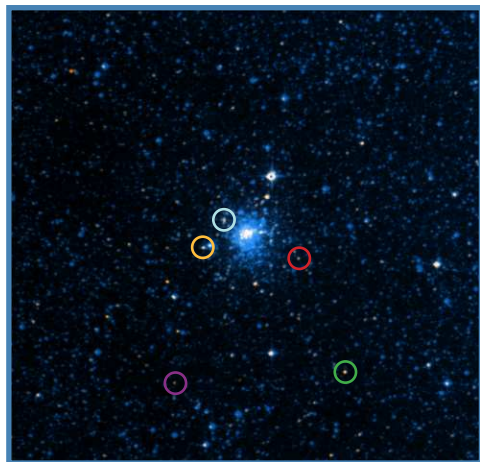
Terzan5
○ V2   ○ V6   ○ V7   ○ V8   ○ V9

Figure C.2: Finding Charts for the Galactic globular clusters II

Appendix D

Example Proposal

This is one of the proposals accepted at 8 m class telescopes that were submitted during my PhD. Even though it was not carried out in the end[1], it is a good example to show the reader how a proposal for observing time at an 8 m class telescope can look like. Since the investigation of effects of stellar variability on the MIR-spectra of AGB stars is an ongoing project, the detailed scientific rational and the technical plan are not published here. The reader is refered to contact the authors for more information.

Beside the scientific questions that should be answered with the achieved observations, a detailed observational plan has to be established while the proposal is prepared. Therefore one has to work with the specific instrument handbook to get used to all the special rules and processes that are needed during the proposal preparation, the so-called Phase I[2]. It is very important to work with the exposure time calculator of the chosen instrument to figure out the required observing time to gain a sufficient signal to noise ratio for the measurements. The time one proposes for in the end will be exactly this observing time plus the time that is assessed for the instrument and telescope overheads, respectively[3]. The presented Phase I proposal shows the final shape of a proposal for the 8 m telescope Gemini South operated by NOAO in Chile. After the proposal is accepted, one needs to prepare the so-called Phase II[4]. In this case[5] the observing tool for the MIR spectrograph *T-ReCS* at Gemini South was used to plan each single observation in detail including the target stars itself as well as the standard stars for the calibration measurements. The exact instrument configuration is established, the

---

[1] Observervations where not carried out twice because of an instrument cooling failure and bad weather conditions.

[2] Phase I rules and processes are often very different for the various telescopes and instruments. Therefore a detailed description of the Phase I at the NOAO Gemini telescopes is skipped.

[3] Probably one will even get less time granted, but never more than applied for.

[4] Phase II processes are changing from semester to semester. Therefore the details of the Phase II of this observation program are not presented in this work.

[5] Observations where accepted in service mode. This means they are carried out by the telescope staff, not by the PI of the proposal.

observing time for the individual observations is set and in collaboration with the scientific staff at Gemini one has to develop each single observation from the basic status "Phase II" to the pre-observation status "Ready"[6]. When the observations are set to "Ready" one has to wait until the observations are performed.

Resubmission of 08B-0131

NOAO Observing Proposal   Standard proposal   Panel: For office use.
Date: March 30, 2009   Category: Low Mass Stars

The role of stellar variability in mid-IR circumstellar spectra

PI: Thomas Lebzelter   Status: P   Affil.: University of Vienna
Department of Astronomy, Tuerkenschanzstrasse 17, Vienna, A1180 Austria
Email: lebzelter@astro.univie.ac.at   Phone: +43 1 4277 51854   FAX: +43 1 4277 9518

Col: Hannes Richter   Status: T   Affil.: University of Vienna
Col: Alessandro Bressan   Status: P   Affil.: INAF, Astronomical Observatory Padova
Col: Ken Hinkle   Status: P   Affil.: NOAO

Abstract of Scientific Justification   (will be made publicly available for accepted proposals) :
Theoretical investigations of the mass loss process in M giants stress the need of suitable observations that are able to clarify the role of dust in the circumstellar envelopes. Such an observational picture has been recently provided by Lebzelter et al. (2006) who showed that there is a well defined sequence of circumstellar dust along the AGB of the globular cluster 47 Tuc. The proposed evolutionary scenario, however, was based on spectra from only one epoch while previous investigations indicated possible variations of the shape of the dust features with pulsation phase. As discussed in Lebzelter et al. (2006) stellar variability would allow us to understand the scatter in the observed mid-IR spectra of AGB stars in this cluster. Here we propose testing this hypothesis by re-observing these stars and a few other stars in this cluster using T-ReCS at Gemini South. Our aim is a thorough sampling of the dust sequence along the AGB that serves as a solid basis for theoretical investigations.

---

[6]This development encludes several steps: For Review, On Hold, etc.

Appendix E

Posters

Two posters are included within this appendix to give the reader an impression of some "status quo" presentations of preliminary results of this work. The first poster was presented at the conference Dust Near And Far (Heidelberg 2008), while the second poster was presented at the conference Why Galaxies Care About AGB Stars II (Vienna 2010).

Hannes Richter[1], Thomas Lebzelter[1]
[1]Department of Astronomy, Türkenschanzstraße 17, 1180 Vienna
Contact: richter@astro.univie.ac.at

universität wien

Tracing A Dust Sequence Along The AGB
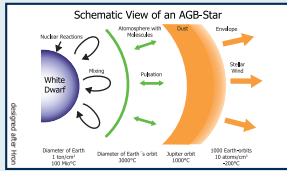
Schematic View of an AGB-Star

Introduction

Evolved stars of low and intermediate mass are considered to be the main dust producers in the universe. In their extended atmospheres and cool stellar winds one finds perfect conditions for the condensation of dust. The mass loss of AGB stars is driven by these solid particles that interact with the gas component to drag material away from the star. The circumstellar shells formed that way leave their fingerprints in the MIR-spectra. Depending on the chemistry of the stars, the C/O-ratio determines the dust species that are formed. In an oxygen-rich environment silicates and iron-oxides are produced were an carbon-rich environment leads to the formation of carbonaceous dust. In this work we will focus on oxygen-rich M-Stars and their MIR-spectra from ISO, Spitzer and ground based observations.
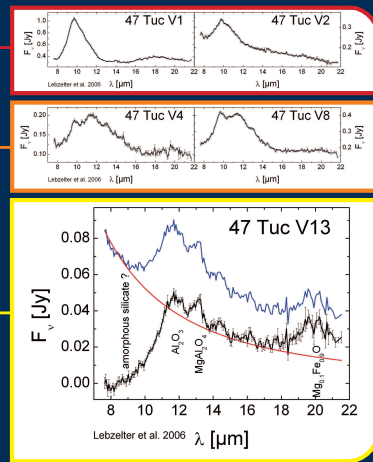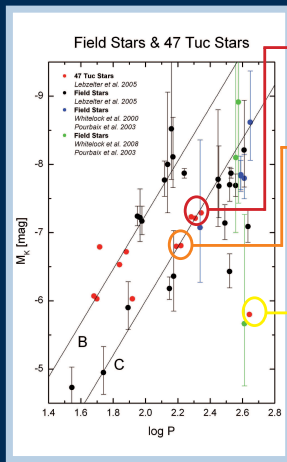
Spitzer: Dust Sequence In 47 Tuc

A detailed observational study of the dust composition of AGB stars in the globular cluster 47 Tuc shows a well defined sequence of circumstellar dust species shaping the MIR spectra as the stars evolve along the AGB. The dust composition seems to be correlated with the position within the Period-Luminosity-Diagram (left panel). Early on the AGB one sees the fingerprints of Mg, Al and Iron Oxides (V4, V8, V13). With further evolution amorphous silicates become the dominant species (V1, V2). The observations of the 47 Tuc AGB stars indicate that the 13 μm feature appears in the least evolved stars, later loses its importance relative to the 11.5 μm silicate peak and finally vanishes completely in the high luminosity stars which show a prominent 9.7 μm silicate emission. The proposed evolutionary scenario is based on Spitzer spectroscopy of a single epoch but indications for possible variations of the feature shape with the pulsation phase were found. [4]
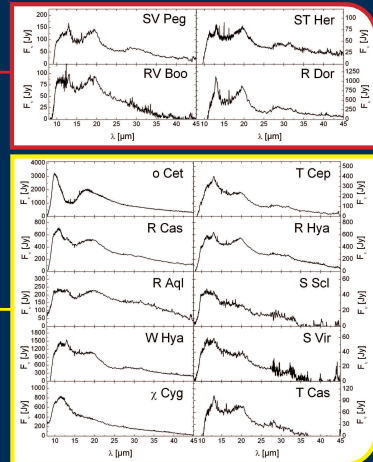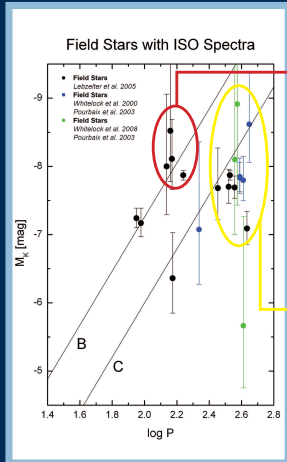
ISO: Tracing Field Star Dust Sequence

While there is a dust sequence for cluster AGB stars it is not simple to determine one in the case of field stars. Several field AGB stars with MIR-spectra from the ISO archive are plotted in a PL-diagram (left panel). One finds that all stars on sequence C are miras with fundamental mode pulsation. W Hya is the only semi-regular variable (SRV) on that sequence while all other SRVs are first overtone pulsators (sequence B). [3]

The sequence B sample of stars shows MIR-spectra with reasonably consistent dust features and prominent peaks at 13, 19.5, 28.5 and 32 μm. This resemblance gives a first hint that certain groups of stars in the PL-Diagram show identical dust features. All stars on sequence B have a 11 μm feature as well, except for the double period star R Dor.

For the group on sequence C the dust residuals show more variety. While several stars show peaks at the same positions as for the spectra of sequence B, the 11 and 13 μm feature now dominate compared to the 19.5 μm feature. No star matches the prominent 10 μm silicate emission of o Cet.

In any empirical dust evolution scenario several effects that have influence on the shape of the MIR-spectra of AGB stars have to be accounted for. Our investigations will therefore focus on the contribution of metallicity, stellar mass and stellar variability. Observations at Gemini North and South within 2008B are considered to be the next step of this multi-effect approach. New light will be shed on the importance of long and short time variability. Changes in shape and strength of the dust features on a long term basis are apparent in IRAS and ISO spectra and were reported by low-res ground based studies [1][2]. Observing field AGB stars 25 years after IRAS and 10 years after ISO will provide proper descriptions of long term effects. Short term effects were suspected for several stars in 47 Tuc [4]. Re-observing these stars will probe the impact of stellar variability on the MIR-spectra and the dust evolution.

Outlook

[1] Monnier et al. 1998   [3] Lebzelter et al. 2005
[2] Monnier et al. 1999   [4] Lebzelter et al. 2006

Hannes Richter[1], Thomas Lebzelter[1], Alessandro Bressan[2]
[1]Department of Astronomy, Türkenschanzstraße 17, 1180 Vienna
[2]INAF, Vicolo dell´Osservatorio, 5 I-35122 Padova
Contact: hannes.richter@univie.ac.at

universität
wien

Tracing Dust in old Stellar Populations

Schematic View of an AGB-Star

Introduction

Evolved stars of low and intermediate mass are considered to be the main dust producers in the universe. In their extended atmospheres and cool stellar winds one finds perfect conditions for the condensation of dust. The mass loss of AGB stars is driven by these solid particles that interact with the gas component to drag material away from the star. The circumstellar shells formed that way leave their fingerprints in the MIR-spectra of AGB stars and old stellar populations. The co-added MIR-spectra of the AGB stars in the globular cluster 47 Tuc could be used to explain the 10 μm dust excess in various early-type galaxies [2]. Co-added MIR-spectra of varous globular clusters covering a wide range of metallicities will help to improve the understanding of the MIR-spectra of old stellar populations.

Globular Clusters and their AGB Stars

38 AGB stars (12 from [6], 26 from [7], primarily **fundamental mode pulsators**) are used to produce co-added MIR-spectra of globular cluster combinations for **three metallicity groups**. Each group consists of serveral globular clusters with same age and similar metallicity. Combining the clusters leads to a higher number of AGB stars with available Spitzer spectra in each group. This poster presents the „low" metallicity group consisting of five globular clusters with 18 AGB star spectra. Stars within the 90% mass radius of each globular cluster are used to generate a **2MASS color-magnitude diagram** of the cluster combination. Binning the stars in the CMD with respect to M_K leads to a **luminosity function of the cluster combination**. To each M_K-bin the available AGB star spectra are assigned to weight the spectra with the star count. This relies on the assumption that stars that occupy the same area in the CMD are of similar mass and age and have similar MIR-spectra.

„Low" Metallicity Cluster Combination

The **co-added spectrum** of the „low" metallicity globular cluster combination **based on the 2MASS CMD** and the resulting luminosity function is compared with spectra obtained using theoretical isochrones from the Padova group [3][1]. The isochrones are used to derive **theoretical luminosity functions** for various ages, dust scenarios and mass loss descriptions. The „low" metallicity group CMD is reproduced best using either a 10 Gyr isochrone with silicate and aluminium dust or with a 12 Gyr isochrone with very low mass loss on the AGB.

A comparison of the mean spectrum with the **co-added spectrum of 47 Tuc** (one weighted with a cluster luminosity function from 2MASS, one with the **number of known variables** from [5]) is presented. In all cases the spectra and the dust residuals are dominated by the strong silicate dust emission at 10 and 20 μm. The flat dust excess of the co-added 47 Tuc MIR-spectrum due to aluminum dust presented by [2] is not reproduced by this approach.
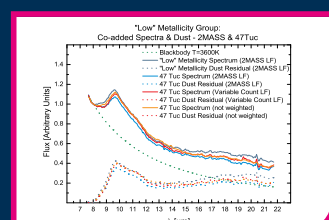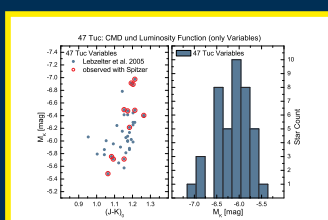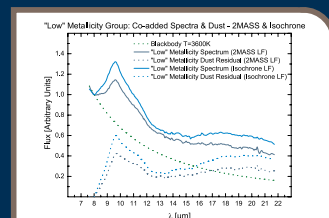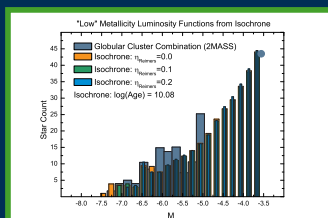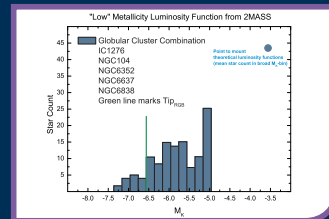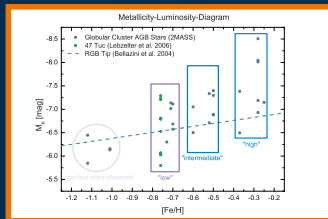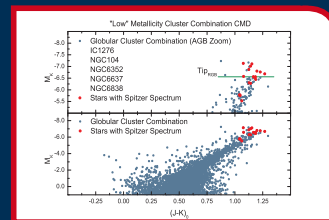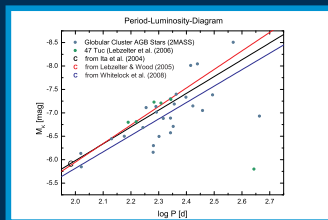
The low number of available AGB star MIR-spectra for the „intermediate" and „high" metallicity globular cluster combinations makes it difficult to generate co-added spectra representing entire old stellar populations. Except for 47 Tuc, no AGB stars have been observed that are below the tip of the RBG leading to a „tip of the iceberg" approach. The need of further observations is evident. A possible solution is to include AKARI observations to this work. AKARI data can be used to identify stars which show dust excess in various globular clusters [4]. These stars are perfect candidates for new MIR spectroscopy using the available MIR instruments at ESO's VLT, Gemini North and Gemini South.

A more complete observational covering of stars evolving up the AGB will lead to a better understanding of the integrated spectra of the hosting globular clusters and of old stellar populations in general.

Outlook

[1] Bertelli et al. 2008   [3] Girardi et al. 2000   [5] Lebzelter et al. 2005   [7] Sloan et al. 2010
[2] Bressan et al. 2007   [4] Ita et al. 2007   [6] Lebzelter et al. 2006

145

Appendix F

Laboratory Astrophysics

During the work on this thesis I was involved in a project to investigate the NIR absorption properties of O-rich stardust analogs. The collaboration with S. Zeidler, Th. Posch, H. Mutschke and O. Wehrhan resulted in a paper that was accepted to A&A and is presented here.

The study reveals the importance of laboratory measurements to improve our knowledge about the optical properties of several stardust analogs in the NIR. The maximum of the spectral energy distribution of AGB stars is located in the NIR. Thus, the absorption properties of solids in the vicinity of the star have to be accounted for especially in this wavelength area. Former studies of stardust materials often lack information on the absorption properties in the NIR due to the difficulties implied in their measurement in the laboratory. The present paper gives insight into methods and results for various stardust analogs.

The measuements of the optical constants of the stardust minerals anatase, rutile and spinel were carried out by myself using small sections of the respective materials. In addition I performed the calculations of the equilibrium dust temperatures presented as an example for the astronomical implication of laboratory astrophysics.

Near-infrared absorption properties
of oxygen-rich stardust analogs

The influence of coloring metal ions

S. Zeidler[1], Th. Posch[2], H. Mutschke[1], H. Richter[2], O. Wehrhan[3]

[1] Astrophysikalisches Institut, Schillergässchen 2-3, D-07745 Jena, Germany
e-mail: sz@astro.uni-jena.de, mutschke@astro.uni-jena.de,
[2] Institut für Astronomie, Türkenschanzstraße 17, A-1180 Wien, Austria
e-mail: thomas.posch@univie.ac.at, hannes.richter@univie.ac.at
[3] Institut für Optik und Quantenelektronik, Max-Wien-Platz 1, D-07743 Jena, Germany
e-mail: ortrud.wehrhan@uni-jena.de

ABSTRACT

Context. Several astrophysically relevant solid oxides and silicates have extremely small opacities in the visual and near-infrared in their pure forms. Datasets for the opacities and for the imaginary part k of their complex indices of refraction are hardly available in these wavelength ranges.
Aims. We aimed at determining k for spinel, rutile, anatase, and olivine, especially in the near-infrared region. Our measurements were made with impurity-containing, natural, and synthetic stardust analogs.
Methods. Two experimental methods were used: preparing small sections of natural minerals and synthesizing melt droplets under the electric arc furnace. In both cases, the aborption properties of the samples were measured by transmission spectroscopy.
Results. For spinel ($MgAl_2O_4$), anatase, rutile (both TiO_2), and olivine (($Mg,Fe)_2SiO_4$), the optical constants have been extended to the visual and near-infrared. We highlight that the individual values of $k(\lambda)$ and the absorption cross section $Q_{abs}(\lambda)$ depend strongly on the content in transition metals like iron. Based on our measurements, we infer that k values below 10^{-5} are very rare in natural minerals including stardust grains, if they occur at all.
Conclusions. Data for k and $Q_{abs}(\lambda)$ are important for various physical properties of stardust grains such as temperature and radiation pressure. With increasing $Q_{abs}(\lambda)$ due to impurities, the equilibrium temperature of small grains in circumstellar shells increases as well. We discuss why and to what extent this is the case.

Key words. stars: circumstellar matter — infrared: stars — methods: laboratory

1. Introduction

Most studies of the absorption properties of stardust analogs are focused on those wavelength ranges where the respective minerals or glasses have strong resonance features. This is usually the case in the ultraviolet range, on the one hand, and in the mid-infrared (MIR) range, on the other. Between these two ranges – i.e. between the range of strong electronic resonances and the range of strong lattice vibration resonances – there is frequently a lack of data for the complex index of refraction $m(\lambda) = n(\lambda) + i\,k(\lambda)$. This is especially true for those insulator materials that are highly transparent in the visible and near infrared (NIR), such as magnesium and aluminum silicates and oxides, since their $k(\lambda)$-values tend towards values that are too small to be measured with respect to several standard methods of spectroscopy. For example, the $k(\lambda)$-values of pure $MgAl_2O_4$-spinel would decrease from 10^{-3} at about $7\mu m$ to 2.2×10^{-13} at about $2\mu m$ according to Tropf and Thomas (1991). For $\lambda < 2\,\mu m$, no k-data are available at all from this source.

The importance of $k(\lambda)$-data characterizing stardust in the visual and NIR region becomes clear by the following argument. Dust in circumstellar shells mostly absorbs ultraviolet, visual, and NIR radiation from the stellar radiation field, thermalizes it via its internal degrees of freedom and re-emits it at mid-, as well at far-infrared wavelengths. Consider an asymptotic giant branch (AGB) star with an effective photospheric temperature of 2500–4000 K: such an object will emit most of its radiation energy close to $1\,\mu m$. Having no information on $k(\lambda)$ for $\lambda \approx 1\,\mu m$ means nothing else than being unable to calculate the energy budget of a dust-enriched stellar atmosphere. Therefore, efforts should be made to close the gaps in $k(\lambda)$ – which are usually much wider than eventual gaps in $n(\lambda)$ – where they show up in optical databases for stardust components.

For a very limited number of potential cosmic dust minerals – namely for spinel, rutile, anatase, and olivine – this task will be approached in the present paper by measuring the absorption properties depending on their content of transition metal ions as 'impurities' (colouring and absorption-enhancing).

Why do standard optical databases – especially those used in astronomical modeling – often lack absorption data for the transparency regions? Reflectance spectroscopy on bulk surfaces, which is very helpful for deriving MIR op-
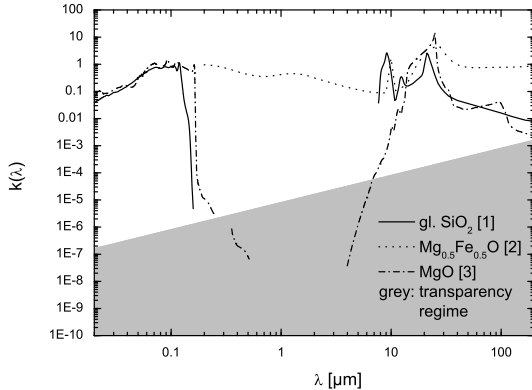
1

Appendix F. Laboratory Astrophysics

Fig. 1. Absorption indices $k(\lambda)$ for glassy SiO_2, crystalline $Mg_{0.5}Fe_{0.5}O$, and crystalline MgO from the ultraviolet to the far infrared. The gray area illustrates the 'transparency regime' as defined by Mitra (1985) and by equation (2). The sources of the data sets are [1] Philipp (1985), [2] Henning et al. (1995), and [3] Roessler & Huffman (1991).

tical constants, hardly deliver any reliable constraints on $k(\lambda)$ in the transparency regime. Here, absorption coefficients based on reflection measurements are usually nothing more than the results of extrapolations. A proper determination of the usually small absorption coefficients in the near-infrared range require transmission measurements at high column densities. Since scattering losses may compete with the effects of absorption in the visual and NIR region, homogeneous (bulk) samples are needed, i.e. sections of millimeter or tenths of millimeter thickness. These are not easy to obtain whether synthetically or from natural sources.

This paper intends to provide a guideline of how to improve $k(\lambda)$ data for the task of modeling dust absorption in the visual and NIR wavelength regions. The paper is structured in the following way. Section 2 aims at characterizing some of the absorption processes relevant to these regions. In Section 3, we describe our measurements on individual stardust analogs, namely spinel, rutile, anatase, and olivine. We present the spectra and optical constants derived for these materials, focusing on their transparency regimes. In the final Section, we discuss a specific astrophysical implication of our work, the influence of the derived $k(\lambda)$-values on dust temperatures in a radiative equilibrium.

2. The concept of the 'transparency regime'

2.1. Definition and illustration

Figure 1 shows $k(\lambda)$ for glassy SiO_2 according to Philipp (1985), for $Mg_{0.5}Fe_{0.5}O$ according to Henning et al. (1995), and for MgO according to Roessler and Huffman (1991), from the ultraviolet to the far infrared (FIR). Between the two ranges of strong absorption, where $k(\lambda)$ reaches and exceeds unity, a large region in the visual and near-infrared (NIR) can be seen, where $k(\lambda)$ drops to very low values both for SiO_2 and MgO, while this is not the case for the iron-rich material $Mg_{0.5}Fe_{0.5}O$. Recalling that the absorption

coefficient $\alpha(\lambda)$ of a solid, which enters into Lambert-Beer's law, is

$$\alpha(\lambda) = \frac{4\pi \, k(\lambda)}{\lambda}, \qquad (1)$$

we can quantitavely *define*, following Mitra (1985), the 'transparency regime' of a crystalline or amorphous solid as the region where

$$\alpha(\lambda) < 1 \, cm^{-1}. \qquad (2)$$

At a thickness of $1\,mm$, a window in this regime would transmit more than about 90% of the light entering at normal incidence; at $1\,cm$ thickness, it would still transmit at least $1/e$ or 37% of the radiation (neglecting reflection losses). In terms of $k(\lambda)$, eq. (2) defines a wavelength-dependent limit as shown in Fig. 1 (border between the gray and white areas). At $\lambda = 1\,\mu m$, for example, we may call a solid 'transparent' if $k < 8 \times 10^{-6}$. This is definitely the case for pure MgO and SiO_2. It is also true for pure crystalline $MgAl_2O_4$, α-Al_2O_3, Fe-free Mg-silicates and indeed most oxygen-rich stardust analogs without impurities. We note that for the visible/near-infrared, our transparency criterion is consistent with the statement by Bohren & Huffman (1983) who point out that already for k-values amounting to $k_{vis} \approx 10^{-4}$ bulk materials appear *black*, even in small pieces.

While the transparency regime is limited towards shorter wavelengths in the UV/visible by the edge of electronic interband transitions and possibly excitonic transitions (we give the energies and wavelengths at which strong absorption sets in Table 1), in the infrared it is limited by the energetically highest lattice vibration mode. As a rule of thumb, if a solid has a transparency region, it sets in at wavelengths shorter than

$$\lambda^* = 1/2 \, \lambda_{LO} = 1/(2\omega_{LO}), \qquad (3)$$

where ω_{LO} denotes the highest longitudinal optical frequency (in wavenumbers) and λ_{LO} denotes the corresponding wavelength (cf. Barker 1975; however, Barker uses a different criterion for the transparency and therefore derives other values for λ^*). Physically, this upper frequency limit corresponds to the limit up to which two-phonon absorption processes can be excited. Photons of shorter wavelengths (i.e. in the transparency region) can be absorbed by higher overtones, i.e. the simultaneous excitation of three or more phonons, which is less likely and does usually not lead to k values above the transparency limit. As can be seen from Table 1, transparent materials like MgO, amorphous SiO_2, $MgAl_2O_4$, and TiO_2 have two properties in common: their highest energy LO mode is located at 700 to 1400 cm^{-1}, and accordingly, their transparency regime sets in at wavelengths below 7.1 to 3.6 μm. This is also the wavelength region where many sets of optical constants derived from infrared measurements come to an end because there is a lack of physically meaningful k values (as mentioned above).

For nonconducting materials, there is an FIR transparency regime as well. At wavelengths greater than a few hundred micrometers, k again drops to values lower than 10^{-3} to 10^{-2}, which are low enough to fulfill (2). Measurements in this wavelength range, therefore, bear some similarities to near-infrared measurements, although

2

Table 1. Electronic band edges including strong excitons in terms of energy E_g, wavelength λ_g, longitudial optical lattice frequencies ω_{LO}, and onset wavelengths λ^* for the transparency regions for different materials (see text for more details).

Material	E_g [eV]	λ_g [μm]	ω_{LO} [cm^{-1}]	λ^* [μm]	Ref.
Am. SiO$_2$	8.3	0.15	1245	4.01	[1]
MgO	7.5	0.17	728	6.87	[2]
MgAl$_2$O$_4$	7.75	0.16	877.2	5.7	[3]
Mg$_2$SiO$_4$	7.5	0.17	1078	4.6	[4],[5]
TiO$_2$ rutile	2.9	0.43	831.3	6	[6]
TiO$_2$ anatase	3.2	0.39	872.8	5.7	[7],[8]
FeO	2.3	0.54	526	9.5	[9],[10]

[1] Philipp (1985); [2] Roessler & Huffman (1991); [3] Tropf and Thomas (1991); [4] Shankland (1968); [5] Sogawa et al. (2006); [6] Ribarsky (1985); [7] Tang et al. (1993); [8] Posch et al. (2003); [9] Park et al. (1999); [10] Henning et al. (1995).

wavelengths and absorption mechanisms are different. Data in this wavelength range are additionally limited by the availability of FIR-spectrometers.

2.2. Causes of transparency and of absorption in the NIR region

It can furthermore be seen from Fig. 1 that there are materials without any transparency regime within the wavelength range shown. $Mg_{0.5}Fe_{0.5}O$ – a solid solution of MgO and FeO – is an example of such a material. FeO is a semiconductor, in contrast to MgO and SiO$_2$. Actually, it is a nonstoichiometric compound, its sum formula should better be written as $Fe_{1-x}O$. Therefore, it contains both Fe^{2+} and Fe^{3+} ions, the content of Fe^{3+} is 0.09 according to Henning et al. (1995). These two properties lead to various absorption mechanisms for wavelengths in the visible and near infrared, as well as the FIR, which are not present or occur at different wavelengths for the previously discussed iron-free oxides, but are efficient in all the members of the series $Mg_xFe_{1-x}O$ (x<1). Among these mechanisms are

1. the fundamental interband absorption edge occurring in the visible wavelength range (band gap 2.3 eV for FeO, according to Park et al. 1999);
2. free electron excitations causing the increase of $k(\lambda)$ towards the FIR. For FeO, this absorption mechanism should be weak, but a part of the material, which is metastable at room temperature, may be decomposed into Fe and Fe$_3$O$_4$, which both have high free-electron densities (at room temperature for Fe$_3$O$_4$);
3. charge transfer transitions between the orbitals of Fe^{3+} and those of other metal or ligand ions, that are an important source of strong absorption in the visible extending into the near infrared;
4. the splitting of the d-electron energy levels in transition metal ions, depending on their coordination by oxygen ions. In case of lower symmetry, transitions between these d-electron states can lead to moderately strong absorption bands (so-called crystal field bands, Burns 1993).

The last three mechanisms can obviously enhance the absorption in otherwise transparent wavelength ranges above the transparency limit. All three of them and even

Table 2. Mean cosmic elemental abundances of selected transition metals according to Palme and Beer (1993).

Element	abundance log N (N(H)=10^{12})
Sc	3.1
Ti	4.96
V	4.00
Cr	5.68
Mn	5.45
Fe	7.49
Co	4.91
Ni	6.24

more absorption mechanisms, such as vibrational excitation, can be introduced by impurities.

If a (stardust) mineral is transparent at near-infrared and visual wavelengths in its pure, ideal, stoichiometric form, it may in reality contain 'impurities' that strongly increase $k(\lambda)$. This phenomenon is well known in geochemistry and mineralogy, but rarely accounted for in astromineralogical applications. The most efficient 'enhancers' of $k(\lambda)$, consequently of mass absorption coefficients (opacities), are transition metals: Sc, Ti, V, Cr, Mn, Fe, Co, and Ni. Among them, Fe, Ni, Cr, and Mn are probably the most relevant for stardust minerals considering the mean cosmic elemental abundances (Burns 1993).

Any significant inclusion of transition metal ions into an originally transparent mineral will turn its appearance in the visual spectral range from colorless to colored or even black. At present, it is hardly known which amounts of transition metal ions are actually present in stardust minerals as 'impurities', but it is unrealistic to expect impurity-free minerals in circumstellar and interstellar environments.

Even though several visually transparent oxides such as spinel and Al$_2$O$_3$ have been identified in presolar grains, it has not yet been possible to determine the transition metal content of these minerals; in other words, their 'color' has not been quantitatively measured. Spectroscopic methods determining the transition metal content of cosmic dust by 'remote sensing' are restricted, up to now, to reflectance spectroscopy of lunar and planetary surfaces (Burns 1993).

Therefore, in the present paper, we chose the following approach when synthetically including transition metals into oxides: We based our measurements of $k(\lambda)$ partly on natural terrestrial samples, which always contain impurities to some extent, and we were partly able to widen the range of possible inclusions of transition metals by producing synthetic samples. For one of our samples, spinel, it was thus possible to create a series of samples and corresponding sets of optical constants such as exploring the possible range of absorption that may occur in samples of cosmic elemental composition.

3. Individual measured stardust analogs

3.1. Derivation of $k(\lambda)$ from the transmission spectra

The method we applied to derive $k(\lambda)$ was transmission spectroscopy of small sections of our materials. For producing these sections we embedded pieces of our materials with sufficient size (diameter >0.5 mm) into resin and cut and abraded the resin slabs to thicknesses between 80 and

3

1100μm. After that, the samples were just polished to have an even and smooth surface.

Some of the examined materials are crystals of non-cubic symmetry and therefore optically anisotropic; i.e. their optical constants depend on their orientation relative to the polarization direction of the light. For these materials, it has been necessary to perform measurements with polarized radiation. An overview of the sample properties such as chemical composition determined by energy-dispersive X-ray analysis (EDX), crystal symmetry, and slab thickness is given in Table 3 (the oxygen content is not a direct result of the EDX measurements, but has been inserted according to stoichiometry).

For the spectroscopic measurements, the following spectrometers have been used: a Perkin Elmer Lambda 19 (for the wavelength range from 0.275 to 2 μm), a Bruker FTIR 113v (for the wavelength range from 1.6 to 25 μm), and a single-beam optical absorption spectrometer constructed on the basis of a SpectraPro-275 triple-grating monochromator. The actual range of the transmission measurements is limited by the wavelengths at which the samples become opaque. For a typical sample thickness of 300 μm, this happens for a k value of about 10^{-3} on the short-wavelength side and at a few 10^{-2} on the long-wavelength side. The transmittance values (transmitted intensity normalized by incident intensity) were converted in $k(\lambda)$ using the relation

$$k(\lambda) = -\frac{\lambda}{4\pi d} \ln\left\{\frac{T}{(1-R)^2}\right\}, \tag{4}$$

where d is the thickness of the small section and the reflectance R is given as

$$R = \frac{(n(\lambda)-1)^2 + k(\lambda)^2}{(n(\lambda)+1)^2 + k(\lambda)^2}. \tag{5}$$

For very small values of $k(\lambda)$ this equation reduces to

$$R = \frac{(n(\lambda)-1)^2}{(n(\lambda)+1)^2}. \tag{6}$$

While using $n(\lambda)$ values from Palik (1985-98) we were able to derive values for $k(\lambda)$ for various samples.

The following subsections contain a presentation and discussion of our results for the individual materials. The derived k values for the NIR will be made publicly available on the Jena Database of Optical Constants, http://www.astro.uni-jena.de/Laboratory/Database/databases.html

3.2. Spinels

3.2.1. Material properties, sample preparation and analysis

Spinel is an abundant component of presolar grains from meteorites (e.g. Hoppe 2004) and has been proposed as the carrier of mid-infrared emission bands observed in the spectra of circumstellar dust shells (e.g. Posch et al. 1999, Fabian et al. 2001). Pure stoichiometric spinel ($MgAl_2O_4$) has an elementary cell that consists of 32 O anions, 16 Al, and 8 Mg cations. In the ideal crystal lattice, the trivalent Al cations are octahedrally coordinated by oxygen ions, while the bivalent Mg cations are tetrahedrally coordinated. The cubic lattice symmetry of this mineral make it optically isotropic.
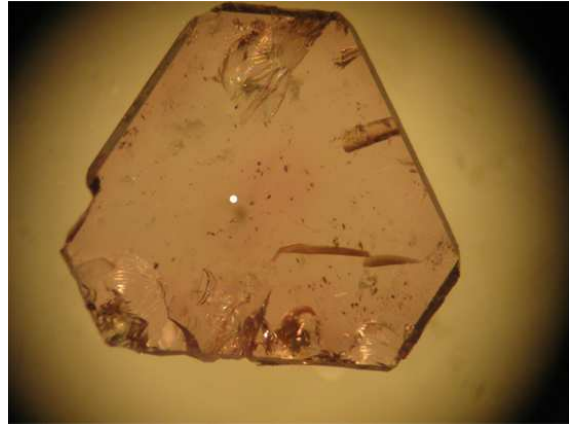
Fig. 2. Section of the spinel crystal from Burma used for deriving $k(\lambda)$ from transmission spectroscopy. From bottom to top this crystal has a size of around 3 mm.

While many previous publications refer to impurity-free spinels, the measurements presented in this paper refer to a series of spinels that contain impurities (mainly chromium and iron). The Cr ions partly substitute Al, so they occupy a part of the octahedral sites. The Fe ions partly substitute Al, partly Mg. Because the lattice structure of the Cr-containing spinels is unambiguous (since Cr is not polyvalent in contrast to Fe), we have chosen synthetic Cr-doped spinels as a representative of the effect of impurities on k, even though it is much more likely to have Fe impurities in spinels due to the much higher stellar abundance of Fe compared to Cr as given in Table 2.

Additionally, a dark-red natural spinel crystal from Burma was examined. Apart from a very small amount of Si, it contains traces of both Fe and Cr. The exact chemical composition of the sample is given in Table 3.

The synthesis of the Cr-doped spinels was performed in the following way (see also Richter et al. 2005). We used a tungsten electric-arc furnace with a water-cooled copper baseplate. Powders of Mg oxide, Al oxide, and Cr(III) oxide have been mixed in corresponding proportions so as to obtain the basic material for the melting procedure. After being homogenized, the mixture was pressed into several pellets of 150–300 mg mass each and a diameter of 1.3 cm each. This densification of the powder was necessary to avoid electrostatic interactions between the tungsten pike in the furnace and the powder particles when starting the melting process. Since Mg oxide in particular is a hardly fusable material, the pellets were broken again into several pieces (4–7 for each pellet) to facilitate the melting process. After putting several pieces into the furnace, the melting process started under a 1 bar argon atmosphere. The samples were exposed to the electric arc until they were fully melted. The formation temperature should be close to the melting point of spinel (about 2400 K), and it probably increased with the Cr content (the melting point of Cr_2O_3 is about 2700 K). After cooling to subliquidus temperature within a few seconds and subsequent cooling to room temperature, we obtained melt-droplets that were 3–5 mm in size and had colors ranging from light red in the most Cr-poor spinel to dark red (almost black) in the most Cr-

4

Table 3. Compositions of the samples and thicknesses of the platelets examined in this paper.

sample	chemical composition	thickness	crystal symmetry
Natural Spinel[†]	$Mg_{1.02}Al_{1.93}Cr_{0.0087}Fe_{0.012}O_4$	$250\mu m$	cubic
Synth. Spinel 1	$Mg_{1.00}Al_{1.98}Cr_{0.02}O_4$	$80\mu m$	cubic
Synth. Spinel 2	$Mg_{0.93}Al_{1.99}Cr_{0.03}O_4$	$270\mu m$	cubic
Synth. Spinel 3	$Mg_{0.98}Al_{1.89}Cr_{0.12}O_4$	$120\mu m$	cubic
Synth. Spinel 4	$Mg_{0.98}Al_{1.78}Cr_{0.23}O_4$	$80\mu m$	cubic
Natural Rutile[†]	$Ti_{0.984}V_{0.008}Fe_{0.008}O_2$	$155\mu m$	tetragonal
Natural Anatase	$Ti_{0.992}V_{0.008}O_2$	$255\ \mu m$	tetragonal
Olivine San Carlos	$Mg_{1.96}Fe_{0.16}Si_{0.89}O_4$	$1063/1115\mu m$	orthorhombic
Olivine Sri Lanka	$Mg_{1.56}Fe_{0.4}Si_{0.91}O_4$	$300\mu m$	orthorhombic

† The natural spinel and rutile samples have small ($< 1\%$) OH contents that are not shown in the formula.
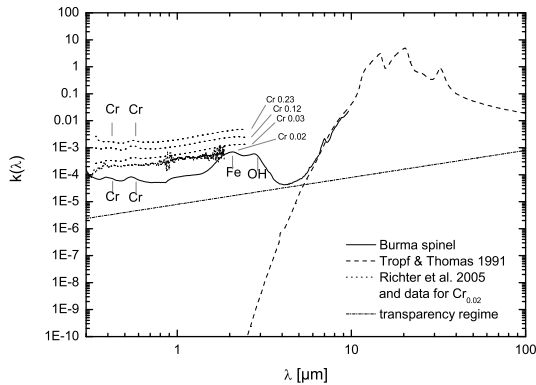
Fig. 3. Absorption indices $k(\lambda)$ of different spinels derived from transmission spectroscopy. For the interpretation of the different bands seen in the spectra, see text.

rich sample. The theoretical compositions of the samples are given by $MgAl_{(2-x)}Cr_xO_4$, with x amounting to 0.02, 0.03, 0.12, and 0.23.

The exact chemical compositions were derived from EDX analyses, where several (typically 12) spots for each of the Cr-spinel droplets were scanned and investigated for inhomogeneities and variations in the Mg/Al/Cr ratios. Tab. 3 gives the resulting mean stoichiometries – also for the TiO_2 and olivine samples discussed in Sections 3.3 and 3.4.

3.2.2. Measured transmission spectra and derived $k(\lambda)$ values

We now present and interpret the results of the transmission spectroscopy performed on the above-mentioned samples at UV-, visual, near-infrared, and mid-infrared wavelengths.

The measured transmittances were converted into $k(\lambda)$ values by applying (4) and Fig. 3 shows the derived results. The dashed line represents $k(\lambda)$ for pure stoichiometric spinel according to Tropf and Thomas (1991). The mid infrared maxima of $k(\lambda)$ – between 10 and $40\mu m$ – correspond to three vibrational modes of the lattice structure: The origin of the $31\text{-}32\mu m$ band is an Mg–O vibration, while the remaining two maxima originate from Al–O vibrations. For further details see Fabian et al. (2001).

It can be clearly seen from Fig. 3 that for the impurity-free spinel – and *only* for this one – a very steep decrease of $k(\lambda)$ with decreasing wavelength occurs at $\lambda < 7\,\mu m$.

The solid line denotes $k(\lambda)$ for our natural sample from Burma which contains about 1% iron and approximately as much chromium. This $k(\lambda)$-curve begins to deviate from the corresponding line for pure spinel at $6\text{-}7\,\mu m$ and never drops below the limit of the transparency regime, in accordance with the opaque character of the 0.25mm thick sample. Within the range of rough agreement between the two curves ($> 7\,\mu m$), there is some structure in our new data, especially a peak at $\sim 7\,\mu m$, which is likely an overtone of the $13\text{-}14\,\mu m$ lattice vibration band.

Between 4 and $1.5\,\mu m$, a *broad* maximum occurs with its origin in the Fe^{2+} and OH^- content of the sample. Even though the OH content is very small (definitely below 1%), it is sufficient for the O-H stretching vibration band to appear in the spectrum as a narrow band at $2.8\,\mu m$. Then $k(\lambda)$ approaches values even close to 10^{-3} at the center of this band. The same holds true for the maximum of the Fe^{2+} band, which is located at $2.0\,\mu m$. A detailed interpretation of the Fe^{2+} and OH^- bands in natural and synthetic spinels can be found in a recent paper by Lenaz et al. (2008). A comparison between our data and those published by Lenaz et al. (2008) is shown in Fig. 4.

The region below $1\,\mu m$ is characterized by further electronic absorption mechanisms. In this region, the $k(\lambda)$ spectra strongly depend on the Cr content of spinel. This can be nicely seen by comparing the solid line with the dotted lines, which represent the Cr-doped synthetic spinels.

The Al to Cr substitution in the samples results in a generally increased visual and UV absorption. Additionally, two distinct absorption bands occur around $0.550\,\mu m$ and $0.387\,\mu m$. The positions of these bands accordance well with the band positions in spectra of low-Cr Mg-Al- spinels – both natural and synthetic ones – published by Wood et al. (1968), Taran et al. (1994), and Ikeda et al. (1997). These bands originate from crystal field electronic transitions, namely $^4T_{2g} \leftarrow {}^4A_{2g}$ for the $0.550\,\mu m$ maximum and $^4T_{1g} \leftarrow {}^4A_{2g}$ for the $0.387\,\mu m$ maximum. Of course, the intensity of the Cr electronic absorption bands is higher for the synthetic Cr-doped samples, and k-values up to 2×10^{-3} are reached at $0.550\,\mu m$ for 12% Cr content.

3.3. Rutile and anatase (TiO$_2$)

Together with Ca and Al oxides, Ti oxides are considered as candidates for the very first condensates in oxygen-rich circumstellar shells, notwithstanding that titanium is rather

5

S. Zeidler, Th. Posch, H. Mutschke, H. Richter, O. Wehrhan: NIR properties of oxygen-rich stardust
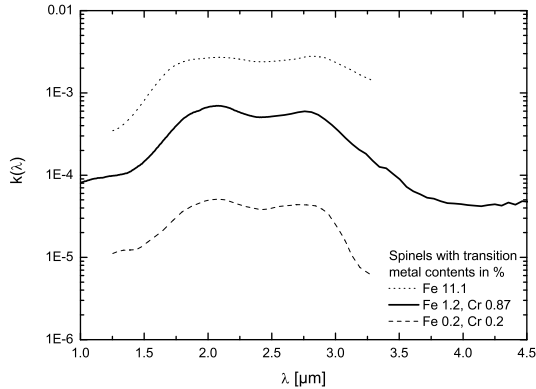

Fig. 4. Comparison between the absorption indices derived for spinels with different transtion metal content. The solid line refers to our sample – with an Fe content of 1.2% and a Cr content of 0.87%. The dotted line refers to a very Fe-rich sample (Fe-content of 11.1%), the dashed line denotes an Fe-poor sample (both according to Lenaz et al (2008)). The Fe content of the samples clearly correlates with the respective k-values at $2\mu m$.

rare according to its mean cosmic elemental abundance (2.5 orders of magnitude less abundant than Si and Mg). With respect to dust formation in circumstellar shells, it is noteworthy that molecular TiO is extremely prominent in the atmospheres of M- and S-stars. Furthermore, titanium is heavily depleted in the interstellar gas, indicating that it is indeed consumed by previous dust formation processes.

Jeong et al. (2003) predict that TiO_2 is the most promising candidate for the first (seed-)condensate in oxygen-rich circumstellar shells. There is also evidence from meteoritics that Ti compounds form in circumstellar shells and a presolar meteoritic TiO_2 grain has been tentatively identified (Nittler 2003).

We examined the two most common terrestrial species of TiO_2 with respect to their near infrared absorption properties, namely anatase and rutile. Both materials have a tetragonal crystal symmetry, hence only one optical axis. Consequently, the measurements for the polarization directions parallel and perpendicular to this optical axis could be performed on a single sample cut along this axis by rotating the polarizer by 90 degrees.

$k(\lambda)_{NIR}$ is not unmeasurably small in the case of our samples due to their Fe and V contents. The Fe- and V-contents of our TiO_2 samples have been determined by energy-dispersive X-ray measurements and are summarized in Table 3

3.3.1. Rutile

Rutile is the most abundant modification of titanium dioxide on the Earth. It has tetragonal symmetry like anatase, but is characterized by a higher density, a greater Ti-Ti distance, and a shorter Ti-O distance than the latter. As for rutile's ultraviolet and mid-infrared properties, Ribarsky (1985) compiled a rather comprehensive table of optical
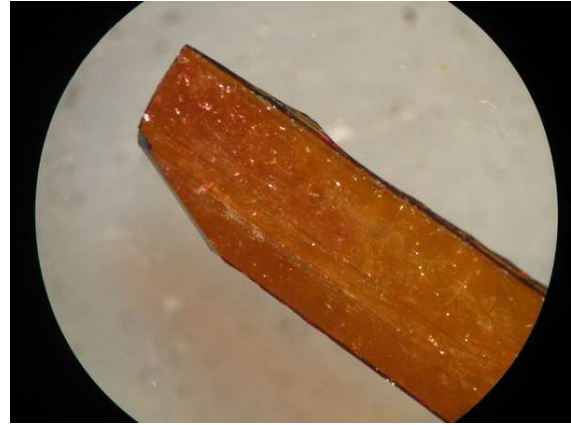
Fig. 5. Section of the rutile crystal used for deriving $k(\lambda)$ from transmission spectroscopy. The crystal has a width of about 1.5 mm.
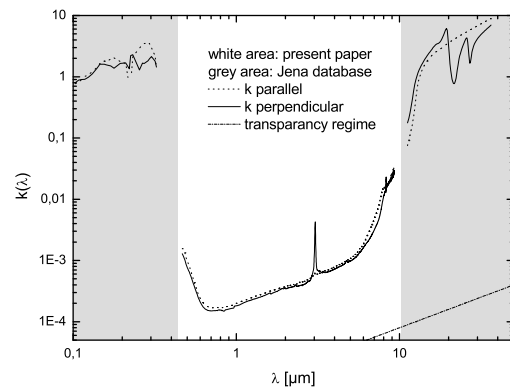
Fig. 6. Absorption index $k(\lambda)$ for rutile (TiO_2) derived from transmission measurements on a small section of $155\,\mu m$ diameter. The $k(\lambda)$ values in the UV and MIR are from Palik (1985-98). The sharp peak in $k(\lambda)$ comes from a small crystal water content of the natural sample.

constants. However, for wavelengths between $0.4\,\mu m$ and $11.2\,\mu m$, data for $k(\lambda)$ are largely missing.

We were able to measure k for a natural rutile sample from 0.5 to $8\,\mu m$, based on a section with a thickness of d=$155\,\mu m$ (see Figs. 5 and 6). The most significant feature in the NIR k-spectrum of rutile is a sharp peak at $3.03\,\mu m$. This peak, which becomes especially prominent when the electric field vector of the polarized radiation is perpendicular to the c-axis of the crystal, is due to an OH stretching mode (see Maldener et al. 2001). It is explained by the presence of H_2O in natural rutile. The $3.03\,\mu m$ band of our sample may be explained with an H_2O content of the order of magnitude of 300 weight ppm, based on the spectra and analytical results by Maldener et al. (2001).

6
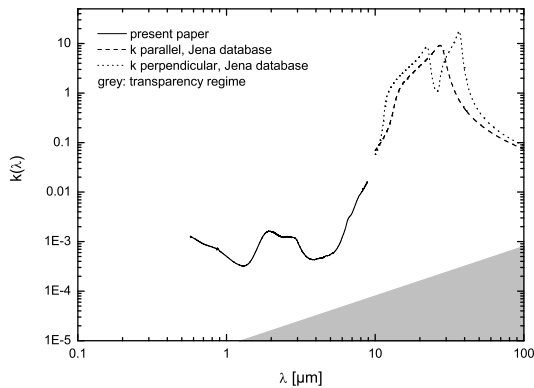
Fig. 7. Absorption index $k(\lambda)$ of the TiO$_2$ modification anatase derived from transmission spectroscopy. The values for $\lambda > 10\,\mu$m are from Posch et al. (2003).

3.3.2. Anatase

Anatase is a modification of tetragonal Ti oxide with a TiO$_6$ octahedron structure consisting of one Ti^{4+} and six O^{2-} ions. It can be transformed to rutile by heating above 1200 K. Its mid-infrared optical constants have been published by Posch et al. (2003).

For anatase we used a section of d=255 μm thickness to perform transmittance measurements between 0.7 and 8 μm. The transmittance spectra obtained for the individual orientations of the sample relative to the polarized radiation did not differ within the measurement's accuracy, therefore only one curve is plotted in Fig. 7.

The most conspicuous feature in the $k(\lambda)$ spectrum of anatase is the broad double-peaked band 2–3 μm. Maximum k values of more than 0.001 are reached in this range. The second of the two peaks, located at 3.0 μm, corresponds to an O–H stretching mode at 3389.7 cm-1. It is an indirect consequence of the V content of our sample, since V-containing TiO$_2$ has a stronger hydroxyl content (Zhou et al. 2010). The primary peak in the absorption, located at 2.0 μm, may be directly caused by the V content of the sample.

3.4. Olivine

Olivine is, together with pyroxene, the most abundant crystalline silicate in space. Its prominent bands are observed in many spectra of accretion disks around young stars and in the outflows of AGB stars (Henning 2003, 2003). Olivine also occurs in our solar system in the form of cometary dust (Hanner 2003), as interplanetary dust particles (Bradley 2003), and on planetary surfaces (e.g. Hartmann 2005).

Olivine has the general sum formula (Mg,Fe)$_2$SiO$_4$ with its Mg end member forsterite and the rarer Fe end member fayalite. On Earth, olivine is the most abundant material in the upper lithosphere. In general, more Mg-rich and less Fe-rich olivines are found. It crystallizes in orthorhombic symmetry with isolated [SiO$_4$]$^{4-}$ tedrahedra surrounded by metal cations (Fe^{2+}, Mg^{2+}), each in coordination to six oxygen atoms. There are two different types of these coordinations, both slightly distorted from the octahedral symmetry. One is centrosymmetric and elongated along one of the O–O axes (cation sites in this coordination are called 'M1'), and the other is non-centrosymmetric and irregular ('M2'; cf. Burns 1993).

Olivine crystals usually have a greenish to yellowish color, which can turn into brown when it contains traces of Fe^{3+} ions. The greenish coloring is caused by a crystal field band of Fe around 1 μm wavelength, which leads to an increased opacity for red light and an increased transmittance of yellow and green light. The brownish coloring comes from charge transfer processes toward the Fe^{3+} ions leading to absorption increasing throughout the visible wavelength range towards the ultraviolet. This kind of absorption has been detected in the central parts of our Sri Lanka olivine sample (see below), where cracks may have given rise to oxidation of Fe^{2+} in interface regions.

In the present paper, we compare near-UV to MIR absorption spectra of $k(\lambda)$ of San Carlos olivine single crystals with spectra of an Fe-rich variety of olivine obtained from Ratnapura (Sri Lanka) (Fe contents: 8% and 20%, respectively – see Table 3). Since olivine crystals have non-cubic symmetry, the polarization of the incoming radiation relative to the three crystallographic axes x, y, and z plays an important role in the resulting spectra. Several platelets of the San Carlos olivine have been prepared to have a surface perpendicular to one of these axes. Two of them, denoted as C and D1, have been chosen to represent the properties of oriented olivine in polarized light due to the quality of their spectra. Sample C has been cut along the y-z plane, sample D1 along the x-y plane, so all three crystallographic axes were available for the measurements. The thicknesses are 1063 μm for sample C and 1115 μm for sample D1. For the Sri Lanka olivine, only measurements of light polarized along the y- and z-axes ($E||y$ and $E||z$) were possible, since only one platelet (thickness: 300 μm) could be prepared. The sample is shown in Fig. 8. For these measurements we chose an area of about 1 mm diameter without cracks, which can be seen in the figure. This area is also free of brownish colouring which occurs along the major cracks in the middle of the sample. The surface of this platelet is also not perfectly oriented perpendicular to the x-axis, because an inclination of approximately 20° could be measured by X-ray diffraction.

The most important differences in the absorption spectra between the different oriented samples of San Carlos olivine are found in the bands caused by transitions of the metal cations, located around 0.7–1.5 μm. While $E||y$ and $E||z$ polarized light creates broad structures with peaks around 1.056 μm and 1.108 μm, light polarized along the x-axis creates a more prominent band around 1.073 μm. Shoulders appear in all three polarizations on both sides of the main peak around 0.87 μm and between 1.25 and 1.35 μm. The value of k in the maxima of this band reaches $\sim 1.8 \times 10^{-4}$ for both $E||y$ and $E||z$, while k reaches a value of $\sim 4 \times 10^{-4}$ for $E||x$. The corresponding values for the Sri Lanka olivine are given in Table 4. The k values of this band are increased compared to the measurements of the San Carlos olivine in the same polarization (in its maxima by a factor of ≈ 2) and also the particular positions of band and shoulders are shifted to longer wavelengths, except for the short-wavelength shoulder that shifts to shorter wavelengths.

7

S. Zeidler, Th. Posch, H. Mutschke, H. Richter, O. Wehrhan: NIR properties of oxygen-rich stardust

Fig. 8. Platelet of the Fe-rich Sri Lanka sample used for transmission measurements under polarized light. The sample has a width of 4 mm and a length of 6 mm. The black circle features the spot of the measurements.
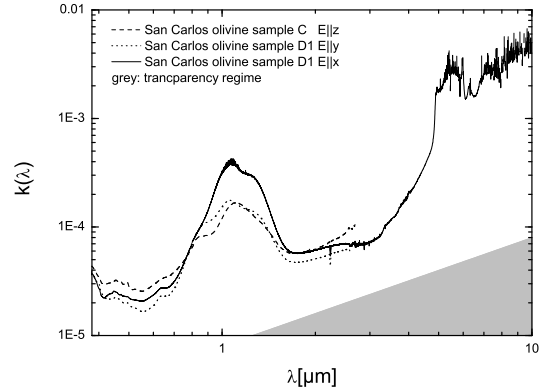

Fig. 9. Spectra of oriented San Carlos olivine in polarized light. The spectra were measured from samples C and D1 (see text for further details).

Table 4. Specific positions and k values for the main peaks ('mp') and shoulders ('sh I' and 'sh II') of the crystal field band caused by Fe ions of the San Carlos (SC) and Sri Lanka olivines (SL), respectively.

	sh I [μm]	k_{max} $\times 10^4$	mp [μm]	k_{max} $\times 10^4$	sh II [μm]	k_{max} $\times 10^4$
SC						
$E\|x$	0.827	0.90	1.074	4	1.232	3.02
$E\|y$	0.882	1.11	1.057	1.78	1.234	1.43
$E\|z$	0.858	0.83	1.114	1.65	1.323	1.12
SL						
$E\|y$	0.838	2.08	1.069	3.77	1.255	3.04
$E\|z$	0.831	1.63	1.14	3.33	1.378	1.76

The continuum k values are in general relatively independent of the polarization and increases constantly towards longer wavelengths (see Fig. 9). Toward shorter wavelengths we cannot see an absorption increase, which indicates noticeable charge transfer processes. The sharp increase in k at around 0.4 μm, which becomes more pronounced with increasing Fe content, is due to the onset of intrinsic transitions of the Fe^{2+} ions. The continuum k value is independent of the Fe content of the olivine, which is remarkable.

Towards longer and towards shorter wavelengths from the crystal field band at around 1 μm, several very weak bands appear. The bands at shorter wavelengths are comparatively sharp and appear independently of the polarization at 0.65, 0.49, 0.47, and 0.45 μm. These bands come from the spin forbidden transitions in the Fe^{2+} ions (Burns 1993). In contrast to that, the structures at longer wavelengths show a polarization dependence. For the Sri Lanka sample in $E\|y$ polarization, a broad and relatively strong band can be seen at 3 μm, which is due to the stretching vibrations of OH groups. For the $E\|z$ polarization this band is much sharper, similar to the corresponding band in the rutile. Around the 5.5 μm wavelength, another band is located, which is likely an overtone of the 10 μm stretching vibration band of the SiO_4-tetrahedron.
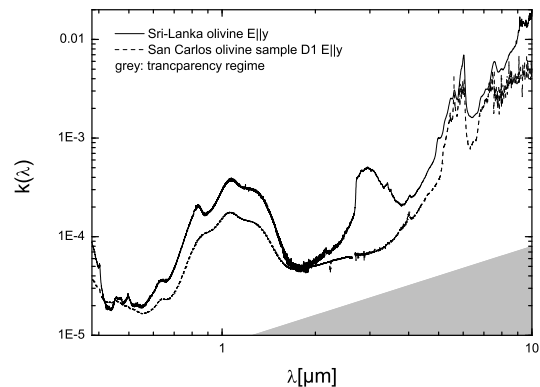
Fig. 10. Spectra of oriented San Carlos and Sri Lanka olivines in polarized light for $E\|y$. For the San Carlos olivine spectra of sample D1 are shown.

4. The influence of $k(\lambda)$ on the temperature of small grains

In the present section, we apply our results for the magnitude of $k(\lambda)$ to the calculation of the radiative equilibrium temperature of dust grains, which is an important parameter characterizing the conditions in dust-forming regions like circumstellar shells, and it indeed depends on absorption and emission properties. In the case of a thermodynamical equilibrium between the stellar radiation field (assuming a star with radius R_* with an effective temperature T_*) and the dust grains in an optically thin circumstellar shell, it is possible to derive the dust temperature T_d for a given distance from the star from the energy balance. The radiative energy *absorbed* by an individual dust grain is then given by

$$E_{abs} = D_{rad}\, I_1, \tag{7}$$

8
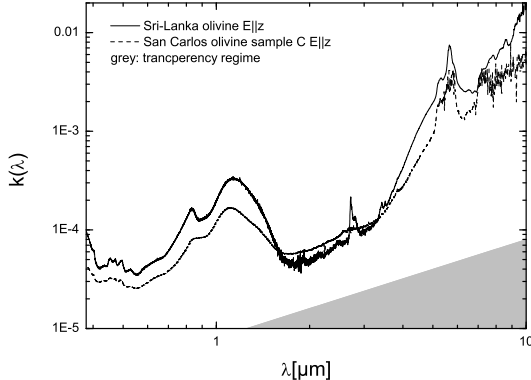
Fig. 11. Spectra of oriented San Carlos and Sri Lanka olivines in polarized light for $E||z$. For the San Carlos olivine, spectra of sample C are shown.

where

$$I_1 = \int_0^\infty \pi a^2 Q_{\mathrm{abs}}(\lambda) \pi B(\lambda, T_*) d\lambda, \tag{8}$$

and D_{rad}, the radial dilution factor of the stellar radiation field, is defined as

$$D_{\mathrm{rad}} = 2[1 - \sqrt{1 - \frac{R_*^2}{R_{\mathrm{d}}^2}}]. \tag{9}$$

Here, R_* denotes the effective stellar radius, and R_{d} is the distance of a dust grain from the star's center. Equation (9) is based on the so-called Lucy-approximation (Lucy 1971), according to which the star is not considered as a point source, but its spatial extension is taken into account, which is important for small distances of the dust grains from the star. Already for a distance of 3 stellar radii, the dilution factor D_{rad} may be simplified to R_*^2/R_{d}^2.

The radiative energy *emitted* by a single (spherical) dust grain with the radius a is given by

$$E_{\mathrm{em}} = I_2 = \int_0^\infty 4\pi a^2 Q_{\mathrm{abs}}(\lambda) \pi B(\lambda, T_{\mathrm{d}}) d\lambda. \tag{10}$$

Numerically, the integrals I_1 and I_2 can not (and don't need to) be calculated from zero to infinity as equations (8) and (10) suggest. It is sufficient to integrate over those wavelengths where the star emits a significant fraction of it total radiative energy. On the other hand, the energy balance of the dust cannot be calculated correctly if optical constants (and hence Q_{abs}-values) are lacking even at NIR wavelengths where the maximum of the stellar radiation field is located.

The combination of eqs. (8) (10) leads to eq. (11), which allows calculating the dependence of the dust temperature T_{d} on the distance from the star R_d:

$$R_{\mathrm{d}}(T_{\mathrm{d}}) = \frac{R_*}{\sqrt{1 - [1 - \frac{2I_2}{I_1}]^2}}. \tag{11}$$

For the simplified dilution factor R_*^2/R_{d}^2, the previous equation can also be simplified, namely to

$$R_d(T_d) = \sqrt{\frac{I_1}{I_2}} R_*. \tag{12}$$

For very small dust grains (with sizes amounting to $0.01\,\mu\mathrm{m}$ or less), the relation between T_d and R_d becomes independent of the grain size (which enters into the absorption efficiency $Q_{abs}(\lambda)$, in both the integrals I_1 and I_2; see Krügel 2003). In this case, the influence of the optical constants on $Q_{abs}(\lambda)$ becomes most decisive for the dust temperature. Again in the small particle limit (also called Rayleigh limit), the relation between Q_{abs} and the optical constants n and k is given by

$$Q_{\mathrm{abs}}(\lambda) = 4 \frac{2\pi a}{\lambda} \frac{6nk}{(n^2 - k^2 + 2)^2 + 4n^2k^2}, \tag{13}$$

from which it follows that in those regions where $n(\lambda)$ is approximately constant, such as in the NIR region for the oxide species discussed in this paper, $k(\lambda)$ becomes *the* decisive quantity for $Q_{\mathrm{abs}}(\lambda)$, hence decisive for the dust temperature as well.

More precisely, it is the magnitude of $k(\lambda)$ and $Q_{\mathrm{abs}}(\lambda)$ in the visual and NIR *relative to the respective MIR/FIR-values* that determines the dust temperature. Consequently, dust species that have small $k(\lambda)$, corresponding to their high transparency in the optical and NIR – such as transition metal free oxides and silicates – will be much less heated by the stellar radiation than absorbing grain species. This can be seen most clearly from Fig. 12. For MgO, the lack of absorption mechanisms operating at short wavelegths leads to inefficient radiative heating, such that the dust temperature T_d drops below $500\,\mathrm{K}$ already at two stellar radii. For $\mathrm{Mg_{0.5}Fe_{0.5}O}$, on the other hand, T_d amounts to $2000\,\mathrm{K}$ close to $2\,R_*$. Furthermore, $T_d(R_d)$ drops much more steeply for MgO than for $\mathrm{Mg_{0.5}Fe_{0.5}O}$.

The difference between MgO and $\mathrm{Mg_{0.5}Fe_{0.5}O}$ with respect to NIR absorbance and radiative equilibrium temperature is obviously an extreme case. Smaller, but still significant differences in $T_d(r)$ show up for the other dust species discussed in the present paper, e.g. for spinel (see Fig. 13).

As a consequence of the differences in the absorption efficiency factors calculated according to eq. (13) for small spherical grains – see insert in Fig. 13 – a difference in T_d results. In this case, it amounts to about 25% at $2\,R_*$ (the precise values are $850\,\mathrm{K}$ vs. $625\,\mathrm{K}$ at $2\,R_*$). While Q_{abs} calculated according to eq. (13) for small spherical grains (Fig. 13 insert) increases linearly with k, the increase in T_d in this case appears to be relatively weak, the gradient of T_d with R remains steep for the Cr-containing spinel.

Notwithstanding, it is important to take the effect of $k_{vis/NIR}$ into account, since when it comes to condensation or evaporation, a few degrees Kelvin may decide about the existence or nonexistence of grains in a particular zone around a dust-forming star. Furthermore, there is still another parameter that linearly increases with k in the small particle limit, namely the radiation pressure efficiency factor Q_{pr}. For particles that are smaller than the wavelength, $Q_{pr} \approx Q_{abs}$, and thus an increase in k leads, via eq. (13), to a corresponding increase in Q_{pr}. The more efficiently a dust grain absorbs radiation around $1\,\mu\mathrm{m}$, the larger the radiation pressure it experiences and the velocity it can reach in

9

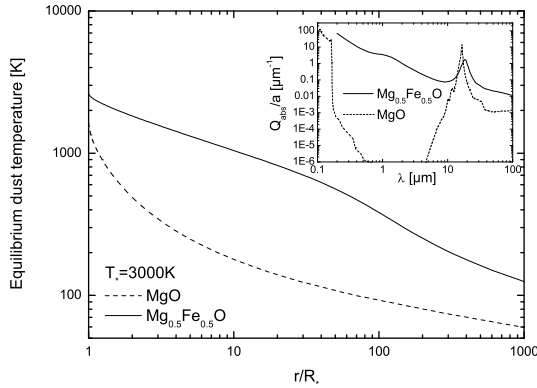S. Zeidler, Th. Posch, H. Mutschke, H. Richter, O. Wehrhan: NIR properties of oxygen-rich stardust

Fig. 12. Comparison of the radiative equilibrium temperature of MgO (characterized by extremely low $k(\lambda)$ values in the NIR region) with the equilibrium temperature of $Mg_{0.5}Fe_{0.5}O$ (its $k(\lambda)$ value is more than seven orders of magnitude larger in the NIR). The stellar effective temperature has been set to 3000 K.
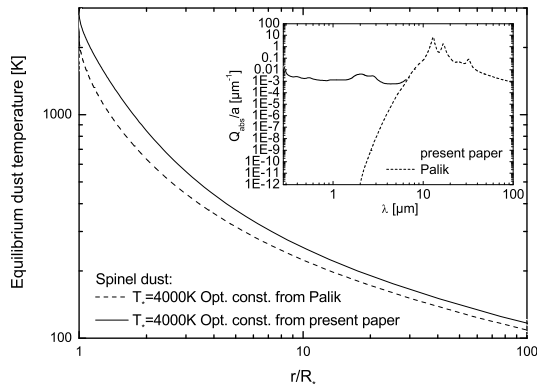

Fig. 13. The radiative equilibrium temperature of natural (terrestrial) spinel dust containing impurities compared to the temperature of impurity-free Mg-Al-spinel according to Palik (1985-98). The stellar effective temperature has been set to 4000 K.

a radiation-pressure driven stellar wind. For a detailed discussion of the influence of absorption *and* scattering on the radiation pressure acting on dust grains, we refer to Höfner (2008).

5. Conclusions

We examined the near-infrared and visual absorption properties of several stardust analogs. Our focus has been on materials for which extremely low k values – or no k values at all – can be found in the literature for the above-mentioned wavelength range: spinel, rutile, anatase, and olivine.

The examined samples were either natural terrestrial ones or synthetic crystals with a defined amount of absorption-enhancing impurities. In all cases, the impurity contents were such as to be compatible with cosmic elemental abundances, and in all cases, the derived k values were 1-2 orders of magnitude higher than the limit of the 'transparency regime' defined at the beginning of this paper (Eq. (1)).

We suggest that even for cosmic dust grains which have smaller impurity contents than our analogs, k values below the limit of transparency will rarely be reached. In cases where no appropriate k data are available, the limit of the 'transparency regime' ($k \approx 10^{-5}$ at $1\,\mu m$ and $k \approx 10^{-4}$ at $10\,\mu m$) may serve as a heuristic lower limit for the absorption of natural materials including stardust grains, although certain circumstances can produce very transparent natural minerals.

Even though the 'real' k values of cosmic dust grains still has to be determinated by further investigations (e.g. on presolar grains), the above constraint seems more realistic than adopting k values dropping to 10^{-8} and below, which can be found in the solid-state physics literature and which mostly refer to synthetic, impurity-free materials.

As an example, we showed that using k data for spinel taken from Palik (1985-98) can lead to underestimating the equilibrium temperature reached by this oxygen-rich dust species in a circumstellar radiation field. More realistic results can be obtained if optical constants with k values above the transparency limit are used. The same holds true for olivine, which is a much more abundant component of circumstellar dust.

The magnitude of absorption also has an important influence on other quantities characterizing an expanding circumstellar shell, such as the radiation pressure. This is, however, beyond the scope of the present paper.

References

Barker, A.J., Wilkinson, G.R., Massa, N.E., et al., 1975, in: Mitra S.S. & Bendow B. (eds.), Optical Properties of Highly Transparent Solids, Plenum, New York

Bohren, C.F., Huffman D.R., 1983, Absorption and Scattering of Light by Small Particles, John Wiley, New York

Bradley, J., in: Henning Th. (ed.), 2003, Astromineralogy, Springer-Verlag, Berlin and Heidelberg, p. 225

Burns, R.G., 1993, Mineralogical Applications of Crystal Field Theory, 2nd ed., Cambridge University Press (= Cambridge Topics in Mineral Physics and Chemistry, vol. 5)

Fabian, D., Posch, Th., Mutschke, H., Kerschbaum, F., Dorschner J., 2001, A&A373, 1125

Hanner, M.S., 2003, in: Henning Th. (ed.), 2003, Astromineralogy, Springer-Verlag, Berlin and Heidelberg, p. 173

Hartmann, W.K., Moons and Planets, 5th ed., Thomson (Belmont, CA), 2005, p. 239

Henning, Th. & Mutschke, H., 1997, A&A, 327, 743

Henning, Th., Begemann, B., Mutschke, H., & Dorschner, J., 1995, A&AS, 112, 143

Henning, T., Il'in, V.B., Krivova, N.A., et al., 1999, A&AS 136, 405

10

Henning, Th., 2003a, in: Solid-State Astrochemistry, eds. V. Pirronello, J. Krelowski and L. Manico, Kluwer, Dordrecht

Henning, Th. (ed.), 2003b, Astromineralogy (= Lecture Notes in Physics, vol. 609), Springer-Verlag, Berlin and Heidelberg

Höfner, S., 2008, A&A491, L1

Hoppe, P., in: ASP Conf. Ser. 309, 265

Ikeda, K., Nakamura, Y., Masumoto, K., Shima, H., 1997, J. Amer. Cer. Soc. 80, 2672

Jeong, K.S., Winters, J.M., LeBertre, T., Sedlmayr, E., 2003 A&A407, 191

Krügel, E., 2003, The Physics of Interstellar Dust, Institute of Physics Publishing, Bristol and Philadelphia

Lenaz, D., Skogby, H., Nestola, F., Princivalle, F., GCA 72, 475

Lucy, L.B., 1971, ApJ, 163, 95

Maldener, J., Rauch, F., Gavranic, M., Beran, A., 2001, Mineralogy & Petrology, 71, 21

Mitra, S.S., 1985, in: Palik E.D. (ed.), Handbook of Optical Constants of Solids I, Academic Press, Boston, p. 213

Nittler, L. R. 2003, EPSL 209, 259

Palik, E.D. (ed.) 1985–1998, Handbook of Optical Constants of Solids, 3 vols., Academic Press, Boston

Palme H., Beer H., 1993, in: O. Madelung (ed.), Landolt-Börnstein, Group VI: Astronomy and Astrophysics, Volume 3, p. 205

Park, J.-C., Kim, D., Lee, Ch.-S., and Kim, D.-K, 1999, Bull. Korean Chem. Soc. 20, 1005

Philipp, H.R., 1985, in: Palik E. D. (ed.), Handbook of Optical Constants of Solids I, Academic Press, Boston, p. 749

Posch, Th., Kerschbaum, F., Mutschke, H., et al., 1999, A&A352, 609

Posch, Th., Kerschbaum, F., Mutschke, H., Dorschner, J., Jäger, C., 2002, A&A393, L7

Posch, Th., Kerschbaum, F., Fabian, D., et al., 2003, Ap&SS149, 437

Ribarsky, M.W., 1985, in: Palik E. D. (ed.), Handbook of Optical Constants of Solids I, Academic Press, Boston, p. 795

Richter, H., Posch, Th., Taran, M., Mutschke, H., 2005, Mineralogy & Petrology, 85, 53

Roessler, D.M., Huffmann, D.R., 1991, in: Palik E. D. (ed.), Handbook of Optical Constants of Solids II, Academic Press, Boston, 919

Shankland, T.J., 1968, Science 161, 51

Sogawa, H., Koike, C., Chihara, H., Suto, H., Tachibana, S., et al., 2006, A&A,451, 357

Tang, H., Berger, H., Schmid, P.E., and Lévy, F., 1993, Solid State Communications 87, 847

Taran, M.N., Langer, K., Platonov, A.N., Indutny, V.V., 1994, Phys. Chem. Minerals 21, 360

Tropf, W.J., Thomas, M.E., 1991, in: Palik E. D. (ed.), Handbook of Optical Constants of Solids II, Academic Press, Boston, p. 883

Wood, D.L., Imbusch, G.F., MacFarlane, R.M., Kisliuk, P., Larkin, P.M., 1968, J. Chem. Phys. 48, 5255

Zhou, W., Liu, Q., Zhu, Z., Zhang, J., 2010, J. Phys. D: Appl. Phys. 43, 035301

11

References

Aarseth, S. J., Henon, M., & Wielen, R. 1974, A&A, 37, 183

Aringer, B., Girardi, L., Nowotny, W., Marigo, P., & Lederer, M. T. 2009, A&A, 503, 913

Barbuy, B., Ortolani, S., & Bica, E. 1998, A&AS, 132, 333

Bellazzini, M., Ferraro, F. R., Sollima, A., Pancino, E., & Origlia, L. 2004, A&A, 424, 199

Bertelli, G., Bressan, A., Chiosi, C., Fagotto, F., & Nasi, E. 1994, A&AS, 106, 275

Bertelli, G., Girardi, L., Marigo, P., & Nasi, E. 2008, A&A, 484, 815

Bessell, M. S. & Brett, J. M. 1988, PASP, 100, 1134

Bessell, M. S., Castelli, F., & Plez, B. 1998, A&A, 333, 231

Blommaert, J. A. D. L., Groenewegen, M. A. T., Okumura, K., et al. 2006, A&A, 460, 555

Boyer, M. L., Woodward, C. E., van Loon, J. T., et al. 2006, AJ, 132, 1415

Bressan, A., Aussel, H., Granato, G. L., et al. 2001, Astrophysics and Space Science Supplement, 277, 251

Bressan, A., Granato, G. L., & Silva, L. 1998, A&A, 332, 135

Bressan, A., Panuzzo, P., Buson, L., et al. 2006, ApJ, 639, L55

Bressan, A., Panuzzo, P., Silva, L., et al. 2007, in Astronomical Society of the Pacific Conference Series, Vol. 374, From Stars to Galaxies: Building the Pieces to Build Up the Universe, ed. A. Vallenari, R. Tantalo, L. Portinari, & A. Moretti, 333

Carpenter, J. M. 2001, AJ, 121, 2851

Clement, C. 1997, VizieR Online Data Catalog, 5097

Clement, C. M., Muzzin, A., Dufton, Q., et al. 2001, AJ, 122, 2587

Cohen, M., Wheaton, W. A., & Megeath, S. T. 2003, AJ, 126, 1090

Conroy, C. & Spergel, D. N. 2010, ArXiv e-prints

Creech-Eakman, M. J., Stencel, R. E., Williams, W. J., & Klebe, D. I. 1997, ApJ, 477, 825

Dotter, A., Chaboyer, B., Jevremović, D., et al. 2007, AJ, 134, 376

Ferraro, F. R., Dalessandro, E., Mucciarelli, A., et al. 2009, Nature, 462, 483

Ferrarotti, A. S. & Gail, H. 2005, A&A, 430, 959

Ferrarotti, A. S. & Gail, H. 2006, A&A, 447, 553

Frogel, J. A. & Elias, J. H. 1988, ApJ, 324, 823

Gail, H. & Sedlmayr, E. 1998, Chemistry and Physics of Molecules and Grains in Space. Faraday Discussions No. 109. The Faraday Division of the Royal Society of Chemistry, London, 1998., p.303, 109, 303

Gilra, D. P. 1973, in IAU Symposium, Vol. 52, Interstellar Dust and Related Topics, ed. J. M. Greenberg & H. C. van de Hulst, 517

Girardi, L., Groenewegen, M. A. T., Hatziminaoglou, E., & da Costa, L. 2005, A&A, 436, 895

Girardi, L. & Salaris, M. 2001, MNRAS, 323, 109

Groenewegen, M. A. T. 1995, A&A, 293, 463

Groenewegen, M. A. T. 2006, A&A, 448, 181

Groenewegen, M. A. T. & Blommaert, J. A. D. L. 2005, A&A, 443, 143

Habing, H. J. 1996, A&A Rev., 7, 97

Habing, H. J. & Olofsson, H., eds. 2003, Asymptotic giant branch stars

Harris, W. E. 1997, VizieR Online Data Catalog, 7202

Henning, T. K., ed. 2003, Lecture Notes in Physics, Berlin Springer Verlag, Vol. 609, Astromineralogy

Heras, A. M. & Hony, S. 2005, A&A, 439, 171

Herwig, F. 2005, ARA&A, 43, 435

Höfner, S. 2008, A&A, 491, L1

Höfner, S., Gautschy-Loidl, R., Aringer, B., & Jørgensen, U. G. 2003, A&A, 399, 589

Iben, Jr., I. 1991, ApJS, 76, 55

Iben, Jr., I. & Renzini, A. 1983, ARA&A, 21, 271

Ita, Y., Tanabé, T., Matsunaga, N., et al. 2007, PASJ, 59, 437

Ita, Y., Tanabé, T., Matsunaga, N., Nakada, Y., & The Irsf/Sirius Team. 2004, in Astronomical Society of the Pacific Conference Series, Vol. 310, IAU Colloq. 193: Variable Stars in the Local Group, ed. D. W. Kurtz & K. R. Pollard, 50

Ivezic, Z. & Elitzur, M. 1997, MNRAS, 287, 799

Jeong, K. S., Winters, J. M., & Sedlmayr, E. 1999, in IAU Symposium, Vol. 191, Asymptotic Giant Branch Stars, ed. T. Le Bertre, A. Lebre, & C. Waelkens, 233

Kinman, T. D. & Rosino, L. 1962, PASP, 74, 499

Kraemer, K. E., Sloan, G. C., Price, S. D., & Walker, H. J. 2002, ApJS, 140, 389

Kroupa, P. 1998, in Astronomical Society of the Pacific Conference Series, Vol. 134, Brown Dwarfs and Extrasolar Planets, ed. R. Rebolo, E. L. Martin, & M. R. Zapatero Osorio, 483

Kroupa, P. 2001, MNRAS, 322, 231

Leão, I. C., de Laverny, P., Mékarnia, D., de Medeiros, J. R., & Vandame, B. 2006, A&A, 455, 187

Le Bertre, T. 1992, A&AS, 94, 377

Lebzelter, T., Posch, T., Hinkle, K., Wood, P. R., & Bouwman, J. 2006, ApJ, 653, L145

Lebzelter, T. & Wood, P. R. 2005, A&A, 441, 1117

Lebzelter, T. & Wood, P. R. 2007, A&A, 475, 643

Lebzelter, T. & Wood, P. R. 2011, A&A, submitted

Lebzelter, T., Wood, P. R., Hinkle, K. H., Joyce, R. R., & Fekel, F. C. 2005, A&A, 432, 207

Levine, D., Wu, X., Good, J., et al. 2009, in Astronomical Society of the Pacific Conference Series, Vol. 411, Astronomical Society of the Pacific Conference Series, ed. D. A. Bohlender, D. Durand, & P. Dowler, 29

Little-Marenin, I. R., Stencel, R. E., & Staley, S. B. 1996, ApJ, 467, 806

Lobel, A., Bagnulo, S., Doyle, J. G., & Power, C. 2000, MNRAS, 317, 391

Marigo, P., Girardi, L., Bressan, A., et al. 2008, A&A, 482, 883

Marín-Franch, A., Aparicio, A., Piotto, G., et al. 2009, ApJ, 694, 1498

Mathis, J. S. 1990, ARA&A, 28, 37

Matsunaga, N., Deguchi, S., Ita, Y., Tanabe, T., & Nakada, Y. 2005, PASJ, 57, L1

McDonald, I. & van Loon, J. T. 2007, A&A, 476, 1261

McDonald, I., van Loon, J. T., Decin, L., et al. 2009, MNRAS, 394, 831

McDonald, I., van Loon, J. T., Dupree, A. K., & Boyer, M. L. 2010, MNRAS, 405, 1711

McDonald, I. et al. 2011, in prep.

Molster, F. J. & Waters, L. B. F. M. 2003, in Lecture Notes in Physics, Berlin Springer Verlag, Vol. 609, Astromineralogy, ed. T. K. Henning, 121–170

Monnier, J. D., Geballe, T. R., & Danchi, W. C. 1998, ApJ, 502, 833

Monnier, J. D., Geballe, T. R., & Danchi, W. C. 1999, ApJ, 521, 261

Omont, A., Gilmore, G. F., Alard, C., et al. 2003, A&A, 403, 975

Onaka, T., de Jong, T., & Yamamura, I. 2002, A&A, 388, 573

Origlia, L., Ferraro, F. R., Fusi Pecci, F., & Rood, R. T. 2002, ApJ, 571, 458

Piotto, G. 2008, Mem. Soc. Astron. Italiana, 79, 334

Posch, T., Kerschbaum, F., Mutschke, H., Dorschner, J., & Jäger, C. 2002, A&A, 393, L7

Posch, T., Kerschbaum, F., Mutschke, H., et al. 1999, A&A, 352, 609

Reimers, D. 1975, Memoires of the Societe Royale des Sciences de Liege, 8, 369

Renzini, A. & Fusi Pecci, F. 1988, ARA&A, 26, 199

Richter, H., Posch, T., Taran, M. N., & Mutschke, H. 2005, Mineralogy and Petrology, 85, 53

Rieke, G. H. & Lebofsky, M. J. 1985, ApJ, 288, 618

Salaris, M., Chieffi, A., & Straniero, O. 1993, ApJ, 414, 580

Sandin, C. & Höfner, S. 2003, A&A, 404, 789

Skrutskie, M. F., Cutri, R. M., Stiening, R., et al. 2006, AJ, 131, 1163

Sloan, G. C., Kraemer, K. E., Goebel, J. H., & Price, S. D. 2003a, ApJ, 594, 483

Sloan, G. C., Kraemer, K. E., Price, S. D., & Shipman, R. F. 2003b, ApJS, 147, 379

Sloan, G. C., Matsunaga, N., Matsuura, M., et al. 2010, ApJ, 719, 1274

Székely, P., Kiss, L. L., Jackson, R., et al. 2007, A&A, 463, 589

Trager, S. C., Djorgovski, S., & King, I. R. 1993, in Astronomical Society of the Pacific Conference Series, Vol. 50, Structure and Dynamics of Globular Clusters, ed. S. G. Djorgovski & G. Meylan, 347

van Loon, J. T., McDonald, I., Oliveira, J. M., et al. 2006, A&A, 450, 339

Vassiliadis, E. & Wood, P. R. 1993, ApJ, 413, 641

Whitelock, P., Marang, F., & Feast, M. 2000, MNRAS, 319, 728

Whitelock, P. A., Feast, M. W., & van Leeuwen, F. 2008, MNRAS, 386, 313

Zinn, R. & West, M. J. 1984, ApJS, 55, 45

List of Figures

List of Tables

Acronyms

AGB	Asymptotic Giant Branch
AOR	Astronomical Observation Request
BCD	Basic Calibrated Data
CMD	Color-Magnitude Diagram
	(Not to be mistaken with the CMD interface for Padova isochrones.)
FP	Feature Position
HRD	Hertzsprung-Russel Diagram
IMF	Initial Mass Function
LF	Luminosity Function
LPV	Long Period Variable
MIR	Mid-Infrared
NIR	Near-Infrared
PN	Planetary Nebula
RGB	Red Giant Branch
SED	Spectral Energy Distribution
SRV	Semiregular Variable
TLF	Theoretical Luminosity Function
TO	Turn-off
TP	Thermal Pulse
ZAMS	Zero-Age Main Sequence

Mag. Hannes Richter, MA

Lorbeergasse 13/5
A-1030 Vienna

hannes.richter@univie.ac.at

Curriculum Vitæ

Personal data

Name	Mag. Hannes Richter, MA
Date of birth	14 July 1981
Place of birth	Vienna
Citizenship	Austria

Education

10/2007 - present	⋆ PhD-study of Astronomy, University of Vienna → Graduate School "The Cosmic Matter Circuit" → PhD Thesis: *Tracing dust in old stellar populations*
03/2010 - 05/2010	⋆ Research detention at INAF, Padova, Italy
10/2006 - 11/2008	⋆ Public Communication, Postgraduate Certificate Program → Specialisation in Public Relations → Master Thesis: *A PR-Concept for the WU Executive Academy*
10/1999 - 07/2005	⋆ Study of Astronomy, University of Vienna, degree with distinction → Master Thesis / *Atlas der optischen Konstanten astronomisch relevanter Festkörper* → $ÖGA^2$ Master Thesis Award 2005 / 2nd place
09/2003 & 06/2004	⋆ Research detention at the Astrophysical Institute of the University of Jena → Infrared spectroscopy of Titanium-Oxides (Anatase & Rutile) → Synthetisation and infrared spectroscopy of Chromium-Spinel
09/1987 - 07/1999	⋆ Bundesrealgymnasium III, Radetzkystraße, 1030 Vienna → AHS-Matura with distinction Volksschule Aspernallee, 1020 Vienna

Employment record / Internships

12/2010 - present	⋆ Scientific employee / VHS Wien / Astronomie Wien
14.11.2010	⋆ Astronomical presentations / Science Brunch / Aula der Wissenschaften
08/2010 - 10/2010	⋆ Conceptual design *Juwelen im Kosmos* / Show / Zeiss Planetarium Wien

10/2009 - present	⋆ Project Manager/ klimaretter.at → Initative against climate change / www.klimaretter.at
08.11.2008	⋆ Co-ordination / 2nd Long Night of Science → Strategic planning, lectures and presentations
10/2007 - 12/2010	⋆ Assistant / Graduate School / University of Vienna
07/2007 - 10/2007	⋆ Event Manager / Club Planetarium
04/2007 - 12/2007	⋆ Editoral Journalist / scIQ - wissen für junge leute (scientific journal)
13.03.2007	⋆ Presentation of astronomical highlights / Eblinger&Partner
02/2007 - 04/2007	⋆ Editoral Journalist / pressetext
11/2006 - 04/2007	⋆ PR Assistant / Temmel, Seywald & Partner Communications → Project Management: Pfizer → Project Assistance: Trivadis, UC4 Software, Anglo Irish Bank, GRÖ ...
07/2006	⋆ Internship / KURIER Department Internal Politics → Inquest, Interviews, Press Conferences, Reports
04/2006 - 06/2006	⋆ Internship / Radio Max → Moderation, News, Reports, Interviews, Speech Training
01.10.2005	⋆ Co-ordination / 1st Long Night of Science → Strategic planning, lectures and presentations
09/2005 - present	⋆ Production of the TV series *SuperNova* (OKTO Community-TV) → Editorial, Direction, Screenplay, Camera, Cut, Moderation
01/2003 - present	⋆ Show-Operator / VHS Wien / Zeiss Planetarium Wien → Live moderation and multimedia operation → Presentation of scientific topics to kids and adults

Scientific publications

2005	⋆ Richter, H., Posch, Th., Taran, M.N. and Mutschke, H. 2005, Mineralogy & Petrology, 85: 53-65 *Absorption Properties of Synthetic Cr-doped Spinels in the UV, Visible and Infrared Range and their Astronomical Implications*
2005	⋆ Posch, Th., Kerschbaum, F., Richter, H. and Mutschke, H. 2005, ESA SP-577, 257 *Solid State Features in the Herschel-Pacs Range*

Skills / Personal interests

Languages

⋆ English (professional fluency)
⋆ Spanish, Frensh (basic knowledge)

Skills / Personal interests (continued)

Computer skills and applications

Operating Systems   ⋆ Windows, Mac OSX

Computer Languages   ⋆ IDL, Fortran90

Applications   ⋆ MS Office, ORIGIN, FinalCut Pro, Filemaker, Photoshop, LaTeX

Personal interests

Hobbies, Sports   ⋆ Climbing, Cooking, Ecology, Origami, Swimming, Volleyball